

Numerical Investigations of Two-Dimensional Photonic Crystal Optical Properties, Design and Analysis of Photonic Crystal Based Structures

THÈSE N° 4315 (2009)

PRÉSENTÉE LE 30 AVRIL 2009

À LA FACULTÉ SCIENCES DE BASE
LABORATOIRE D'OPTOÉLECTRONIQUE QUANTIQUE
PROGRAMME DOCTORAL EN PHYSIQUE

ÉCOLE POLYTECHNIQUE FÉDÉRALE DE LAUSANNE

POUR L'OBTENTION DU GRADE DE DOCTEUR ÈS SCIENCES

PAR

Vasily ZABELIN

acceptée sur proposition du jury:

Prof. G. Meylan, président du jury
Dr R. Houdré, directeur de thèse
Dr D. Gallagher, rapporteur
Prof. H. P. Herzig, rapporteur
Dr R. Stanley, rapporteur



ÉCOLE POLYTECHNIQUE
FÉDÉRALE DE LAUSANNE

Suisse
2009

Contents

Abstract	iii
Résumé	v
Preface	vii
1 Basic properties of the photonic crystals	1
1.1 Introduction to photonic crystals	1
1.2 Light propagation in a periodic media	5
1.2.1 The Bloch-Floquet theorem	5
1.2.2 The scaling properties of the photonic crystals	7
1.3 One-dimensional photonic crystals	8
1.4 Two-dimensional photonic crystals	11
1.4.1 The slab polarization	12
1.4.2 Dispersion properties of 2D photonic crystals	14
1.5 Defects in two-dimensional photonic crystals	16
2 Light mode properties of the two-dimensional photonic crystals	21
2.1 The Maxwell's equations for the electromagnetic field	21
2.2 The plane wave expansion method	22
2.3 Approximation of the dielectric permittivity distribution	24
2.3.1 Filtering of the Gibbs phenomenon	33
2.3.2 Calculation of the permittivity Fourier expansion coefficients . .	37
2.4 Frequency-based plane wave expansion method	38
2.5 Light propagation in photonic crystals	42
2.5.1 Dispersion properties of photonic crystals	42
2.5.2 Group velocity of the propagating Bloch modes	49
2.5.3 Shape of the frequency isolines and the self-collimation effect . .	53
2.6 Field distribution of the Bloch modes	59
2.6.1 In-plane field components and the effect of the Gibbs phenomenon	59
2.6.2 Field distribution of the propagating Bloch modes	62
2.7 Cavities and localized states	66
2.8 Evanescent modes in photonic crystals	69
2.8.1 Ministop band in the W3 waveguide	69
2.8.2 Penetration of the guided modes into the cladding regions . . .	71

3	The guided mode expansion method	75
3.1	Introduction	75
3.2	Guided modes of the planar waveguide	75
3.3	Guided modes expansion	80
3.4	Comparison of the PWE and the GME methods	83
4	Analysis of small variations of photonic crystal parameters	87
4.1	The Bloch mode calculation and the perturbation theory	88
4.2	Variations of the permittivity distribution	90
4.3	Application of the perturbation method	92
5	Polarization Beam Splitter design	99
5.1	Simple design	100
5.2	Self-collimation based design	101
6	Conclusions and perspectives	107
A	Optical properties of the 2D photonic crystals	109
A.1	Dispersion properties of photonic crystals	109
A.1.1	Square lattice photonic crystals	109
A.1.2	Triangular lattice photonic crystals	111
A.2	Group velocity of the propagating Bloch modes	113
A.2.1	Square lattice photonic crystals	113
A.2.2	Triangular lattice photonic crystals	114
A.3	Shape of the frequency isolines	115
A.3.1	Square lattice photonic crystals	115
A.3.2	Triangular lattice photonic crystals	117
	Acknowledgments	119
	Bibliography	121
	Conference presentations and publications	129
	Curriculum Vitae	131

Abstract

Two-dimensional (2D) photonic crystals (PhCs) operating in the near-infrared wavelengths are promising candidates for novel integrated optics applications. In this work the optical properties of the Bloch modes in 2D photonic crystals have been investigated theoretically using different numerical methods. The plane wave expansion (PWE) method have been formulated in a general form for arbitrary 2D photonic crystal and applied for detailed analysis of the properties of the Bloch modes. The k space based and the frequency based PWE methods have been derived and used, which allowed us to analyze both propagating and evanescent modes.

The guided mode expansion method have been used to take into account three-dimensional distribution of the electromagnetic field in the planar photonic crystals and improve the accuracy of the analysis.

A new method of calculation of the sensitivity of the photonic crystal optical properties to small variations of the photonic crystal parameters have been developed. This method is based on the perturbation theory and allows fast and accurate estimation of the optical properties corrections as a result of a change the parameters of the photonic crystal.

The developed methods have been used for design and analysis of different photonic crystal based structures, such as cavities, waveguides, coupled-cavity waveguides and polarization beam splitter.

The developed methods proved to be efficient and accurate tools for modelling two-dimensional photonic crystal properties and design of photonic crystal based devices.

Keywords:

photonic crystals - numerical modelling - Bloch mode optical properties - plane wave expansion method - guided mode expansion method - polarization beam splitter

Résumé

Les cristaux photoniques bidimensionnels (2D) conçus pour fonctionner dans la plage de longueur d'onde du proche infrarouge sont des candidats prometteurs pour de nouvelles applications en optique intégrée. Dans ce travail, les propriétés optiques des modes de Bloch dans des cristaux photoniques 2D ont été étudiées de façon théorique à partir de différentes méthodes numériques. La méthode de développement en onde plane (DOP) a été établie dans un cadre général pour des cristaux photoniques 2D arbitraires et ensuite appliquée pour l'analyse détaillée des propriétés des modes de Bloch. La méthode DOP a été développée soit à partir des fréquences spatiales soit à partir des fréquences angulaires, ce qui nous a permis d'analyser à la fois les modes propagatifs et les modes évanescents.

La méthode de développement en mode guidés a été utilisée pour prendre en compte la distribution tridimensionnelle du champ électromagnétique dans les cristaux photoniques planaires. Cette méthode a permis d'améliorer la précision de l'analyse.

Une nouvelle méthode de calcul de la sensibilité des propriétés optiques des cristaux photoniques vis-à-vis de petites variations de leurs paramètres structuraux a été développée. Cette méthode repose sur la théorie de la perturbation et permet une estimation rapide et précise de la modification des propriétés optiques des cristaux photoniques en fonction des changements de leurs paramètres structuraux.

Les méthodes développées ont été utilisées pour la conception et l'analyse de différentes structures en cristaux photoniques, tels que des cavités, guides, guides-cavités couplées et séparateurs de polarisation.

Les méthodes développées se sont révélées efficaces et précises pour modéliser les propriétés des cristaux photoniques bidimensionnels et pour concevoir des dispositifs à cristaux photoniques.

Mots de clés:

cristaux photoniques - méthodes numériques - propriétés optiques des modes de Bloch - développement en onde plane - développement en mode guidés - séparateurs de polarisation

Preface

Periodic modulation of the dielectric permittivity and/or the magnetic permeability of the media creates the structures called photonic crystals. In these structures the periodicity affects the photons with the comparable wavelength in a way similar to that in which the crystals affect the properties of electrons. As a result the photonic structure consisting of the photonic bands and band gaps (similar to the electronic structures in semiconductor or metal crystals) are formed.

Complex dispersion structure of the light states opens many possibilities to control the light propagation in the photonic crystals. The light dispersion properties in photonic crystals are, in general, polarization-sensitive and direction-sensitive [1, 2]. Proper design of the photonic crystal allows to tailor light properties for the desired application.

If the light frequency is inside the band gap, the propagation of the light modes is forbidden and the photonic crystal serves as a photonic insulator. Such structures can be used to reflect all incident light or to confine light in a small volume, creating a microcavity [3, 4] or a waveguide [5].

High sensitivity of the dispersion properties to the light frequency leads to the superprism effect [6] and can be used to create new-generation sensors.

Two-dimensional photonic crystals are considered among the key components of modern and future integrated optics because they open many new possibilities of light control and can be fabricated using well-developed technologies with high accuracy and reproducibility.

Development of photonic crystal based devices and structures requires careful analysis of interaction between light and the photonic crystal and numerical modelling is an essential part of the design process.

There are many methods to describe properties of the light modes in photonic crystals. The most popular and versatile are:

- Mode expansion methods. This is a family of the methods based on the idea of decomposition of the a light mode in a photonic crystal over the basis of known functions.
- Scattering matrix methods [7, 8]. In these methods modulation of the dielectric permittivity is considered as the system of scattering sources located in a layer which is repeated periodically in a particular direction. Propagation of the light through the media is described using the scattering matrix of the layer.
- Finite-Difference Time-Domain (FDTD) method [9]. In this method the Maxwell's equations for the electromagnetic field are discretized over a regular grid in space

and time evolution of the field in each grid site is calculated using the finite-difference formulas.

All these methods have their advantages and disadvantages.

The FDTD method is a “brute force” method which can be used to calculate light evolution in almost any structure, periodic or not, and provides direct information about the electromagnetic field distribution. Among the disadvantages are: high demands for the computational resources (calculation time and required memory), especially in the 3D case; special treatment for the boundaries with discontinuous dielectric permittivity and/or magnetic permeability to suppress approximation errors; the method provides a raw data for the field distribution, special sophisticated treatment is required to extract necessary information like frequency and Bloch vector of a mode, transmission coefficient of a device etc.

The scattering matrix method also can treat the non-periodic structures but because scattering of the light on the scattering centers usually is calculated analytically the scattering centers with simple shape (spheres, cylinders, etc.) are considered. Since the scattering centers have to be arranged in the layers there are some restrictions on the photonic crystal structures (lattice symmetry, positions of the scattering centers, etc.) which can be taken into account.

The mode expansion methods (particular cases of which are the Plane Wave Expansion method and the Guided Mode Expansion method) are based on decomposition of the field distribution in the photonic crystal using the basis of functions associated with the considered photonic crystal. Choosing the proper basis set the Maxwell’s equations can be written in a simplified form which allows to find the decomposition coefficients. The advantage of such methods is that they are quite flexible and can take into account almost any photonic crystal structure. Another important point is that these methods give details about the behavior of the intrinsic properties of the light states in photonic crystals and facilitate understanding of light behavior in photonic crystals. The disadvantage of the mode expansion methods is that they are quite sensitive to selection of basis functions and non-optimal basis can lead to poor convergence of the method.

In this thesis the plane wave expansion method and the guided mode expansion method have been considered. Implementation of these methods for the two-dimensional photonic crystal have been analyzed and several ways how to improve the methods have been proposed.

The manuscript is organized as follows:

In the first chapter the basis properties of the photonic crystals are introduced and discussed. This chapter defines the concepts which are used throughout the manuscript. In the second chapter the plane wave expansion method is derived for arbitrarily two-dimensional photonic crystals. The effect of the discontinuity of the dielectric permittivity and magnetic permeability is discussed and methods to minimize the errors introduced by the discontinuity are proposed. Bloch vector based and frequency based plane wave expansion methods are considered and implemented for the detailed analysis of propagating and evanescent light modes in typical two-dimensional photonic crystals.

The third chapter describes the guided mode expansion method derived for quasi-2D photonic crystals fabricated using the planar waveguide for the light confinement in the vertical direction. The optical properties of such photonic crystals are discussed and

accuracy of the plane wave expansion method and the guided mode expansion method are compared.

In the fourth chapter a new method of analysis of small variations of photonic crystal parameters is proposed. This method is based on the perturbation theory and can greatly speed-up analysis of the sensitivity of the optical properties to modification of the photonic crystal.

In the fifth chapter a polarization beam splitter is discussed. Utilization of the developed methods for design of the device structure and analysis of the device performance illustrates application and utility of the modelling as an essential tool for engineering new integrated optics devices.

Additional information about the optical properties of two-dimensional photonic crystals is collected in the appendix.

The manuscript is rounded off by the conclusions and discussion of future perspectives of presented work.

Chapter 1

Basic properties of the photonic crystals

1.1 Introduction to photonic crystals

Physics of crystalline materials now is one of the most developed parts of natural science. Properties of natural crystals (*e.g.* gems) have been object of many researches since the antiquity. The tremendous progress of physics and technology in past century in many respects has been inspired and leaded by the progress in material science, especially related with the physics of metals and semiconductors. Understanding how the crystalline structure determines physical properties of the crystals allows one to design and fabricate such indispensable devices as computer chips and semiconductor lasers.

Periodic arrangements of atoms in the crystal lattice determines the periodic potential for the valence electrons and set the behavior of the electrons in the crystal. Materials with different crystalline structures exhibit broad range of physical properties and according to their electronic structures can be metals, insulators, semiconductors, superconductors etc.

The developed ability to control electrons in crystals and to design devices with many important properties inspired the interest to create artificial structures which can control the photons in a way similar to electrons in crystals.

Such structures are called the photonic crystals (PhCs). They can be created by a periodic modulation of the dielectric permittivity and/or the magnetic permeability of the media. Propagation of the light in a periodic media was object of the research for many years (see, for example [10–12]).

It has been shown that the the spontaneous emission rate of the atoms in the media can be affected by changing the optical properties of the media and the emission rate can be enhanced due to coupling with the resonant states [13] or can be forbidden if no light states are available for the given frequency [14].

Possibility to control the spontaneous emission rate inspires the search for the periodic structures which have the full photonic band gap – frequency region where the light cannot propagate through the structure.

The full photonic band gap has been predicted for structure consisting of the dielectric spheres arranged in the diamond structure [15] and for the face-centered-cubic

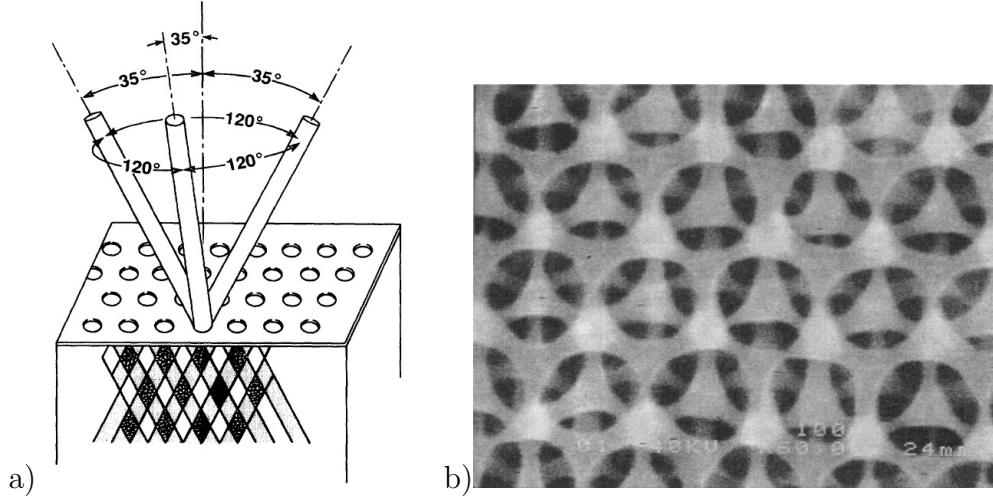


Figure 1.1: a) The photonic crystal structure proposed by Yablonovitch *et al.* in [16]. b) Yablonovite structure fabricated by the ion beam etching (from [17]).

structure with non-spherical atoms [16]. The latter structure (called Yablonovite) is created by etching (or drilling) cylindrical holes in high-permittivity dielectric, as it is schematically shown in the Fig. 1.1(a). The photonic band gap has been demonstrated for this type of photonic crystal in the microwave range [16]. Utilization of the ion beam etching allows one to significantly decrease size of the holes and demonstrate the photonic band gap effect for infrared light [17].

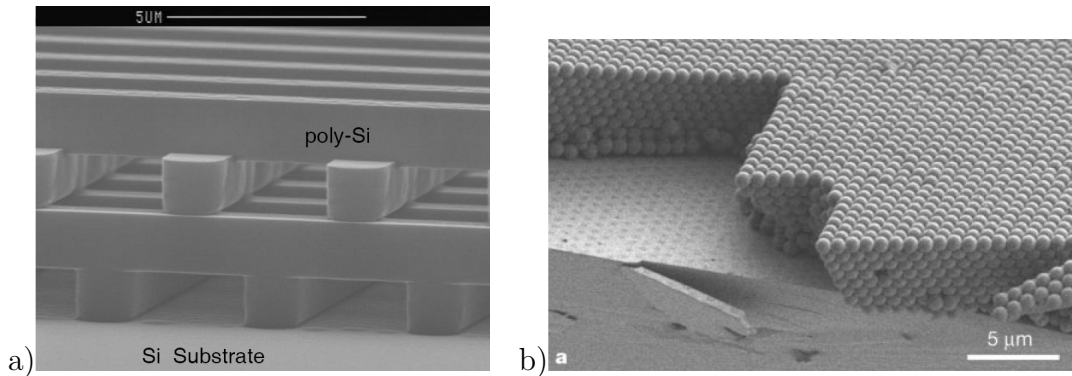


Figure 1.2: a) 3D photonic crystal consisting a stack of Si bars (from [18]). b) 3D photonic crystal with the opal structure (from [19]).

Many three-dimensional photonic crystal structures have been proposed in past years and are subject of intense research now. Two main ways of 3D photonic crystal structures fabrication can be selected: artificial fabrication and self-assembled structures. The first is artificial assembly layer-by-layer structures consisting high-dielectric bars in air (usually with the woodpile arrangement) [18, 20, 21]. A typical 3D photonic crystal with the woodpile structure is shown in the Fig. 1.2(a). The second is working with the opal structures (closely-packed lattice of SiO_2 spheres in air), which are self-assembled from the water colloid of monodisperse silica spheres [19, 22]. By filling the inter-sphere space with high-dielectric material and subsequent etching of the silica the inverse opal

structures can be fabricated [19, 23]. 3D photonic crystal with the opal structure is shown in the Fig. 1.2(b).

The advantage of 3D photonic crystals is that they can control propagation of the light in all three dimensions, which allows, for example, total suppression of the spontaneous emission by creation of the full photonic band gap. But the main disadvantage of 3D photonic crystals is difficult fabrication process, which limits types of possible structures (lattice symmetry, materials etc.) and incorporation of desired defects in the photonic crystal.

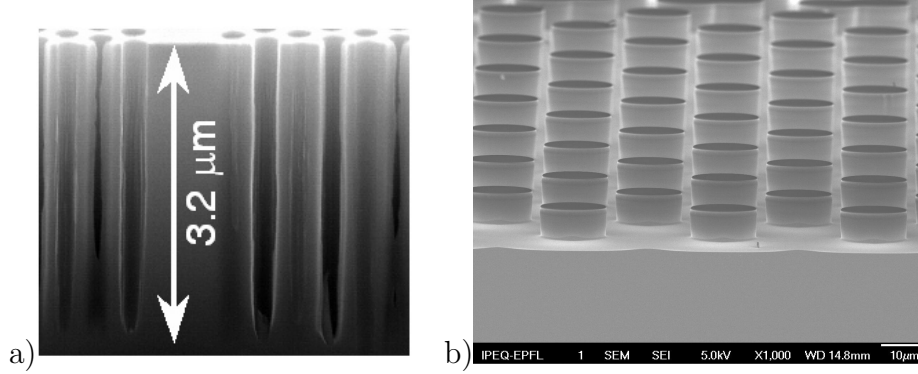


Figure 1.3: a) Air holes etched in a GaAs/AlGaAs planar waveguide. b) GaAs/AlGaAs pillars in air.

The fabrication problem can be overcome by working with two-dimensional structures, where the mature modern planar technology is used. In this case the light is localized in the vertical direction by a planar waveguide and the photonic crystal structure is created by periodic modulation of the waveguide in plane. Two main types of the modulation are shown in the Fig. 1.3: low-dielectric (usually air) holes in the high-dielectric planar waveguide (Fig. 1.3(a)) and high-dielectric pillars in low-dielectric (usually air) media Fig. 1.3(b). High quality etching technology allows one to produce almost vertical holes/pillars boundaries, which decrease out-of-plane light scattering losses to acceptable values [24, 25]. Due to their fabrication quality and flexibility of structure designs which can be implemented two-dimensional photonic crystals now become most used type of photonic crystals.

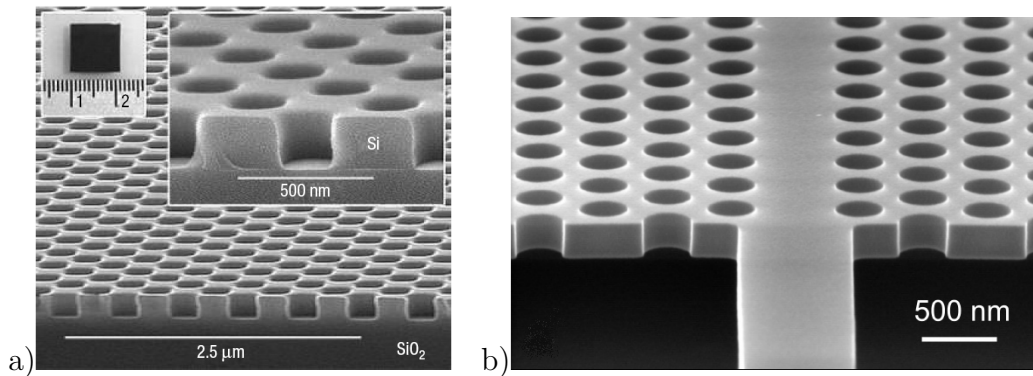


Figure 1.4: a) SOI based photonic crystal structure (from [26]). b) Membrane based photonic crystal structure (from [27]).

Planar waveguides with low index contrast have weak light localization in the vertical direction and usually have the thickness of a few microns. It requires high-quality etching at this depth (such as presented in the (Fig. 1.3(a)), which is still a challenging task. Utilization of waveguides with high index contrast, like SOI structures (shown in the Fig. 1.4(a)) or Si membrane in air (shown in the Fig. 1.4(b)) allows one to localize the light in the vertical direction with the typical scale less than micron, which facilitates fabrication process and decrease the radiation losses.

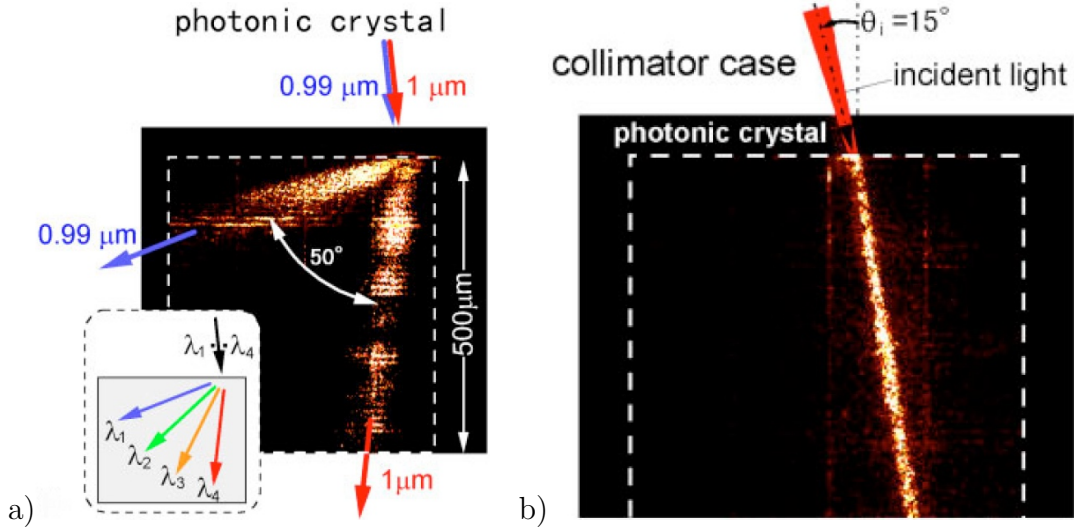


Figure 1.5: a) The superprism effect in a 2D photonic crystal (from [28]). b) The self-collimation effect in a 2D photonic crystal (from [29]).

Interaction of propagating light with the periodic modulation of the dielectric permittivity modifies the dispersion relation of the light modes and leads to many important phenomena, among them are the superprism effect (very strong dependence of the light propagation direction on the light frequency) [6, 28, 30, 31] demonstrated in the Fig. 1.5(a), and the self-collimation effect (propagation of the light beam with a very small divergence for a long distance) [26, 29, 32–39] presented in the Fig. 1.5(b).

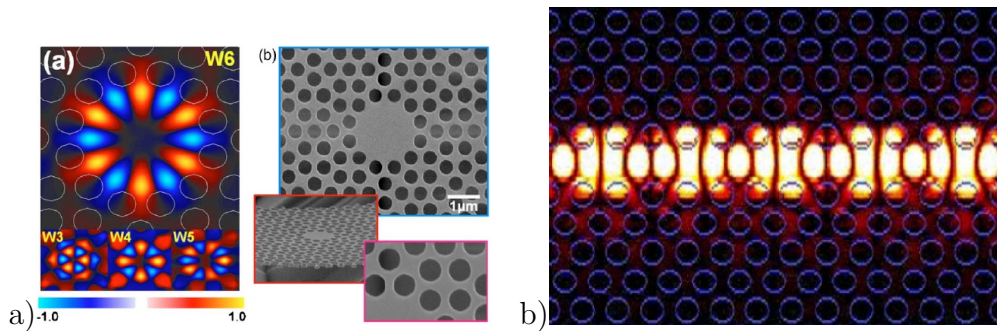


Figure 1.6: a) Light localization in a photonic crystal cavity (from [40]). b) Light guiding in a photonic crystal waveguide (from [41]).

The full 2D (for all in-plane directions) photonic band gap can also be achieved for 2D photonic crystals. It allows one to fabricate microcavities where the light is strongly localized (see the Fig. 1.6(a)). Such cavities are building blocks for nanolasers [40, 42]

and frequency filters [3, 43], can be used to control light emission from quantum dots [4] etc. One-dimensional defects of the photonic crystal can be used as waveguides with small waveguide core and strong light localization (see the Fig. 1.6(b)) [5, 41].

Such a broad variety of phenomena exhibited by photonic crystals inspired many designs of photonic crystal based devices. A good understanding of the background physical nature of photonic crystal optical properties and accurate theoretical description of light propagation in a periodic media are key elements for future progress in photonic crystal based integrated optics.

Later in this chapter the basis theoretical concepts required to describe light propagation in photonic crystals will be introduced and basic types of photonic crystal based structures will be discussed.

1.2 Light propagation in a periodic media

1.2.1 The Bloch-Floquet theorem

There are many analogies between the properties of the light propagating through a periodic media and electrons propagating through a crystal with a periodic potential. So, many ideas and theories initially developed for physics of the solid-state may be applied for photonic crystals. One of the most useful and important is the Bloch-Floquet theorem, which describes properties of the electron wave function in a crystal with the periodic potential. This stationary wave functions $\psi(\mathbf{r})$ of the electrons are the eigenfunctions of the equation

$$\mathcal{H} \psi(\mathbf{r}) = E \psi(\mathbf{r}), \quad \text{where} \quad \mathcal{H} = -\frac{\hbar^2}{2m} \nabla^2 + U(\mathbf{r}) \quad (1.1)$$

Here \mathcal{H} is the Hamiltonian of the electron in a potential field and E is the energy of the state. The potential $U(\mathbf{r})$ has the periodicity $U(\mathbf{r} + \mathbf{R}) = U(\mathbf{r})$, where \mathbf{R} is a vector of the period.

For the electromagnetic field the master equations are

$$\begin{aligned} \mathcal{V} \mathbf{E} &= \frac{w^2}{c^2} \mathbf{E}, \quad \text{where} \quad \mathcal{V} = \frac{1}{\varepsilon(\mathbf{r})} \nabla \times \frac{1}{\mu(\mathbf{r})} \nabla \times \\ \mathcal{W} \mathbf{H} &= \frac{w^2}{c^2} \mathbf{H}, \quad \text{where} \quad \mathcal{W} = \frac{1}{\mu(\mathbf{r})} \nabla \times \frac{1}{\varepsilon(\mathbf{r})} \nabla \times \end{aligned} \quad (1.2)$$

for the electric field \mathbf{E} and the magnetic field \mathbf{H} , respectively. The master operators for the electric field (\mathcal{V}) and the magnetic field (\mathcal{W}) depend on the dielectric permittivity of the media $\varepsilon(\mathbf{r})$ and the magnetic permeability $\mu(\mathbf{r})$. In photonic crystals the permittivity and the permeability have the same periodicity: $\varepsilon(\mathbf{r}) = \varepsilon(\mathbf{r} + \mathbf{R})$, $\mu(\mathbf{r}) = \mu(\mathbf{r} + \mathbf{R})$.

The relations 1.2 can also be written in a general form of an eigenvalue problem as

$$\mathcal{L} \psi(\mathbf{r}) = \lambda \psi(\mathbf{r}) \quad (1.3)$$

where \mathcal{L} represents either \mathcal{V} or \mathcal{W} and ψ represents either \mathbf{E} or \mathbf{H} .

Let $\mathcal{T}_{\mathbf{R}}$ be the translation operator, which shifts argument of any function f :

$$\mathcal{T}_{\mathbf{R}} f(\mathbf{r}) = f(\mathbf{r} + \mathbf{R}) \quad (1.4)$$

Because of the periodicity of the permittivity and the permeability

$$\mathcal{T}_{\mathbf{R}} \mathcal{L} \psi(\mathbf{r}) = \mathcal{L}(\mathbf{r} + \mathbf{R}) \psi(\mathbf{r} + \mathbf{R}) = \mathcal{L}(\mathbf{r}) \psi(\mathbf{r} + \mathbf{R}) = \mathcal{L} \mathcal{T}_{\mathbf{R}} \psi(\mathbf{r}) \quad (1.5)$$

Since the equation (1.5) is valid for any function ψ

$$\mathcal{T}_{\mathbf{R}} \mathcal{L} = \mathcal{L} \mathcal{T}_{\mathbf{R}}. \quad (1.6)$$

The result of two consequent translations doesn't depend on the order of the translations because

$$\mathcal{T}_{\mathbf{R}} \mathcal{T}_{\mathbf{R}'} \psi(\mathbf{r}) = \mathcal{T}_{\mathbf{R}'} \mathcal{T}_{\mathbf{R}} \psi(\mathbf{r}) = \psi(\mathbf{r} + \mathbf{R} + \mathbf{R}') \quad (1.7)$$

and hence,

$$\mathcal{T}_{\mathbf{R}} \mathcal{T}_{\mathbf{R}'} = \mathcal{T}_{\mathbf{R}'} \mathcal{T}_{\mathbf{R}} = \mathcal{T}_{\mathbf{R} + \mathbf{R}'} \quad (1.8)$$

Equations (1.5) and (1.8) show that the master operator \mathcal{L} and the translation operators for all possible periodic translations generate the set of commuting operators. Then it is possible to choose the eigenstates of the operator \mathcal{L} which are simultaneously the eigenstates of the operator $\mathcal{T}_{\mathbf{R}}$:

$$\begin{cases} \mathcal{L} \psi &= \lambda \psi \\ \mathcal{T}_{\mathbf{R}} \psi &= c(\mathbf{R}) \psi \end{cases}$$

It is worth to note, that the eigenvalues of the equation (1.9) can be mutually degenerated, *i.e.* for a given eigenvalue λ there may be several eigenvalues $c(\mathbf{R})$ and vice versa.

Since the eigenvalues of the translation operator \mathcal{T} satisfy the relation

$$c(\mathbf{R} + \mathbf{R}') = c(\mathbf{R}) \cdot c(\mathbf{R}') \quad (1.9)$$

they can be represented in the form

$$c(\mathbf{R}) = e^{i\mathbf{k}\mathbf{R}} \quad (1.10)$$

where \mathbf{k} is the Bloch vector.

Then an eigenstate of the equation (1.3) can be represented in the form

$$\psi(\mathbf{r}) = e^{i\mathbf{k}\mathbf{r}} u_{\mathbf{k}}(\mathbf{r}) \quad (1.11)$$

where $u_{\mathbf{k}}(\mathbf{r})$ has the same periodicity as the photonic crystal.

Since the exponent has the period equal to $i2\pi$ ($e^{\phi+i2\pi} = e^{\phi}$) for a given eigenvalue $c(\mathbf{R})$ of the translation operator $\mathcal{T}_{\mathbf{R}}$ the Bloch vector in the equation (1.10) cannot be uniquely determined. If a wave vector \mathbf{k}' is so that $\mathbf{k}' \cdot \mathbf{R} = 2\pi$ then $e^{i(\mathbf{k}+\mathbf{k}')\mathbf{R}} = e^{i\mathbf{k}\mathbf{R}}$. So, two states with such Bloch vectors \mathbf{k} and $\mathbf{k} + \mathbf{k}'$ actually correspond to the same state. Usually it is convenient to select in k-space an area where the Bloch vectors can be uniquely defined and then use these vectors to select the translation properties of the light states in the periodic media.

1.2.2 The scaling properties of the photonic crystals

An interesting property of the photonic crystals is the scalability, *i.e.* a possibility to scale all geometrical dimensions of the sample or to scale the values of the dielectric permittivity or magnetic permeability keeping all the features related to the light propagation (but for the scaled light wavelength).

The master equation for the magnetic field is

$$\frac{1}{\mu(\mathbf{r})} \nabla \times \frac{1}{\varepsilon(\mathbf{r})} \nabla \times \mathbf{H}_w(\mathbf{r}) = \left(\frac{w}{c}\right)^2 \mathbf{H}_w(\mathbf{r}) \quad (1.12)$$

If the distribution of the dielectric permittivity $\varepsilon(\mathbf{r})$ and the magnetic permeability $\mu(\mathbf{r})$ are shrunk or expanded by a scaling factor α , *i.e.* the new distributions are $\varepsilon'(\mathbf{r}) = \varepsilon(\mathbf{r}/\alpha) = \varepsilon(\mathbf{r}')$ and $\mu'(\mathbf{r}) = \mu(\mathbf{r}/\alpha) = \mu(\mathbf{r}')$. After changing the variables in equation (1.12) by substituting $\mathbf{r}' = \mathbf{r}/\alpha$ the nabla operator ∇ turns to $\nabla' = \alpha \nabla$ and the equation (1.12) transforms into

$$\frac{1}{\mu(\mathbf{r}')} \nabla' \times \frac{1}{\varepsilon(\mathbf{r}')} \nabla' \times \mathbf{H}_w(\mathbf{r}') = \left(\frac{w}{\alpha c}\right)^2 \mathbf{H}_w(\mathbf{r}') \quad (1.13)$$

It means that for the photonic crystal shrunk (expanded) by a factor of α the frequency of the state is multiplied (divided) by α , while the profile of the electromagnetic field is just scaled by α .

Since the periodicity of the field remains the same the eigenvalue of the translation operator doesn't change:

$$e^{i\mathbf{k}\mathbf{R}} = e^{i\mathbf{k}'\mathbf{R}'} = e^{i(\alpha\mathbf{k})(\mathbf{R}/\alpha)}, \quad (1.14)$$

but the scaled period corresponds to the scaled Bloch vector.

This scaling properties can be automatically taken into account by introducing a dimensionless Bloch vector and a dimensionless frequency:

$$\tilde{\mathbf{k}} = \frac{a}{2\pi} \mathbf{k} \quad (1.15)$$

$$u = \frac{a}{2\pi c} w = \frac{a}{\lambda} \quad (1.16)$$

where a is any characteristic scale of the photonic crystal (usually the length of the period is chosen) and λ is the light wavelength in the vacuum. It also has the meaning of measuring the Bloch vector \mathbf{k} in the units $\frac{2\pi}{a}$ and the frequency w in the units $\frac{2\pi c}{a}$.

The dimensionless Bloch vector $\tilde{\mathbf{k}}$ and the dimensionless frequency u usually are referred to as the *reduced Bloch vector* and the *reduced frequency* or the *reduced energy*, respectively. The reduced Bloch vector and the reduced frequency uniquely identify the Bloch state independently on the spatial scaling of the photonic crystal.

Another scaling property is related with the dielectric permittivity (or the magnetic permeability) values and contrast. By changing the permittivity by a factor of β^2 : $\varepsilon'(\mathbf{r}) = \beta^2 \varepsilon(\mathbf{r})$ the equation (1.12) becomes

$$\frac{1}{\mu(\mathbf{r})} \nabla \times \frac{1}{\varepsilon'(\mathbf{r})} \nabla \times \mathbf{H}_w(\mathbf{r}) = \left(\frac{w}{\beta c}\right)^2 \mathbf{H}_w(\mathbf{r}) \quad (1.17)$$

Hence, the field profile stays the same but the frequency of the state is multiplied by the factor β . Because the refractive index of a media equals to the square root of the permittivity scaling of the permittivity by a factor β^2 corresponds to changing of the refractive index by the factor β . It means that the change of the state frequency (for the same Bloch vector) is proportional to the change of the refractive index. Similar relation corresponds to the scaling of the magnetic permeability.

1.3 One-dimensional photonic crystals

One-dimensional photonic crystals have the dielectric permittivity modulated in one direction, for example, y : $\varepsilon(\mathbf{r}) = \varepsilon(y)$. (Here and later in this chapter it is assumed that the magnetic permeability $\mu \equiv 1$. It is true for most of the used photonic crystals.) This is the simplest type of photonic crystals and it allows us to introduce many important properties of the photonic crystals, which will be used later. If the minimum period of the modulation is equal to a the Bloch vector of the light can be uniquely defined in the area where $-\pi/a < k_y < \pi/a$, because adding of a vector $\mathbf{k}' = m \cdot (0, 2\pi/a, 0)$ (where m is any integer nonzero value) doesn't change the translation properties of the light state.

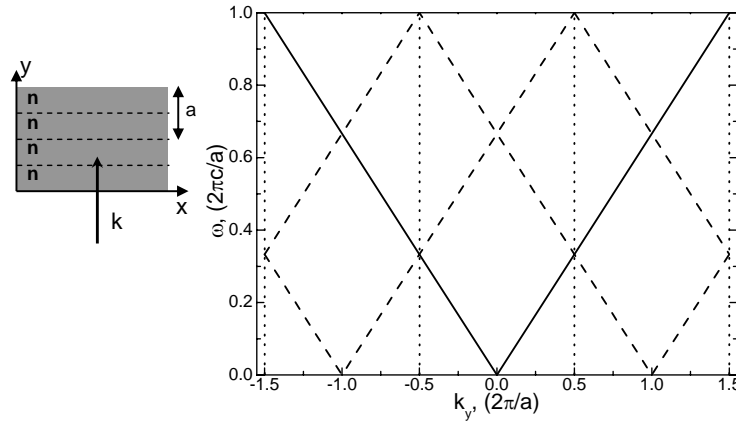


Figure 1.7: Dispersion of the light propagating in the uniform media with the artificial period a .

The dispersion of the light propagating along the y axis in a media with the refractive index $n = 1.5$ is shown in the Fig. 1.7. There is the main part (plotted as a thick line), where $w = k/n$. Because of the periodicity the Bloch vector is defined with the uncertainty $k' = m \cdot 2\pi/a$ (see the section 1.2.1), which results in the additional parts (plotted by the dashed lines) obtained by shifting the main part by k' . Hence, the dispersion in the whole k -space can be described considering only area where $-\pi/a < k_y < \pi/a$, since the Bloch vector \mathbf{k} is the equivalent of the vector $\mathbf{k} + \mathbf{k}'$. This area is the first Brillouin zone for one-dimensional crystal. For a selected \mathbf{k} there are several possible solutions with different frequencies, called bands. Then the light state can be uniquely specified as $\psi_{\mathbf{k},n}$ by the Bloch vector \mathbf{k} and the band number n .

If the permittivity is non-uniform it leads to an important change of the light dispersion. An example of the dispersion of the light propagating along the y axis through

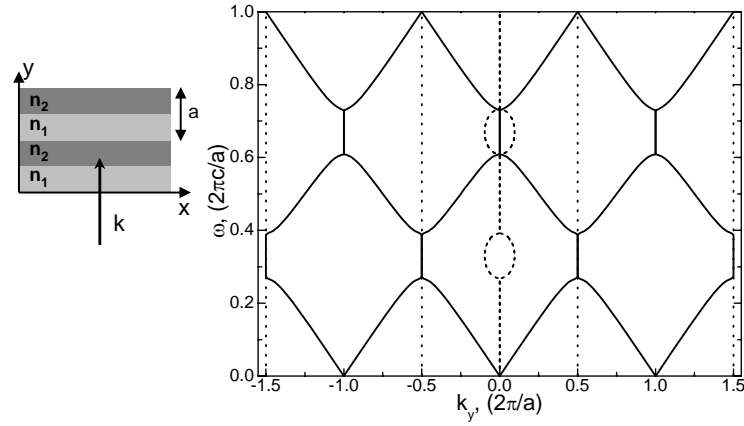


Figure 1.8: Dispersion of the 1D photonic crystal.

the multilayer structure consisting of the layers with thickness $a/2$ and the refractive indices $n_1 = 1$ and $n_2 = 2$ is presented in the Fig. 1.8. The real part of the Bloch vector is plotted as a solid line and the imaginary part as a dashed line. The anticrossing of the lines leads to opening the gaps where the Bloch vector has imaginary part. In this case the amplitude of the field of the light state exponentially decays in the photonic crystal and such states cannot exist in an infinite crystal (but can exist near the crystal boundaries or defects, as it will be discussed later). This frequency regions are referred to as the band gaps and there are no propagating states inside them. The width of the band gaps depends on thicknesses the layers and the index contrast $n_{high} - n_{low}$ and grows with increasing of the contrast.

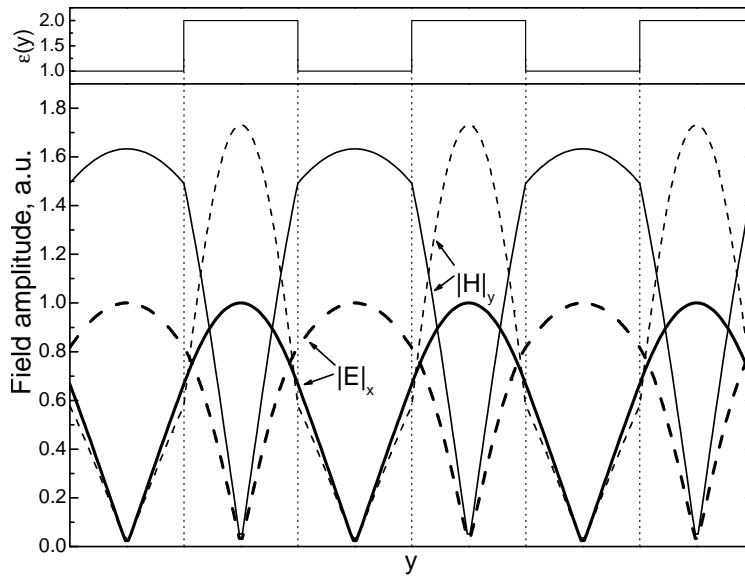


Figure 1.9: Electric and magnetic field amplitudes for different Bloch states of the photonic crystal shown in the Fig. 1.8.

The anticrossing of the dispersion lines is the result of the coupling of the states with the same Bloch vector. Because such states have the same periodicity the electromagnetic field can be redistributed to form the states with different energy and, hence,

frequency. The amplitudes of the field for two states with $k_y = \pi/a$ are presented in the Fig. 1.9. The fields corresponding to the top of the first band are plotted as solid lines while the ones for the bottom of the second band are shown as dashed lines. Thick lines show the amplitude of the electric field (here the linear polarization along the x axis is assumed) and the thin ones are related to the amplitude of the magnetic field.

For the state with the lower frequency the electric field tends to be localized in the layers with high permittivity (the distribution of the permittivity is shown as the inset at the top of the figure) and the magnetic field is maximum in the layers with lower permittivity. For the state with the higher frequency the situation is opposite: the electric field is localized in the layers with low permittivity while the magnetic field is maximum in the layers with high permittivity.

When the light propagates with an incidence angle, situation becomes more complex. Assuming the Bloch vector in the (xy) plane there are two different solutions which correspond to different light polarizations. The first (called s-polarization) has the electric field only in the z direction and the magnetic field in the (xy) plane. The second (called p-polarization) has the magnetic field only in the z direction and the electric field in the (xy) plane.

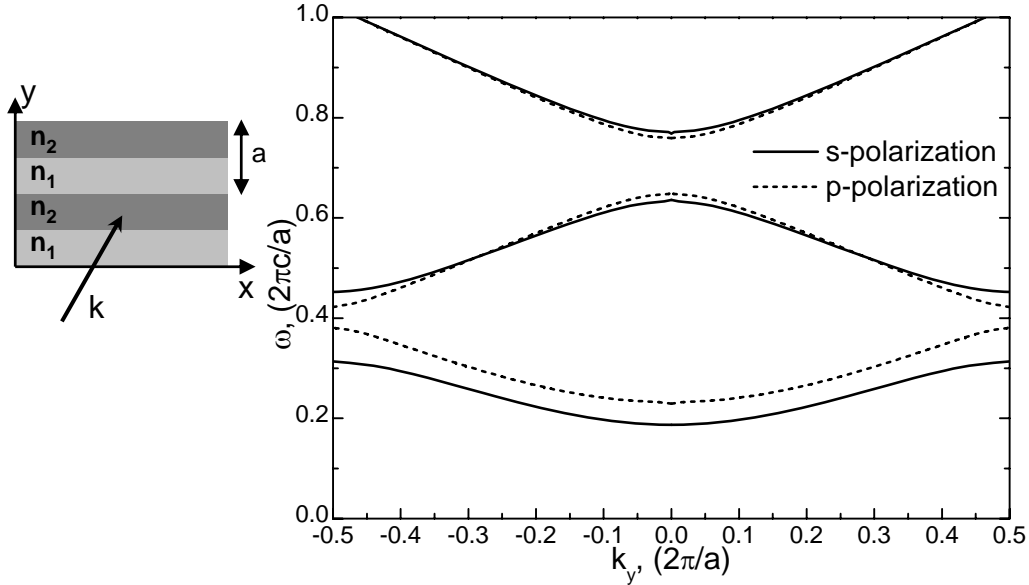


Figure 1.10: Dispersion relations of the Bloch modes with different light polarizations.

The dispersion relations of light with different polarizations are presented in the Fig. 1.10. Only propagating states (with real Bloch vectors) are shown. The x component of the Bloch vector $k_x = 0.3 (2\pi/a)$. Because of different interaction of the light with these polarizations with the media (and especially with the internal boundaries) they have different dispersion properties: different shape and position of the bands, different position and width of the band gaps.

1.4 Two-dimensional photonic crystals

In two-dimensional photonic crystals the permittivity is modulated in two directions, for example, in the (xy) plane: $\varepsilon(\mathbf{r}) = \varepsilon(x, y)$. Any period \mathbf{R} can be represented as $\mathbf{R} = m_1 \mathbf{a}_1 + m_2 \mathbf{a}_2 + m_3 \mathbf{a}_3$, where \mathbf{a}_j are translation vectors, which form the basis of the photonic crystal lattice. m_j are integer numbers. For the 2D photonic crystals \mathbf{a}_1 and \mathbf{a}_2 are in the (xy) plane and \mathbf{a}_3 can be chosen to be in the z direction. Because the permittivity is constant along the z direction the length of \mathbf{a}_3 can be chosen arbitrarily, it doesn't affect the results.

Two main types of 2D lattices are presented in the Fig. 1.11: a) square lattice ($a_1 = a_2 = a$, $\angle(\mathbf{a}_1, \mathbf{a}_2) = 90^\circ$) and b) triangular lattice ($a_1 = a_2 = a$, $\angle(\mathbf{a}_1, \mathbf{a}_2) = 60^\circ$). The translation vectors \mathbf{a}_1 and \mathbf{a}_2 are plotted by dark arrows and the lattice primitive cell is indicated by dashed line. Photonic crystal “atoms” are shown as gray circles.

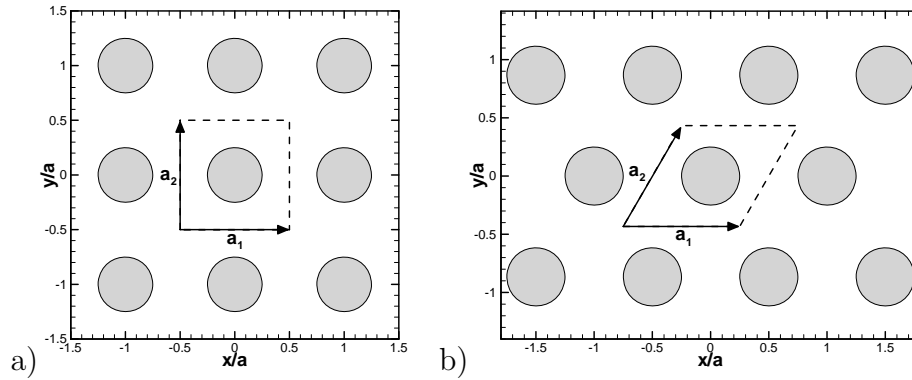


Figure 1.11: Main types of 2D PhC lattices. a) Square lattice. b) Triangular lattice.

For a given set of the basis vectors $\{\mathbf{a}_j\}$ the corresponding set of the reciprocal basis vectors $\{\mathbf{b}_j\}$ is defined by $\mathbf{a}_i \cdot \mathbf{b}_j = 2\pi\delta_{ij}$. The solution to these equations is:

$$\mathbf{b}_1 = 2\pi \frac{\mathbf{a}_2 \times \mathbf{a}_3}{V_c}, \quad \mathbf{b}_2 = 2\pi \frac{\mathbf{a}_3 \times \mathbf{a}_1}{V_c}, \quad \mathbf{b}_3 = 2\pi \frac{\mathbf{a}_1 \times \mathbf{a}_2}{V_c} \quad (1.18)$$

where $V_c = (\mathbf{a}_1 \times \mathbf{a}_2) \cdot \mathbf{a}_3$ is the volume of the primitive unit cell.

The reciprocal basis vectors form the basis set in the reciprocal space and they define the reciprocal lattice of the crystal. The reciprocal lattices for the selected types of the 2D lattices are shown in the Fig. 1.12. The sites of the reciprocal lattices are indicated by dark points and the reciprocal basis vectors are plotted as dark arrows.

Because $\mathbf{a}_i \cdot \mathbf{b}_j = 2\pi\delta_{ij}$ for any vector of the reciprocal lattice $\mathbf{k}' = p_1 \mathbf{b}_1 + p_2 \mathbf{b}_2 + p_3 \mathbf{b}_3$ (where p_j are any integer numbers) $\mathbf{k}' \cdot \mathbf{R} = 2\pi(m_1 p_1 + m_2 p_2 + m_3 p_3)$ and $e^{i\mathbf{k}' \cdot \mathbf{R}} = 1$. Hence, \mathbf{k} and $\mathbf{k} + \mathbf{k}'$ are equivalent Bloch vectors. There are many ways to select the area where the Bloch vector can be uniquely defined. The most common is to choose an area in k -space where all k -vectors are closer to a selected site of the reciprocal lattice than to all other sites. These areas are called the first Brillouin zones of the lattice. They surround each site of the reciprocal lattice and the set of all Brillouin zones completely fills the plane.

The first Brillouin zones are shown in the Fig. 1.12 as gray polyhedrons around the reciprocal lattice sites.

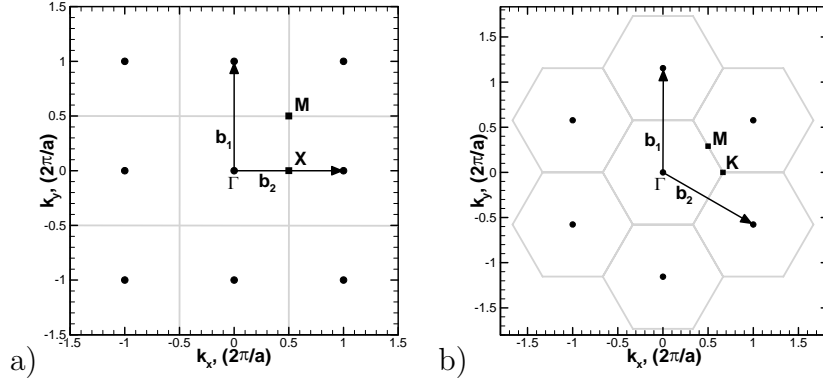


Figure 1.12: Main types of 2D PhC reciprocal lattices. a) Square lattice. b) Triangular lattice.

The reciprocal lattice for the square lattice has several points with high symmetry: Γ point – any reciprocal lattice site, X point – center of the line connected two nearest reciprocal lattice sites, and M point – center of the line connected two second-nearest-neighbour reciprocal lattice sites. Positions of such high symmetry points are indicated in the Fig. 1.12(a).

The corresponding points of the reciprocal lattice for the triangular lattice are: Γ point – any reciprocal lattice site, M point – center of the line connected two nearest reciprocal lattice sites, and K point – center of the triangle formed by three nearest reciprocal lattice sites. These points are shown in the Fig. 1.12(b).

An important parameter of the photonic crystal is the filling factor which is defined as the fraction of the photonic crystal primitive cell area occupied by the photonic crystal “atoms”. This parameter reflects the coupling strength of the light and the photonic crystal and greatly affects the Bloch mode dispersion properties.

For the square lattice photonic crystal consisting of a single circular atom in the primitive cell the filling factor $f = \frac{\pi R^2}{a^2}$, where R is the radius of the atom and a is the lattice constant.

For the triangular lattice photonic crystal consisting of a single circular atom in the primitive cell the filling factor $f = \frac{2\pi}{\sqrt{3}} \frac{R^2}{a^2}$.

1.4.1 The slab polarization

In an ideal 2D photonic crystal there is a translational symmetry along the z direction. In this case there are two different polarization of the light. For the first one the electric field has no component along the z direction: $E_z = 0$. So, the electric field has only components in the (xy) plane and such states are called as the *transverse electric* or TE-polarized light. For the second one the magnetic field has no component along the z direction and these states are referred to as the *transverse magnetic* or TM-polarized light.

But real photonic crystals have finite thickness and the breaking of the translation symmetry in the z direction modifies the field properties. In order to confine the light in the z direction a planar waveguide is often used. It has a core with higher refractive index surrounded by cladding layers with lower refractive indices. Such waveguide has

no translational symmetry in the z direction, but has the translation symmetry in the (xy) plane.

Consider the light propagating in such waveguide along the x direction. All fields are uniform in the y direction: $\psi = \text{const}(y)$. Because of the translation symmetry along the x direction there are two different polarizations: the first has $E_x = 0$ and the second has $H_x = 0$. For the first case the electric field has only one component $E_y \neq 0$ and the magnetic field has non-zero components in the (xz) plane. It can be considered as the *quasi*-TE polarization. In the second case the magnetic field has only one component $H_y \neq 0$ and non-zero electric field components in the (xz) plane. It can be considered as the *quasi*-TM polarization.

The optical properties of the photonic crystal slabs have been considered in many papers, see, for example [44–47]

Two examples of the planar waveguide have been examined in this thesis. The first is an InP-based waveguide with weak refractive index contrast [48]. The waveguide consists of the GaInAsP core layer of thickness 522 nm with the refractive index $n_{refr} = 3.35$ sandwiched between two InP cladding layers of thickness 300 nm (upper) and 600 nm (lower) with the refractive index $n_{refr} = 3.17$. The substrate is n^+ -doped InP layer with the refractive index $n_{refr} = 3.24$. This waveguide later will be referred to as the thick waveguide.

The second waveguide is an SOI (Silicon-On-Insulator) structure with the high refractive index contrast. The waveguide core is a Si layer of thickness 220 nm with the refractive index $n_{refr} = 3.477$ and the waveguide lower cladding layer is SiO_2 substrate with the refractive index $n_{refr} = 1.444$. This waveguide will be referred to as the thin waveguide.

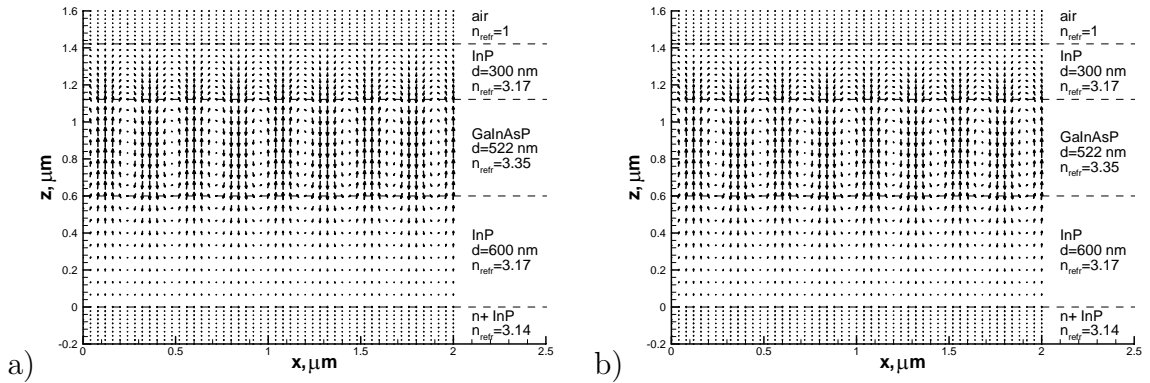


Figure 1.13: Field distribution of guided modes propagating in the thick planar waveguide. a) Magnetic field distribution \mathbf{H}_{xz} for the *quasi*-TE light polarization. b) Electric field distribution \mathbf{E}_{xz} for the *quasi*-TM light polarization.

Examples of the corresponding field distributions for the light with the vacuum wavelength $\lambda = 1.55 \mu\text{m}$ propagating in the thick waveguide are shown in the Fig. 1.13.

One can see that for the TE-polarized light the magnetic field is mainly vertical (especially in the core layer, where the field amplitude is maximum). Electric field distribution for the TM-polarized light has similar structure. Hence, the horizontal components of the fields can be neglected and it is assumed, that there is only H_z component for

the TE-polarized light and only E_z -component for the TM-polarized light. It means, that the distribution of the entire electromagnetic field can be described using only one scalar variable ($H_z(\mathbf{r})$ or $E_z(\mathbf{r})$, respectively) which simplifies the calculations.

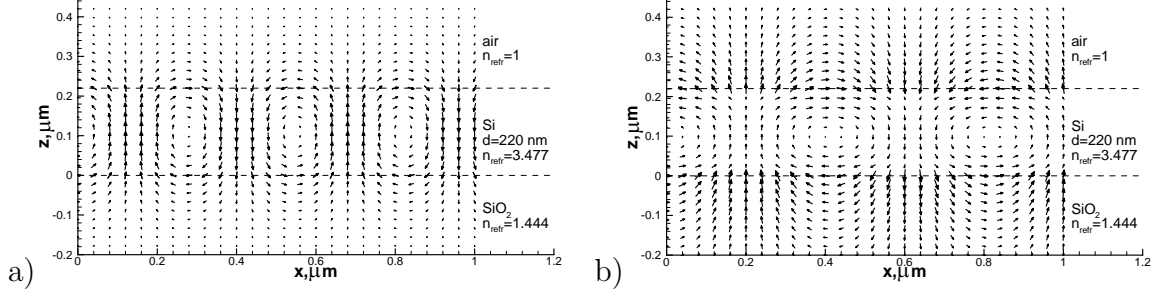


Figure 1.14: Field distribution of guided modes propagating in the thin planar waveguide. a) Magnetic field distribution \mathbf{H}_{xz} for the *quasi*-TE light polarization. b) Electric field distribution \mathbf{E}_{xz} for the *quasi*-TM light polarization.

But for thin waveguides with high refractive index contrast the situation is more complex. Because the light is more confined in the z direction the field distribution is changed.

Examples of the electromagnetic field distributions for the light propagating in the thin waveguide are presented in the Fig. 1.14. The magnetic and the electric fields now have noticeable horizontal components. However, the fields still can be considered as mainly vertical and the approximation of single z -component can be used. But the error of this approximation is larger in case of the thin waveguides.

1.4.2 Dispersion properties of 2D photonic crystals

The dispersion of the Bloch modes of two-dimensional photonic crystals has many similarities with the dispersion of the Bloch modes in one-dimensional photonic crystals, but is more complex, because in this case the frequency is a function of the Bloch vector $\omega = \omega(\mathbf{k})$, instead of the scalar k as for 1D photonic crystals. As it has been discussed above in the section 1.4 the dispersion has the same periodicity as the reciprocal lattice and the Bloch vector can be uniquely defined in the Brillouin zone. For a given \mathbf{k} vector there are several possible values of frequencies: $\omega = \omega_n(\mathbf{k})$. These values form series of surfaces in the (ω, \mathbf{k}) space, called the photonic bands of the photonic crystal.

The examples of the Bloch mode dispersions are shown in the Fig. 1.15. Here only real Bloch vectors are assumed. The considered photonic crystal has the triangular lattice and the corresponding first Brillouin zone is the regular hexagon (indicated in the figure by the white dash line). The circular holes etched in the planar waveguide serve as the “atoms” of the photonic crystal. For small frequency (and corresponding large wavelength) the shape of the frequency isolines are almost circular. When the wavelength is much larger than the size of the crystal unit cell the light reacts on the averaged permittivity and the photonic crystal can be considered as an homogenous media [49]. Because the “atoms” in this example are circular (and so have high rotational symmetry) the effective media is almost isotropic. If the PhC atoms are anisotropic

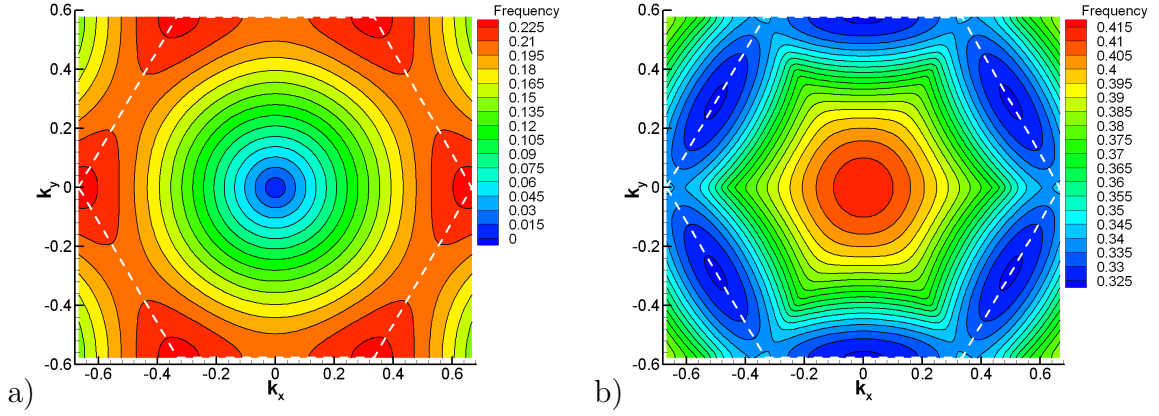


Figure 1.15: Dispersion of the TE-polarized Bloch modes for the triangular lattice photonic crystal consisting of the circular air holes (the filling factor $f = 0.4$) in the dielectric slab with the effective refractive index $n_{eff} = 3.24$. a) The first band. b) The second band.

the intrinsic anisotropy of the permittivity distribution leads to the anisotropy of the effective media even for the small frequencies.

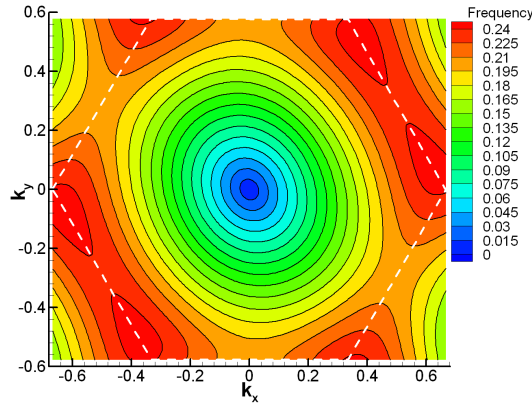


Figure 1.16: Dispersion of the first band TE-polarized Bloch modes for the triangular lattice photonic crystal consisting of the elliptical air holes (the filling factor $f = 0.4$) in the dielectric slab with the effective refractive index $n_{eff} = 3.24$.

An example of the dispersion of the first band Bloch modes for the photonic crystal consisting of the elliptical atoms is presented in the Fig. 1.16. The ratio of the length of the main axes of the ellipse $\beta = 2$ and the angle between the ellipse longer axis and the x axis is 30° . High eccentricity of the atoms leads to strong anisotropy of the dispersion near the Γ point.

When the Bloch vector \mathbf{k} is close to the boundary of the Brillouin zone (and the wavelength is comparable with the size of the unit cell) the shape of the frequency isolines is different from the circle and we can see the effect of the periodicity of the permittivity distribution.

For the second band the shape of the frequency isolines is quite complex. Because it corresponds to the higher frequency the light wavelength is less and such states depends

more on the exact permittivity distribution inside the photonic crystal primitive cell.

The standard way for the representation of the dispersion properties is to plot the cross-sections of the surfaces $w_n(\mathbf{k})$. It is convenient to use the directions where the Brillouin zone has the symmetry, like ΓM or ΓK for the triangular PhC lattice.

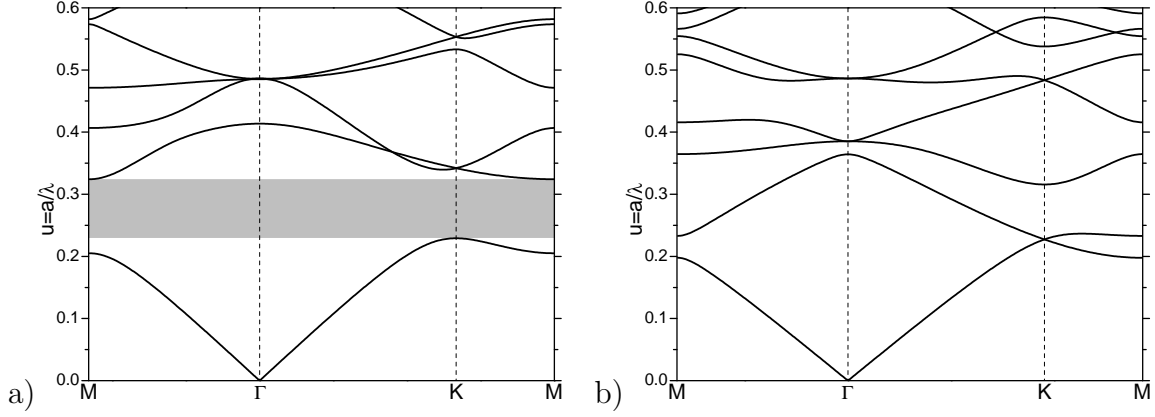


Figure 1.17: Dispersion of the Bloch modes for the triangular lattice photonic crystal consisting of the circular air holes (the filling factor $f = 0.4$) in the dielectric slab with the effective refractive index $n_{eff} = 3.24$. a) TE polarization. b) TM polarization.

Examples of such cross-sections are shown in Fig. 1.17. For the TE polarization there is a band gap between the first and the second gaps indicated by the grey color. For this frequency range only states with non-zero imaginary part of the Bloch vector \mathbf{k} exist. Such states cannot propagate through the photonic crystal and carry the energy. For the TM polarization there is no full band gap but there are partial band gaps (for example, along the ΓM direction) where the transmission of the light is forbidden.

1.5 Defects in two-dimensional photonic crystals

Any irregularities in the photonic crystal lattice destroy the translation symmetry and modifies the photonic crystal optical properties. In perfect photonic crystal Bloch modes with different frequencies and/or different Bloch vectors are orthogonal. Presence of the defects introduces coupling between the different Bloch modes and so, defects serve as scattering centers for propagating Bloch modes.

Another way of changing the optical properties is creation of new states. A defect has a core (zone where the photonic crystal is modified) surrounded by the undisturbed photonic crystal. A light state associated with the defect in the outer region has to satisfy the periodicity of the lattice and therefore, can be represented as a superposition of the Bloch modes of the original photonic crystal. But because there is the boundary between the defect core and the outer region the full basis of possible Bloch modes includes not only propagating modes, but also the evanescent modes with the non-zero imaginary part of the Bloch vector. Such modes included in the basis have to decay with increasing the distance from the defect core. Hence, the states localized near the defect core and exponentially decaying outside of the core can exist.

The photonic crystal can be disturbed in many ways, among them are: changing the size or shape of the photonic crystal “atoms”, shifting the “atoms” in the photonic crystal lattice, modifying the dielectric permittivity and/or magnetic permeability of the “atoms”, introducing additional “atoms” into the lattice cell, etc.

The effect on the optical properties of the original photonic crystal depends on the size and parameters of the defects. The larger the defect core size or the lattice disturbance the more pronounced modification of the optical properties can be observed. One of the simplest way to achieve large disturbance of the original lattice is removing/adding “atoms” from the photonic crystal. Because most of the used photonic crystals have large permittivity contrast between the “atoms” and the background media such disturbance greatly modifies the optical properties of the sample. Fine tuning of the created defect can be done by shifting and modifying the “atoms” near the defect core.

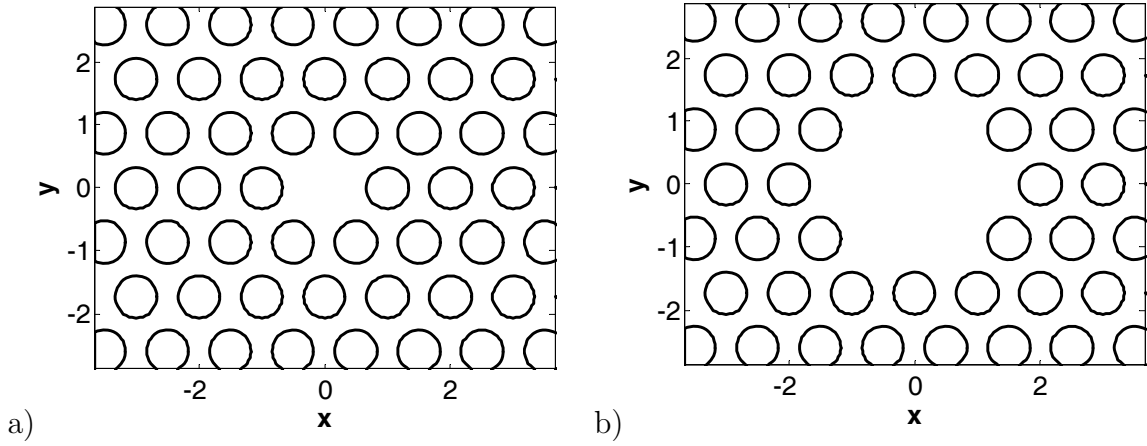


Figure 1.18: Cavities in triangular lattice photonic crystals. a) H1 cavity. b) H2 cavity.

The defects can be separated into several categories, according to size of their core. If the size of the defect core is of the order of the photonic crystal lattice primitive cell it is called that the defect is the zero-dimensional (0D) defect, also called cavity. If the defect is long (much longer than the lattice period) in one particular direction the defect is one-dimensional (1D). The defect which have a large size in two different directions this is two-dimensional defect (2D). In three-dimensional photonic crystals three-dimensional defects are also possible, if their size is large enough in all three principal directions.

Examples of typical zero-dimensional defects in the triangular lattice photonic crystal are shown in the Fig. 1.18. They are created by removing atoms from the lattice. The simplest cavity (called H1 cavity) is presented in the Fig. 1.18(a) and is created by removing one atom from the photonic crystal lattice. The remaining atoms are shown as black circles. A larger cavity (called H2 cavity) consists of seven removed atoms is depicted in the Fig. 1.18(b).

Another type of cavities in two-dimensional photonic crystal is plotted in the Fig. 1.19. These cavities are created by removing the atoms along the line in one of the lattice principal directions (such as ΓK or ΓM directions for the triangular lattice and ΓX and ΓM directions for the square lattice). The Fig. 1.19(a) shows the L2 cavity: two

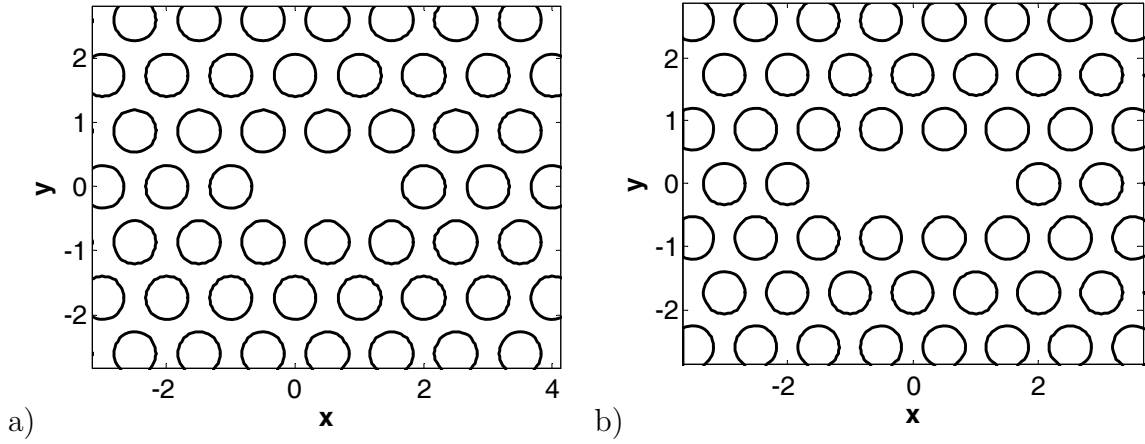


Figure 1.19: Cavities in triangular lattice photonic crystals. a) L1 cavity. b) L3 cavity.

adjacent atoms along the ΓK direction removed from the lattice. The L3 cavity (three removed atoms) is presented in the Fig. 1.19(b) [50, 51].

The cavities are usually designed to be able to support modes with the frequencies inside the full photonic band gap. It ensures strong light localization in the cavity, because only evanescent modes exist outside of the defect core [3].

Increasing the number of the removed atoms in the L-type cavity leads to creation of the one-dimensional defect – the chain of missing atoms along the ΓK direction. This defect is called W1 waveguide and is shown in the Fig. 1.20(a). Two neighbour lines of missing atoms create the W2 waveguide, depicted in the Fig. 1.20(b).

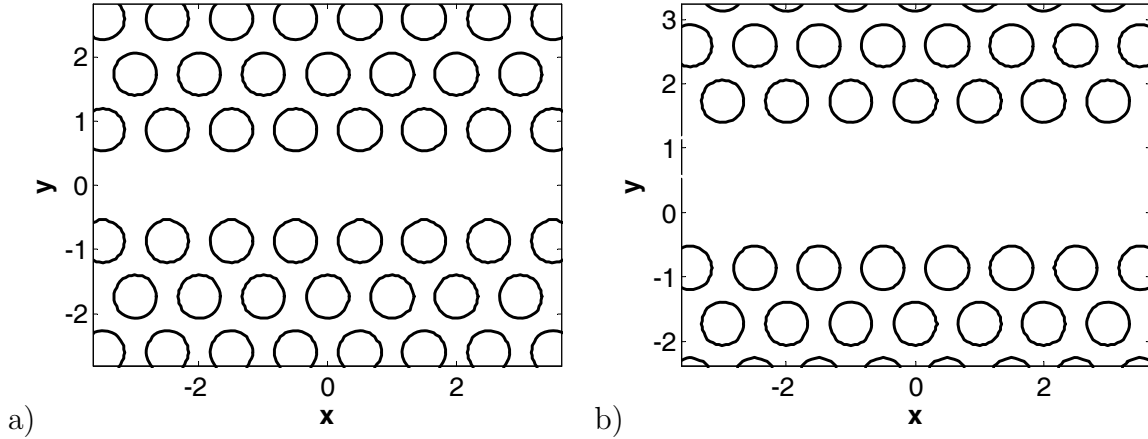


Figure 1.20: Waveguides in triangular lattice photonic crystals. a) W1 waveguide. b) W2 waveguide.

Because a one-dimensional defect is long enough in a particular direction the effect on the light dispersion is more pronounced for the light modes propagated along this direction because the interaction between the defect and the light is maximum in this case.

Modification of the dispersion relation for the Bloch modes propagating along a linear defect can create states with the frequency inside the full photonic band gap of

the perfect photonic crystal. Modes with such frequencies cannot propagate inside the photonic crystal and so they are localized near the defect, but they can propagate along the defect. This effect creates guided modes which are guided because of the features of the photonic crystal dispersion, not because of the refractive index guiding, like in the typical waveguides.

Parameters of the photonic crystal waveguides determine the dispersion properties and the field distribution of the guided modes. For example, the W1 waveguide has the mirror symmetry relative to the reflection in the (xz) plane which contains the waveguide axis (the plane $y = 0$). Such waveguide can support the mode which also has even symmetry relative to the reflection in the plane $y = 0$ [5]. The W2 waveguide doesn't have the mirror symmetry and so the corresponding guided modes have different symmetry properties in comparison with the modes of the W1 waveguide.

Chapter 2

Light mode properties of the two-dimensional photonic crystals

2.1 The Maxwell's equations for the electromagnetic field

The electromagnetic field in an electric polarisable and magnetizable material is governed by the Maxwell's equations, which in the Gaussian Centimetre-Gram-Second (CGS) units are:

$$\nabla \cdot \mathbf{D} = 4\pi\rho \quad (2.1)$$

$$\nabla \cdot \mathbf{B} = 0 \quad (2.2)$$

$$\nabla \times \mathbf{E} = -\frac{1}{c} \frac{\partial \mathbf{B}}{\partial t} \quad (2.3)$$

$$\nabla \times \mathbf{H} = \frac{4\pi}{c} \mathbf{j} + \frac{1}{c} \frac{\partial \mathbf{D}}{\partial t} \quad (2.4)$$

where $\mathbf{E}(\mathbf{r})$ and $\mathbf{B}(\mathbf{r})$ are the mean values of the electric field and the magnetic induction in the media. For the isotropic materials if the electric field and the magnetic induction strengths are small enough (so that there are no non-linear effects in the media) the electric displacement $\mathbf{D}(\mathbf{r})$ and the magnetic field $\mathbf{H}(\mathbf{r})$ are given by the equations:

$$\mathbf{D} = \varepsilon \mathbf{E} \quad (2.5)$$

$$\mathbf{H} = \frac{1}{\mu} \mathbf{B} \quad (2.6)$$

where $\varepsilon(\mathbf{r})$ is the dielectric permittivity and $\mu(\mathbf{r})$ is the magnetic permeability of the media.

Assuming that there are no external charges ($\rho = 0$) and currents ($\mathbf{j} = 0$) the

Maxwell's equations become:

$$\nabla \cdot (\varepsilon \mathbf{E}) = 0 \quad (2.7)$$

$$\nabla \cdot \mathbf{H} = 0 \quad (2.8)$$

$$\nabla \times \mathbf{E} = -\frac{\mu}{c} \frac{\partial \mathbf{H}}{\partial t} \quad (2.9)$$

$$\nabla \times \mathbf{H} = \frac{\varepsilon}{c} \frac{\partial \mathbf{E}}{\partial t} \quad (2.10)$$

Considering a monochromatic light with the standard time dependence $\exp(-i\omega t)$ the following equations can be derived:

$$\frac{1}{\varepsilon(\mathbf{r})} \nabla \times \frac{1}{\mu(\mathbf{r})} \nabla \times \mathbf{E}(\mathbf{r}) = \frac{\omega^2}{c^2} \mathbf{E}(\mathbf{r}) \quad (2.11)$$

$$\frac{1}{\mu(\mathbf{r})} \nabla \times \frac{1}{\varepsilon(\mathbf{r})} \nabla \times \mathbf{H}(\mathbf{r}) = \frac{\omega^2}{c^2} \mathbf{H}(\mathbf{r}) \quad (2.12)$$

According to these equations the electric field and the magnetic field can be decoupled and treated separately. (But known distribution of the electric field allows to find the distribution of the magnetic field and vice versa.) The equations (2.11) and (2.12) have structure of eigenvalue problems for the vectorial functions. The eigenvalues of the problems provide the allowed light frequencies and the corresponding eigenfunctions gives the field distributions.

2.2 The plane wave expansion method

The plane wave expansion method, initially proposed by Maradudin *et al.* [52], now became a standard tool for calculation of the dispersion properties of photonic crystals [53, 54]. Due to it's simplicity and high flexibility it allows one to describe not only photonic crystals with perfect periodicity but also point defects (cavities) and linear defects (waveguides).

As has been discussed in the section 1.2.1, any light state of the photonic crystal can be written as:

$$\psi(\mathbf{k}, \mathbf{r}) = e^{i\mathbf{k}\mathbf{r}} u_{\mathbf{k}}(\mathbf{r}) \quad (2.13)$$

where the function $u_{\mathbf{k}}(\mathbf{r})$ having the same periodicity as the photonic crystal and \mathbf{k} denoting the Bloch vector.

Such a periodic function $u_{\mathbf{k}}(\mathbf{r})$ can be decomposed using the plane waves which correspond to the reciprocal lattice:

$$u_{\mathbf{k}}(\mathbf{r}) = \sum_m u_m(\mathbf{k}) e^{i\mathbf{G}_m \mathbf{r}} \quad (2.14)$$

where \mathbf{G}_m are the vectors of the reciprocal lattice. It is convenient to index them so that $\mathbf{G}_{-m} = -\mathbf{G}_m$ and this is assumed in the text below.

The permittivity and the permeability can be decomposed in a similar way:

$$\varepsilon(\mathbf{r}) = \sum_m \varepsilon_m e^{i\mathbf{G}_m \mathbf{r}} \quad (2.15)$$

$$\mu(\mathbf{r}) = \sum_m \mu_m e^{i\mathbf{G}_m \mathbf{r}} \quad (2.16)$$

Because the equations (2.11) and (2.12) contain the inverse permittivity and the inverse permeability it is also convenient to introduce the following decompositions:

$$\frac{1}{\varepsilon(\mathbf{r})} = \sum_m \theta_m e^{i\mathbf{G}_m \mathbf{r}} \quad (2.17)$$

$$\frac{1}{\mu(\mathbf{r})} = \sum_m \eta_m e^{i\mathbf{G}_m \mathbf{r}} \quad (2.18)$$

As it has been discussed in the section 1.4.1 for the two-dimensional photonic crystals the full-vectorial electric and magnetic fields have one master component and can be approximated as the fields with only H_z component for the TE-polarized light and only E_z component for the TM-polarized light.

For the states with the Bloch vector \mathbf{k} these components are represented as:

$$E_z(\mathbf{r}) = e^{i\mathbf{k}\mathbf{r}} \sum_m A_m e^{i\mathbf{G}_m \mathbf{r}} = \sum_m A_m e^{i(\mathbf{k}+\mathbf{G}_m)\mathbf{r}} \quad \text{“TM polarization”} \quad (2.19)$$

$$H_z(\mathbf{r}) = e^{i\mathbf{k}\mathbf{r}} \sum_m B_m e^{i\mathbf{G}_m \mathbf{r}} = \sum_m B_m e^{i(\mathbf{k}+\mathbf{G}_m)\mathbf{r}} \quad \text{“TE polarization”} \quad (2.20)$$

Since the nabla operator in the basis of the plane waves corresponds to the componentwise product:

$$\nabla \times \sum_m \mathbf{F}_m e^{i\mathbf{S}_m \mathbf{r}} = \sum_m [\mathbf{S}_m \times \mathbf{F}_m] e^{i\mathbf{S}_m \mathbf{r}} \quad (2.21)$$

the expression for the operator $\nabla \times \frac{1}{\mu} \nabla \times$ can be derived using the equations (2.18), (2.19), and (2.21) as follows:

$$\begin{aligned} \nabla \times \frac{1}{\mu} \nabla \times E_z &= \nabla \times \frac{1}{\mu} \nabla \times \left[\sum_m A_m e^{i(\mathbf{k}+\mathbf{G}_m)\mathbf{r}} \right] \\ &= \sum_{m,n} A_n \cdot [(\mathbf{k} + \mathbf{G}_m) \cdot (\mathbf{k} + \mathbf{G}_n)] \cdot \eta_{m-n} \cdot e^{i(\mathbf{k}+\mathbf{G}_m)\mathbf{r}} \end{aligned} \quad (2.22)$$

The full governing operator in the equation (2.11) then can be written as:

$$\frac{1}{\varepsilon} \nabla \times \frac{1}{\mu} \nabla \times E_z = \sum_{m,n,l} A_n \cdot [(\mathbf{k} + \mathbf{G}_n) \cdot (\mathbf{k} + \mathbf{G}_l)] \cdot \theta_{m-l} \cdot \eta_{l-n} \cdot e^{i(\mathbf{k}+\mathbf{G}_m)\mathbf{r}} \quad (2.23)$$

The expression for the magnetic field can be derived in the similar way and is

$$\frac{1}{\mu} \nabla \times \frac{1}{\varepsilon} \nabla \times H_z = \sum_{m,n,l} B_n \cdot [(\mathbf{k} + \mathbf{G}_n) \cdot (\mathbf{k} + \mathbf{G}_l)] \cdot \eta_{m-l} \cdot \theta_{l-n} \cdot e^{i(\mathbf{k}+\mathbf{G}_m)\mathbf{r}} \quad (2.24)$$

If the magnetic permeability $\mu(\mathbf{r}) \equiv 1$, which is true for the vast majority of dielectrics, $\eta_m = \delta_{m,0}$ and the equations (2.23) and (2.24) can be simplified as follows:

$$\frac{1}{\varepsilon} \nabla \times \nabla \times E_z = \sum_{m,n} A_n \cdot [(\mathbf{k} + \mathbf{G}_n) \cdot (\mathbf{k} + \mathbf{G}_n)] \cdot \theta_{m-n} \cdot e^{i(\mathbf{k}+\mathbf{G}_m)\mathbf{r}} \quad \text{“TM pol.”} \quad (2.25)$$

$$\nabla \times \frac{1}{\varepsilon} \nabla \times H_z = \sum_{m,n} B_n \cdot [(\mathbf{k} + \mathbf{G}_m) \cdot (\mathbf{k} + \mathbf{G}_n)] \cdot \theta_{m-n} \cdot e^{i(\mathbf{k}+\mathbf{G}_m)\mathbf{r}} \quad \text{“TE pol.”} \quad (2.26)$$

Combining these equations with the decompositions (2.19) and (2.20) one can derive that for any m

$$\sum_n A_n \cdot [(\mathbf{k} + \mathbf{G}_n) \cdot (\mathbf{k} + \mathbf{G}_n)] \cdot \theta_{m-n} = \frac{w^2}{c^2} A_m \quad \text{“TM polarization”} \quad (2.27)$$

$$\sum_n B_n \cdot [(\mathbf{k} + \mathbf{G}_m) \cdot (\mathbf{k} + \mathbf{G}_n)] \cdot \theta_{m-n} = \frac{w^2}{c^2} B_m \quad \text{“TE polarization”} \quad (2.28)$$

For the computational purpose the number of the plane waves used for the decomposition is limited. The common way to choose used plane waves is to work with the waves with $|\mathbf{G}_m| \leq G_{max}$. It corresponds to best isotropic approximation of the details of all considered functions (electro-magnetic field, dielectric permittivity etc.). Increasing the parameter G_{max} allows to improve the accuracy of the approximation but the drawback is fast increasing of the number of used plane waves, which greatly increase demanding computational resources.

After truncation of the set of the reciprocal vectors $\{\mathbf{G}_m\}$ to a finite number the equations (2.27) and (2.28) have the form of the matrix eigenvalue problems. Due to the truncation some of the indices for the coefficients of the permittivity decomposition may be out of the scope. Such coefficients are substituted by zero. For any given Bloch vector \mathbf{k} and the set of the reciprocal vectors $\{\mathbf{G}_m\}$ the matrices in the these equation can be constructed and the eigenvalues provide the light frequencies for the TE and TM polarized states. The corresponding eigenvectors provide the coefficients of the E_z or H_z fields decomposition. These coefficients are used to reconstruct the full electromagnetic field distribution of the found modes.

2.3 Approximation of the dielectric permittivity distribution

Optical properties of the photonic crystals depends on the multiple light scattering on the inhomogeneities of the permittivity and/or the magnetic permeability. The larger the amplitude of the variations of these parameters, the more pronounced the effect on the light dispersion. Hence, photonic crystals with large contrast of the permittivity are preferable. In most of popular methods of photonic crystal fabrication (like etching of the holes in semiconductor slabs or assembling dielectric rods in air) there is a sharp change of the permittivity with the discontinuity at the boundaries between the “atoms” and the background media. Though the Fourier series approximation converges to the original function with increasing the number of the used plane waves, this convergence is not uniform. Representation of the functions with discontinuities using the finite number of terms in the Fourier series expansion exhibits the so-called Gibbs phenomenon: oscillations of the approximated functions near the original function discontinuities.

Example of the Gibbs phenomenon for the box function is presented in the Fig. 2.1. Here the considered function $g(x)$ is the periodic function with the period equals to 2π and defined (inside the period) as:

$$g(x) = \begin{cases} 5, & |x| \leq \pi/2 \\ 3, & \pi/2 < |x| \leq \pi \end{cases} \quad (2.29)$$

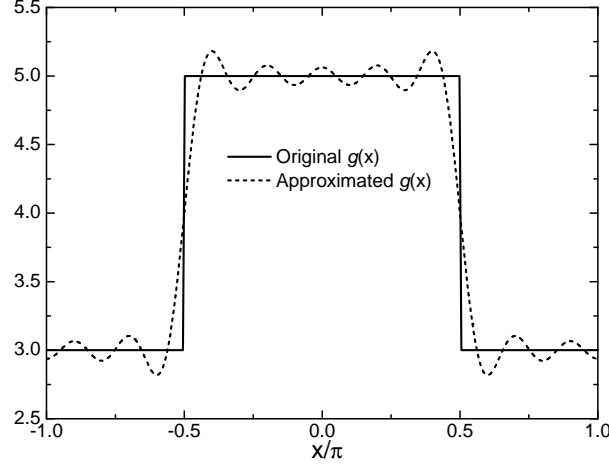


Figure 2.1: Approximation accuracy of the box function and the Gibbs phenomenon.

Near the discontinuities of $g(x)$ at $x = \pm\pi/2$ there are oscillations of the approximated function. The period of the oscillations is determined by the number of harmonics used for the approximation (In this example 21 harmonics are used, which gives the spatial resolution comparable with typical values used for calculation of the dispersion properties of photonic crystals.) The amplitude of the oscillations is proportional to the value of the function discontinuity. The particular feature of the Gibbs phenomenon is that it cannot be removed with increasing the number of the terms in the Fourier series expansion.

The Gibbs phenomenon deteriorates the accuracy of the approximation of the initial master equations (2.12) and (2.12) by the algebraic matrix eigenvalue problems (2.27) and (2.28) and special mathematical techniques have been developed to suppress this problem.

One of the important problem related to the Gibbs phenomenon is approximation of the product of the discontinues functions. If there are two functions $f(x)$ and $g(x)$ that have discontinuities at $x = x_0$ but $h(x) = f(x) \cdot g(x)$ is a continuous function at $x = x_0$ these functions have so-called complementary jumps at $x = x_0$. A physical example of such behavior is the electric field and the permittivity. At the boundary with the jump of the permittivity the electric field also has the jump, but the normal component of the displacement vector $D_n = \varepsilon E_n$ is continuous.

An example of such functions is shown in the Fig. 2.2. Here $f(x)$ is the periodic function with the period equals to 2π and defined (inside the period) as:

$$f(x) = \begin{cases} 1.2, & |x| \leq \pi/2 \\ 2, & \pi/2 < |x| \leq \pi \end{cases} \quad (2.30)$$

Function $h(x) = f(x) \cdot g(x) = 6$ is a continuous function.

Taking into account the truncation of the Fourier series decomposition the considered

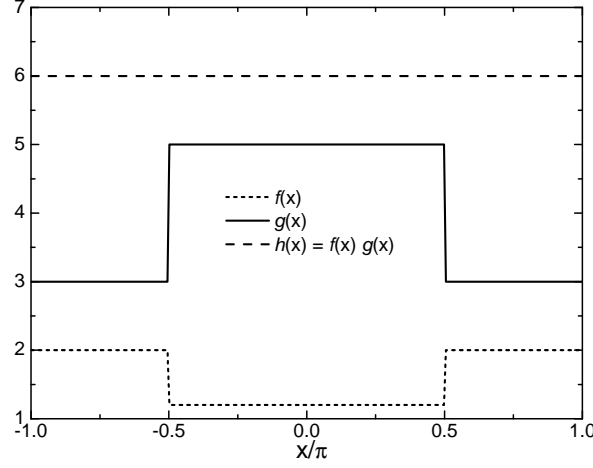


Figure 2.2: The product of two box-shaped functions.

function can be represented as:

$$f(x) = \sum_{m=-M}^M f_m e^{imx} \quad (2.31)$$

$$g(x) = \sum_{m=-M}^M g_m e^{imx} \quad (2.32)$$

$$h(x) = \sum_{m=-M}^M h_m e^{imx} \quad (2.33)$$

The standard way to obtain coefficients h_m (also called the Laurent's rule) is:

$$h_m = \sum_{n=-M}^M f_{m-n} \cdot g_n \quad (2.34)$$

It is assumed, that if the subscript index is out of the truncation scope ($[-M, M]$) the corresponding Fourier decomposition coefficient equals to zero. The Laurent's rule can also be written in the matrix form:

$$\mathbf{h} = \mathbb{F} \cdot \mathbf{g}, \quad (2.35)$$

where \mathbf{g} and \mathbf{h} are the vectors of the coefficients g_m and h_m while \mathbb{F} is the Toeplitz matrix (the matrix where the elements $\mathbb{F}_{mn} = f_{m-n}$).

The result of this approximation is presented in the Fig. 2.3. The Laurent's rule leads to the oscillations of the approximated function at the positions of the complimentary jumps $x = \pm\pi/2$. It has been shown in [55] that despite the convergence of the Fourier series obtained using the Laurent's rule this convergence is non-uniform and there are always oscillations near the positions of the complementary jumps. The period of these oscillations decreases with increasing the number of used terms, but the maximum amplitude of the oscillations is proportional to the product of jumps of the original functions f and g and the oscillations remain even at the limit $M \rightarrow \infty$.

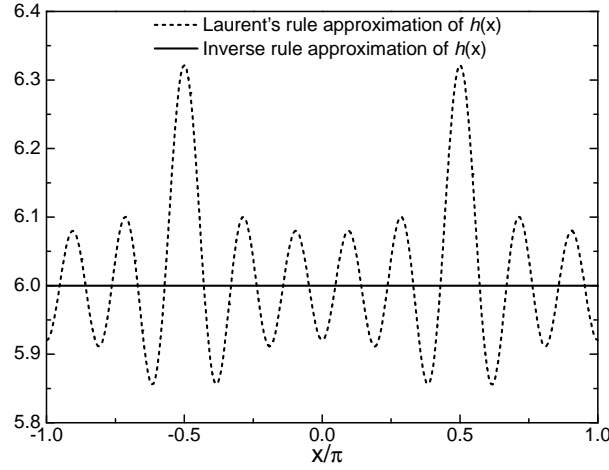


Figure 2.3: Approximation of the function $h(x)$.

Another way to avoid this problem and calculate h_m has been proposed. It is known as the inverse rule:

$$h_m = \sum_{n=-M}^M g_n \cdot \left(\left[\frac{1}{f} \right]^{-1} \right)_{mn} \quad (2.36)$$

Here $[1/f]$ denotes the Toeplitz matrix generated by the Fourier coefficients of $1/f$ (it is assumed that $f \neq 0$).

The inversion rule means:

1. Calculate the Fourier coefficients of the inverse functions $l = 1/f$.
2. Construct the Toeplitz matrix \mathbb{L} of the coefficients l_m .
3. Calculate the inverse matrix $\overline{\mathbb{F}} = \mathbb{L}^{-1}$.
4. Use the matrix $\overline{\mathbb{F}}$ instead of the matrix \mathbb{F} .

The comparison of the results obtained by the Laurent's rule and the inverse rule is shown in the Fig. 2.3. It is clearly seen that the inverse rule provides the exact approximation of $h(x)$ without any oscillations.

Approximation of a continuous function is less challenging. The Fourier series converge uniformly and fast. An example is presented in the Fig. 2.4. The periodic function (with the period equals to 2π) $g(x)$ here is defined as $g(x) = 2 \exp(\cos x)$. The approximated function is very close to the original one even for relatively small number of used terms (equals to 11 here). The small discrepancy has an oscillatory behavior with the period and amplitude determined by the number of used terms.

Consider the product of two continuous functions $f(x)$ and $g(x)$ (depicted in the Fig. 2.5). Here $f(x) = 1.5 \exp(-2 \cos x)$ and $h(x) = f(x)g(x) = 3 \exp(-\cos x)$.

Both strategies can be used to approximate the product of two functions. Comparison of the results obtained by the Laurent's rule and the inversion rule is presented in the Fig. 2.6. The difference between them is quite small which allows to use both methods for approximation of the product of two continuous functions.

The worst case is a combination of the discontinuous functions without the complementary jumps. An example of such functions is shown in the Fig. 2.7.

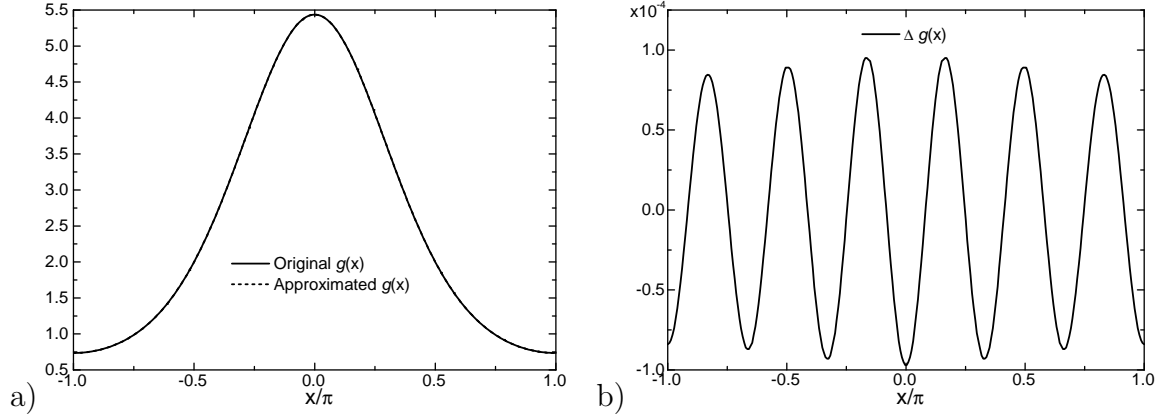


Figure 2.4: Approximation accuracy of the continuous periodic function. a) The original function $g(x)$ and the approximated function $g_1(x)$. b) The approximation error $\Delta g(x) = g_1(x) - g(x)$.

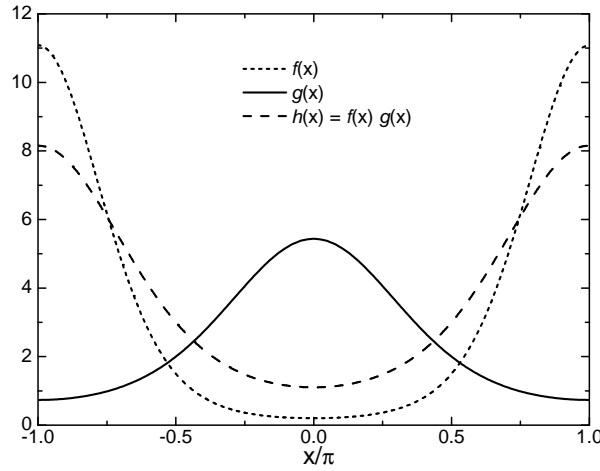


Figure 2.5: Product of two continuous periodic function.

Here

$$f(x) = \begin{cases} 2.5, & |x| \leq \pi/2 \\ 1.5, & \pi/2 < |x| \leq \pi \end{cases} \quad (2.37)$$

$$g(x) = 2 \exp(-1/2 \cos x) \quad (2.38)$$

$$h(x) = f(x)g(x) \quad (2.39)$$

Because the jump persists for the $h(x)$ one can suggest that the approximated function exhibits the oscillations. Indeed, both methods provide similar approximation quality (which is depicted in the Fig. 2.8).

Based on the examples discussed above it can be said that the inverse rule is more favorable method to approximate a product of two (continuous or discontinuous) functions using the Fourier series expansion.

The Gibbs phenomenon also appears when two-dimensional discontinuous functions are approximation by the Fourier series expansion. For typical photonic crystals such discontinuous function is the dielectric permittivity. An example of approximation of

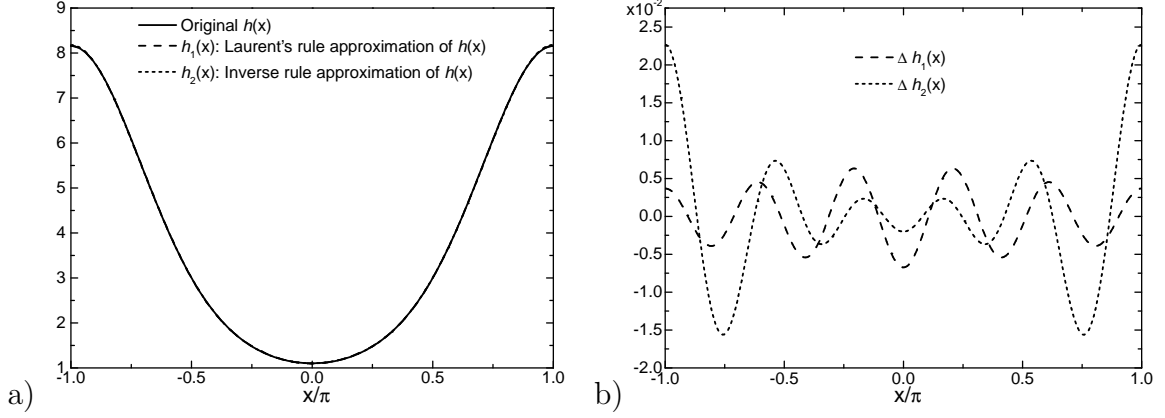


Figure 2.6: Approximation of the function $h(x)$. a) The Laurent's rule and the inverse rule approximation results. b) The approximation errors $\Delta h_1(x) = h_1(x) - h(x)$ and $\Delta h_2(x) = h_2(x) - h(x)$.

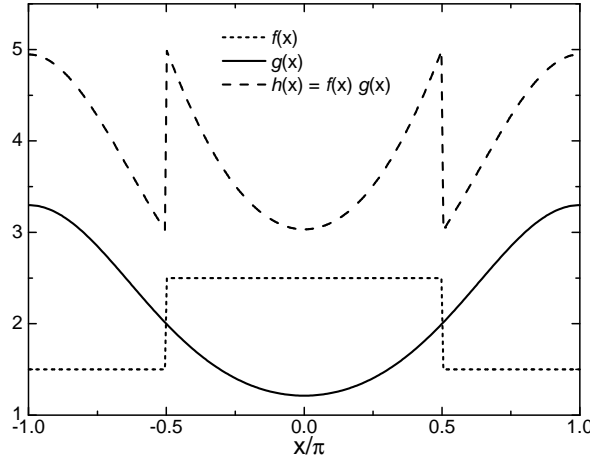


Figure 2.7: Product of two functions without the complementary jumps.

the permittivity for a square-lattice photonic crystal is shown in the Fig. 2.9. Here the photonic crystal consists of air holes (with the refractive index $n = 1$) with the diameter $d = 0.35a$ etched in a semiconductor slab with the effective refractive index $n_{eff} = 3.24$ (and corresponding permittivity $\varepsilon \approx 10.5$). The size of the hole is plotted as the black dashed line. The color map of the approximated permittivity distribution is presented in the Fig. 2.9(a) and the cross-section along the line with $y = 0$ (indicated as the white dashed line) is shown in the Fig. 2.9(b). The approximated permittivity exhibits a clear oscillating behavior with the spacial scale of the oscillations roughly inversely proportional to the maximum length of the used plane waves (indicated by the parameter G_{max}). Since the number of used plane waves is proportional to the G_{max}^2 , increasing of G_{max} in order to improve the approximation accuracy leads to fast growth of the dimension of the matrices in equations (2.27) and (2.28) and the computational resources required to solve these problems.

As it has been mentioned before, the main field components for the plane wave expansion model are E_z for the TM-polarized light and H_z for the TE-polarized light. These components are continuous at the boundaries of the photonic crystal atoms.

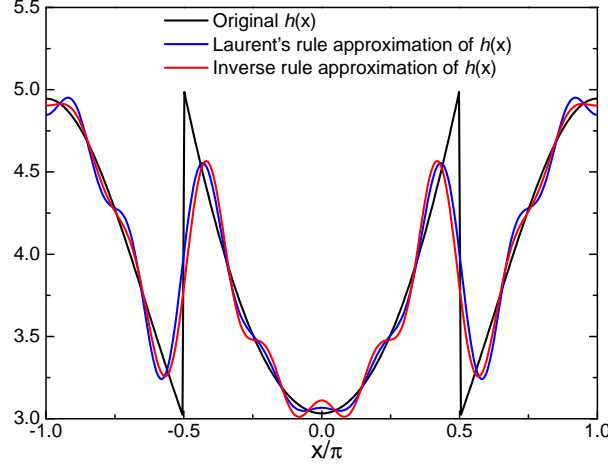


Figure 2.8: Approximation of the product of two functions without the elementary jumps.

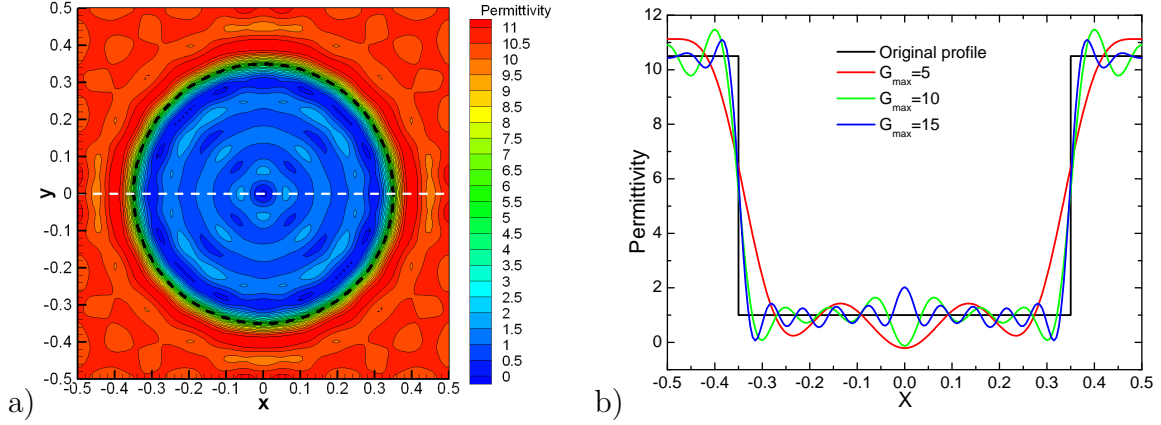


Figure 2.9: a) Distribution of the permittivity for a square photonic crystal ($G_{max} = 10$). b) Cross-section of the distribution of the permittivity for different number of used plane waves.

According to the equations (2.9) and (2.10), the curl operator of these fields gives

$$\nabla \times \mathbf{E} = i \frac{w}{c} \mu \mathbf{H} = i \frac{w}{c} \mathbf{B} \quad (2.40)$$

$$\nabla \times \mathbf{H} = -i \frac{w}{c} \varepsilon \mathbf{E} = -i \frac{w}{c} \mathbf{D} \quad (2.41)$$

At the boundaries of the photonic crystal atoms (it is assumed that the boundaries are sharp, where the dielectric permittivity and/or the magnetic permeability have a jump) the tangential components of the electric field \mathbf{E}_{xy} and the magnetic field \mathbf{H}_{xy} are continuous, while for the case of the normal components the electric displacement $\mathbf{D}_{xy} = \varepsilon \mathbf{E}_{xy}$ and the magnetic induction $\mathbf{B}_{xy} = \mu \mathbf{H}_{xy}$ are continuous. In order to preserve the continuity of the components of the field the inverse rule should be used.

According to the inverse rule the coefficients of the decomposition of the inverse permittivity θ_{m-n} and the inverse permeability η_{m-n} in the equations (2.27) and (2.28)

should be substituted by the components of the matrices

$$\theta_{m-n} \rightarrow \Theta_{mn}, \quad \text{where} \quad \Theta = \hat{\varepsilon}^{-1}, \quad \hat{\varepsilon}_{mn} = \varepsilon_{m-n} \quad (2.42)$$

$$\eta_{m-n} \rightarrow \Xi_{mn}, \quad \text{where} \quad \Xi = \hat{\mu}^{-1}, \quad \hat{\mu}_{mn} = \mu_{m-n} \quad (2.43)$$

Here the matrices $\hat{\varepsilon}$ and $\hat{\mu}$ are constructed from the coefficients of the Fourier series decompositions of the permittivity $\varepsilon(\mathbf{r})$ and the permeability $\mu(\mathbf{r})$. The matrices Θ and Ξ are the inverse matrices $\hat{\varepsilon}$ and $\hat{\mu}$, respectively.

Because the permittivity of a lossless dielectric is a real value the coefficients of the Fourier decomposition satisfy the following relation: $\varepsilon_m = \varepsilon_{-m}^*$. It means that the matrices $\hat{\varepsilon}$ and Θ are hermitian. The same is true for the decomposition of the magnetic permeability.

The coefficients ε_{m-n} and μ_{m-n} should be substituted in the similar way as

$$\varepsilon_{m-n} \rightarrow \hat{\varepsilon}_{mn}, \quad \text{where} \quad \hat{\varepsilon} = \hat{\theta}^{-1}, \quad \hat{\theta}_{mn} = \theta_{m-n} \quad (2.44)$$

$$\mu_{m-n} \rightarrow \hat{\kappa}_{mn}, \quad \text{where} \quad \hat{\kappa} = \hat{\eta}^{-1}, \quad \hat{\eta}_{mn} = \eta_{m-n} \quad (2.45)$$

Then the inversion rule for the tangential components leads to the relations

$$\mathbf{E}^t = \frac{1}{\varepsilon} \mathbf{D}^t \quad \Rightarrow \quad \mathbf{E}^t = \Theta \cdot \mathbf{D}^t \quad (2.46)$$

$$\mathbf{H}^t = \frac{1}{\mu} \mathbf{B}^t \quad \Rightarrow \quad \mathbf{H}^t = \Xi \cdot \mathbf{B}^t \quad (2.47)$$

and for the normal components

$$\mathbf{D}^n = \varepsilon \mathbf{E}^n \quad \Rightarrow \quad \mathbf{D}^n = \hat{\varepsilon} \cdot \mathbf{E}^n \quad \Rightarrow \quad \mathbf{E}^n = \hat{\theta} \cdot \mathbf{D}^n \quad (2.48)$$

$$\mathbf{B}^n = \mu \mathbf{H}^n \quad \Rightarrow \quad \mathbf{B}^n = \hat{\kappa} \cdot \mathbf{H}^n \quad \Rightarrow \quad \mathbf{H}^n = \hat{\eta} \cdot \mathbf{B}^n \quad (2.49)$$

It means, that for the best accuracy of the representation of the Maxwell's equations using the Fourier series expansion it requires to separate the in-plane field into the components normal and tangential to the boundaries of the atoms and treat them separately. In each point of the plane a local basis $\{\mathbf{e}_n, \mathbf{e}_t\}$ should be introduced and the in-plane field decomposed according to the local basis. For example, $\mathbf{E} = E^n \mathbf{e}_n + E^t \mathbf{e}_t$. At the boundaries of the atoms the basis corresponds to the normal and the tangential components. An example of such basis for the square lattice primitive cell is shown in the Fig. 2.10. The coefficients of the decomposition of the in-plane field are scalar functions of the coordinates ($E^t = E^t(\mathbf{r})$, $E^n = E^n(\mathbf{r})$) and have the meaning of the tangential and the normal components of the field. These components are decomposed using the plane wave expansion and, for example, E^t corresponds to the vector of the decomposition coefficients for the tangential component of the electric field and E^n corresponds to the vector of the decomposition coefficients for the normal component of the electric field. The same notation is used for the in-plane magnetic field. The inverse rule should be used for the tangential components of the field and the Laurent's rule (but using the matrices of the inverse permittivity $\hat{\theta}$ and the inverse magnetic permeability $\hat{\eta}$) for the normal components.

The idea of decomposition the in-plane components of the electromagnetic field into the normal and the tangential parts with different subsequent treatments has been

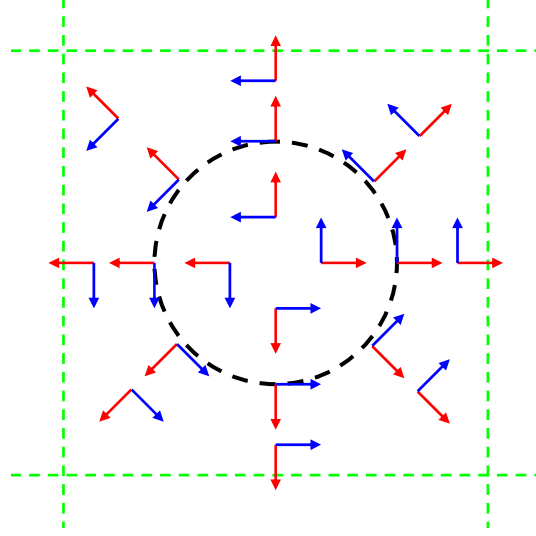


Figure 2.10: An example of the local basis for the square lattice. Red vectors correspond to the normal component and blue vectors correspond to the tangential component.

proposed in [56] and allows one to improve the accuracy of the plane wave expansion method. However, such decomposition is a non-trivial problem. Potential problems can be seen in the Fig. 2.10 at the center of the atom (depicted by the black dashed line), where the singularity problem for the basis vectors direction exists, and at the boundaries of the primitive cell (depicted by the green line), where because of the translation symmetry the basis vectors should change the sign. The situation become even more complex when there are several atoms in the primitive cell. If the introduced basis is discontinuous even a continuous in-plane field has (after the decomposition) discontinuous components which leads to additional errors for the Fourier series representation.

As a compromise between the complexity of the method and the accuracy of the results in the presented approach both components are treated in the same way (as the tangential components in the expressions (2.46) and (2.47)) using the inverse rule. In this case any local basis can be used (for example, the Cartesian basis).

The equations (2.27) and (2.28) can be written in the matrix form as

$$\mathbb{V} \cdot \mathbf{A} = \frac{w^2}{c^2} \mathbf{A} \quad \text{“TM polarization”} \quad (2.50)$$

$$\mathbb{W} \cdot \mathbf{B} = \frac{w^2}{c^2} \mathbf{B} \quad \text{“TE polarization”} \quad (2.51)$$

where the components of the matrices \mathbb{V} and \mathbb{W} are defined as:

$$\mathbb{V}_{mn} = [(\mathbf{k} + \mathbf{G}_n) \cdot (\mathbf{k} + \mathbf{G}_n)] \cdot \Theta_{mn} \quad (2.52)$$

$$\mathbb{W}_{mn} = [(\mathbf{k} + \mathbf{G}_m) \cdot (\mathbf{k} + \mathbf{G}_n)] \cdot \Theta_{mn} \quad (2.53)$$

The disadvantage of the equation (2.50) is that the matrix \mathbb{V} is not hermitian (in contrast to the matrix \mathbb{W}) and it adds unnecessary computational complexity to the problem (symmetric eigenvalue problems can be handled more efficiently than asymmetric ones). However, the substitution proposed by Maradudin *et al.* in [52] allows to

convert the equation (2.50) into a normal hermitian eigenvalue problem. This substitution is

$$A_m \rightarrow C_m = |\mathbf{k} + \mathbf{G}_m| A_m \quad (2.54)$$

and it leads to the equation

$$\mathbb{U} \cdot \mathbf{C} = \frac{w^2}{c^2} \mathbf{C} \quad \text{“TM polarization”} \quad (2.55)$$

where

$$\mathbb{U}_{mn} = [|\mathbf{k} + \mathbf{G}_m| \cdot |\mathbf{k} + \mathbf{G}_n|] \cdot \Theta_{mn} \quad (2.56)$$

2.3.1 Filtering of the Gibbs phenomenon

Another way to decrease the effect of the Gibbs phenomenon is to reduce the phenomenon itself. Any discontinuous function $g(x)$ of a scalar argument (which have a countable set of the jumps at $x \in \{x_i\}$) can be represented as a sum of a continuous function $f_c(x)$ and the series of the Heaviside step function $h(x)$:

$$g(x) = g_c(x) + \sum_{x \in \{x_i\}} \alpha_i h(x - x_i) \quad (2.57)$$

For a periodic function a similar decomposition can be done using the box-shape functions. It has been shown in [57] that the origin of the Gibbs phenomenon is the behavior of the coefficients of the Fourier decomposition of the box-shape (or the Heaviside) function. The coefficients of the box function decomposition $g_n \propto e^{\beta nk} / (nk)$, where $k = 2\pi/a$ is the wave vector of the period and β is a parameter which depends on the width of the box. The decay of g_n with increasing of the index n is slow and non-monotone. It leads to the oscillatory behavior of the approximated function with the increasing number of used terms. A way to suppress it is to increase the decay rate of the coefficients g_n . If a finite number of the coefficients is used for the decomposition ($n \leq N$)

$$g(x) = \sum_{n=-N}^N g_n e^{inkx} \quad (2.58)$$

a way to increase the decay rate is to introduce the filter function f :

$$\tilde{g}(x) = \sum_{n=-N}^N f(n/N) g_n e^{inkx} \quad (2.59)$$

Multiplication of the Fourier decomposition coefficients corresponds to the convolution of the functions:

$$\tilde{g}(x) = \hat{f} \circ g = \int_{-\infty}^{\infty} g(x-t) \hat{f}(t) dt \quad (2.60)$$

where the function \hat{f} is the function which have the Fourier decomposition coefficients $f_n = f(n/N)$. Such function should have the maximum at $t = 0$ and decays to zero when $|t|$ increases. The convolution with \hat{f} smooths the jumps of g and suppress the Gibbs phenomenon. Because the coefficients f_n depend on N the function \hat{f} varies for

different number of used Fourier series terms. It becomes more localized around $t = 0$ for larger N and less affects g .

The requirements for f are:

$$\begin{cases} f(0) = 1 \\ f(1) = 0 \\ f'(0) = 0 \\ f(-t) = f(t) \end{cases} \quad (2.61)$$

and the function f should monotonically decrease from 1 to 0 when t varies from 0 to 1. Such type of the filter function suppress the high-order harmonics of the Fourier decomposition and improve the convergence of the Fourier series.

Different filter functions have been proposed in [57]. Among them are

$$f_1(t) = \frac{\sin(\pi t)}{\pi t} \quad \text{Lanczos filter} \quad (2.62)$$

$$f_2(t) = \frac{\cos(\pi t) + 1}{2} \quad \text{Rising cosine filter} \quad (2.63)$$

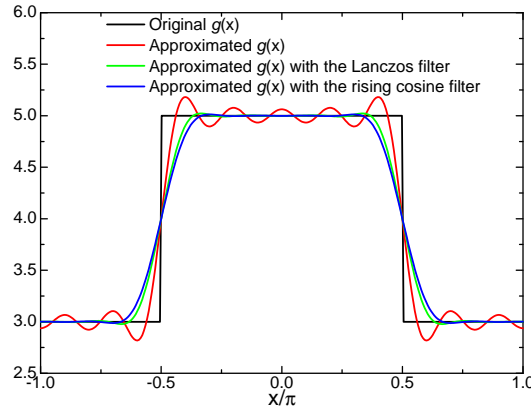


Figure 2.11: Approximation of the box function using different filters.

Examples of the effect of different filters are presented in the Fig. 2.11. Here

$$g(x) = \begin{cases} 5, & |x| \leq \pi/2 \\ 3, & \pi/2 < |x| \leq \pi \end{cases} \quad (2.64)$$

and 21 harmonics are used for the decomposition. The approximated $g(x)$ exhibits large oscillations near the jump points. Utilization of the filters allows to significantly suppress them. Because for the rising cosine filter function $f_2(t)$ the derivative $f_2'(1) = 0$ it suppress the high-order harmonics more efficiently and the resulting approximated function is smoother. The drawback of using the filters is smoothing of the jumps and decreasing the slope of the approximated function. Despite the smoothing region becomes narrower with increasing of the number of used harmonics and the slope rises it remains about two times less in comparison with the approximation without filters. The advantage of using filters is that outside of the smoothing region the shape of the original function is preserved.

This type of filtering can be easily generalized for the case of two dimensions as

$$\tilde{g}(\mathbf{r}) = \sum_m f(G_m/G_{max}) g_m e^{i\mathbf{G}_m \mathbf{r}} \quad (2.65)$$

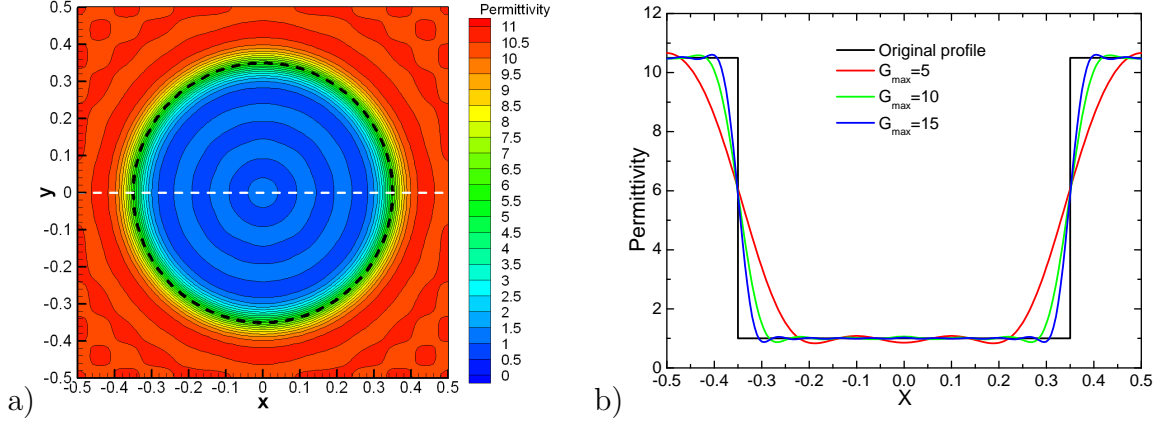


Figure 2.12: The effect of the Lanczos-type filter to the distribution of the permittivity. a) Distribution of the permittivity for a square photonic crystal. b) Cross-section of the distribution of the permittivity for different number of used plane waves.

The effect of the filtering on the approximation of the permittivity distribution for a square lattice photonic crystal is shown in the Fig. 2.12. The parameters of the photonic crystal are the same as used for the Fig. 2.9. The Lanczos filter almost completely removes the oscillations of the permittivity and improve the approximation accuracy.

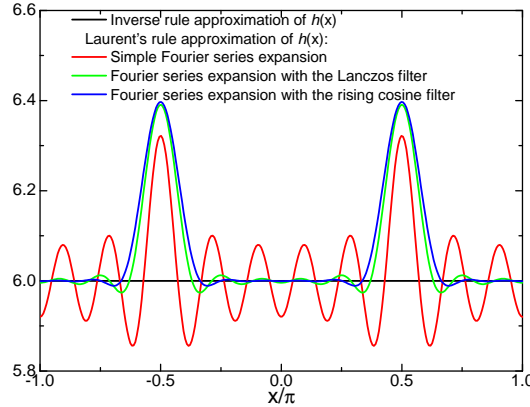


Figure 2.13: Approximation of the product of two box functions using different filters.

The effect of the filters on the product of two functions is illustrated in the Fig. 2.13. The parameters of the box functions are the same as used for the Fig. 2.3. The inverse rule approximation provides the results almost identical to the original function for all types of filters. But for the Laurent's rule the effect of the filters are important. Keeping the discrepancy with the original function near the jumps positions the oscillations are almost completely suppressed outside of these regions.

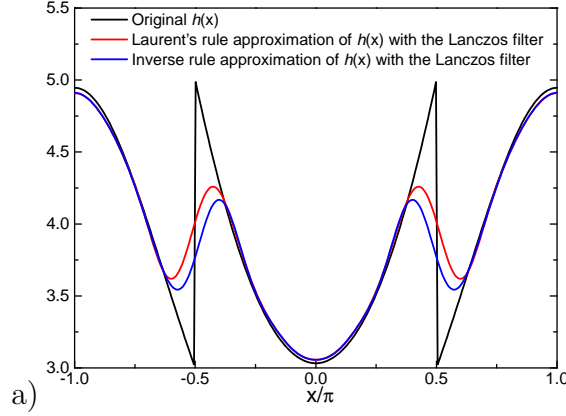


Figure 2.14: Approximation of the product of two functions without the complementary jumps using different filters.

Similar effect is observed when the product of two functions is discontinuous. The approximation of the product of two functions without the complementary jumps is presented in the Fig. 2.14. Parameters of the functions are the same as used for the Fig. 2.8.

The Lanczos filter efficiently smooths out the oscillations and restore the shape of the original function (compare with the Fig. 2.8). The disadvantage of using the filter is that the jumps are almost completely removed but nevertheless the overall results are better than the simple approximation without the filters. The Laurent's rule and the inverse rule provide quite similar results.

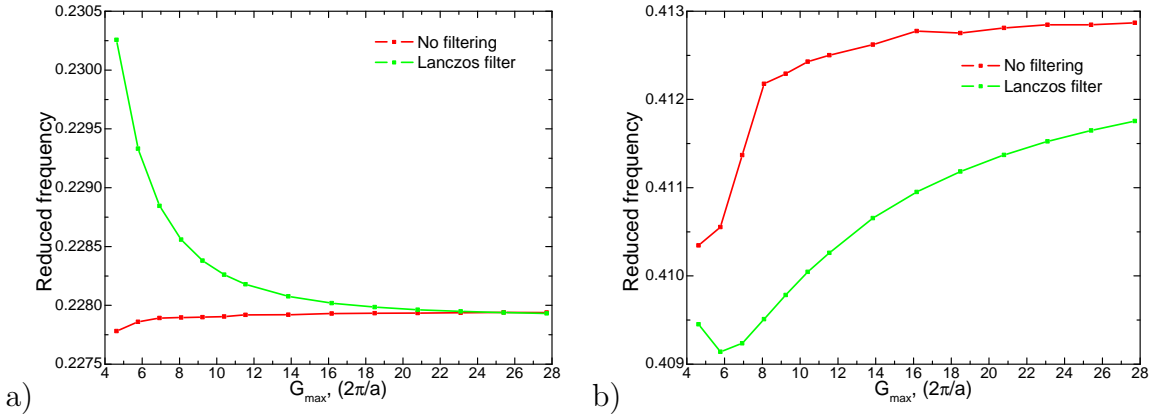


Figure 2.15: Convergence of the reduced frequency values of the TE polarized Bloch modes calculated with and without the filtering of the permittivity distribution. a) The Bloch vector at the K point, the first band. b) The Bloch vector at the Γ point, the second band.

The effect of the utilization of the filtering of the Fourier decomposition of the permittivity distribution on the calculated reduced frequencies of the Bloch modes is illustrated in the Fig. 2.15. The triangular lattice photonic crystal consists of the air holes with the filling factor $f = 40\%$ etched in the thick planar waveguide. G_{max} is the maximum value of the wave vectors for the plane waves used in the calculations.

Fig. 2.15(a) corresponds to the Bloch modes of the first band with the Bloch vector

at the K point. The frequencies obtained with and without the filtering are quite similar because the electric field for this Bloch mode is mainly localized in the regions with high permittivity, where the effect of the Gibbs phenomenon on the field is less pronounced (The absolute value of the permittivity variation is large, but the relative change of the permittivity is small). Utilization of the Lanczos-type filter gives lower convergence rate because the permittivity step is approximated by the a smoother function with lower slope (see, for example, Fig. 2.11).

Fig. 2.15(b) corresponds to the Bloch modes of the second band with the Bloch vector at the Γ point. In this case the electric field penetrates deeper into the holes and the effect of the permittivity approximation is more important. (See the section 2.6 for more details about the field distribution.) The relative variations of the permittivity distribution due to the Gibbs phenomenon are high which leads to lower convergence rate of the PWE method. It is important to note, that the Gibbs oscillations remains even for high values of G_{max} (and, correspondingly, for large numbers of used plane waves), while they are almost completely removed by using of the Lanczos-type filter. It leads to different calculated electromagnetic field distribution of the Bloch modes and different convergence limits of the mode frequencies calculated with an without the filtering.

It can be concluded based on the presented results that one of the key point of the plane wave expansion method is how to treat the dielectric permittivity and/or magnetic permeability in the photonic crystals. Approximation of these functions and constructing the master equations for the electromagnetic field require an elaborated technique in order to improve the accuracy of the plane wave expansion method.

2.3.2 Calculation of the permittivity Fourier expansion coefficients

The coefficients ε_m of the Fourier decomposition of the permittivity are obtained as

$$\varepsilon_m = \frac{1}{S_c} \int_{cell} \varepsilon(\mathbf{r}) e^{-i\mathbf{G}_m \mathbf{r}} d\mathbf{r} \quad (2.66)$$

where S_c is the area of the unit cell and integration is performed over the primitive cell of the photonic crystal.

Assuming that the photonic crystal consists of atoms with constant dielectric permittivities ε^j immersed in a material with the constant background permittivity ε^b

$$\varepsilon_m = \frac{1}{S_c} \sum_{j \in atoms} \int (\varepsilon^j - \varepsilon^b) e^{-i\mathbf{G}_m \mathbf{r}} d\Omega_j + \varepsilon^b \delta_{\mathbf{G}_m, \mathbf{0}} \quad (2.67)$$

Here each integral is performed over the area of j -th atom. The background permittivity gives an additional term for zero wave vector \mathbf{G}_m .

For each atom the function

$$g = \int e^{-i\mathbf{G}_m \mathbf{r}} d\Omega = e^{-i\mathbf{G}_m \mathbf{s}} \int e^{-i\mathbf{G}_m \mathbf{r}'} d\Omega' \quad (2.68)$$

is the product of the position factor, determined by the position of the atom center \mathbf{s} (in the coordinate system related with the unit cell), and the form-factor of the atom, determined by the atom shape.

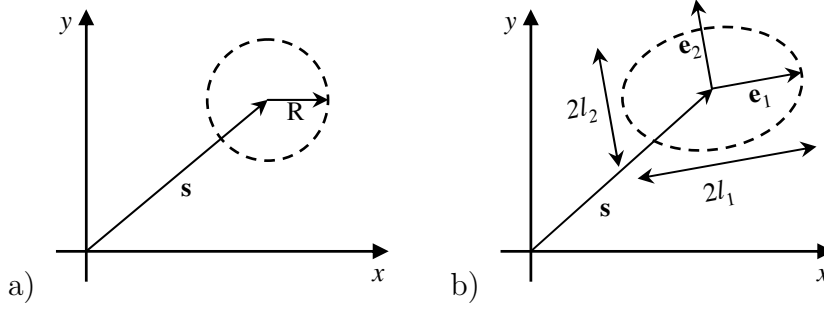


Figure 2.16: Parameters of an atom of the photonic crystal. a) Circular atom. b) Elliptical atom.

Two atom types considered in this thesis are shown in the Fig. 2.16. The circular atom is determined by the radius R and the the position of the atom center \mathbf{s} . The corresponding form-factor and the position factor are

$$g = \frac{2\pi R}{G_m} J_1(G_m R) e^{-i\mathbf{G}_m \mathbf{s}} = \pi R^2 [J_0(G_m R) + J_2(G_m R)] e^{-i\mathbf{G}_m \mathbf{s}} \quad (2.69)$$

where J_0 , J_1 , and J_2 are the Bessel functions of the first kind.

The elliptical atom is determined by the position of the atom center \mathbf{s} and the parameters of the ellipse: two semi-axes l_1 and l_2 and the orientation unit vectors \mathbf{e}_1 and \mathbf{e}_2 . The form factor of the elliptical atom can be calculated in the frame of reference connected with the atom orientation: $(x, y) \rightarrow (x', y')$. Then $\mathbf{G}_m = k_1 \cdot \mathbf{e}_1 + k_2 \cdot \mathbf{e}_2$.

$$g = \int e^{-i\mathbf{G}_m \mathbf{r}} d\Omega = e^{-i\mathbf{G}_m \mathbf{s}} \int e^{-i\mathbf{G}_m \mathbf{r}'} d\Omega' = e^{-i\mathbf{G}_m \mathbf{s}} \int e^{-i(k_1 x' + k_2 y')} d\Omega' \quad (2.70)$$

Here the scale of the y' axis can be changed as $\tilde{y}' = y' \cdot l_1/l_2$ as well as $\tilde{k}_2 = k_2 \cdot l_2/l_1$. Then $\tilde{k} = \sqrt{k_1^2 + \tilde{k}_2^2}$ and $d\tilde{\Omega}' = d\Omega' \cdot l_2/l_1$. The expression (2.70) transforms into

$$g = e^{-i\mathbf{G}_m \mathbf{s}} \int e^{-i(k_1 x' + \tilde{k}_2 \tilde{y}')} d\tilde{\Omega}' \quad (2.71)$$

and the integration is actually performed over a circle with the radius l_1 . It gives

$$g = \frac{2\pi l_2}{\tilde{k}} J_1(\tilde{k} l_1) e^{-i\mathbf{G}_m \mathbf{s}} = \pi l_1 l_2 [J_0(\tilde{k} l_1) + J_2(\tilde{k} l_1)] e^{-i\mathbf{G}_m \mathbf{s}} \quad (2.72)$$

Using the given expressions the coefficients of the Fourier decomposition of the permittivity distribution can be calculated. With the vectors of the reciprocal lattice (determined by the symmetry of the photonic crystal lattice) it completely determines the parameters required for calculation of the photonic crystal optical properties.

2.4 Frequency-based plane wave expansion method

The standard (Bloch vector based) plane wave expansion method allows for any given Bloch vector \mathbf{k} to find the frequencies and the field profile of the corresponding Bloch

states. However, there are several features of this method which makes it not well suited for particular problems.

Firstly, because the frequencies of the states are unknown and can be found only as a final result of the calculation, the dispersion of the dielectric permittivity and magnetic permeability of the materials of a photonic crystal cannot be taken into account directly [58–60]. It is possible to introduce an iterative numerical scheme to fit the results using known dispersion relations but this is time-consuming and not very convenient.

Secondly, the standard plane wave expansion method is not designed to provide full information about all possible solutions of the master equations (2.11) and (2.12). For a particular light frequency the full set of the solutions consists of the propagating Bloch modes (with real corresponding Bloch vectors) and the evanescent modes (where the Bloch vectors have imaginary parts). When the frequency is inside the full photonic band gap only evanescent modes can exist in a photonic crystal. Such states exponentially decay in a photonic crystal and are localized near boundaries and defects. So, they play an important role in the coupling of the light from an external source with the photonic crystal light states [54, 61], or mode coupling at the internal boundaries inside a photonic crystal. Working with the evanescent states using the standard plane wave expansion method leads to many difficulties. In general, substitution of a complex \mathbf{k} into equations (2.55) and (2.51) makes the matrices non-hermitian and the corresponding eigenvalues (as well as the state frequencies) also become complex. Hence, it requires a search in multidimensional space (effective 4D space for 2D complex Bloch vectors) in order to find the states with real frequencies.

An alternative approach to solve these difficulties of the standard plane wave expansion method is to fix the frequency and scan the \mathbf{k} -space in order to find the appropriate states. The Bloch vector \mathbf{k} is defined by two complex components. An efficient algorithm may be constructed to find only one coefficient at the time, so the search may be performed along a line in 2D complex \mathbf{k} -space (or along a plane in the equivalent 4D space).

A method which considers real and imaginary parts of the Bloch vector pointed in the same direction (*i.e.* modes which decay or growth along the phase velocity direction) has been proposed in [61] and used to investigate mode coupling at photonic crystal heterointerfaces in [60]. In this thesis an extended approach has been derived. This method can consider Bloch modes with arbitrary direction of the real and the imaginary components of the Bloch vector. It allows us to describe evanescent states which decay and propagate in different directions, for example penetration of the electromagnetic field of a PhC waveguide guided modes into photonic crystal cladding regions.

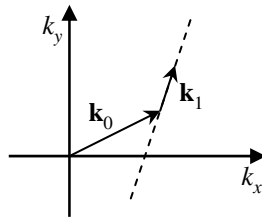


Figure 2.17: The Bloch vector search scheme.

In the derived method the Bloch vector is represented as

$$\mathbf{k} = \mathbf{k}_0 + \alpha \mathbf{k}_1, \quad (2.73)$$

where \mathbf{k}_0 is any 2D complex vector and \mathbf{k}_1 is a real 2D vector of the unit length. This is schematically shown in the Fig. 2.17.

The equations (2.11) and (2.12) can be rewritten as

$$\nabla \times \frac{1}{\mu(\mathbf{r})} \nabla \times \mathbf{E}(\mathbf{r}) = \frac{w^2}{c^2} \varepsilon(\mathbf{r}) \mathbf{E}(\mathbf{r}) \quad \text{“TM polarization”} \quad (2.74)$$

$$\nabla \times \frac{1}{\varepsilon(\mathbf{r})} \nabla \times \mathbf{H}(\mathbf{r}) = \frac{w^2}{c^2} \mu(\mathbf{r}) \mathbf{H}(\mathbf{r}) \quad \text{“TE polarization”} \quad (2.75)$$

Using the same derivation as for the equation (2.22) one can obtain

$$\sum_{m,n} A_n \cdot [(\mathbf{k} + \mathbf{G}_m) \cdot (\mathbf{k} + \mathbf{G}_n)] \cdot \eta_{m-n} \cdot e^{i(\mathbf{k} + \mathbf{G}_m)\mathbf{r}} = \frac{w^2}{c^2} \sum_{m,n} A_n \cdot \varepsilon_{m-n} \cdot e^{i(\mathbf{k} + \mathbf{G}_m)\mathbf{r}} \quad (2.76)$$

or

$$\sum_n A_n \cdot [(\mathbf{k} + \mathbf{G}_m) \cdot (\mathbf{k} + \mathbf{G}_n)] \cdot \eta_{m-n} = \frac{w^2}{c^2} \sum_n A_n \cdot \varepsilon_{m-n} \quad (2.77)$$

As it has been discussed in the section 2.3, in order to achieve better approximation accuracy the coefficients of the Fourier decompositions of the dielectric permittivity ε_{m-n} and the the magnetic permeability η_{m-n} should be replaced by the coefficients of the matrices Θ_{nm} and Ξ_{mn} , respectively.

The equations (2.74) and (2.75) transform then into

$$\sum_n A_n \cdot [(\mathbf{k} + \mathbf{G}_m) \cdot (\mathbf{k} + \mathbf{G}_n)] \cdot \Xi_{mn} = \frac{w^2}{c^2} \sum_n A_n \cdot \hat{\varepsilon}_{mn} \quad \text{“TM polarization”} \quad (2.78)$$

$$\sum_n B_n \cdot [(\mathbf{k} + \mathbf{G}_m) \cdot (\mathbf{k} + \mathbf{G}_n)] \cdot \Theta_{mn} = \frac{w^2}{c^2} \sum_n B_n \cdot \hat{\mu}_{mn} \quad \text{“TE polarization”} \quad (2.79)$$

The direct matrix $\hat{\varepsilon}$ is used in the right part of the equation (2.78) because in the original equation (2.11) division by the permittivity $\varepsilon(\mathbf{r})$ in the left part corresponds (according to the inverse rule) to the multiplication of the vector of the Fourier decomposition coefficients to the inverse matrix of the permittivity Θ . It gives us the direct matrix $\hat{\varepsilon}$ if the equation (2.11) is written as (2.74). Because of the same reason the direct matrix $\hat{\mu}$ is used in the right part of the equation (2.79).

Using the expression (2.73) one can obtain

$$(\mathbf{k} + \mathbf{G}_m) \cdot (\mathbf{k} + \mathbf{G}_n) = \alpha^2 + \alpha \mathbf{k}_1 (2\mathbf{k}_0 + \mathbf{G}_m + \mathbf{G}_n) + (\mathbf{k}_0 + \mathbf{G}_m)(\mathbf{k}_0 + \mathbf{G}_n) \quad (2.80)$$

Introducing the vector of the coefficients A the equation (2.78) can be rewritten as:

$$\alpha^2 \Xi \cdot \mathbf{A} + \alpha \mathbb{R} \cdot \mathbf{A} + \mathbb{S} \cdot \mathbf{A} = \frac{w^2}{c^2} \hat{\varepsilon} \cdot \mathbf{A} \quad (2.81)$$

where matrices \mathbb{R} and \mathbb{S} are auxiliary matrices with the coefficients:

$$\mathbb{R}_{mn} = \Xi_{mn} \cdot [\mathbf{k}_1 \cdot (2\mathbf{k}_0 + \mathbf{G}_m + \mathbf{G}_n)] \quad (2.82)$$

$$\mathbb{S}_{mn} = \Xi_{mn} \cdot [(\mathbf{k}_0 + \mathbf{G}_m) \cdot (\mathbf{k}_0 + \mathbf{G}_n)] \quad (2.83)$$

Multiplying the equation (2.81) by the matrix $\hat{\mu}$ one obtains

$$\alpha^2 \mathbf{A} + \alpha \hat{\mu} \cdot \mathbb{R} \cdot \mathbf{A} + \hat{\mu} \cdot \mathbb{S} \cdot \mathbf{A} = \frac{w^2}{c^2} \hat{\mu} \cdot \hat{\varepsilon} \cdot \mathbf{A} \quad (2.84)$$

or

$$\alpha(\alpha \mathbf{A}) = \hat{\mu} \cdot \mathbb{R} \cdot (\alpha \mathbf{A}) + \hat{\mu} \cdot \left(\frac{w^2}{c^2} \hat{\varepsilon} - \mathbb{S} \right) \cdot \mathbf{A} \quad (2.85)$$

The unknown α can be found using the extended eigenvalue problem:

$$\begin{pmatrix} \mathbb{O} & \mathbb{I} \\ \hat{\mu} \cdot \left(\frac{w^2}{c^2} \hat{\varepsilon} - \mathbb{S} \right) & \hat{\mu} \cdot \mathbb{R} \end{pmatrix} \cdot \begin{pmatrix} \mathbf{A} \\ \alpha \mathbf{A} \end{pmatrix} = \alpha \begin{pmatrix} \mathbf{A} \\ \alpha \mathbf{A} \end{pmatrix} \quad \text{“TM polarization”} \quad (2.86)$$

where \mathbb{O} is the zero matrix and \mathbb{I} is the identity matrix.

The corresponding equation for the magnetic field can be obtained by simultaneous substituting $\hat{\mu} \rightarrow \hat{\varepsilon}$, $\hat{\varepsilon} \rightarrow \hat{\mu}$, and $\Xi \rightarrow \Theta$:

$$\begin{pmatrix} \mathbb{O} & \mathbb{I} \\ \hat{\varepsilon} \cdot \left(\frac{w^2}{c^2} \hat{\mu} - \mathbb{Q} \right) & \hat{\varepsilon} \cdot \mathbb{P} \end{pmatrix} \cdot \begin{pmatrix} \mathbf{B} \\ \alpha \mathbf{B} \end{pmatrix} = \alpha \begin{pmatrix} \mathbf{B} \\ \alpha \mathbf{B} \end{pmatrix} \quad \text{“TE polarization”} \quad (2.87)$$

where

$$\mathbb{P}_{mn} = \Theta_{mn} \cdot [\mathbf{k}_1 \cdot (2\mathbf{k}_0 + \mathbf{G}_m + \mathbf{G}_n)] \quad (2.88)$$

$$\mathbb{Q}_{mn} = \Theta_{mn} \cdot [(\mathbf{k}_0 + \mathbf{G}_m) \cdot (\mathbf{k}_0 + \mathbf{G}_n)] \quad (2.89)$$

If $\mu(\mathbf{r}) \equiv 1$ the equations (2.86) and (2.87) simplify a lot, because $\hat{\mu} = \Xi = \mathbb{I}$ and hence:

$$\begin{pmatrix} \mathbb{O} & \mathbb{I} \\ \left(\frac{w^2}{c^2} \hat{\varepsilon} - \mathbb{S} \right) & \mathbb{R} \end{pmatrix} \cdot \begin{pmatrix} \mathbf{A} \\ \alpha \mathbf{A} \end{pmatrix} = \alpha \begin{pmatrix} \mathbf{A} \\ \alpha \mathbf{A} \end{pmatrix} \quad \text{“TM polarization”} \quad (2.90)$$

$$\begin{pmatrix} \mathbb{O} & \mathbb{I} \\ \hat{\varepsilon} \cdot \left(\frac{w^2}{c^2} \mathbb{I} - \mathbb{Q} \right) & \hat{\varepsilon} \cdot \mathbb{P} \end{pmatrix} \cdot \begin{pmatrix} \mathbf{B} \\ \alpha \mathbf{B} \end{pmatrix} = \alpha \begin{pmatrix} \mathbf{B} \\ \alpha \mathbf{B} \end{pmatrix} \quad \text{“TE polarization”} \quad (2.91)$$

while \mathbb{R} and \mathbb{S} become

$$\mathbb{R}_{mn} = 2\mathbf{k}_1 \cdot (\mathbf{k}_0 + \mathbf{G}_m) \cdot \delta_{m,n} \quad (2.92)$$

$$\mathbb{S}_{mn} = (\mathbf{k}_0 + \mathbf{G}_m)^2 \cdot \delta_{m,n} \quad (2.93)$$

Using the expressions above it is possible for a given frequency w and vectors \mathbf{k}_0 and \mathbf{k}_1 to find values for α and completely determine the Bloch vectors of the state. Because the matrices in the equations (2.86) and (2.87) are non-hermitian most of the eigenvalues are complex even for a frequency where the propagating states (with purely real Bloch vector) exist. Also, because the search of the Bloch vectors is performed along a line in the \mathbf{k} -space, the states from the high-order Brillouin zones are also included in the set of the obtained eigenvalues. It requires a special treatment to find the unique solutions which corresponds to the first Brillouin zone.

Examples of calculation of the evanescent modes properties using the frequency-based plane wave expansion method are discussed in the section 2.8.

2.5 Light propagation in photonic crystals

The light eigenstates in a photonic crystal are the Bloch modes, determined by the Bloch vector \mathbf{k} , the frequency w , and the polarizations. If the Bloch vector is purely real such a state can propagate in the photonic crystal without the attenuation. Most of the photonic crystal based devices rely on the properties of the propagating light modes and, hence determination of the Bloch modes is the key point for the design of such devices.

2.5.1 Dispersion properties of photonic crystals

The plane wave expansion method allows for each Bloch wave vector to find the eigenfrequency of the Bloch modes. Hence, the dispersion of the light in a photonic crystal (*i. e.*, the dependence $w(\mathbf{k})$) can be reconstructed. Dispersion of the Bloch modes is one of the most important properties of the photonic crystals. It determines propagation of the modes in the photonic crystal and, consequently, the performance of many photonic crystal based devices.

Dispersion of the Bloch modes depends on many parameters of the photonic crystal. The most important among them are:

- The type of the photonic crystal lattice (square, triangular, graphite, etc.), which affects the dispersion symmetry properties.
- The type of the permittivity and/or the permeability contrast (for example, air holes in the high-permittivity background, dielectric rods in the air, etc.), which modifies the dependence of the dispersion on the light polarization.
- Distribution of the “atoms” in the photonic crystal primitive cell (single atom in a simple cell or several atoms in a super-cell) and the shapes of the atoms (for example, high symmetrical circular atoms or elliptical atoms with lower symmetry), which also affects the dispersion symmetry properties.

2.5.1.1 Square lattice photonic crystals

Examples of the dispersion of the TE polarized Bloch modes for the square lattice photonic crystal are shown in the Fig. 2.18. Here the photonic crystal consists of the circular air holes (one hole in the primitive cell) etched in the thick planar waveguide. The effective refractive index for both TE and TM polarizations is equal to 3.24. The filling factor $f = 0.4$. The maximum length of the reciprocal lattice vector $G_{max} = 8\frac{2\pi}{a}$ and the number of used plane waves $N = 197$, which ensures a good accuracy of calculated Bloch modes frequencies.

At the first band near the Γ point the frequency is linearly proportional to the Bloch vector which is similar to the properties of light propagating in a homogeneous media. Closer to the boundary of the first Brillouin zone the effect of the photonic crystal becomes visible since the shape of the isolines are different from the circles. At the second band the effect of the photonic crystal is much more pronounced. The square-like shape of the isolines means strong anisotropy of the light propagation properties for the light with the corresponding frequency. The bands with larger index have more complex

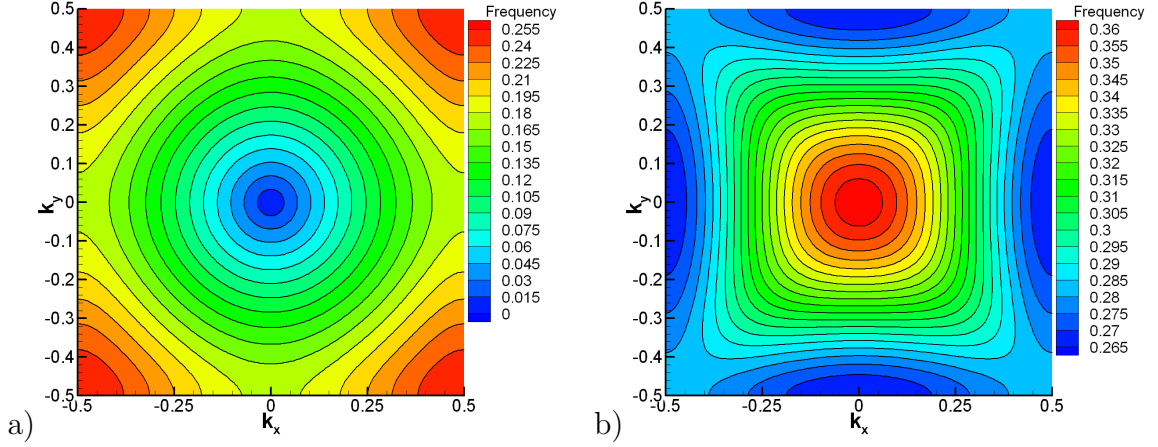


Figure 2.18: Dispersion of the TE-polarized Bloch modes for the square lattice photonic crystal consisting of the circular air holes (the filling factor $f = 0.4$) in the dielectric slab with the effective refractive index $n_{eff} = 3.24$. a) The first band. b) The second band.

structure. In general, the larger the index of the band the larger the corresponding mode frequency and the less equivalent light wavelength. Such light modes interact stronger with the inhomogeneities of the permittivity and are more sensitive to the details of the permittivity distribution (like the shape of the photonic crystal atoms). It leads to a complex dispersion of the bands with the large index.

The dispersion of the same photonic crystal for the TM polarized Bloch modes is presented in the Fig. 2.19. The dispersion of two lowest bands is similar to the dispersion of two lowest bands for the TE polarized light but with increasing the index of the band (and the corresponding mode frequency) the difference between the dispersions of the TE and TM polarized light become more pronounced. It happens because of the different direction of the electric field (as well as the displacement field) for TE and TM polarizations. Boundary conditions for the field at the photonic crystal atom boundaries lead to different field distributions for TE and TM polarized light which results in the different mode frequency for the same Bloch vector.

The cross-section of the Bloch modes dispersion is shown in the Fig. 2.20. Two full photonic band gaps (indicated by the gray regions) exist for the TE polarized light. Only partial photonic band gaps (for example, along the ΓX and the ΓM directions) exist for the TM polarized light because the widths of these gaps are not enough to overlap and create a full band gap.

The effect of the photonic crystal on the light dispersion depends on the filling factor. The larger the filling factor the larger the interaction between the electromagnetic field and the atom material and the larger effect on the light dispersion. The dependence of the position and the width of the full photonic band gaps on the filling factor is shown in the Fig. 2.21. The maximum theoretical filling factor achievable for the square lattice photonic crystal with one circular atom is $f_{max} = \pi/4 \approx 0.785$. Because of the fabrication reason in order to avoid to have the atom boundaries too close each other the filling factor should be less than this limit.

The dependence of the position and the width of the full photonic band gaps on the filling factor is presented in the Fig. 2.21. For the case of the “holes in the dielectric”

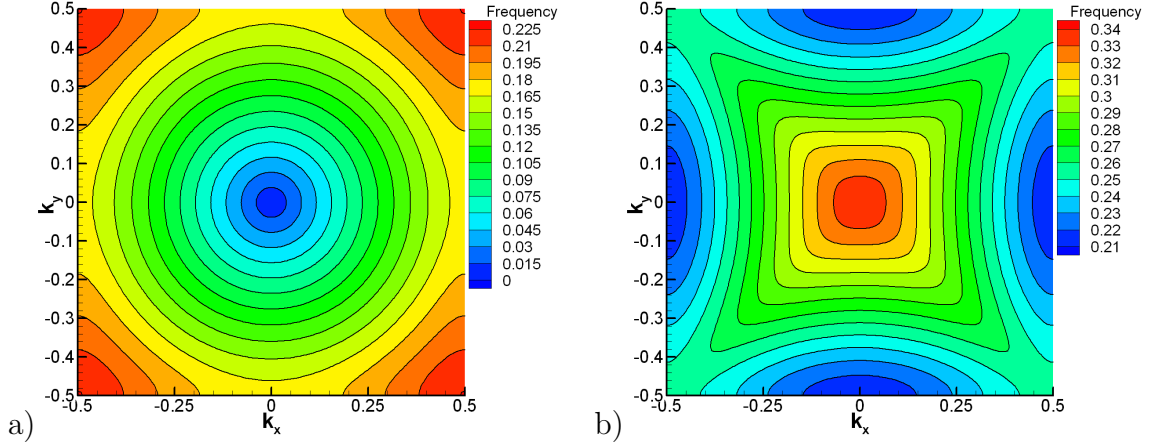


Figure 2.19: Dispersion of the TM-polarized Bloch modes for the square lattice photonic crystal consisting of the circular air holes (the filling factor $f = 0.4$) in the dielectric slab with the effective refractive index $n_{eff} = 3.24$. a) The first band. b) The second band.

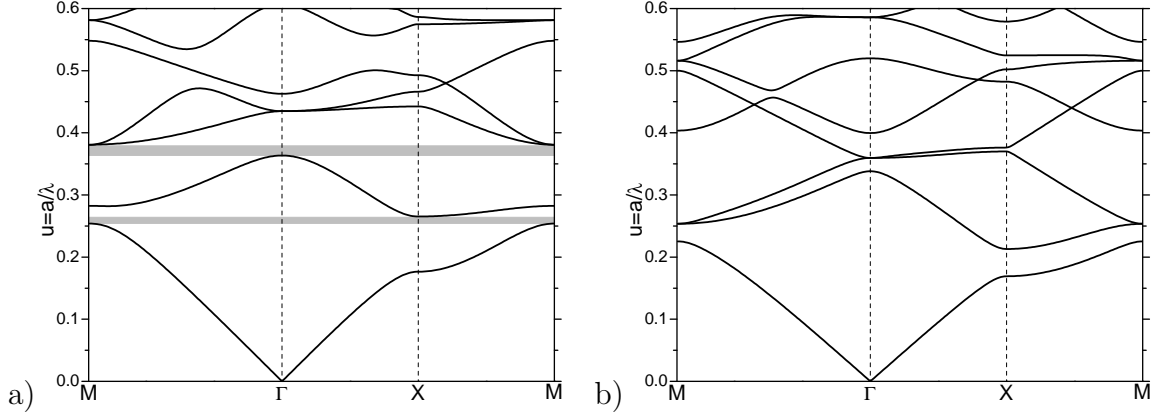


Figure 2.20: Dispersion of the Bloch modes for the square lattice photonic crystal consisting of the circular air holes (the filling factor $f = 0.4$) in the dielectric slab with the effective refractive index $n_{eff} = 3.24$. a) TE polarization. b) TM polarization.

photonic crystal the full photonic band gaps open for the TE-polarized light when the filling factor is larger than about 0.32 and for the TM-polarized light when the filling factor is larger than about 0.48. The widths of the band gaps are relatively small, which means that light can propagate in the photonic crystal for a wide range of the frequencies and it is difficult to create photonic crystal based structures which constrain Bloch modes propagation and can efficiently localize the light. When the photonic crystal is of the “pillars in the air” type the full photonic band gaps exist mainly for the TM polarization. In this case propagation of the TM-polarized light can be efficiently limited.

The dispersion relation of the square lattice pillar-based photonic crystals is presented in the appendix A.1.1.

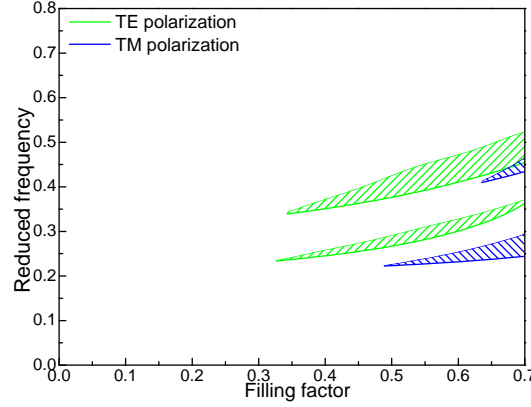


Figure 2.21: The full photonic band gaps for the square lattice photonic crystals consisting of air holes in a dielectric slab ($n_{eff} = 3.24$).

2.5.1.2 Triangular lattice photonic crystals

Examples of the dispersion of the TE polarized Bloch modes for the triangular lattice photonic crystal are shown in the Fig. 2.22. The corresponding dispersion of the TM polarized Bloch modes are shown in the Fig. 2.23. Here the photonic crystal consists of the circular air holes (one hole in the primitive cell) etched in the thick planar waveguide. The effective refractive index for both TE and TM polarizations is equal to 3.24. The filling factor $f = 0.4$. The maximum length of the reciprocal lattice vector $G_{max} = 7 \frac{2}{\sqrt{3}} \frac{2\pi}{a}$ and the number of used plane waves $N = 187$. The first Brillouin zone has the hexagon shape and is indicated in the figures by the white dashed line.

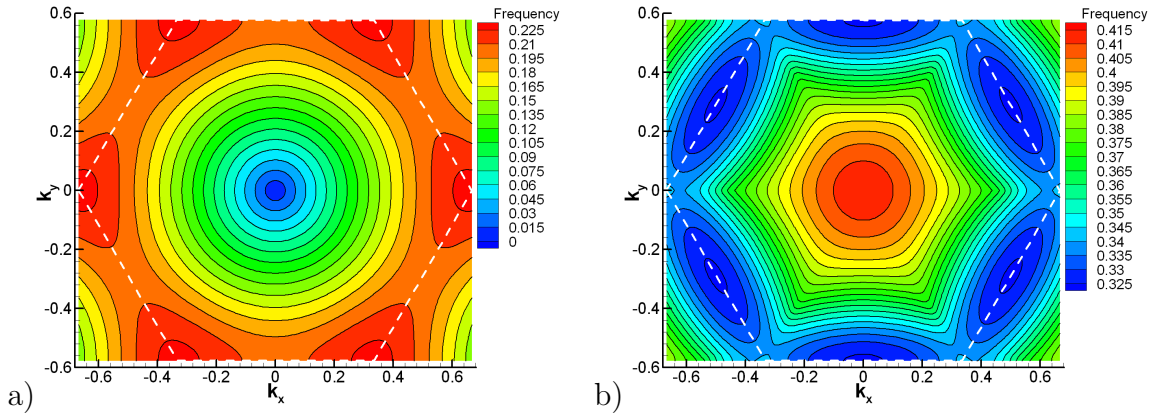


Figure 2.22: Dispersion of the TE-polarized Bloch modes for the triangular lattice photonic crystal consisting of the circular air holes (the filling factor $f = 0.4$) in the dielectric slab with the effective refractive index $n_{eff} = 3.24$. a) The first band. b) The second band.

The behavior of the dispersion relation for the triangular lattice photonic crystal is similar to the dispersion relations of the square lattice photonic crystals. The noticeable difference is that the triangular lattice has higher symmetry which leads to higher symmetry of the corresponding reciprocal lattice. Then the difference of the distances between the center of the first Brillouin zone (Γ point) and the centers of the sides (ΓM distance) and the corners (ΓK distance) is smaller for the triangular lattice than

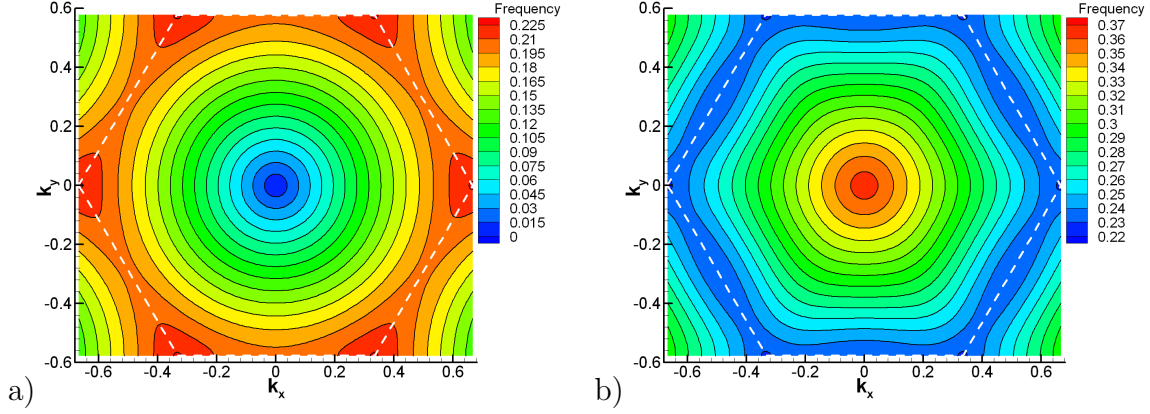


Figure 2.23: Dispersion of the TM-polarized Bloch modes for the triangular lattice photonic crystal consisting of the circular air holes (the filling factor $f = 0.4$) in the dielectric slab with the effective refractive index $n_{eff} = 3.24$. a) The first band. b) The second band.

for the square lattice (here the distances ΓM and ΓX are compared). It leads to better overlap of the partial photonic band gaps for the ΓM and the ΓK directions and wider full photonic band gaps.

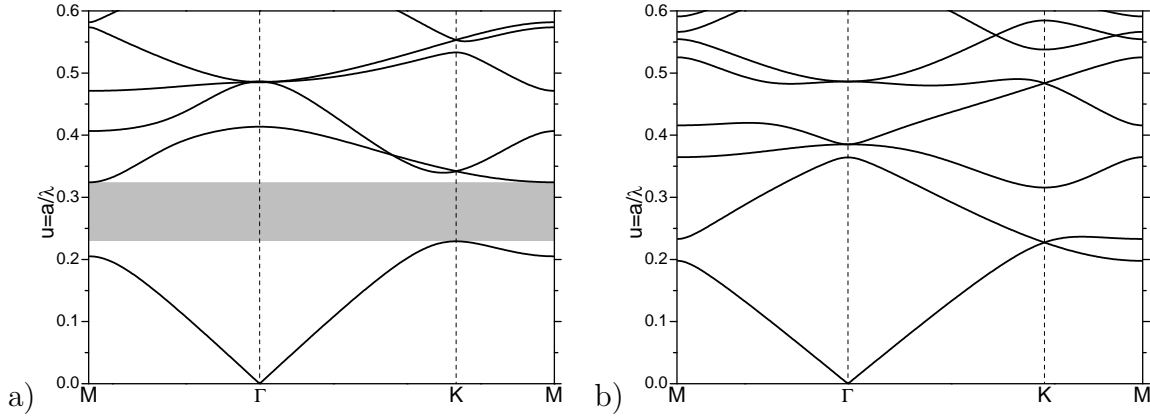


Figure 2.24: Dispersion of the Bloch modes for the triangular lattice photonic crystal consisting of the circular air holes (the filling factor $f = 0.4$) in the dielectric slab with the effective refractive index $n_{eff} = 3.24$. a) TE polarization. b) TM polarization.

The cross-sections of the dispersion of the Bloch modes are presented in the Fig. 2.24. The full photonic band gap exists between the first and the second bands for the TE-polarized light.

The dependence of the position and the width of the full photonic band gap on the filling factor is plotted in the Fig. 2.25. The maximum achievable filling factor for the triangular lattice is $f_{max} = \frac{\pi}{2\sqrt{3}} \approx 0.907$ but because of the fabrication reason it should be less than this limit.

The dispersion properties of the triangular lattice pillar type photonic crystals are shown in the appendix A.1.2.

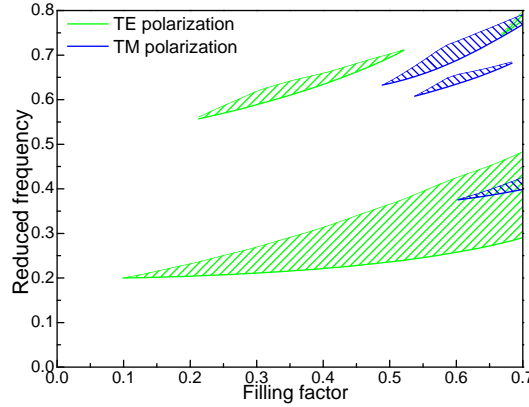


Figure 2.25: The full photonic band gaps for the triangular lattice photonic crystals consisting of air holes in a dielectric slab ($n_{eff} = 3.24$).

2.5.1.3 Effect of the dispersion of the planar waveguide effective refractive index

Two-dimensional approximation of the photonic crystal doesn't take into account the real vertical structure of the sample. If the light is confined in the vertical direction using the planar waveguide the effective refractive index of the waveguide is usually used as the refractive index of the background media in the 2D approximation. In the standard Bloch vector based plane wave expansion method it is assumed that the effective refractive index is a constant and doesn't depend on the frequency. For a thick waveguide with weak vertical light confinement the effective refractive index is almost constant and this approximation is valid. But for the thin waveguide with the high index contrast the dispersion of the effective refractive index may be very strong.

The examples of the dispersion of the SOI waveguide (230 nm thick Si layer on SiO_2 substrate) effective refractive index for the TE and the TM polarized light are shown in the Fig. 2.26(a). The corresponding dispersions using the reduced frequency units for the photonic crystal lattice constant $0.43 \mu\text{m}$ are plotted in the Fig. 2.26(b). It is clearly seen that the effective index strongly depends of the light frequency (especially for the TM light polarization) that should affect the dispersion of the Bloch modes in the photonic crystals.

The dispersion of the Bloch modes for the triangular lattice consisting of the air holes etched in the Si layer of the SOI structure is plotted in the Fig. 2.27(a) for the TE polarized light and in the Fig. 2.27(b) for the TM polarized light.

The results provided by the standard PWE method (where the waveguide effective refractive indices for the wavelength $\lambda = 1.55 \mu\text{m}$ have been used) are plotted by the green solid lines. The results provided by the frequency-based PWE method (with the same values of the effective refractive indices) are plotted by the blue squares. They perfectly coincide with the results of the standard PWE method. The results of the frequency-based PWE method with the dispersion of the effective refractive indices are plotted by the red circles. Now the shape of the band curves is distorted. The effect of the dispersion of the effective refractive index is like that the original dispersion curve (obtained using the constant effective refractive index) is compressed in the vertical direction according the dispersion of the effective refractive index. The

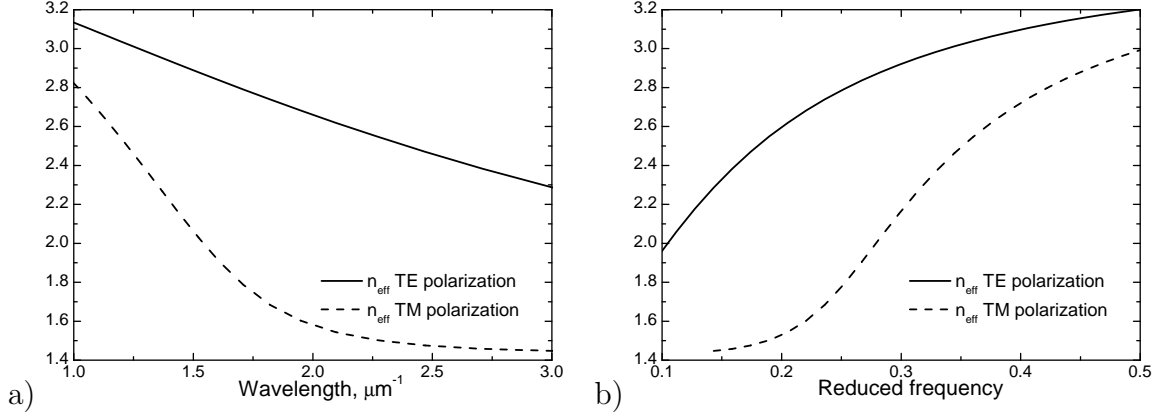


Figure 2.26: Dispersion of the effective refractive index for the SOI structure. a) n_{eff} as a function of the light wavelength. b) n_{eff} as a function of the PhC reduced frequency.

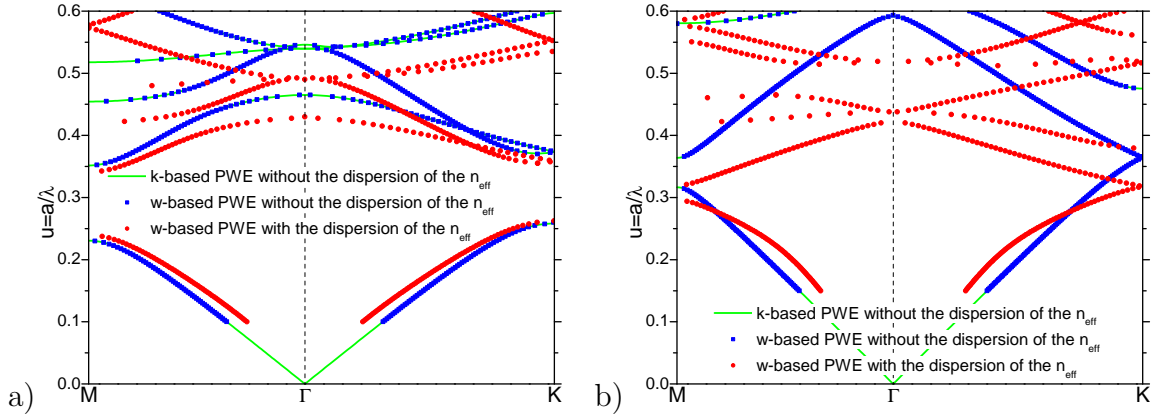


Figure 2.27: Dispersion of the Bloch modes for the triangular lattice photonic crystal consisting of the circular air holes (the filling factor $f = 0.4$) etched in the SOI structure calculated with and without taking into account the dispersion of the effective index. a) TE polarization. b) TM polarization.

chosen wavelength $\lambda = 1.55 \mu\text{m}$ corresponds to the reduced frequency $u \approx 0.2774$ and this frequency serves as a central (fixed) point for the compression transformation.

Because the dispersion of the effective index is more pronounced for the TM polarization the dispersion of the TM polarized Bloch modes is more distorted.

2.5.1.4 W1 photonic crystal waveguide

The W1 photonic crystal waveguide has been chosen as an example to illustrate the application of the PWE method for analysis of the dispersion properties of a photonic crystal based structure. Such waveguide is one of the key components of many modern photonic crystal based devices and detailed knowledge of the W1 waveguide properties is required to design them carefully.

The dispersion of the TE polarized light for the W1 photonic crystal waveguide is shown in the Fig. 2.28. The photonic crystal here consists of the circular air holes etched

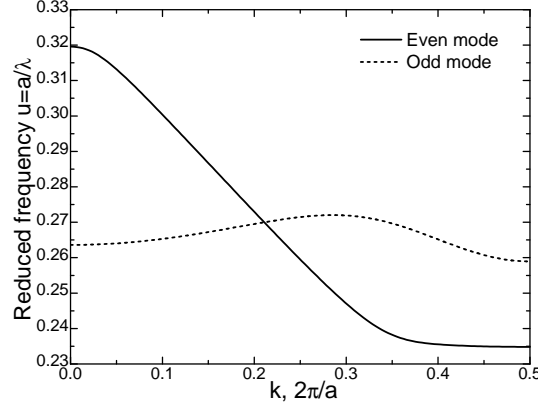


Figure 2.28: Dispersion of the even and the odd modes of the W1 photonic crystal waveguide.

in the thick planar waveguide. The filling factor $f = 40\%$. The maximum length of the reciprocal lattice vector $G_{max} = 6 \frac{2}{\sqrt{3}} \frac{2\pi}{a}$ and the number of used plane waves $N = 1159$.

There are two modes with different symmetry properties relative to the reflection in the (xz) plane located in the middle of the waveguide ($y = 0$). For the even mode the magnetic field H_z is symmetric and keep the sign after the reflection. For the odd mode the magnetic field is antisymmetric and changes the sign after the reflection.

The dispersion of the guided modes can be tuned by modifying parameters of the photonic crystal atoms near the waveguide core or changing the photonic crystal lattice by shrinking/expanding in the x or y direction.

2.5.2 Group velocity of the propagating Bloch modes

A Bloch mode with a given Bloch vector \mathbf{k}_0 and the frequency w_0 is a mode which exists everywhere in space and is infinitely long in time. Similar to the case of light propagating in a continuous media such mode cannot carry the information or transfer the energy. Light pulses of a finite duration and localized in a finite volume are natural states used for these purposes.

In general, light pulse in a photonic crystal can be represented as a superposition of the Bloch modes with different Bloch vectors and frequencies:

$$u(\mathbf{r}, t) = \sum_m \int f(\mathbf{k}, m) \psi_{\mathbf{k}, m}(\mathbf{r}, t) d\mathbf{k} \quad (2.94)$$

where $\psi_{\mathbf{k}, m}$ is m -th Bloch mode with the Bloch vector \mathbf{k} and $f(\mathbf{k}, m)$ is the amplitude of the mode.

If the amplitude function f noticeably differs from zero only in the vicinity of the vector \mathbf{k}_0 and only for the index of the state $m = m_0$ (which corresponds to the frequency w_0) it is said that the pulse has the carrier mode $\psi_{\mathbf{k}_0, m_0}$ and the carrier frequency w_0 .

Such pulse can be obtained by multiplying the carrier mode by the envelope function $f(\mathbf{r}, t)$ which has a long duration (much longer than the period of the carrier mode) and is localized in space with a large localization scale (much larger than the wavelength of the carrier mode).

The motion of such wave packet is governed by the group velocity which is equal to the gradient of the Bloch mode dispersion $\mathbf{V}_g = \nabla_{\mathbf{k}} \cdot w(\mathbf{k})$.

Using the Bloch vector based plane wave expansion method the dispersion of the light can be calculated for a grid in the \mathbf{k} -space determined as $\{\mathbf{k}_{ij}\}$, where $i = 1 \dots M$ and $j = 1 \dots N$. The gradient operator then can be calculated using the finite-difference formulas for each node of the grid. Here the formulas of the second-order accuracy have been used in order to calculate the group velocity.

2.5.2.1 Square lattice photonic crystals

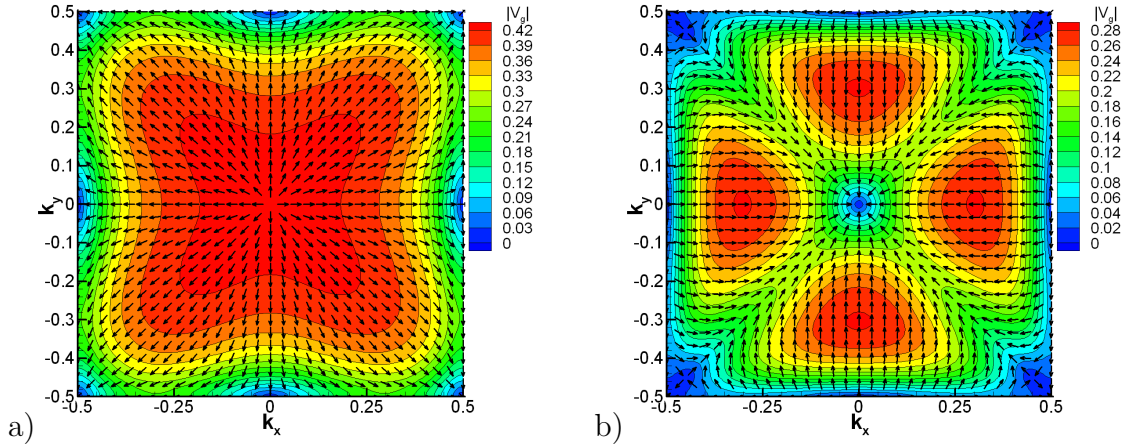


Figure 2.29: Group velocity of the TE-polarized Bloch modes for the square lattice photonic crystal consisting of the circular air holes (the filling factor $f = 0.4$) in the dielectric slab with the effective refractive index $n_{eff} = 3.24$. a) The first band. b) The second band.

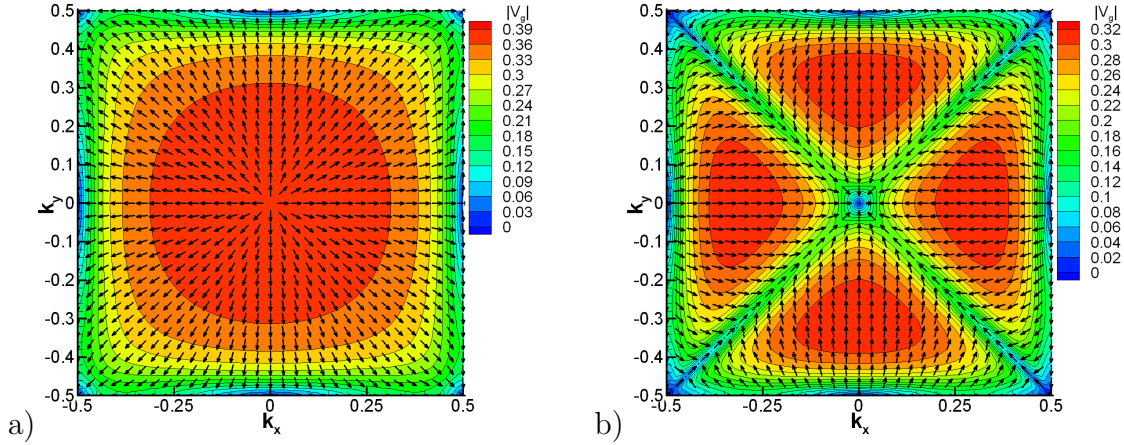


Figure 2.30: Group velocity of the TM-polarized Bloch modes for the square lattice photonic crystal consisting of the circular air holes (the filling factor $f = 0.4$) in the dielectric slab with the effective refractive index $n_{eff} = 3.24$. a) The first band. b) The second band.

Examples of the group velocity for the square lattice photonic crystal are plotted in the Fig. 2.29 and the Fig. 2.30. The calculation parameters are the same as used for the Fig. 2.18 and the Fig. 2.19. The group velocity here is measured in the units of the

vacuum light speed c . The modulus of the group velocity $|\mathbf{V}_g|$ is plotted as the color map and the direction is indicated by the vector field. In the first band for both light polarizations the group velocity is directed outwards from the Γ point and the value is almost constant near this point. Hence, the light with low frequency propagates in the photonic crystals like in a homogeneous media. The effective refractive index of this media has been estimated by Kirchner *at al.* in [62] and depends on the light polarization and the filling factor of the photonic crystal. Despite the symmetry of the photonic crystal lattice the dispersion for the low-frequency modes is almost isotropic (mainly due to the high symmetry of the “atoms”, which have the circular shapes in this examples). For higher order bands the group velocity, in general, strongly depends on the Bloch vector.

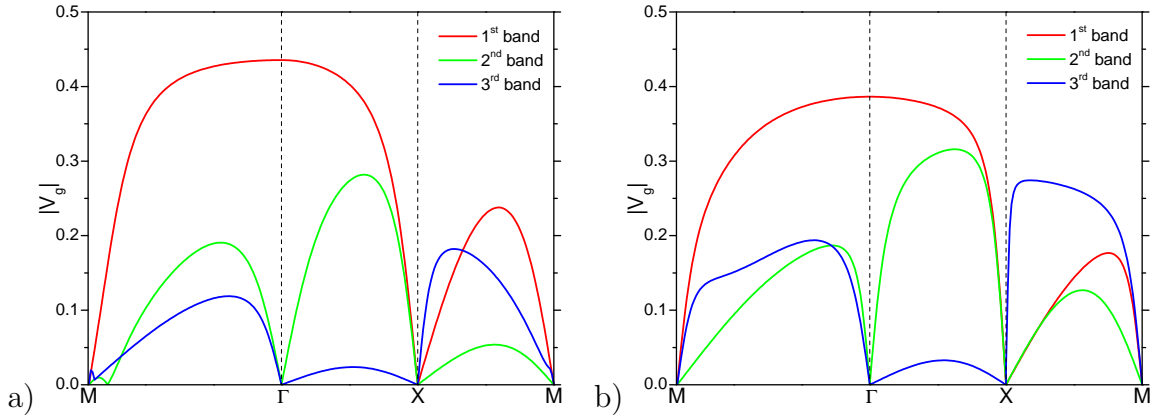


Figure 2.31: Group velocity of the Bloch modes for the square lattice photonic crystal consisting of the circular air holes (the filling factor $f = 0.4$) in the dielectric slab with the effective refractive index $n_{eff} = 3.24$. a) TE polarization. b) TM polarization.

The group velocity of the Bloch modes for the Bloch vector along the high-symmetry directions is plotted for the first three bands in the Fig. 2.31(a) for the TE light polarization and in the Fig. 2.31(b) for the TM light polarization.

At the boundary of the first Brillouin zone the derivative of the mode frequency in the direction normal to the boundary equals to zero $\frac{\partial \omega}{\partial \mathbf{k}_n} = 0$. This leads to zero group velocity at the high-symmetry points M and X.

While in the first and the group velocity is directed outwards from the Γ point in the second band the direction strongly depends on the \mathbf{k} vector and for some Bloch vectors may be even opposite the direction of \mathbf{k} . Such complex dependence of the group velocity on the carrier mode Bloch vector leads to many important phenomenons, like the superprism effect [6, 28, 30, 31] and the self-collimation effect [26, 29, 32–39].

2.5.2.2 Triangular lattice photonic crystals

Examples of the group velocity for the TE and TM polarized Bloch modes for the triangular lattice photonic crystal are shown in the Fig. 2.32 and Fig. 2.33, respectively. The calculation parameters are the same as used for the Fig. 2.22 and the Fig. 2.23. They have many similarities with the group velocity for the square lattice photonic crystal. For the first band near the Γ point the group velocity is almost constant and

directed outwards from the Γ point, while for the second band a complex dependence $V_g(\mathbf{k})$ is observed.

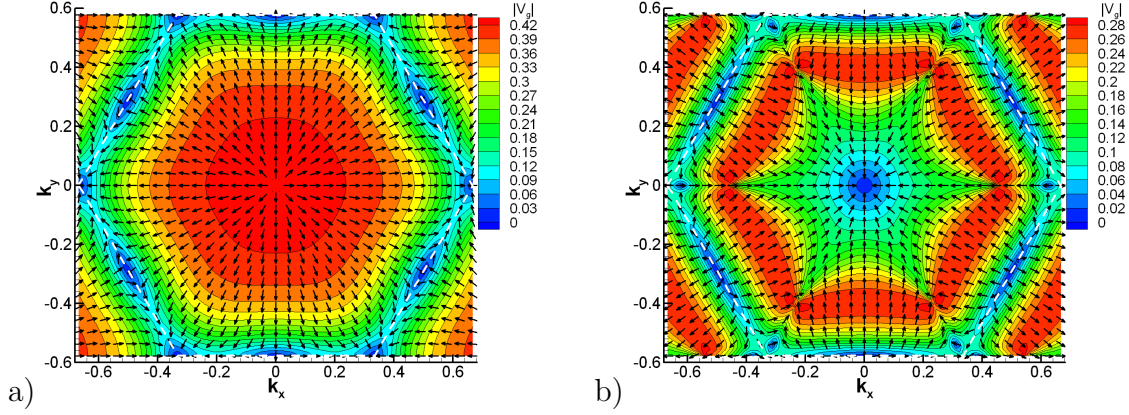


Figure 2.32: Group velocity of the TE-polarized Bloch modes for the triangular lattice photonic crystal consisting of the circular air holes (the filling factor $f = 0.4$) in the dielectric slab with the effective refractive index $n_{eff} = 3.24$. a) The first band. b) The second band.

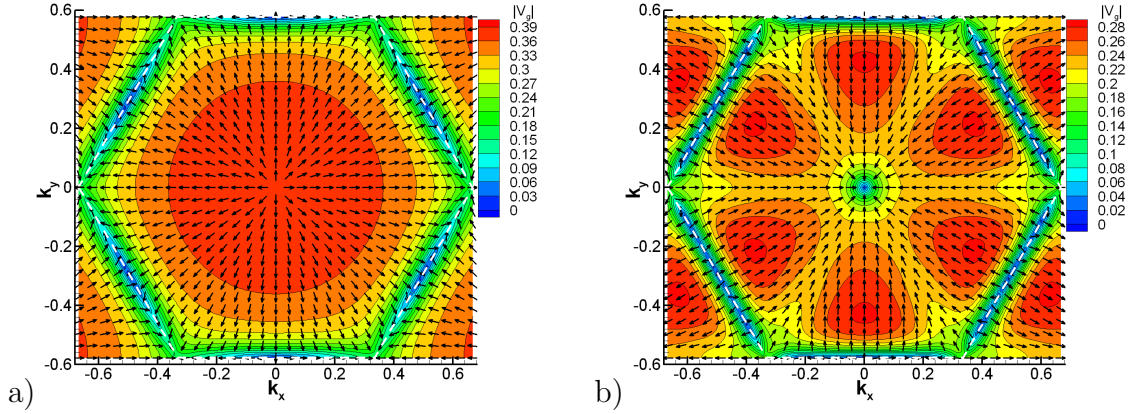


Figure 2.33: Group velocity of the TM-polarized Bloch modes for the triangular lattice photonic crystal consisting of the circular air holes (the filling factor $f = 0.4$) in the dielectric slab with the effective refractive index $n_{eff} = 3.24$. a) The first band. b) The second band.

The group velocity of the Bloch modes for the Bloch vector along the high-symmetry directions is plotted for the first three bands in the Fig. 2.34(a) for the TE light polarization and in the Fig. 2.34(b) for the TM light polarization.

A noticeable effect which can be seen in the Fig. 2.34 is the switching of the group velocity between different bands (like the switching between the second and the third bands between the Γ and K points and at the K point in the Fig. 2.34). The reason for this effect is crossing of the dispersion curves for the corresponding bands (which can be observed in the Fig. 2.24(a)). This crossing leads to the exchange of the band indices when we follow the curves (because the states are indexed in the frequency ascending order) and exchange of the group velocity values for the corresponding bands.

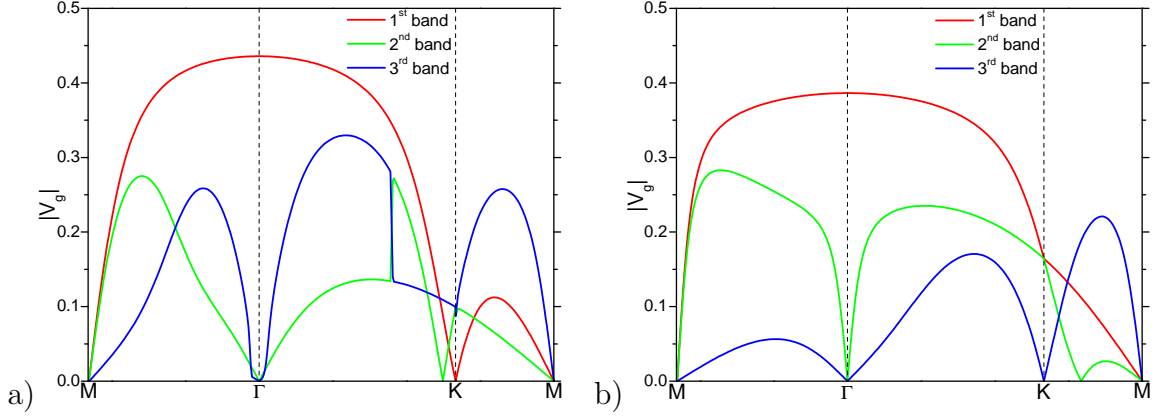


Figure 2.34: Group velocity of the Bloch modes for the triangular lattice photonic crystal consisting of the circular air holes (the filling factor $f = 0.4$) in the dielectric slab with the effective refractive index $n_{eff} = 3.24$. a) TE polarization. b) TM polarization.

2.5.2.3 W1 photonic crystal waveguide

The group velocity of the W1 waveguide is shown in the Fig. 2.35(a). The calculation parameters are the same as used for the Fig. 2.28. The even mode have relatively large and almost constant group velocity for $0.1\frac{2\pi}{a} < k < 0.25\frac{2\pi}{a}$. The odd mode changes the sign of the slope at $k \approx 0.285\frac{2\pi}{a}$ and the group velocity changes the direction.

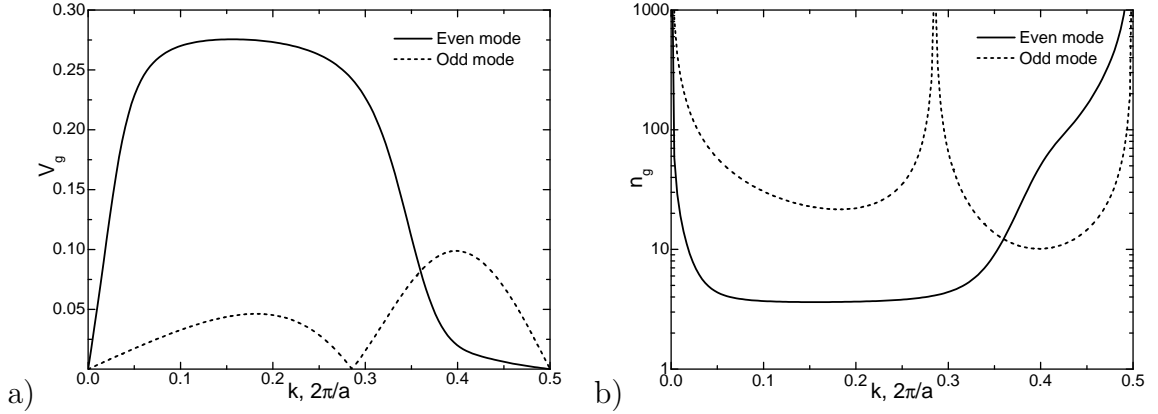


Figure 2.35: a) Modulus of the group velocity of the even and the odd modes of the W1 waveguide. b) The group index of the even and the odd W1 waveguide modes.

Near the boundary of the Brillouin zone ($\mathbf{k} = 0.52\pi/a$) the group velocity goes to zero and the slow light regime [63–65] is achieved.

2.5.3 Shape of the frequency isolines and the self-collimation effect

The motion of the light pulse in photonic crystal is governed by the group velocity $\mathbf{V}_g = \nabla_{\mathbf{k}} \cdot w(\mathbf{k})$. This approximation is valid for a light pulse which has the carrier

mode $\psi_{\mathbf{k}_0}$ and slightly localized envelope function $f(\mathbf{r}, t)$ in the real space and, hence, the envelope function $g(\mathbf{k})$ in the reciprocal space strongly localized near the Bloch vector \mathbf{k}_0 of the carrier mode. Increasing the light localization in the real space leads to widening the envelope function in the reciprocal space and the second-order effects start to be important.

Wide envelope function $g(\mathbf{k})$ in the reciprocal space can be considered as a superposition of several narrow envelope functions $g_i(\mathbf{k})$, each localized near their specific carrier mode Bloch vector \mathbf{k}_i . It corresponds to decomposition of the original light pulse into superposition of several pulses and considering them independently. Each secondary pulse has the group velocity $\mathbf{V}_{g,i} = \nabla_{\mathbf{k}} \cdot w(\mathbf{k})|_{\mathbf{k}=\mathbf{k}_i}$. In this case the evolution of the original pulse shape depends on the differences between the group velocity of the secondary pulses.

If the group velocities $\mathbf{V}_{g,i}$ are close each other the distortion of the original pulse will be minimal. If the group velocities have a noticeable difference the original pulse will enlarge because different parts of the pulse will have different group velocities.

Consider the most important case when the original pulse is almost monochromatic (for example, excited by a laser) with the frequency w_0 , but localized in the real space (for example, excited in a finite spot). Then the envelope function in the reciprocal space is localized along the frequency isoline $w(\mathbf{k}) = w_0$ (in general, it is also called the equifrequency surface (EFS) to keep the notation accepted in the solid-state physics).

The direction of the secondary pulses group velocities are normal to the frequency isoline, so the widening of the original pulse is determined by the shape of the isoline. If the curvature of the isoline is large the original pulse will diverge or focus, depending on the sign of the curvature. The flat isoline with the zero curvature corresponds to the case when the original pulse can propagate with small distortion, because all secondary pulses have the same group velocity. This is called the self-collimation effect [26, 34–38].

The curvature of the frequency isoline near the Bloch vector \mathbf{k}_0 can be calculated using the analysis described below.

The dispersion relation near a point in the \mathbf{k} -space can be approximated using the Taylor series:

$$w(\mathbf{k}_0 + \Delta\mathbf{k}) = w(\mathbf{k}_0) + (\Delta\mathbf{k} \cdot \nabla_{\mathbf{k}})w(\mathbf{k}) + \frac{1}{2!}(\Delta\mathbf{k} \cdot \nabla_{\mathbf{k}})^2 w(\mathbf{k}) + \frac{1}{3!}(\Delta\mathbf{k} \cdot \nabla_{\mathbf{k}})^3 w(\mathbf{k}) + \dots \quad (2.95)$$

where the derivatives are calculated at the point \mathbf{k}_0 .

It is convenient to introduce here a new local coordinate system where the direction of one basis vector (here it is \mathbf{e}'_y) is along the gradient of the $w(\mathbf{k})$ and the origin is at the point \mathbf{k}_0 . If the gradient equals to zero the following analysis is not applicable, but concerning the shape of the dispersion relation surface it is a very rare situation. In the new coordinate system (denoted by the prime) $\mathbf{k}_0 \rightarrow \mathbf{0}$, $\Delta\mathbf{k} \rightarrow \mathbf{k}'$ and the equation (2.95) transforms into

$$w(\mathbf{k}') = w(\mathbf{0}) + (\mathbf{k}' \cdot \nabla_{\mathbf{k}'})w(\mathbf{k}') + \frac{1}{2!}(\mathbf{k}' \cdot \nabla_{\mathbf{k}'})^2 w(\mathbf{k}') + \frac{1}{3!}(\mathbf{k}' \cdot \nabla_{\mathbf{k}'})^3 w(\mathbf{k}') + \dots \quad (2.96)$$

Using the second order approximation

$$\begin{aligned} w(\mathbf{k}') &= w(\mathbf{0}) + (\mathbf{k}' \cdot \nabla_{\mathbf{k}'})w(\mathbf{k}') + \frac{1}{2}(\mathbf{k}' \cdot \nabla_{\mathbf{k}'})^2 w(\mathbf{k}') \\ &= a_{00} + a_{10}k'_x + a_{01}k'_y + a_{11}k'_x k'_y + a_{20}k'^2_x + a_{02}k'^2_y \end{aligned} \quad (2.97)$$

where

$$\begin{aligned} a_{00} &= w(\mathbf{0}) & a_{10} &= \left. \frac{\partial w(\mathbf{k}')}{\partial k'_x} \right|_{\mathbf{0}} & a_{01} &= \left. \frac{\partial w(\mathbf{k}')}{\partial k'_y} \right|_{\mathbf{0}} \\ a_{11} &= \left. \frac{\partial^2 w(\mathbf{k}')}{\partial k'_x \partial k'_y} \right|_{\mathbf{0}} & a_{20} &= \left. \frac{1}{2} \frac{\partial^2 w(\mathbf{k}')}{\partial k'^2_x} \right|_{\mathbf{0}} & a_{02} &= \left. \frac{1}{2} \frac{\partial^2 w(\mathbf{k}')}{\partial k'^2_y} \right|_{\mathbf{0}} \end{aligned} \quad (2.98)$$

Because of the chosen coordinate system $a_{10} = 0$ and $a_{01} \neq 0$.

The equifrequency line for $w = w(\mathbf{0})$ is locally approximated by the curve $k'_y = k'_y(k'_x)$ which is defined by the equation

$$a_{02}k'^2_y + (a_{01} + a_{11}k'_x)k'_y + a_{20}k'^2_x = 0 \quad (2.99)$$

Then

$$k'_y = \begin{cases} -\frac{a_{01} + a_{11}k'_x + \sqrt{(a_{01} + a_{11}k'_x)^2 - 2a_{02}a_{20}}}{2a_{02}}, & a_{02} \neq 0 \\ -\frac{a_{20}}{a_{01} + a_{11}k'_x}, & a_{02} = 0 \end{cases} \quad (2.100)$$

The curvature of a curve $y = y(x)$ is calculated according to $s = \frac{d^2y}{dx^2} / \sqrt{1 + \left(\frac{dy}{dx}\right)^2}$. For the equifrequency line

$$\left. \frac{dk'_y}{dk'_x} \right|_{k'_x=0} = 0, \quad \left. \frac{d^2k'_y}{dk'^2_x} \right|_{k'_x=0} = -2 \frac{a_{20}}{a_{01}} \quad (2.101)$$

and the curvature $s = -2a_{20}/a_{01}$. The curvature has the positive sign then the contour is concave in the direction of the frequency gradient (and the group velocity \mathbf{V}_g) and is negative when the contour is convex in the direction of the frequency gradient.

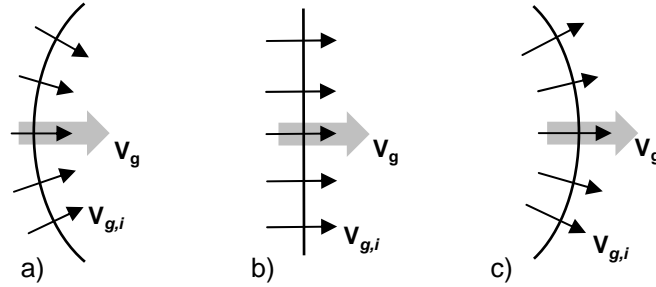


Figure 2.36: EFS curvature and the divergence of the light pulse. a) Positive EFS curvature: pulse focuses. b) Zero EFS curvature: self-collimation of the pulse. c) Negative EFS curvature: pulse diverges.

Three principal cases of the EFS curvature are illustrated in the Fig. 2.36. The frequency isoline is shown as a solid line and the group velocity \mathbf{V}_g is shown as a grey arrow. Group velocities of the secondary pulses $\mathbf{V}_{g,i}$ are plotted as black arrows. Positive curvature (Fig. 2.36(a)) leads to focusing of the original pulse. Zero curvature (Fig. 2.36(b)) means that all secondary pulses propagate in the same direction and the pulse is collimated. Negative curvature (Fig. 2.36(c)) leads to the divergence of the pulse.

Because it is adopted to use the dimensionless value of the Bloch vector (*i.e.* measure it in the special units $2\pi/a$) it is convenient also to work with a dimensionless EFS curvature. It corresponds to measuring the curvature in the $\frac{a}{2\pi}$ units.

2.5.3.1 Square lattice photonic crystals

The maps of the EFS curvatures as functions of the Bloch vector for the square lattice photonic crystal are plotted in the Fig. 2.37 for the TE polarization and in the Fig. 2.38 for the TM polarization. The calculation parameters are the same as used for the Fig. 2.18 and the Fig. 2.19.

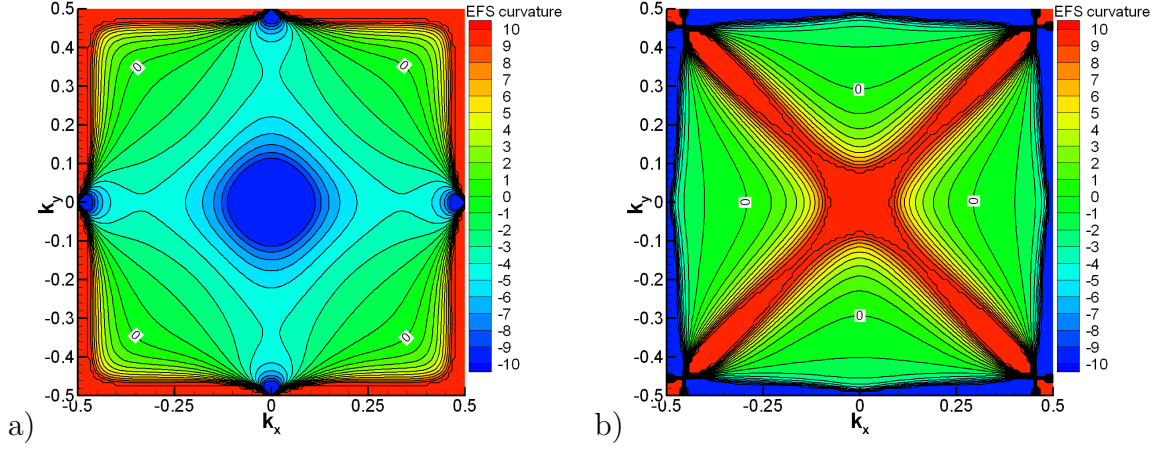


Figure 2.37: EFS curvature of the TE-polarized Bloch modes for the square lattice photonic crystal consisting of the circular air holes (the filling factor $f = 0.4$) in the dielectric slab with the effective refractive index $n_{eff} = 3.24$. a) The first band. b) The second band.

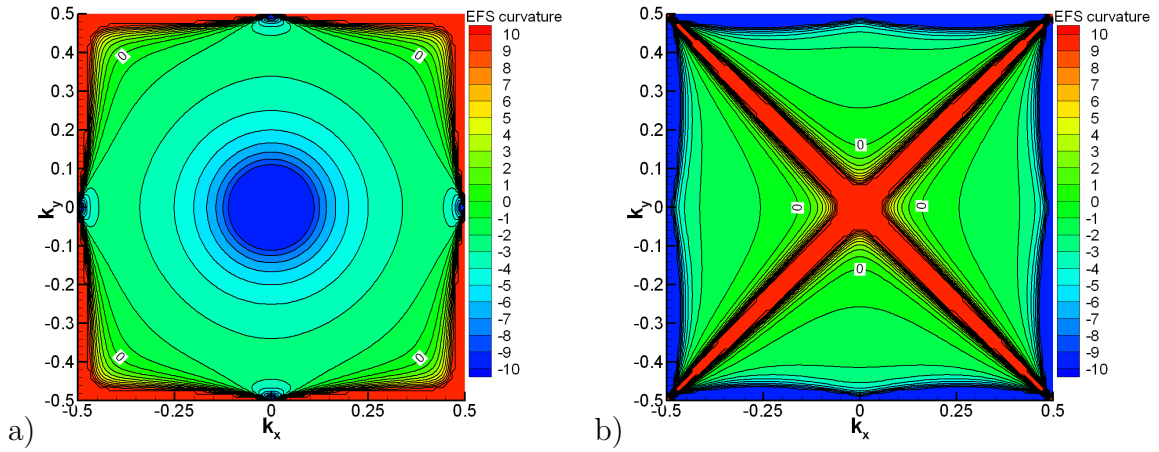


Figure 2.38: EFS curvature of the TM-polarized Bloch modes for the square lattice photonic crystal consisting of the circular air holes (the filling factor $f = 0.4$) in the dielectric slab with the effective refractive index $n_{eff} = 3.24$. a) The first band. b) The second band.

As it can be seen in the Fig. 2.18 and Fig. 2.19 near the Γ point the frequency isolines have almost circular shape with the radius going to zero at the Γ point. This leads to the infinite EFS curvature when $\mathbf{k} \rightarrow \Gamma$. Near the boundaries of the Brillouin zone the frequency isolines also have a large curvature because the isolines have to be normal to the boundary. In order to highlight the features of the EFS curvature distributions a

limited range of the EFS curvature values s is selected: $-10 < s < 10$. Values above and below the limits are plotted with the constant colors. Isolines $s = 0$ are indicated in all figures.

Several general features of the EFS curvature distribution may be noticed. Near the Γ point the curvature tends to minus infinity for the first band and tends to plus infinity for the second band. At the boundary of the Brillouin zone the curvature tends to have large positive values for the first band and to large negative values for the second band. The curvature tends to have large positive values at the ΓM line for the second band.

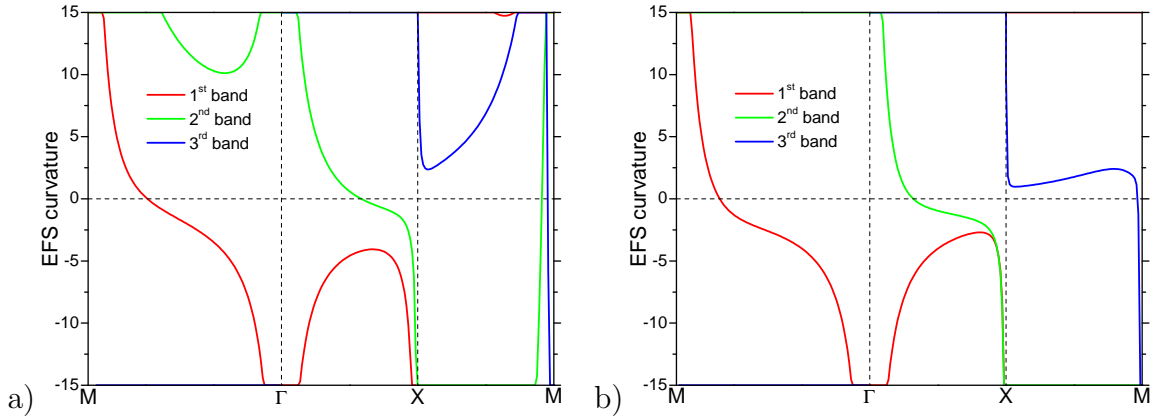


Figure 2.39: EFS curvature of the Bloch modes for the square lattice photonic crystal consisting of the circular air holes (the filling factor $f = 0.4$) in the dielectric slab with the effective refractive index $n_{eff} = 3.24$. a) TE polarization. b) TM polarization.

The cross-sections of the EFS curvatures are presented in the Fig. 2.39 for the TE and the TM polarizations. The self-collimation condition (zero EFS curvature) can be satisfied for the pulses with the carrier mode which have the Bloch vector along the ΓM direction (at the first band) and along the ΓX direction (at the second band).

2.5.3.2 Triangular lattice photonic crystals

The distributions of the EFS curvature for the triangular lattice photonic crystal are plotted in the Fig. 2.40 and Fig. 2.41. The calculation parameters are the same as used for the Fig. 2.22 and the Fig. 2.23. They exhibit basic features similar to the case of the square lattice photonic crystal.

The difference is that for the triangular lattice the equivalent of the ΓM direction is the ΓK direction.

The cross-sections of the EFS curvatures are shown in the Fig. 2.42 for the TE and the TM polarizations. It is seen that the self-collimation condition can be satisfied for the ΓM direction at the second band and for the ΓK direction at the first and the third bands.

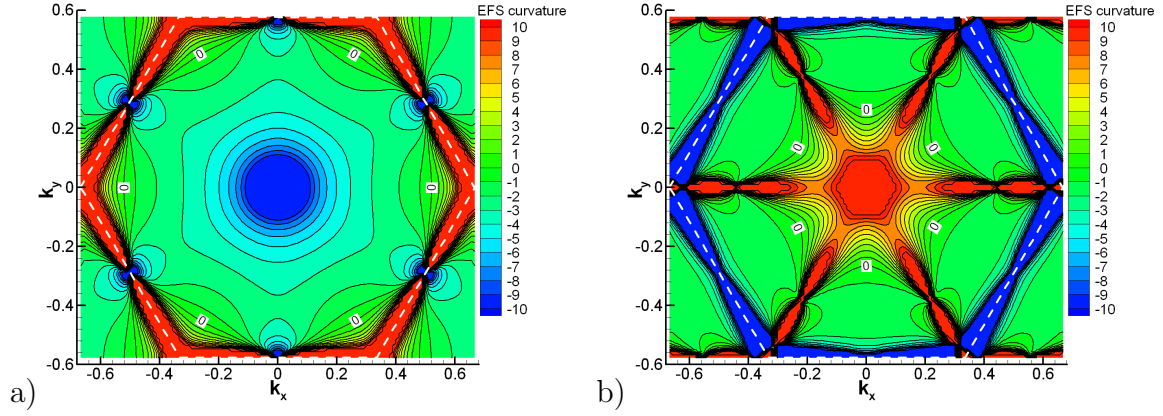


Figure 2.40: EFS curvature of the TE-polarized Bloch modes for the triangular lattice photonic crystal consisting of the circular air holes (the filling factor $f = 0.4$) in the dielectric slab with the effective refractive index $n_{eff} = 3.24$. a) The first band. b) The second band.

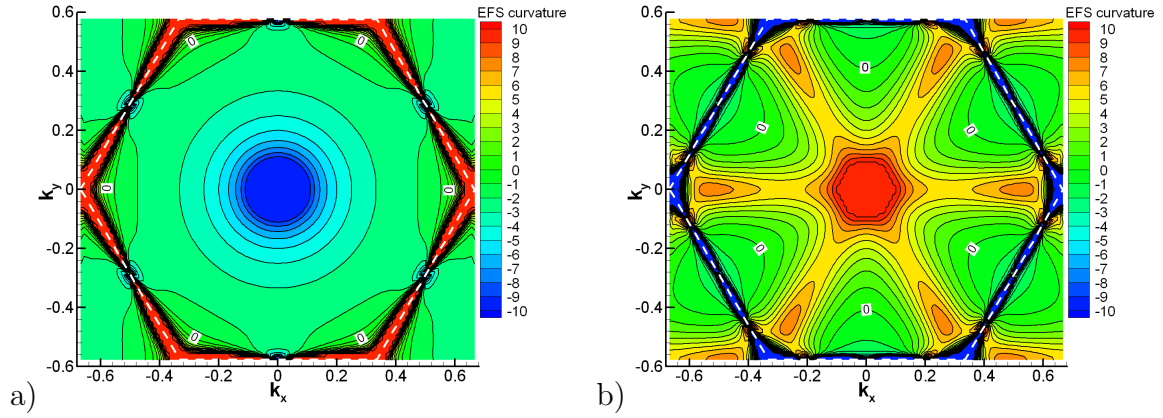


Figure 2.41: EFS curvature of the TM-polarized Bloch modes for the triangular lattice photonic crystal consisting of the circular air holes (the filling factor $f = 0.4$) in the dielectric slab with the effective refractive index $n_{eff} = 3.24$. a) The first band. b) The second band.

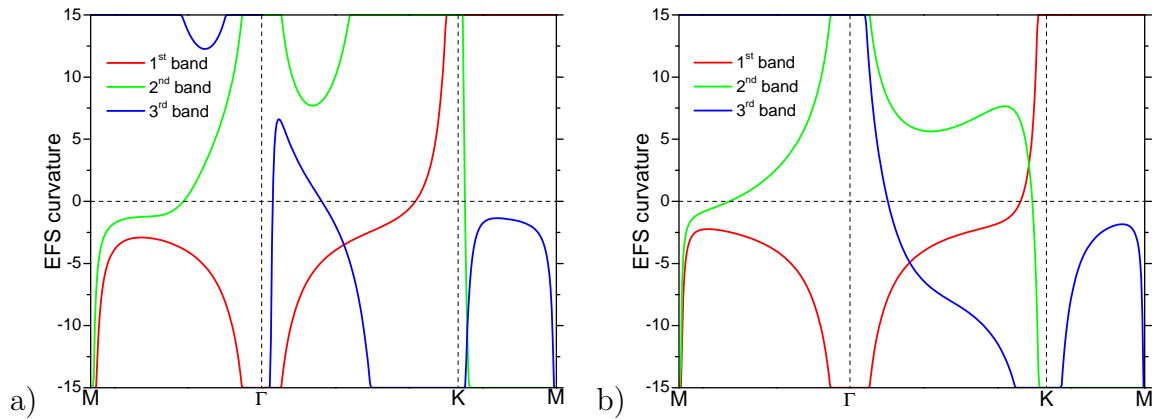


Figure 2.42: EFS curvature of the Bloch modes for the triangular lattice photonic crystal consisting of the circular air holes (the filling factor $f = 0.4$) in the dielectric slab with the effective refractive index $n_{eff} = 3.24$. a) TE polarization. b) TM polarization.

2.6 Field distribution of the Bloch modes

According to the two-dimensional approximation of the 2D photonic crystals there are two principal components of the electromagnetic field: H_z for the TE polarized light and E_z for the TM polarized light. These components are represented using the plane wave decomposition introduced in the equations (2.19) and (2.20). The coefficients of the decompositions can be obtained as the components of the eigenvectors in the equations (2.51) and (2.55) for the standard PWE method or in the equations (2.86) and (2.87) for the frequency-based PWE method.

The in-plane components can be calculated using the relations (2.40) and (2.41), which leads to the expressions

$$\mathbf{B}_{xy} = -i \frac{c}{\omega} \nabla \times \mathbf{E} = \sum_m A_m [(\mathbf{k} + \mathbf{G}_m) \times \mathbf{e}_z] e^{i(\mathbf{k} + \mathbf{G}_m) \cdot \mathbf{r}} \quad \text{“TM polarization”} \quad (2.102)$$

$$\mathbf{D}_{xy} = i \frac{c}{\omega} \nabla \times \mathbf{H} = \sum_m B_m [(\mathbf{k} + \mathbf{G}_m) \times \mathbf{e}_z] e^{i(\mathbf{k} + \mathbf{G}_m) \cdot \mathbf{r}} \quad \text{“TE polarization”} \quad (2.103)$$

In order to convert the electric field \mathbf{E} into the displacement field \mathbf{D} (and vice versa) the permittivity have to be used and hence, the results depends on the quality of the permittivity distribution approximation. The same treatment should be applied for the magnetic field \mathbf{H} and the magnetic induction \mathbf{B} , connected by the magnetic permeability μ if μ is discontinues in the photonic crystal.

The amplitude and the phase of the field can be chosen arbitrarily and in this section all modes are normalized to have the maximum amplitude $\max(E_z(\mathbf{r})) = 1$ for the TM polarized modes and $\max(H_z(\mathbf{r})) = 1$ for the TE polarized modes.

2.6.1 In-plane field components and the effect of the Gibbs phenomenon

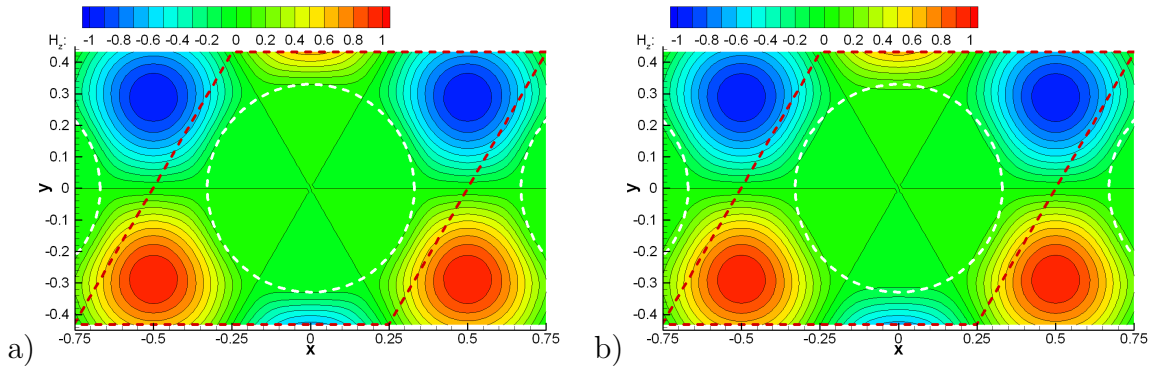


Figure 2.43: Magnetic field H_z component of the second band TE-polarized Bloch mode with the Bloch vector at the Γ point. The photonic crystal consists of the circular air holes (the filling factor $f = 0.4$) in the dielectric slab with the effective refractive index $n_{eff} = 3.24$. a) Calculation without the filtering of the permittivity distribution. b) Calculation using the Lanczos filter.

As it has been discussed in the section 2.3.1 the Gibbs phenomenon leads to the oscillation of the approximated permittivity distribution near the atom boundaries. The filtering of the Fourier expansion coefficients can be used to prevent such oscillations.

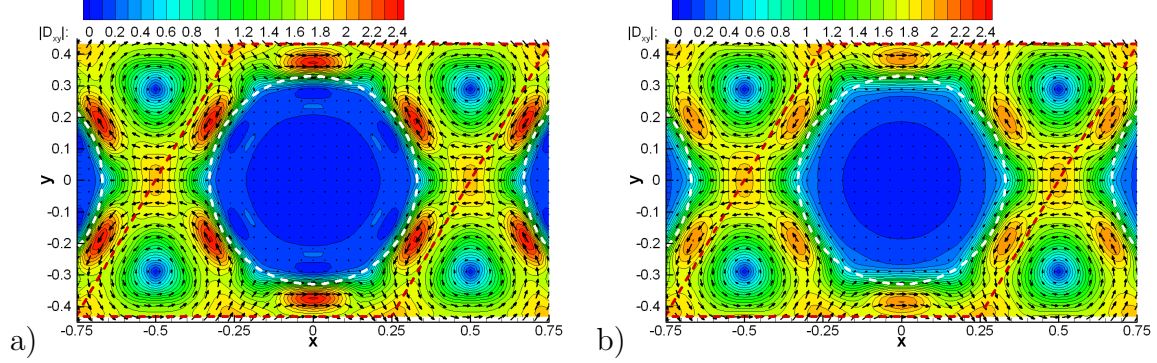


Figure 2.44: Displacement field \mathbf{D}_{xy} amplitude and the direction of the second band TE-polarized Bloch mode with the Bloch vector at the Γ point. The photonic crystal consists of the circular air holes (the filling factor $f = 0.4$) in the dielectric slab with the effective refractive index $n_{eff} = 3.24$. a) Calculation without the filtering of the permittivity distribution. b) Calculation using the Lanczos filter.

The effect of the filtering of the Gibbs phenomenon on the magnetic field distribution is presented in the Fig. 2.43. The lattice primitive cell is indicated by the red dashed line and the circular holes are indicated by the white dashed lines. The difference of the calculated mode frequency is quite small: $u \approx 0.4124$ without the filtering and $u \approx 0.4101$ for the Lanczos filtering ($G_{max} = 10.5 \cdot 2\pi/a$). The distributions of the magnetic field are also very similar.

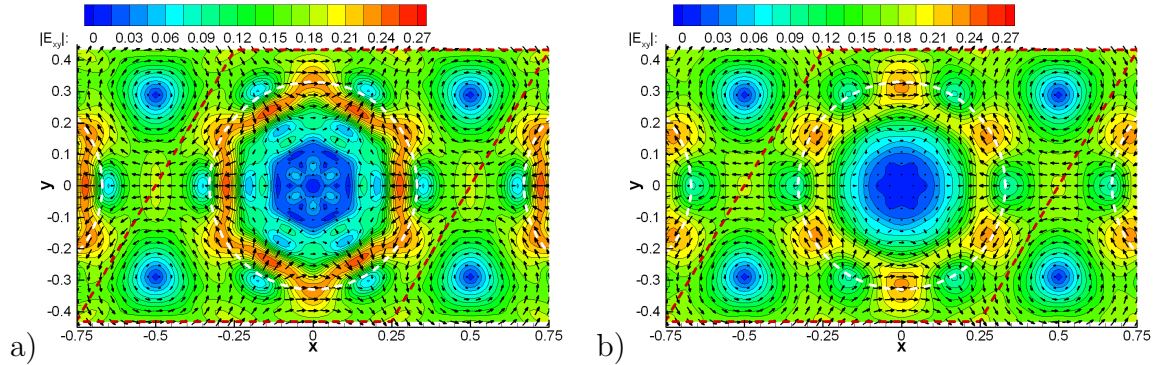


Figure 2.45: Electric field \mathbf{E}_{xy} amplitude and the direction of the second band TE-polarized Bloch mode with the Bloch vector at the Γ point. The photonic crystal consists of the circular air holes (the filling factor $f = 0.4$) in the dielectric slab with the effective refractive index $n_{eff} = 3.24$. a) Calculation without the filtering of the permittivity distribution. b) Calculation using the Lanczos filter.

The displacement field \mathbf{D}_{xy} is plotted in the Fig. 2.44. The color map indicates the field intensity and the vector map shows the field direction. Now the difference is visible:

the field obtained using the filtering is smoother near the atom boundary. Using the unfiltered approximation the oscillations of the field intensity are observed along some directions.

The electric field is obtained from the displacement field by division to the permittivity $\mathbf{E}_{xy} = \frac{1}{\varepsilon} \mathbf{D}_{xy}$ (or, operating with the Fourier decompositions, by multiplying the vector of the coefficients by the inverse permittivity matrix $\mathbf{E} = \boldsymbol{\Theta} \cdot \mathbf{D}$) and is quite sensitive to the oscillations of the permittivity around unity inside the hole. The calculated distribution of the electric field \mathbf{E}_{xy} is presented in the Fig. 2.45.

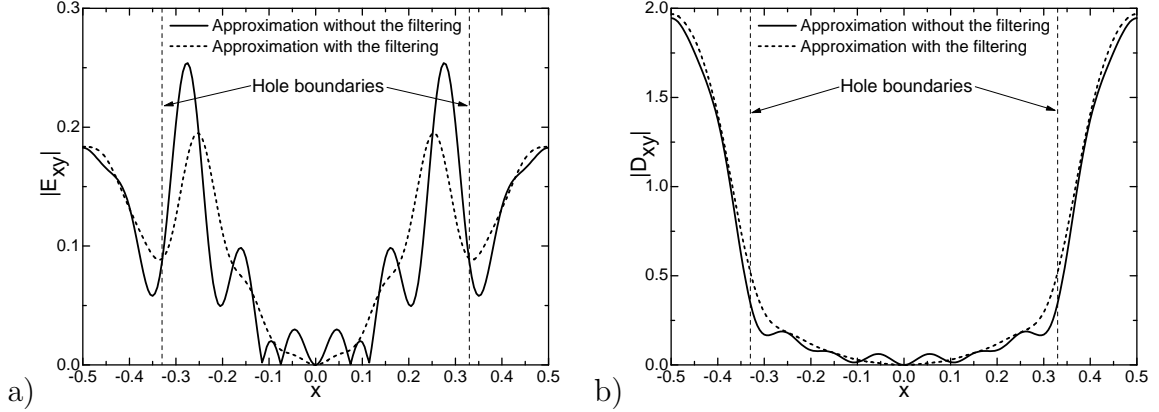


Figure 2.46: Cross-section along the line $y = 0$ of the electromagnetic field distribution of the second band TE-polarized Bloch mode with the Bloch vector at the Γ point. The photonic crystal consists of the circular air holes (the filling factor $f = 0.4$) in the dielectric slab with the effective refractive index $n_{eff} = 3.24$. a) Amplitude of the electric field E_{xy} . b) Amplitude of the displacement field D_{xy} .

The field distribution calculated using the approximation without the filtering exhibits the oscillations inside the hole while the approximation with the filtering provides relatively smooth result.

The cross-section of the fields distributions along the line $y = 0$ is shown in the Fig. 2.46(a) for the electric field and in the Fig. 2.46(b) for the displacement field. It is clearly seen that filtering of the Gibbs phenomenon allows to obtain smooth field distribution without the oscillations introduced by the approximation error.

Hence, filtering of the Gibbs phenomenon is important if the precise distribution of the in-plane field is required.

The electromagnetic field distribution for the TM polarized light can be calculated in a similar way. The E_z field is obtained directly from the equation (2.55) or the equation (2.86) and $D_z = \varepsilon E_z$.

The electric field E_z and the displacement field D_z for the second band Bloch mode with the Bloch vector $\mathbf{k} = 0$ are plotted in the Fig. 2.47. The electric field (as well as the displacement field) tends to be localized in the media with high permittivity, which is typical for the second band modes.

The in-plane magnetic field \mathbf{H}_{xy} is shown in the Fig. 2.48. It is also localized in the dielectric between the air holes.

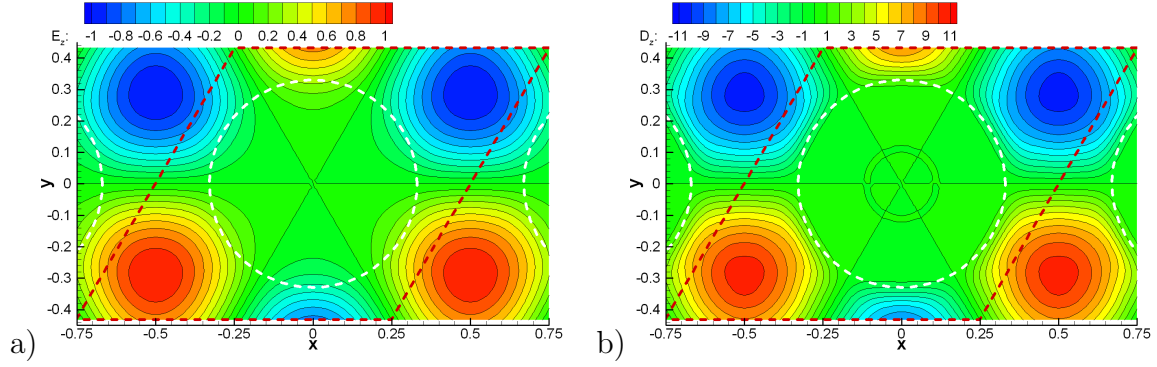


Figure 2.47: a) Electric field E_z and the displacement field D_z amplitudes of the second band TM polarized Bloch mode with the Bloch vector at the Γ point. The photonic crystal consists of the circular air holes (the filling factor $f = 0.4$) in the dielectric slab with the effective refractive index $n_{eff} = 3.24$.

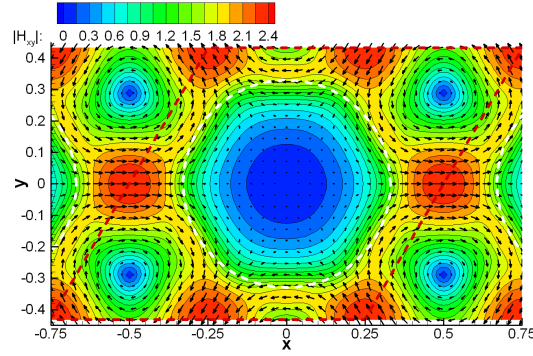


Figure 2.48: Magnetic field \mathbf{H}_{xy} amplitude and the direction of the second band TM polarized Bloch mode with the Bloch vector at the Γ point. The photonic crystal consists of the circular air holes (the filling factor $f = 0.4$) in the dielectric slab with the effective refractive index $n_{eff} = 3.24$.

2.6.2 Field distribution of the propagating Bloch modes

The field distribution of the propagating Bloch modes (with $\mathbf{k} \neq 0$) is more complex than the field of the standing modes. As it has been discussed in the section 1.2.1, in a periodic media the field distribution can be written as

$$\psi_{\mathbf{k}}(\mathbf{r}) = e^{i\mathbf{k}\mathbf{r}} u_{\mathbf{k}}(\mathbf{r}) \quad (2.104)$$

where $u_{\mathbf{k}}$ is a stationary function which have the same periodicity as the media.

It is convenient to remove the plane wave factor $e^{i\mathbf{k}\mathbf{r}}$ and analyze only $u_{\mathbf{k}}(\mathbf{r})$ because this function is same for all photonic crystal cells. Later in this section $u_{\mathbf{k}}(\mathbf{r})$ is assumed as the field distribution instead of $\psi_{\mathbf{k}}(\mathbf{r})$.

Another important feature of the field distribution of the Bloch mode with $\mathbf{k} \neq 0$ is that the field cannot be normalized to have only real or only imaginary part. Both real and imaginary parts have to be taken into account. This is a common feature of both field: $\psi_{\mathbf{k}}(\mathbf{r})$ and $u_{\mathbf{k}}(\mathbf{r})$. Multiplication or division of the field by the plane wave

$e^{i\mathbf{k}\mathbf{r}}$ cannot compensate the distribution of the field phase.

The magnetic field H_z distribution of the first band TE polarized Bloch mode with the Bloch vector at the middle between the Γ and the K points ($\mathbf{k} = (1/3, 0) 2\pi/a$) is shown in the Fig. 2.49. The real and the imaginary parts have comparable contributions to the total magnetic field.

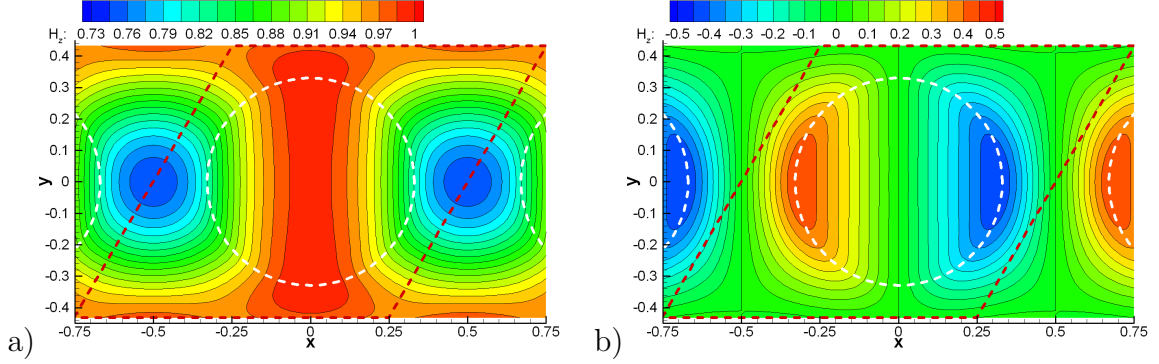


Figure 2.49: Magnetic field H_z component of the first band TE polarized Bloch mode with the Bloch vector at the middle between the Γ and the K points. The photonic crystal consists of the circular air holes (the filling factor $f = 0.4$) in the dielectric slab with the effective refractive index $n_{eff} = 3.24$. a) Real part $\Re(H_z)$. b) Imaginary part $\Im(H_z)$.

Similar effect can be observed for the H_z distribution of the second band TE polarized Bloch modes with the same Bloch vectors \mathbf{k} , which is plotted in the Fig. 2.50.

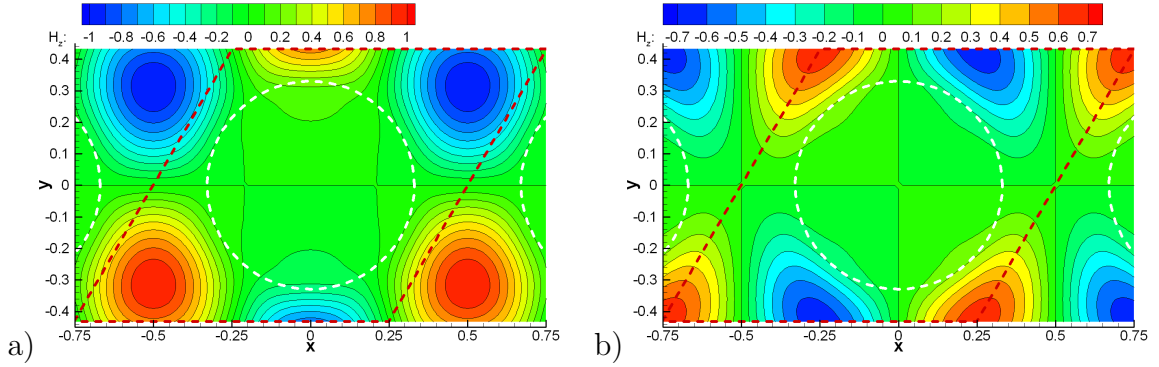


Figure 2.50: Magnetic field H_z component of the second band TE-polarized Bloch mode with the Bloch vector at the middle between the Γ and the K points. The photonic crystal consists of the circular air holes (the filling factor $f = 0.4$) in the dielectric slab with the effective refractive index $n_{eff} = 3.24$. a) Real part $\Re(H_z)$. b) Imaginary part $\Im(H_z)$.

The modulus of the H_z for the first band and the second band Bloch modes are presented in the Fig. 2.51. For the first band the magnetic field has the maximum in the air hole, while for the second band the field is maximum in the dielectric.

For the propagating Bloch modes the in-plane field components form a 2D complex vector field. Consider as an example the electric field \mathbf{E}_{xy} :

$$\mathbf{E}_{xy}(\mathbf{r}, t) = (\mathbf{E}_{Re}(\mathbf{r}) + i\mathbf{E}_{Im}(\mathbf{r})) e^{i(\mathbf{k}\mathbf{r} - \omega t)} \quad (2.105)$$

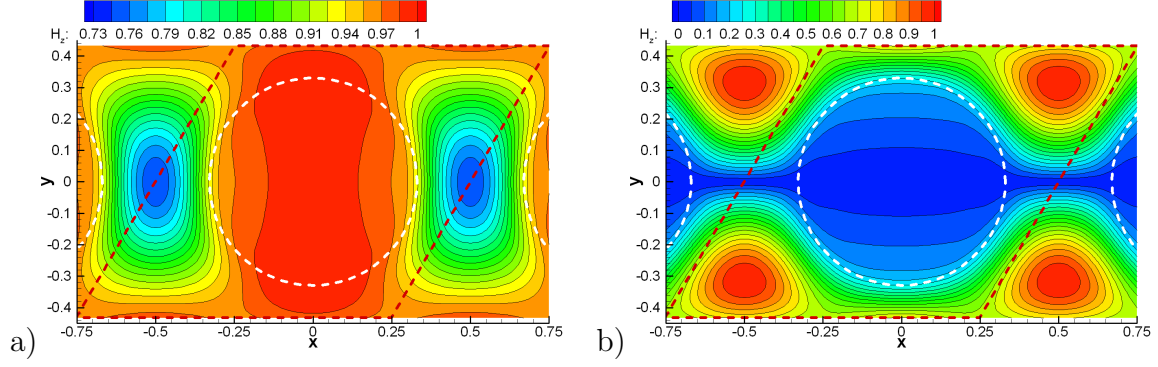


Figure 2.51: Magnetic field modulus $|H_z|$ of the TE-polarized Bloch modes with the Bloch vector at the middle between the Γ and the K points. The photonic crystal consists of the circular air holes (the filling factor $f = 0.4$) in the dielectric slab with the effective refractive index $n_{eff} = 3.24$. a) The first band mode. b) The second band mode.

where $\mathbf{E}_{Re}(\mathbf{r})$ and $\mathbf{E}_{Im}(\mathbf{r})$ are the real and the imaginary parts of the field, correspondingly.

The expression (2.105) describes, in general, the elliptically polarized field where the directions of the principal polarization axes and the ellipticity depend on the position inside the photonic crystal cell.

This expression can be rewritten as

$$\mathbf{E}_{xy}(\mathbf{r}, t) = (\mathbf{E}_1(\mathbf{r}) + i\mathbf{E}_2(\mathbf{r})) e^{i(\varphi(\mathbf{r}) + \mathbf{k}\mathbf{r} - \omega t)} \quad (2.106)$$

by introducing the phase $\varphi(\mathbf{r})$ chosen so that for any given \mathbf{r} the scalar product $(\mathbf{E}_1(\mathbf{r}) \cdot \mathbf{E}_2(\mathbf{r})) = 0$ and both vectors are real. Then the vectors $\mathbf{E}_1(\mathbf{r})$ and $\mathbf{E}_2(\mathbf{r})$ define the amplitudes and the directions of the principal polarization axis.

The same treatment should be done with other in-plane fields (\mathbf{D}_{xy} for the TE polarized light and \mathbf{H}_{xy} for the TM polarized light).

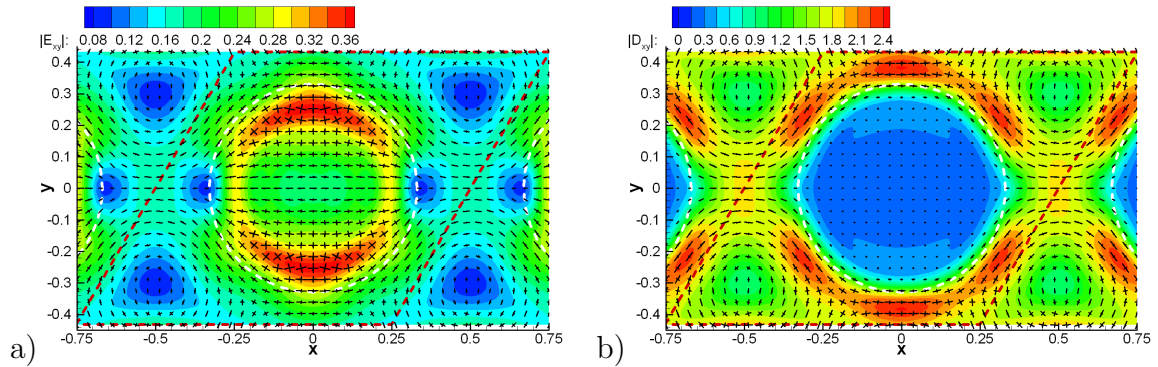


Figure 2.52: The amplitude and the directions of the principal polarization axes for (a) the electric field \mathbf{E}_{xy} and (b) the displacement field \mathbf{D}_{xy} of the second band TE-polarized Bloch mode with the Bloch vector at the middle between the Γ and the K points. The photonic crystal consists of the circular air holes (the filling factor $f = 0.4$) in the dielectric slab with the effective refractive index $n_{eff} = 3.24$.

While for the modes with $\mathbf{k} = 0$ the in-plane field is always linearly polarized when $\mathbf{k} \neq 0$ the ellipticity can be noticeable. Such ellipticity has been directly measured for the guided modes of the W1 waveguide in [66].

The distributions of the electric field \mathbf{E}_{xy} and the displacement field \mathbf{D}_{xy} are presented in the Fig. 2.52. The modulus of the field amplitude is plotted as the colormap and the directions and amplitudes of the principal polarization axis are indicated by black lines. Almost circular polarizations is observed for the electric field at the regions inside the air holes.

The ellipticity of the electric field polarization can affect the tunability of the photonic crystal infiltrated by the liquid crystals (LQ) [67–69]. Optical properties of such photonic crystals may be tuned by changing the orientation of the LQ molecules or by the phase transition between the nematic and the isotropic phases. If the polarization is elliptical the effective permittivity of the liquid crystal, obtained from the permittivity tensor by the averaging according to the local orientation of the electric field, is less sensitive to the orientation of the LQ molecules. It deteriorates the tunability of the LQ PhCs.

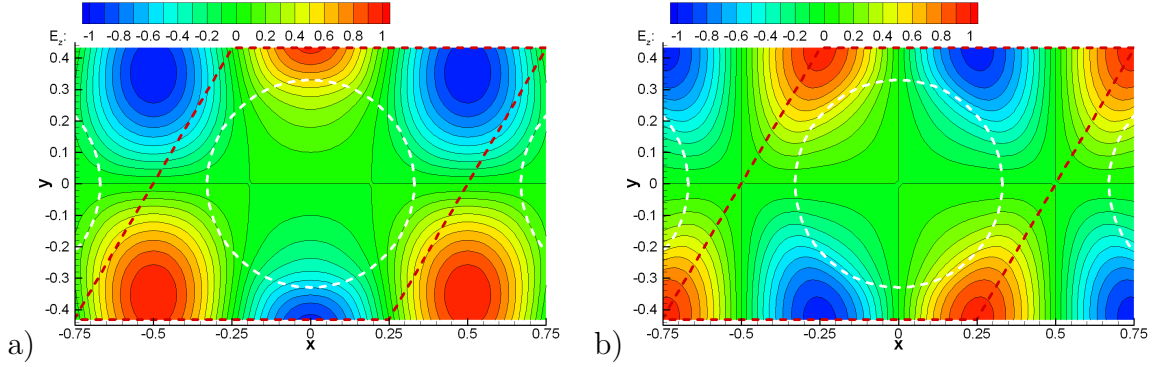


Figure 2.53: Electric field E_z component of the second band TM-polarized Bloch mode with the Bloch vector at the middle between the Γ and the K points. The photonic crystal consists of the circular air holes (the filling factor $f = 0.4$) in the dielectric slab with the effective refractive index $n_{eff} = 3.24$. a) Real part $\Re(E_z)$. b) Imaginary part $\Im(E_z)$.

The electric field E_z distribution of the TM polarized propagating Bloch modes is similar to the case of the TE polarized modes. The example of the electric field distribution for the second band Bloch mode with the Bloch vector \mathbf{k} in the middle between the Γ and the K points is presented in the Fig. 2.53. Here both real and imaginary parts have equal contributions into the total field amplitude.

The modulus of the total field amplitude $|E_z|$ is shown in the Fig. 2.54(a). For the second band the electric field tends to be localized in the regions with high dielectric permittivity, *i.e.* outside of the air holes. The corresponding distribution of the modulus of the displacement field $|D_z|$ is plotted in the Fig. 2.54(b). This distribution is similar to one shown in the Fig. 2.54(a) but is even more localized outside of the holes.

The magnetic field \mathbf{H}_{xy} also have an elliptical polarization, where the principal polarization directions and the ellipticity depend on the position inside the photonic crystal cell. The magnetic field distribution is presented in the Fig. 2.55. The magnetic field has a minimum inside the holes and maximums at the hole boundaries and in the

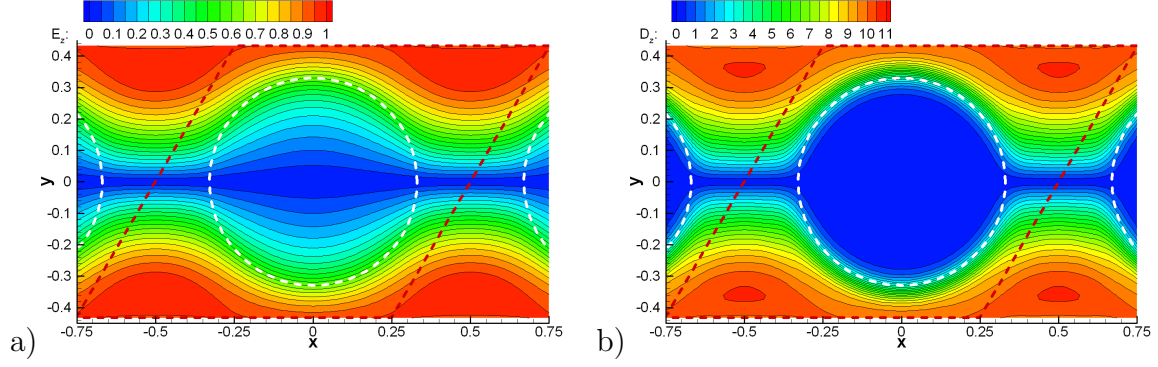


Figure 2.54: Electric field modulus $|E_z|$ (a) and displacement field modulus $|D_z|$ (b) of the second band TM-polarized Bloch modes with the Bloch vector at the middle between the Γ and the K points. The photonic crystal consists of the circular air holes (the filling factor $f = 0.4$) in the dielectric slab with the effective refractive index $n_{eff} = 3.24$.

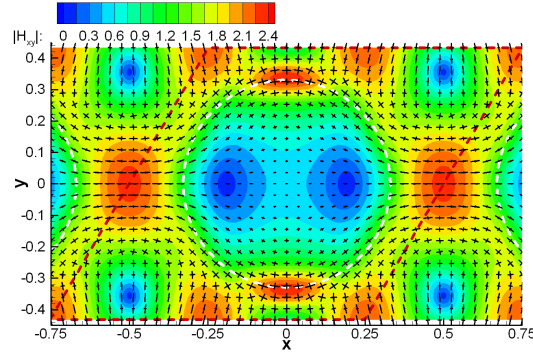


Figure 2.55: The amplitude and the directions of the principal polarization axes for the magnetic field \mathbf{H}_{xy} of the second band TM-polarized Bloch mode with the Bloch vector at the Γ point. The photonic crystal consists of the circular air holes (the filling factor $f = 0.4$) in the dielectric slab with the effective refractive index $n_{eff} = 3.24$.

regions with high permittivity. The local polarization varies from the linear to almost circular, depending on the position inside the photonic crystal cell.

2.7 Cavities and localized states

Breaking of the photonic crystal periodicity creates new light states associated with the lattice defect. If the frequency of a created state is inside the full photonic band gap of the original photonic crystal this state is localized near the defect. Zero-dimensional lattice defects serve as microcavities with small localization volume (the characteristic scale is square PhC lattice constant) and high quality factor [43, 50, 70].

One of the main attribute of the localized state is the field distribution. Since the frequency of the state is inside the photonic band gap the field in the region around the defect (where the photonic crystal has the perfect lattice) can be only evanescent, decaying with increasing the distance from the defect. Such field cannot carry the energy,

so when the defect is surrounded by a large area photonic crystal the in-plane losses are negligible small. The only loss channels are material absorption and out-of-plane radiation losses. In the 2D approximation the out-of-plane losses are neglected, so if the material is non-absorptive the theoretical quality factor is infinitely large. Taking into account the third dimension (which is discussed in the chapter 3) the radiation losses can be calculated by coupling between the localized states and the radiative states of the planar waveguide cladding layers [71]. The coupling intensity depends on the overlap between the field distribution of the localized state and the field of the radiative states, so the detailed knowledge of the cavity mode field distribution is required to design a cavity with desired quality factor [43, 51, 72, 73].

The distribution of the magnetic field H_z for the 1st localized state of the L3 cavity is shown in the Fig. 2.56. This is the state with the lowest reduced frequency $u \approx 0.2384$.

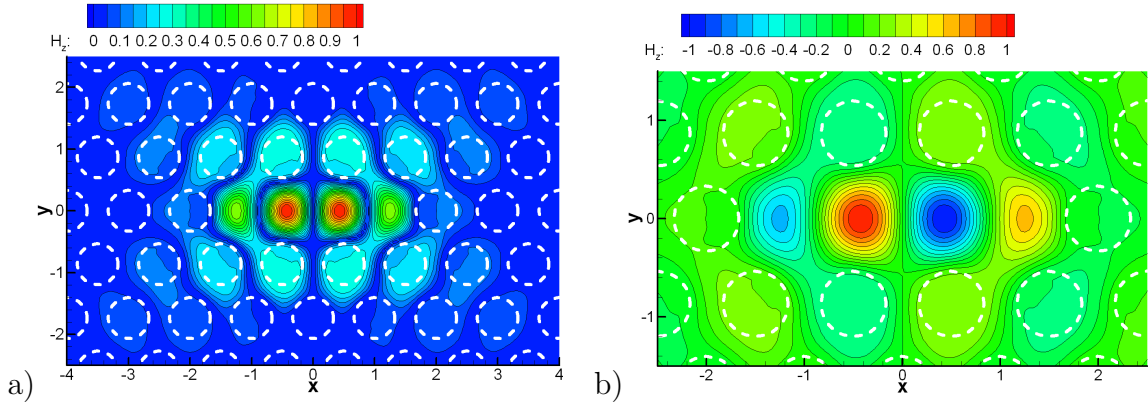


Figure 2.56: Magnetic field H_z component modulus (a) and amplitude (b) of the 1st localized state of the L3 cavity. The photonic crystal consists of the circular air holes (the filling factor $f = 0.4$) in the dielectric slab with the effective refractive index $n_{eff} = 3.24$.

The magnetic field has the even symmetry relative to the reflection in the (xz) plane ($y = 0$) and the odd symmetry relative to the reflection in the (yz) plane ($x = 0$), where the origin of the coordinates corresponds to the center of the cavity.

Other states can have different symmetry properties. The example of the magnetic field distribution of the 3rd localized state with the reduced frequency $u \approx 0.2625$ is presented in the Fig. 2.57. This state has the odd symmetry relative to the reflection in the (xz) plane and the even symmetry relative to the reflection in the (yz) plane. Different symmetry properties of the modes lead to different coupling with the radiation states and different quality factors.

Another important aspect is distribution of the in-plane fields (\mathbf{E}_{xy} and \mathbf{D}_{xy} for the TE polarized light). Fabrication of the PhC cavity based light source [4] requires an emitter (quantum dot/dots, quantum wire, or quantum well) coupled with the desired cavity state. In order to have a good coupling the light source should be located at the place where the amplitude of the electric field is maximum. Because the coupling strength can also depends on the direction of the electric field (which is important, for example, for quantum wires) the full vectorial distribution of the in-plane electric field should be taken into account.

Examples of the in-plane fields distributions are shown in the Fig. 2.58 and the

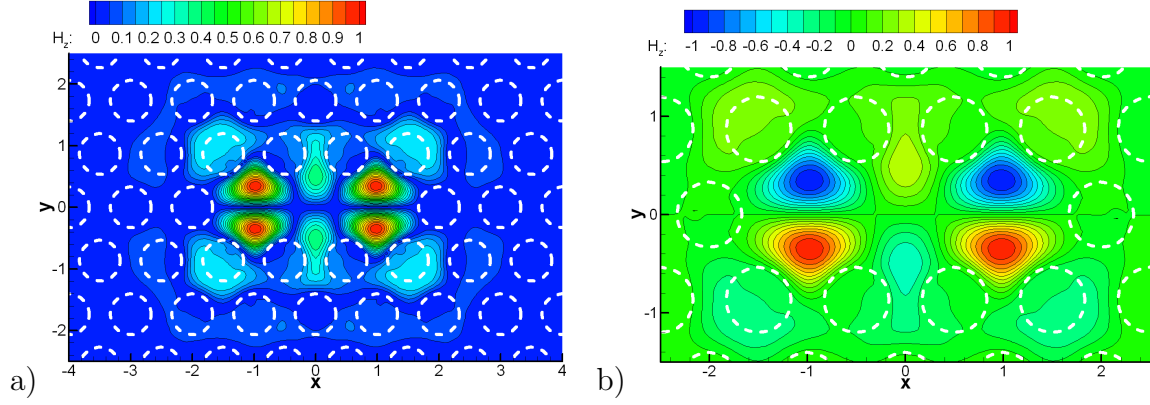


Figure 2.57: Magnetic field H_z component modulus (a) and amplitude (b) of the 3^{rd} localized state of the L3 cavity. The photonic crystal consists of the circular air holes (the filling factor $f = 0.4$) in the dielectric slab with the effective refractive index $n_{eff} = 3.24$.

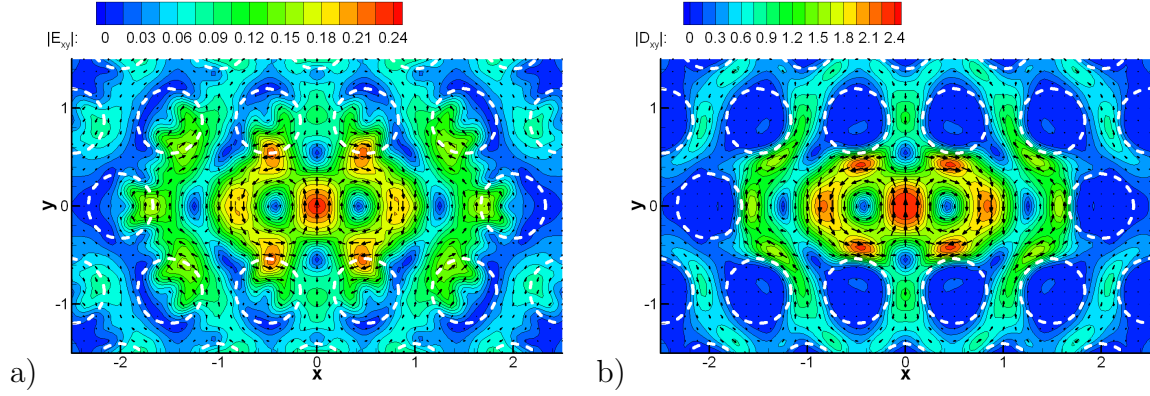


Figure 2.58: The amplitude and the direction of (a) the electric field \mathbf{E}_{xy} and (b) the displacement field \mathbf{D}_{xy} of the 1^{st} localized state of the L3 cavity. The photonic crystal consists of the circular air holes (the filling factor $f = 0.4$) in the dielectric slab with the effective refractive index $n_{eff} = 3.24$.

Fig. 2.59 for the 1^{st} and the 3^{rd} cavity states, respectively. The amplitudes of the field are plotted as the colormaps and the direction of the field is indicated by black arrows.

The 1^{st} cavity state has a clear maximum of the electric field at the cavity center where the field is directed along the y axis. The 3^{rd} state has two maximums inside the cavity where the field is directed along the x axis.

Variation of the parameters of the cavity and position of the light emitter change the coupling between the source and the cavity mode [4] and is the main way to design PhC cavity based lasers [42].

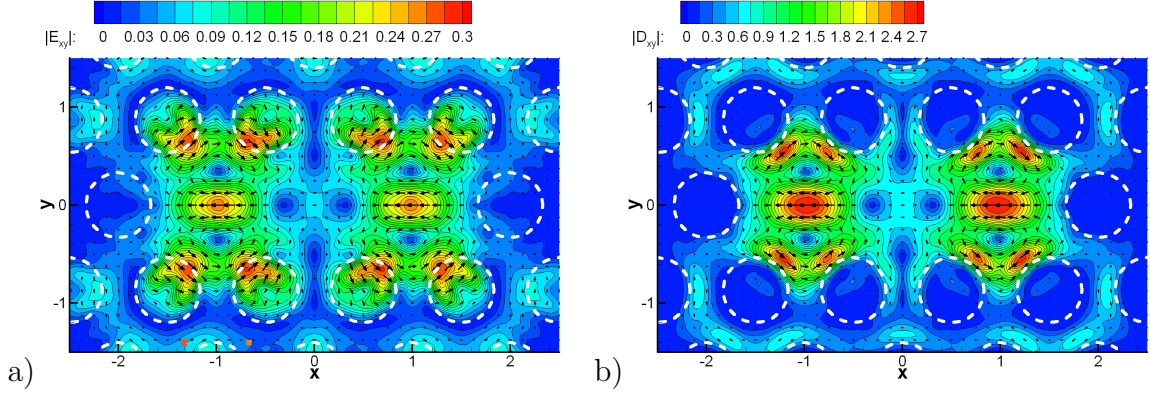


Figure 2.59: The amplitude and the direction of (a) the electric field \mathbf{E}_{xy} and (b) the displacement field \mathbf{D}_{xy} of the 3rd localized state of the L3 cavity. The photonic crystal consists of the circular air holes (the filling factor $f = 0.4$) in the dielectric slab with the effective refractive index $n_{eff} = 3.24$.

2.8 Evanescent modes in photonic crystals

2.8.1 Ministop band in the W3 waveguide

The dispersion relation of the guided modes of the W1 waveguide has been discussed in the section 2.5.1.4. Increasing of the waveguide width increases the number of allowed modes. If the field distributions of two modes have same symmetry relative to the reflection in the (xz) plane these modes can interact with each other and it leads to formation of the anticrossing of the mode dispersion curves. The anticrossing creates the ministop band (MSB) [5] – frequency range where the light propagation is suppressed.

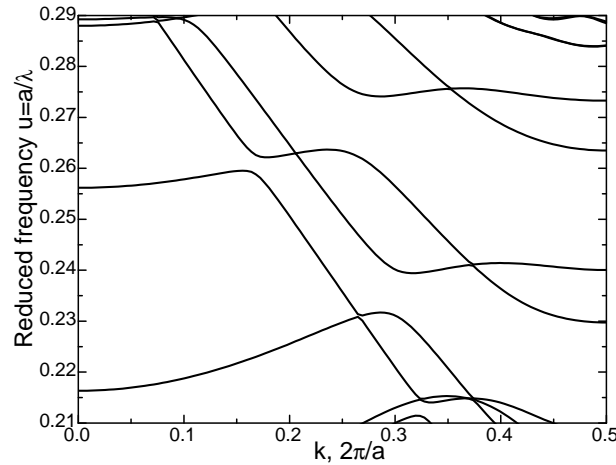


Figure 2.60: Dispersion of the Bloch modes for the W3 photonic crystal waveguide consisting of the circular air holes (the filling factor $f = 0.31$) in the dielectric slab with the effective refractive index $n_{eff} = 3.25$.

The dispersion of guided modes of the W3 waveguide calculated using the plane wave expansion method is shown in the Fig. 2.60. Anticrossing of two modes with the even symmetry creates the ministop band near $k \approx 0.172\pi/a$ and $u \approx 0.261$. Although

the modes with the frequency inside the ministop band have the imaginary part of the Bloch vector and exponentially decay in the waveguide this imaginary part is relatively small and the dispersion relation can be measured experimentally [74].

The W3 waveguide (triangular lattice parameter $a = 0.40 \mu\text{m}$, hole diameter $d = 0.27 \mu\text{m}$, and total length $L = 24 \mu\text{m}$ was designed to operate in the vicinity of the ministop band for the TE polarized light around a wavelength of $1.55 \mu\text{m}$. The GaInAsP/InP planar waveguide is single mode in the frequency range of interest with an effective index of 3.25. Details about the structural parameters and the fabrication are given in [74]. The method of dispersion relation measuring is described in [75].

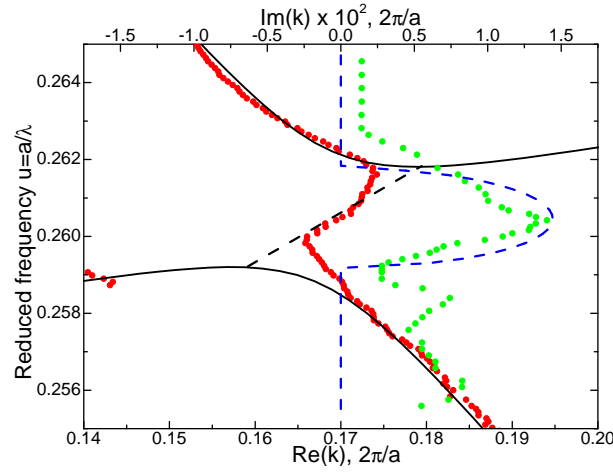


Figure 2.61: Dispersion of the Bloch modes for the W3 photonic crystal waveguide near the ministop band. Solid lines are calculated using the standard PWE method and dashed lines are obtained using the frequency-based PWE method; real (black) and imaginary (blue) parts of the Bloch vector \mathbf{k} are shown. Scatter points correspond to experimental results: real part of \mathbf{k} is red and imaginary part is green.

The comparison of the theoretical results (obtained using the frequency-based plane wave expansion method) and the experimental dispersion relation of the W3 waveguide modes is presented in the Fig. 2.61. Solid lines are calculated using the standard (\mathbf{k} -based) plane wave expansion method and dashed lines are obtained using the frequency-based plane wave expansion method. For the frequencies where guided modes exist (with purely real Bloch vectors) the results obtained by both methods are identical. But inside the ministop band the frequency-based PWE method finds the evanescent modes with non-zero imaginary part of the Bloch vector. The imaginary part $\Im(\mathbf{k})$ starts from zero at the boundaries of the ministop band and reaches the maximum in the MSB center.

The experimental results are plotted by red circles (real part of \mathbf{k}) and green circles (imaginary part of \mathbf{k}). There is a good agreement between the theoretical and the experimental results, which proves validity of the frequency-based PWE method. The discrepancy near the edges of the ministop band is the result of the intrinsic disorder of the W3 waveguide [74].

2.8.2 Penetration of the guided modes into the cladding regions

As it has been discussed in the section 2.5.1.4 the W1 waveguide supports two guided modes with different symmetry properties. The dispersion of the guided modes is shown in the Fig. 2.62.

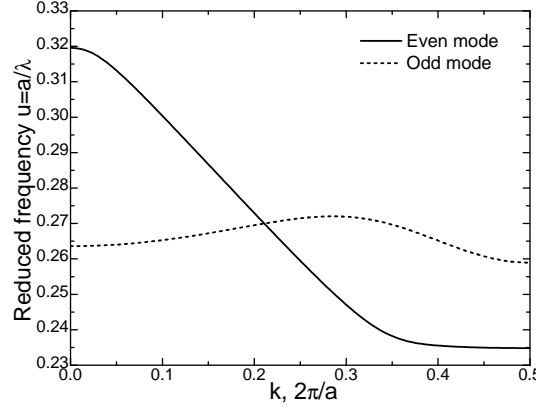


Figure 2.62: Dispersion of the even and the odd modes of the W1 photonic crystal waveguide.

The light propagated in the W1 photonic crystal waveguide is localized because the frequencies of the guided modes are inside the full photonic band gap. The light in the cladding regions, where photonic crystal have the perfect lattice, exponentially decays with increasing the distance from the waveguide but has a finite penetration depth. The light distribution in the cladding regions can be considered as a special evanescent state in a perfect photonic crystal.

For a selected guided modes (with the given frequency w and the Bloch vector k_x) due to the conservation rules the frequency of the evanescent state equals to w and the projection of the Bloch vector on the waveguide direction equals to k_x . The only free parameter is the component of the Bloch vector normal to the waveguide direction: k_y .

In general, the light in the photonic crystal regions can be represented as a sum of the Bloch modes of the infinite photonic crystal with the given frequency and the projection of the Bloch vectors on the waveguide direction. The Bloch vectors also have to have the imaginary part directed outwards the waveguide. The contribution of the states with larger $\Im(k_y)$ decays faster with increasing the distance from the waveguide than the contribution of the states with lower $\Im(k_y)$. Hence, the field penetration depth is determined mainly by the states with the lowest imaginary parts of the Bloch vectors $\Im(k_y)$.

The imaginary parts $\Im(k_y)$ of the Bloch vectors for the states with the lowest $\Im(\mathbf{k})$ are plotted in the Fig. 2.63. The imaginary part depends on the guided mode Bloch vector k_x (and also on the corresponding mode frequency) and the mode symmetry. The light can penetrate deeper into the photonic crystal regions when the modes with lower imaginary part exists.

In order to check the correlation between the guided modes penetration depth and the calculated imaginary parts of the cladding modes Bloch vectors the profiles of the guided modes have been analyzed.

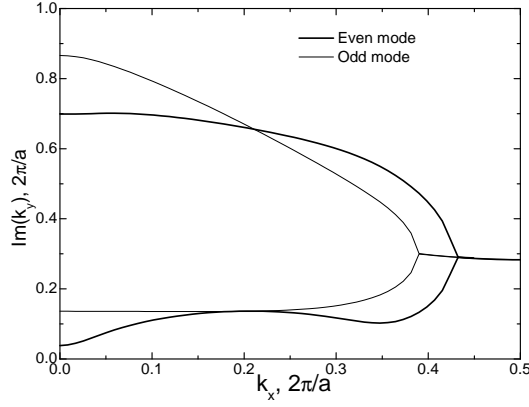


Figure 2.63: Imaginary part of the cladding modes for the W1 photonic crystal waveguide guided modes.

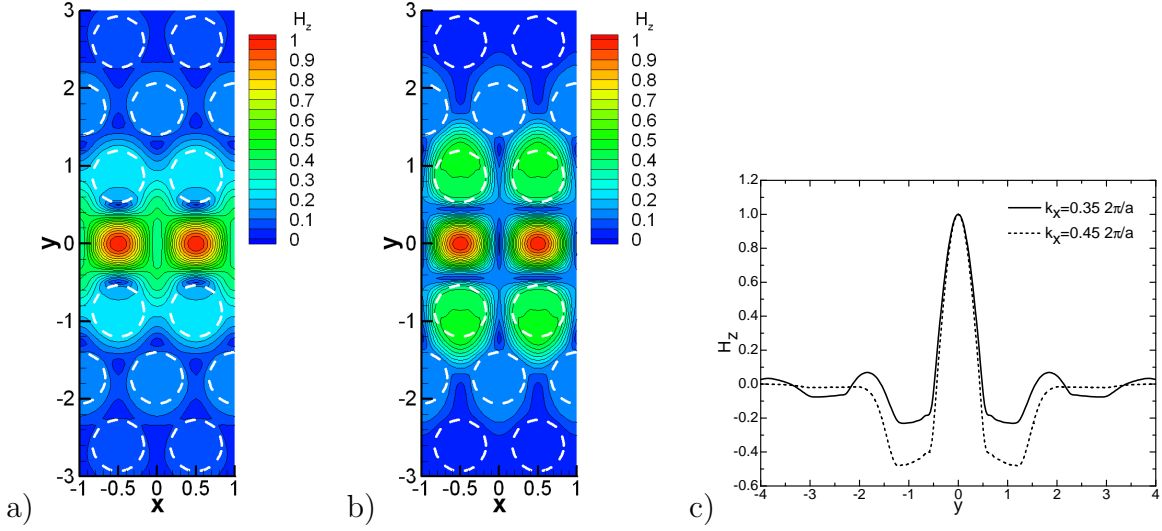


Figure 2.64: Magnetic field distribution of the periodic part of the Bloch modes. a) $|H_x|$ for $k_x = 0.35 \, 2\pi/a$. b) $|H_x|$ for $k_x = 0.45 \, 2\pi/a$. c) Cross-section of the H_z field distribution for $x = 0.5 \, a$.

The magnetic field distribution for the even guided modes are plotted in the Fig. 2.64. Two Bloch states have been chosen: with $k_x = 0.35$ (where the evanescent state with a small $\Im(k_y)$ exist) and with $k_x = 0.45$ (where all evanescent states have larger $\Im(k_y)$). The cross-sections of the field distribution are shown in the Fig. 2.64(c). It is seen that despite the field intensity in the nearest vicinity of the waveguide is larger for the state with $k_x = 0.45$ the field for the state with the $k_x = 0.35$ penetrates deeper into the photonic crystal region.

The same effect is observed for the odd guided modes for which the magnetic field distribution is plotted in the Fig. 2.65. The states with the same Bloch vectors as in the Fig. 2.64 have been selected. The cross-sections of the field distribution exhibit a similar behavior: the field penetrates deeper into the photonic crystal regions when the corresponding evanescent states with small $\Im(k_y)$ exist.

It is worth to note, that according to this analysis there is no direct dependence between the group velocity and the penetration of the field into the cladding regions, as

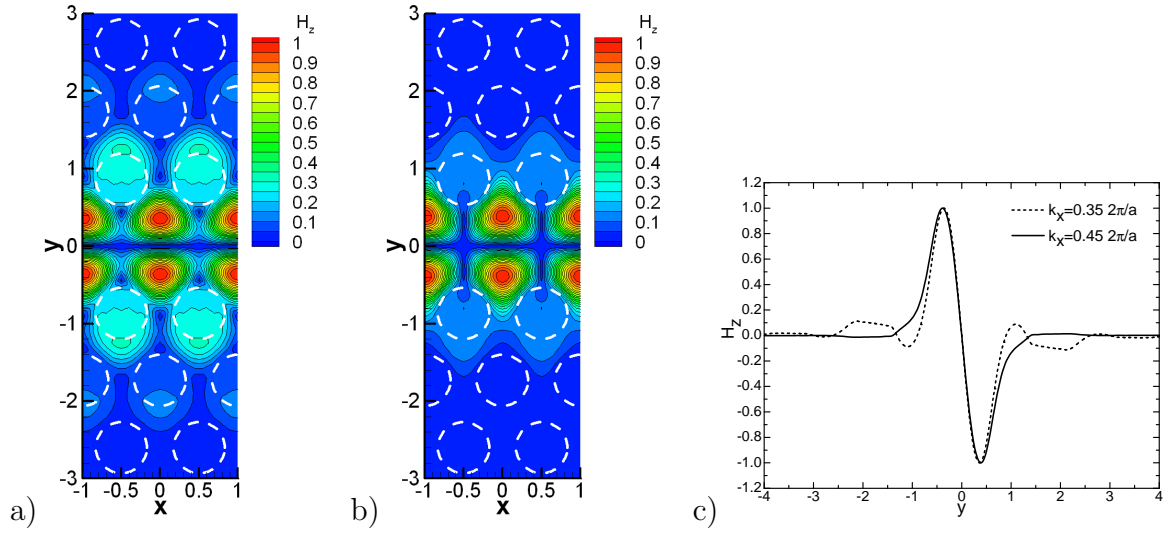


Figure 2.65: Magnetic field distribution of the periodic part of the Bloch modes.

a) $|H_x|$ for $k_x = 0.35 \cdot 2\pi/a$. b) $|H_x|$ for $k_x = 0.45 \cdot 2\pi/a$. c) Cross-section of the H_z field distribution for $x = 0$.

it has been erroneously suggested in [76], but the key parameter of the field penetration depth is the Bloch wave vector.

Chapter 3

The guided mode expansion method

3.1 Introduction

An ideal two-dimensional photonic crystal has the translation symmetry along the z axis, which leads to the existence of two independent polarizations: TE and TM. Real fabricated devices, meanwhile, have a limited thickness and use the planar waveguide in order to confine the light in the vertical direction. As it has been discussed in the section 1.4.1, the field distribution of the guided modes can be quite different from the field distribution of the 2D plane waves. Also, the dispersion properties of the guided modes are more complex than the simple linear dispersion of the plane waves. These effects should be taken into account in order to increase accuracy of calculation of the optical properties of the two-dimensional photonic crystals. A natural extension of the plane wave expansion method is the guided mode expansion method (GME), where the set of the guided modes of the planar waveguide is used instead of the set of the plane waves as the basis set for the Bloch mode decomposition [71, 77]. In these papers the GME method has been formulated for a photonic crystal slab based on a three-layer planar waveguide. In this thesis the guided mode expansion method has been derived for structures with arbitrary number of layers in the planar waveguide. The results of the GME and the PWE methods has been compared for different structures based on the thick and the thin planar waveguides.

3.2 Guided modes of the planar waveguide

Consider the planar waveguide determined by the distribution of the material permittivity $\varepsilon(z)$, where ε is a piecewise constant function. The vertical structure of the waveguide is schematically shown in the Fig. 3.1. It consists of the stack of the layers where the layer permittivity is denoted as $\varepsilon^{(j)}$ ($j = 0 \dots M$) and the layer thickness is d_j . The boundary between the j -th and the $(j+1)$ -th layer has the coordinate z_{j+1} . The bottom ($j = 0$) and the top ($j = M$) layers are the cladding layers and it is assumed that they have infinite thicknesses.

The light waves propagating in the (xy) plane along the x direction can be represented in the form of $\psi = \psi(y, z)e^{igx - iwt}$, where g is the wave vector and w is the light frequency. Because of the translation symmetry along the y direction all components of the electromagnetic field are constant along this direction and $\frac{\partial}{\partial y} = 0$. Hence,

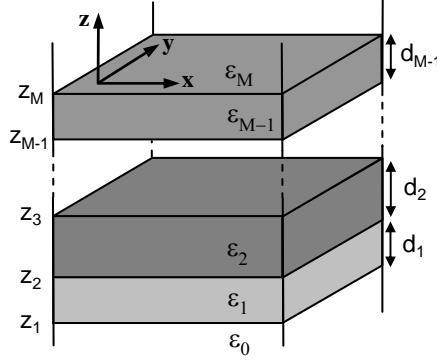


Figure 3.1: Vertical structure of the planar waveguide.

$\psi = \psi(z)e^{igx - i\omega t}$. It is assumed below that all components of the electromagnetic field satisfy this dependence.

In each layer (where the permittivity $\varepsilon^{(j)}$ is a constant) the governing equations (2.11) and (2.12) become

$$\Delta \mathbf{E}_j + \varepsilon^{(j)} \frac{w^2}{c^2} \mathbf{E}_j = 0 \quad (3.1)$$

$$\Delta \mathbf{H}_j + \varepsilon^{(j)} \frac{w^2}{c^2} \mathbf{H}_j = 0 \quad (3.2)$$

There are two general solutions with different light polarizations. For the TE-polarized light $E_x = 0$ and the main variable is H_x . The governing equation is

$$\frac{\partial^2 H_{xj}}{\partial z^2} + \chi_j^2 H_{xj} = 0, \quad \text{where} \quad \chi_j^2 = \varepsilon^{(j)} \frac{w^2}{c^2} - g^2 \quad (3.3)$$

Other components can be obtained using the equations:

$$\begin{aligned} E_{yj} &= i \frac{1}{\chi_j^2} \frac{w}{c} \frac{\partial H_{xj}}{\partial z} & H_{yj} &= i \frac{g}{\chi_j^2} \frac{\partial H_{xj}}{\partial y} = 0 \\ E_{zj} &= -i \frac{1}{\chi_j^2} \frac{w}{c} \frac{\partial H_{xj}}{\partial y} = 0 & H_{zj} &= i \frac{g}{\chi_j^2} \frac{\partial H_{xj}}{\partial z} \end{aligned} \quad (3.4)$$

For the TM-polarized light $H_x = 0$ and the main variable is E_x . The governing equation is

$$\frac{\partial^2 E_{xj}}{\partial z^2} + \chi_j^2 E_{xj} = 0, \quad \text{where} \quad \chi_j^2 = \varepsilon^{(j)} \frac{w^2}{c^2} - g^2 \quad (3.5)$$

Other components satisfy the equations:

$$\begin{aligned} H_{yj} &= -i \frac{\varepsilon^{(j)}}{\chi_j^2} \frac{w}{c} \frac{\partial E_{xj}}{\partial z} & E_{yj} &= i \frac{g}{\chi_j^2} \frac{\partial E_{xj}}{\partial y} = 0 \\ H_{zj} &= i \frac{\varepsilon^{(j)}}{\chi_j^2} \frac{w}{c} \frac{\partial E_{xj}}{\partial y} = 0 & E_{zj} &= i \frac{g}{\chi_j^2} \frac{\partial E_{xj}}{\partial z} \end{aligned} \quad (3.6)$$

The equations (3.3) and (3.5) for the main variables in each layer have the form

$$\frac{\partial^2 \varphi_j}{\partial z^2} + \chi_j^2 \varphi_j = 0, \quad (3.7)$$

where φ_j represents H_{xj} or E_{xj} . The solution of the equation (3.7) can be written for all layers (except the bottom one) as:

$$\varphi_j = A_j e^{\imath \chi_j (z - z_j)} + B_j e^{-\imath \chi_j (z - z_j)} \quad (3.8)$$

where $z_j \leq z \leq z_{j+1}$ for intermediate layers ($j = 1 \dots M - 1$) and $z_M \leq z$ for the top cladding layer ($j = M$).

For the bottom cladding layer, where $j = 0$, the solution is written as:

$$\varphi_0 = A_0 e^{\imath \chi_1 (z - z_1)} + B_1 e^{-\imath \chi_0 (z - z_0)}. \quad (3.9)$$

This exceptional dependence on the z coordinate is assumed below for all field components without special notifications.

The coefficients in the neighboring layers are connected by the layer transmission matrix \mathbb{T} and the interface matrix \mathbb{S} as

$$\begin{pmatrix} A_{j+1} \\ B_{j+1} \end{pmatrix} = \mathbb{S}_j \cdot \mathbb{T}_j \cdot \begin{pmatrix} A_j \\ B_j \end{pmatrix} \quad (3.10)$$

The transmission matrix for the layer with the thickness d_j defines the new coefficients A and B when the coordinate is changed $z_j \rightarrow z_j + d_j = z_{j+1}$. It equals to

$$\mathbb{T}_j = \begin{pmatrix} e^{\imath \chi_j d_j} & 0 \\ 0 & e^{-\imath \chi_j d_j} \end{pmatrix} \quad (3.11)$$

The interface matrix determines the change of the coefficients A and B at the different sides of the layers boundary.

The boundary conditions for the TE polarized mode are continuation of H_x and H_z at the interface. The corresponding interface matrix

$$\mathbb{S}_j = \frac{1}{2\chi_j} \begin{pmatrix} \chi_j + \chi_{j+1} & \chi_j - \chi_{j+1} \\ \chi_j - \chi_{j+1} & \chi_j + \chi_{j+1} \end{pmatrix} \quad (3.12)$$

The boundary conditions for the TM polarized mode are continuation of E_x and $D_z = \varepsilon E_z$ at the interface. The corresponding interface matrix

$$\mathbb{S}_j = \frac{1}{2\varepsilon^{(j+1)} \cdot \chi_j} \begin{pmatrix} \varepsilon^{(j+1)} \cdot \chi_j + \varepsilon^{(j)} \cdot \chi_{j+1} & \varepsilon^{(j+1)} \cdot \chi_j - \varepsilon^{(j)} \cdot \chi_{j+1} \\ \varepsilon^{(j+1)} \cdot \chi_j - \varepsilon^{(j)} \cdot \chi_{j+1} & \varepsilon^{(j+1)} \cdot \chi_j + \varepsilon^{(j)} \cdot \chi_{j+1} \end{pmatrix} \quad (3.13)$$

The coefficients of the field distribution in the first and the last layers of the waveguide are connected as

$$\begin{pmatrix} A_M \\ B_M \end{pmatrix} = \mathbb{S}_{M-1} \cdot \mathbb{T}_{M-1} \cdot \mathbb{S}_{M-2} \dots \mathbb{S}_1 \cdot \mathbb{T}_1 \cdot \mathbb{S}_0 \cdot \begin{pmatrix} A_0 \\ B_0 \end{pmatrix} = \mathbb{D} \cdot \begin{pmatrix} A_0 \\ B_0 \end{pmatrix} \quad (3.14)$$

Here the matrix \mathbb{D} is the characteristic matrix of the planar waveguide. The matrix $\mathbb{D} = \mathbb{D}(g, w)$ connects the field coefficients in the top and the bottom cladding layers.

For the guided modes the parameter χ^2 have to be negative in the top and the bottom cladding layers, so the field exponentially decays when $z \rightarrow -\infty$ and $z \rightarrow +\infty$. It leads to the conditions for the coefficients:

$$\begin{cases} A_0 = 0 \\ B_0 \neq 0 \end{cases} \quad \text{and} \quad \begin{cases} A_M \neq 0 \\ B_M = 0 \end{cases} \quad (3.15)$$

The corresponding condition for the matrix \mathbb{D} is

$$\mathbb{D}_{22} = 0. \quad (3.16)$$

The dispersion relation $w(g)$ can be found as a solution of the equation (3.16). For a given wave vector g there may be several values for the frequency w that nullify \mathbb{D}_{22} . They correspond to different guided modes which have different spatial distribution of the electromagnetic field. If the wave vector is too small there are no solutions of the equation (3.16) and, hence, the waveguide cannot support a guided mode. The values w and g allow to obtain $\chi^{(j)}$ for each layer and reconstruct the mode field distribution.

A guided mode is defined by the wave vector \mathbf{g} , the mode index l , the frequency w_l and the polarization $s = \text{TE, TM}$. The Greek letters will be used below to index the modes, which denote combinations (\mathbf{g}, s, l) . For example, the field distribution in the j -th layer will be written as:

$$\varphi_{\mu j} = A_{\mu j} e^{i\chi_{\mu j}(z-z_j)} + B_{\mu j} e^{-i\chi_{\mu j}(z-z_j)} \quad (3.17)$$

For the TE polarized mode the equations (3.4) provide the components of the electromagnetic field in the j -th layer:

$$\begin{aligned} H_{x\mu j} &= (A_{\mu j} e^{i\chi_{\mu j}(z-z_j)} + B_{\mu j} e^{-i\chi_{\mu j}(z-z_j)}) e^{ig_\mu x} \\ E_{y\mu j} &= -\frac{1}{\chi_{\mu j}} \frac{w_\mu}{c} (A_{\mu j} e^{i\chi_{\mu j}(z-z_j)} - B_{\mu j} e^{-i\chi_{\mu j}(z-z_j)}) e^{ig_\mu x} \\ H_{z\mu j} &= -\frac{g_\mu}{\chi_{\mu j}} (A_{\mu j} e^{i\chi_{\mu j}(z-z_j)} - B_{\mu j} e^{-i\chi_{\mu j}(z-z_j)}) e^{ig_\mu x} \end{aligned} \quad (3.18)$$

For the TM polarized mode the equations (3.6) give the electromagnetic field components in the j -th layer:

$$\begin{aligned} E_{x\mu j} &= (A_{\mu j} e^{i\chi_{\mu j}(z-z_j)} + B_{\mu j} e^{-i\chi_{\mu j}(z-z_j)}) e^{ig_\mu x} \\ H_{y\mu j} &= \frac{\varepsilon^{(j)}}{\chi_{\mu j}} \frac{w_\mu}{c} (A_{\mu j} e^{i\chi_{\mu j}(z-z_j)} - B_{\mu j} e^{-i\chi_{\mu j}(z-z_j)}) e^{ig_\mu x} \\ E_{z\mu j} &= -\frac{g_\mu}{\chi_{\mu j}} (A_{\mu j} e^{i\chi_{\mu j}(z-z_j)} - B_{\mu j} e^{-i\chi_{\mu j}(z-z_j)}) e^{ig_\mu x} \end{aligned} \quad (3.19)$$

For a guided mode propagating along an arbitrary direction in the (xy) plane it is convenient to use the coordinate system with the unit basis vectors \mathbf{p} , \mathbf{q} , and \mathbf{z} . The vector \mathbf{p} is chosen along the propagation direction, the vector \mathbf{z} along the z direction and the vector $\mathbf{q} = \mathbf{z} \times \mathbf{p}$ lays in the (xy) plane and is normal to the propagation direction.

The electromagnetic field of the guided TE polarized mode in each layer is:

$$\begin{aligned} \mathbf{E}_{\mu j} &= -\frac{1}{\chi_{\mu j}} \frac{w_\mu}{c} (A_{\mu j} e^{i\chi_{\mu j}(z-z_j)} - B_{\mu j} e^{-i\chi_{\mu j}(z-z_j)}) \mathbf{q}_\mu e^{ig_\mu \mathbf{r}} \\ \mathbf{H}_{\mu j} &= \left[(A_{\mu j} e^{i\chi_{\mu j}(z-z_j)} + B_{\mu j} e^{-i\chi_{\mu j}(z-z_j)}) \mathbf{p}_\mu - \right. \\ &\quad \left. \frac{g_\mu}{\chi_{\mu j}} (A_{\mu j} e^{i\chi_{\mu j}(z-z_j)} - B_{\mu j} e^{-i\chi_{\mu j}(z-z_j)}) \mathbf{z} \right] e^{ig_\mu \mathbf{r}} \end{aligned} \quad (3.20)$$

For the TM polarized light the electromagnetic field in each layer is:

$$\begin{aligned}\mathbf{E}_{\mu j} &= \left[(A_{\mu j} e^{\imath \chi_{\mu j}(z-z_j)} + B_{\mu j} e^{-\imath \chi_{\mu j}(z-z_j)}) \mathbf{p}_\mu - \right. \\ &\quad \left. \frac{g_\mu}{\chi_{\mu j}} (A_{\mu j} e^{\imath \chi_{\mu j}(z-z_j)} - B_{\mu j} e^{-\imath \chi_{\mu j}(z-z_j)}) \mathbf{z} \right] e^{\imath \mathbf{g}_\mu \mathbf{r}} \\ \mathbf{H}_{\mu j} &= \frac{\varepsilon^{(j)}}{\chi_{\mu j}} \frac{w_\mu}{c} (A_{\mu j} e^{\imath \chi_{\mu j}(z-z_j)} - B_{\mu j} e^{-\imath \chi_{\mu j}(z-z_j)}) \mathbf{q}_\mu e^{\imath \mathbf{g}_\mu \mathbf{r}}\end{aligned}\quad (3.21)$$

All guided modes can be normalized according to

$$\int \mathbf{H}_\mu^* \cdot \mathbf{H}_\nu d\mathbf{r} = \delta_{\mu\nu} = \delta(\mathbf{g}_1 - \mathbf{g}_2) \cdot \delta_{l_1, l_2} \cdot \delta_{s_1, s_2} \quad (3.22)$$

where $\mu = (\mathbf{g}_1, l_1, s_1)$ and $\nu = (\mathbf{g}_2, l_2, s_2)$.

The integration of the periodic part over the (xy) plane gives

$$\int e^{\imath(\mathbf{g}_2 - \mathbf{g}_1)\mathbf{r}} d\mathbf{r} = \frac{1}{(2\pi)^2} \delta(\mathbf{g}_1 - \mathbf{g}_2) \quad (3.23)$$

If $\mathbf{g}_1 = \mathbf{g}_2$ and $l_1 \neq l_2$ or $s_1 \neq s_2$ the integration over the z coordinate nullifies the result because the field distributions \mathbf{H}_μ and \mathbf{H}_ν are the eigenfunctions of the Maxwell's equations with different eigenvalues. Hence, only the case $\mu = \nu$ should be considered to calculate the coefficients $\{A_{\mu j}, B_{\mu j}\}$. The index μ is omitted below for the simplicity.

The required integral over the z coordinate is composed as a sum of the integrals over all layers and may be represented as:

$$\int \mathbf{H}^* \cdot \mathbf{H} dz = \left(\int_{-\infty}^{z_1} + \sum_{j=1}^{M-1} \int_{z_j}^{z_{j+1}} + \int_{z_M}^{\infty} \right) \mathbf{H}^* \cdot \mathbf{H} dz \quad (3.24)$$

It is convenient to introduce two functions which will be used for the calculation of the integrals in the equation (3.24) over the intermediate and the cladding layers of the waveguide:

$$I_j(\alpha) = \int_0^{d_j} e^{\imath \alpha_j z} dz = -\frac{\imath}{\alpha_j} (e^{\imath \alpha_j d_j} - 1) \quad \text{and} \quad J_j(\alpha) = \int_0^{\infty} e^{\imath \alpha_j z} dz = \frac{\imath}{\alpha_j} \quad (3.25)$$

The index j here corresponds to the j -th layer of the structure. It is assumed, that α_j for the $J_j(\alpha)$ has the imaginary part $\Im(\alpha_j) > 0$. The corresponding integral over the bottom cladding layer can be expressed via $J_j(\alpha)$: $\int_{-\infty}^0 e^{\imath \alpha_j z} dz = -\frac{\imath}{\alpha_j} = J_j(-\alpha)$. In this case $\Im(\alpha_j) < 0$.

Using the expressions (3.20) for the TE polarized light one can derive that in the j -th layer

$$\begin{aligned}\mathbf{H}_j^* \cdot \mathbf{H}_j &= \left(A_j^* e^{-\imath \chi_j(z-z_j)} + B_j^* e^{\imath \chi_j^*(z-z_j)} \right) \left(A_j e^{\imath \chi_j(z-z_j)} + B_j e^{-\imath \chi_j(z-z_j)} \right) + \\ &\quad \frac{g^2}{|\chi_j|^2} \left(A_j^* e^{-\imath \chi_j^*(z-z_j)} - B_j^* e^{\imath \chi_j^*(z-z_j)} \right) \left(A_j e^{\imath \chi_j(z-z_j)} - B_j e^{-\imath \chi_j(z-z_j)} \right)\end{aligned}\quad (3.26)$$

Combining this expression with the (3.24) and (3.25) one can obtain the following equation:

$$\begin{aligned} \int \mathbf{H}^* \cdot \mathbf{H} dz = & |B_0|^2 J_0(\chi - \chi^*) \left(1 + \frac{g^2}{|\chi_0|^2}\right) + |A_M|^2 J_M(\chi - \chi^*) \left(1 + \frac{g^2}{|\chi_M|^2}\right) + \\ & \sum_{j=1}^{M-1} \left\{ [|A_j|^2 I_j(\chi - \chi^*) + |B_j|^2 I_j(\chi^* - \chi)] \left(1 + \frac{g^2}{|\chi_j|^2}\right) + \right. \\ & \left. [A_j^* B_j I_j(-\chi - \chi^*) + A_j B_j^* I_j(\chi + \chi^*)] \left(1 - \frac{g^2}{|\chi_j|^2}\right) \right\} \end{aligned} \quad (3.27)$$

The expressions (3.21) provide the following relation for the TM polarized light in the j -th layer:

$$\mathbf{H}_j^* \cdot \mathbf{H}_j = \frac{(\varepsilon^{(j)})^2 w^2}{|\chi_j|^2 c^2} \left(A_j^* e^{-i\chi_j(z-z_j)} - B_j^* e^{i\chi_j^*(z-z_j)} \right) \left(A_j e^{i\chi_j(z-z_j)} - B_j e^{-i\chi_j(z-z_j)} \right) \quad (3.28)$$

Using the expressions (3.24) and (3.25) the following equation is derived:

$$\begin{aligned} \int \mathbf{H}^* \cdot \mathbf{H} dz = & \frac{(\varepsilon^{(0)})^2 w^2}{|\chi_0|^2 c^2} |B_0|^2 J_0(\chi - \chi^*) + \frac{(\varepsilon^{(M)})^2 w^2}{|\chi_M|^2 c^2} |A_M|^2 J_M(\chi - \chi^*) + \\ & \sum_{j=1}^{M-1} \frac{(\varepsilon^{(j)})^2 w^2}{|\chi_j|^2 c^2} \left\{ |A_j|^2 I_j(\chi - \chi^*) + |B_j|^2 I_j(\chi^* - \chi) - \right. \\ & \left. A_j^* B_j I_j(-\chi - \chi^*) - A_j B_j^* I_j(\chi + \chi^*) \right\} \end{aligned} \quad (3.29)$$

According to these normalization rules the orthonormal basis set $\{\mathbf{H}_\mu\}$ of the guided modes can be constructed. These modes can be used to calculate the electromagnetic field in photonic crystal slab structures.

3.3 Guided modes expansion

The Maxwell's equations lead to the following master equation for a monochromatic magnetic field:

$$\mathcal{W}\mathbf{H}(\mathbf{r}) = \nabla \times \frac{1}{\varepsilon(\mathbf{r})} \nabla \times \mathbf{H}(\mathbf{r}) = \frac{w^2}{c^2} \mathbf{H}(\mathbf{r}) \quad (3.30)$$

The magnetic field of a Bloch mode may be expanded using the orthonormal set of the basis states as

$$\mathbf{H}(\mathbf{r}) = \sum_{\nu} c_{\nu} \mathbf{H}_{\nu}(\mathbf{r}) \quad (3.31)$$

After substitution of the equation (3.31) into (3.30) and multiplying it by $\mathbf{H}_{\mu}^*(\mathbf{r})$ the following relation is obtained:

$$\sum_{\nu} c_{\nu} \mathbf{H}_{\mu}^* \nabla \times \frac{1}{\varepsilon} \nabla \times \mathbf{H}_{\nu} = \frac{w^2}{c^2} \sum_{\nu} c_{\nu} \mathbf{H}_{\mu}^* \mathbf{H}_{\nu} \quad (3.32)$$

This expression may be integrated over a volume, which leads to the eigenvalue problem:

$$\sum_{\nu} \mathbb{W}_{\mu\nu} c_{\nu} = \frac{w^2}{c^2} c_{\mu} \quad (3.33)$$

where the elements of the matrix $\mathbb{W}_{\mu\nu}$ are given by

$$\mathbb{W}_{\mu\nu} = \int \left(\mathbf{H}_{\mu}^* \nabla \times \frac{1}{\varepsilon} \nabla \times \mathbf{H}_{\nu} \right) d\mathbf{r} \quad (3.34)$$

Since

$$\mathbf{H}_{\mu}^* \nabla \times \frac{1}{\varepsilon} \nabla \times \mathbf{H}_{\nu} = \nabla \cdot \left(\mathbf{H}_{\mu}^* \times \frac{1}{\varepsilon} \nabla \times \mathbf{H}_{\nu} \right) + \frac{1}{\varepsilon} (\nabla \times \mathbf{H}_{\mu}^*) \cdot (\nabla \times \mathbf{H}_{\nu}) \quad (3.35)$$

the first term in this expression may be converted into a surface integral and vanishes. It can be explained using the fact, that if the considered modes have been emitted a finite time ago the field is localized in a finite volume and the integral over the infinitely far surface equals zero. Because the integration volume can be chosen arbitrarily big the lifetime of the modes can be infinitely long and the spectrum of the modes can be infinitely narrow. Hence, this assumption is valid for the monochromatic guided modes.

Finally,

$$\mathbb{W}_{\mu\nu} = \int \frac{1}{\varepsilon(\mathbf{r})} (\nabla \times \mathbf{H}_{\mu}^*) \cdot (\nabla \times \mathbf{H}_{\nu}) d\mathbf{r} \quad (3.36)$$

It is worth to note, that $\mathbb{W}_{\mu\nu} = \mathbb{W}_{\nu\mu}^*$ and so the matrix in the eigenvalue problem (3.33) is hermitian. This ensures positive eigenvalues and, hence, real Bloch mode frequencies.

The guided modes of the planar waveguide depend on the wave vector \mathbf{g} which can take any value in the (xy) plane. However, light modes in the photonic crystal have the form dictated by the Bloch-Floquet theorem and they depend on the Bloch vector \mathbf{k} . So, in order to preserve the periodicity of the photonic crystal lattice, only guided modes with the wave vector $\mathbf{g} = \mathbf{k} + \mathbf{G}$, where \mathbf{G} is a vector of the reciprocal lattice, may be used. Then the guided mode expansion of the magnetic field is:

$$\mathbf{H}_{\mathbf{k}} = \sum_{\mathbf{G}} \sum_l \sum_{s=\text{TE, TM}} c(\mathbf{k} + \mathbf{G}, l, s) \mathbf{H}_{\mathbf{k}+\mathbf{G}, l, s}^{\text{guided}} \quad (3.37)$$

Here l is the mode index for the given wave vector $\mathbf{k} + \mathbf{G}$ and $s = \text{TE, TM}$ represents the mode polarization. If the photonic crystal is non-symmetric relative to the mirror reflection in the (xy) plane (which may be because of the planar waveguide structure or because of the etched holes) the TE and TM polarized guided modes are coupled and the Bloch mode has a mixed TE+TM polarization. If the photonic crystal has the mirror symmetry the guided modes with the different polarizations are decoupled and Bloch modes are TE or TM polarized.

The matrix element (3.36) should be calculated for all possible combinations of the guided modes.

Inside each layer the following expressions can be derived (assuming $\mu = (\mathbf{k} + \mathbf{G}, l)$):

$$\nabla \times \mathbf{H}_{\mu j} = i \frac{\varepsilon^{(j)}}{\chi_{\mu j}} \frac{w^2}{c^2} \left(A_{\mu j} e^{i\chi_{\mu j}(z-z_j)} - B_{\mu j} e^{-i\chi_{\mu j}(z-z_j)} \right) \mathbf{q}_{\mu} e^{i\mathbf{g}_{\mu} \mathbf{r}} \quad (3.38)$$

for the TE polarized modes and

$$\begin{aligned} \nabla \times \mathbf{H}_{\mu j} = & -\imath \varepsilon^{(j)} \frac{w}{c} \left[(A_{\mu j} e^{\imath \chi_{\mu j}(z-z_j)} + B_{\mu j} e^{-\imath \chi_{\mu j}(z-z_j)}) \mathbf{p}_\mu - \right. \\ & \left. \frac{g_\mu}{\chi_{\mu j}} (A_{\mu j} e^{\imath \chi_{\mu j}(z-z_j)} - B_{\mu j} e^{-\imath \chi_{\mu j}(z-z_j)}) \mathbf{z} \right] e^{\imath \mathbf{g}_\mu \mathbf{r}} \end{aligned} \quad (3.39)$$

for the TM polarized modes.

The inverse dielectric permittivity in each layer is approximated using the plane wave decomposition of the permittivity and inversion of the permittivity matrix following the procedure described in the section 2.3. Then $\Theta_{\mu\nu}^{(j)}$ corresponds to element Θ_{mn} of the inverse matrix $\hat{\varepsilon}$ in the j -th layer, where $\mu = (\mathbf{k} + \mathbf{G}_m, l_1)$ and $\nu = (\mathbf{k} + \mathbf{G}_n, l_2)$.

Using these expressions the matrix elements for all combinations of the guided modes polarizations can be calculated using the following formulas:

TE-TE element:

$$\begin{aligned} \mathbb{W}_{\mu\nu} = & \frac{w_\mu^2 w_\nu^2}{c^4} (\mathbf{q}_\mu \cdot \mathbf{q}_\nu) \left[\frac{\Theta_{\mu\nu}^{(0)} (\varepsilon^{(0)})^2}{\chi_{\mu 0}^* \chi_{\nu 0}} B_{\mu 0}^* B_{\nu 0} J_0(\chi_\nu - \chi_\mu^*) + \right. \\ & \sum_{j=1}^{M-1} \frac{\Theta_{\mu\nu}^{(j)} (\varepsilon^{(j)})^2}{\chi_{\mu j}^* \chi_{\nu j}} \left\{ A_{\mu j}^* A_{\nu j} I_j(\chi_\nu - \chi_\mu^*) + B_{\mu j}^* B_{\nu j} I_j(\chi_\mu^* - \chi_\nu) - \right. \\ & \left. A_{\mu j}^* B_{\nu j} I_j(-\chi_\nu - \chi_\mu^*) - B_{\mu j}^* A_{\nu j} I_j(\chi_\nu + \chi_\mu^*) \right\} + \\ & \left. \frac{\Theta_{\mu\nu}^{(M)} (\varepsilon^{(M)})^2}{\chi_{\mu M}^* \chi_{\nu M}} A_{\mu M}^* A_{\nu M} J_M(\chi_\nu - \chi_\mu^*) \right] \end{aligned} \quad (3.40)$$

TM-TM element:

$$\begin{aligned} \mathbb{W}_{\mu\nu} = & \frac{w_\mu w_\nu}{c^4} \left[\Theta_{\mu\nu}^{(0)} (\varepsilon^{(0)})^2 \left((\mathbf{p}_\mu \cdot \mathbf{p}_\nu) + \frac{g_\mu g_\nu}{\chi_{\mu 0}^* \chi_{\nu 0}} \right) B_{\mu 0}^* B_{\nu 0} J_0(\chi_\nu - \chi_\mu^*) + \right. \\ & \sum_{j=1}^{M-1} \Theta_{\mu\nu}^{(j)} (\varepsilon^{(j)})^2 \left\{ \left((\mathbf{p}_\mu \cdot \mathbf{p}_\nu) + \frac{g_\mu g_\nu}{\chi_{\mu j}^* \chi_{\nu j}} \right) [A_{\mu j}^* A_{\nu j} I_j(\chi_\nu - \chi_\mu^*) + B_{\mu j}^* B_{\nu j} I_j(\chi_\mu^* - \chi_\nu)] + \right. \\ & \left. \left((\mathbf{p}_\mu \cdot \mathbf{p}_\nu) - \frac{g_\mu g_\nu}{\chi_{\mu j}^* \chi_{\nu j}} \right) [A_{\mu j}^* B_{\nu j} I_j(-\chi_\nu - \chi_\mu^*) - B_{\mu j}^* A_{\nu j} I_j(\chi_\nu + \chi_\mu^*)] \right\} + \\ & \left. \Theta_{\mu\nu}^{(M)} (\varepsilon^{(M)})^2 \left((\mathbf{p}_\mu \cdot \mathbf{p}_\nu) + \frac{g_\mu g_\nu}{\chi_{\mu M}^* \chi_{\nu M}} \right) A_{\mu M}^* A_{\nu M} J_M(\chi_\nu - \chi_\mu^*) \right] \end{aligned} \quad (3.41)$$

TE-TM element:

$$\begin{aligned} \mathbb{W}_{\mu\nu} = & -\frac{w_\mu^2 w_\nu}{c^3} (\mathbf{q}_\mu \cdot \mathbf{p}_\nu) \left[-\frac{\Theta_{\mu\nu}^{(0)} (\varepsilon^{(0)})^2}{\chi_{\mu 0}^*} B_{\mu 0}^* B_{\nu 0} J_0(\chi_\nu - \chi_\mu^*) + \right. \\ & \sum_{j=1}^{M-1} \frac{\Theta_{\mu\nu}^{(j)} (\varepsilon^{(j)})^2}{\chi_{\mu j}^*} \left\{ A_{\mu j}^* A_{\nu j} I_j(\chi_\nu - \chi_\mu^*) - B_{\mu j}^* B_{\nu j} I_j(\chi_\mu^* - \chi_\nu) + \right. \\ & A_{\mu j}^* B_{\nu j} I_j(-\chi_\nu - \chi_\mu^*) - B_{\mu j}^* A_{\nu j} I_j(\chi_\nu + \chi_\mu^*) \left. \right\} + \\ & \left. \frac{\Theta_{\mu\nu}^{(M)} (\varepsilon^{(M)})^2}{\chi_{\mu M}^*} A_{\mu M}^* A_{\nu M} J_M(\chi_\nu - \chi_\mu^*) \right] \end{aligned} \quad (3.42)$$

TM-TE element:

$$\begin{aligned} \mathbb{W}_{\mu\nu} = & -\frac{w_\mu w_\nu^2}{c^3} (\mathbf{p}_\mu \cdot \mathbf{q}_\nu) \left[-\frac{\Theta_{\mu\nu}^{(0)} (\varepsilon^{(0)})^2}{\chi_{\nu 0}} B_{\mu 0}^* B_{\nu 0} J_0(\chi_\nu - \chi_\mu^*) + \right. \\ & \sum_{j=1}^{M-1} \frac{\Theta_{\mu\nu}^{(j)} (\varepsilon^{(j)})^2}{\chi_{\nu j}} \left\{ A_{\mu j}^* A_{\nu j} I_j(\chi_\nu - \chi_\mu^*) - B_{\mu j}^* B_{\nu j} I_j(\chi_\mu^* - \chi_\nu) - \right. \\ & A_{\mu j}^* B_{\nu j} I_j(-\chi_\nu - \chi_\mu^*) + B_{\mu j}^* A_{\nu j} I_j(\chi_\nu + \chi_\mu^*) \left. \right\} + \\ & \left. \frac{\Theta_{\mu\nu}^{(M)} (\varepsilon^{(M)})^2}{\chi_{\nu M}} A_{\mu M}^* A_{\nu M} J_M(\chi_\nu - \chi_\mu^*) \right] \end{aligned} \quad (3.43)$$

3.4 Comparison of the PWE and the GME methods

The comparison of the dispersion of the Bloch modes in a photonic crystal calculated using the Plane Wave Expansion method and the Guided Mode Expansion method is presented in the Fig. 3.2. The photonic crystal consists in the circular holes etched in a thick waveguide with the weak refractive index modulation. In the selected frequency range the waveguide is monomode for both TE and TM light polarizations and the effect of the higher order modes is very small. The effective refractive indices for the PWE method have been calculated for the light wavelength in the vacuum $\lambda = 1.55 \mu\text{m}$ which corresponds for the used lattice constant of the photonic crystal $a = 0.43 \mu\text{m}$ to the reduced frequency $u = 0.2774$.

Both methods provide similar general structure of the dispersion diagrams, but there are several noticeable differences. For the first band, when the light frequency is small, the guided modes of the planar waveguide are weakly localized near the waveguide core and the effective index of such modes is small. Because for the first photonic band the light modes with the wave vectors inside the first Brillouin zone have dominant contribution into the Bloch modes the band dispersion curve is similar to the dispersion of a guided modes of the planar waveguide. This is why the dispersion curve obtained using the GME method corresponds to higher frequencies.

Another important effect is that the field distribution of guided modes have a complex vertical profile. The field intensity is maximum near the waveguide core and decays into the cladding layers. It means that the effective overlap between the field and the

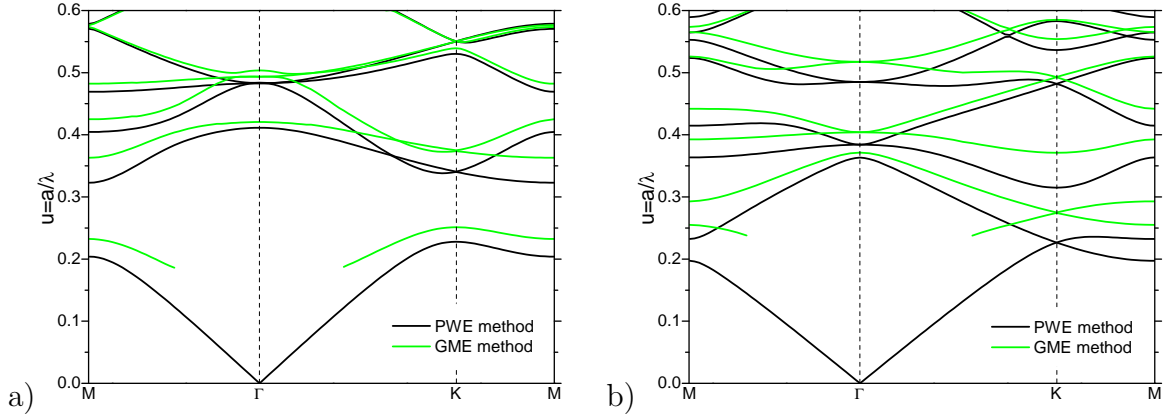


Figure 3.2: Dispersion of the Bloch modes for the triangular lattice photonic crystal consisting of the circular holes with the filling factor $f = 40\%$ etched in the thick waveguide. a) TE polarization. b) TM polarization.

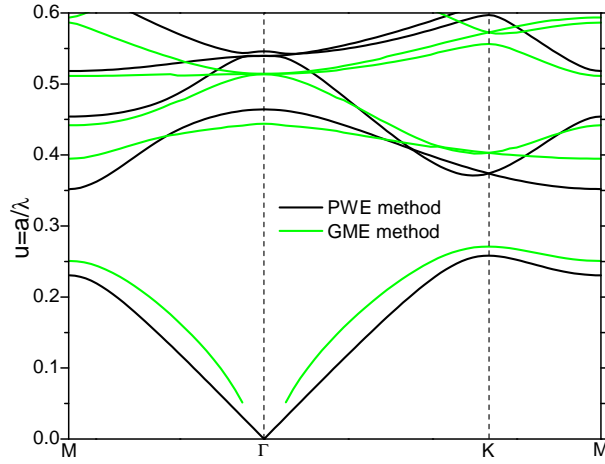


Figure 3.3: Dispersion of the TE-polarized Bloch modes for the triangular lattice photonic crystal consisting of the circular holes with the filling factor $f = 40\%$ etched in the SOI waveguide.

holes is different in the GME method and the PWE method. It can be described in terms of the effective size of the atoms, which depends on the mode frequency and the Bloch vector. This effect modifies the shape of the dispersion diagram.

Similar effects are observed for the photonic crystals based on thin waveguide with high refractive index contrast. The dispersion diagram for the triangular lattice photonic crystal based on the SOI structure with the Si layer thickness $0.23 \mu\text{m}$ is shown in the Fig. 3.3.

In this case the effective index of the waveguide grows noticeably with increasing frequency which leads to some kind of the “compression” of the dispersion diagram in comparison with the results calculated using the PWE method.

An accurate prediction of the shape of the dispersion curve is important to design the structures which can slow down the group velocity of the propagating Bloch modes. Because the group velocity equals to the gradient of the dispersion relation $w(\mathbf{k})$ it is

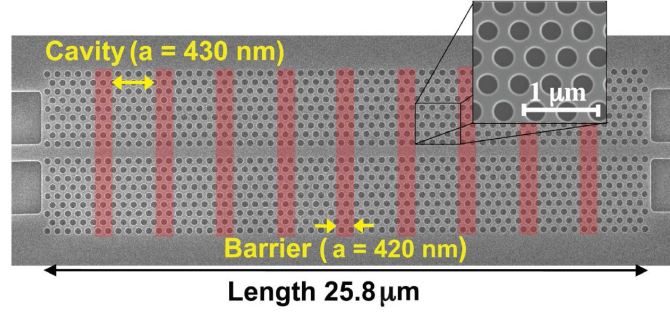


Figure 3.4: Top-view scanning electron microscope (SEM) image of the heterostructure coupled-cavity waveguide (CCW).

quite sensitive to small variations of the dispersion relation. The guided mode expansion method allows one to take into account real vertical structure of the planar waveguide and increase accuracy of the dispersion calculation, especially for the planar waveguides with strong light confinement, like SOI and semiconductor membrane in air.

One of the way to achieve the slow group velocity is to fabricate a chain of the optical cavities, where each cavity weakly coupled with the nearest neighbors. Such structure called *coupled cavity waveguide* (CCW) [78, 79]. Because the cavities are coupled there is energy transfer between them, which allows the light modes to propagate along the chain. The velocity of the light modes is determined by the coupling strength and decreasing the coupling strength the group velocity can be made very small.

An example of the coupled cavity waveguide is shown in the Fig. 3.4. It is based on a standard photonic crystal single-line-defect waveguide (W1), the lattice constant of which is periodically decreased in the propagation direction by 10 nm to create a double heterostructure [79]. The optical cavities are formed by four successive periods of lattice constant $a = 430$ nm and they are separated by potential barriers consisting of two periods of $a_b = 420$ nm (highlighted by red in Fig. 3.4). The total length of the CCW is $25.8 \mu\text{m}$ and it comprises 8 cavities, which are coupled to the access waveguides by an intermediate photonic crystal waveguide region of $a = 430$ nm. Hole diameter of $d = 286$ nm is constant in the whole photonic crystal, corresponding to the filling factor

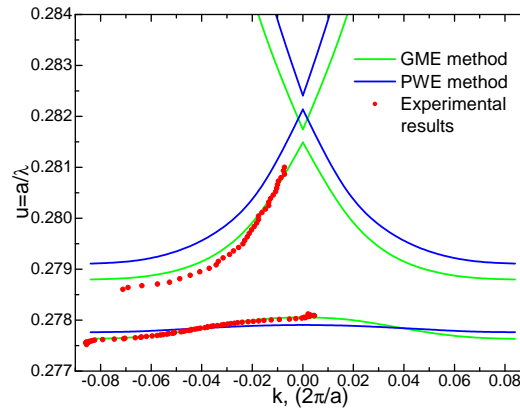


Figure 3.5: Experimental dispersion diagram of the CCW waveguide compared with the Plane Wave Expansion and the Guided Mode Expansion calculations.

of $f = 40\%$ in the cavities.

Coupled cavities create an additional band for the dispersion, which has very small bandwidth and, hence, small slopes.

The comparison of the experimental dispersion curve on the coupled-cavity waveguide and the calculations is presented in the Fig. 3.5. The experimental points have been measured using the Fourier-space imaging technique [75], which allows one to obtain directly the dispersion relation of the CCW. Theoretical dispersion relations have been calculated using the plane wave expansion and the guided mode expansion methods. 3925 guided modes (or plane waves) have been used for the theoretical calculations. The effective refractive index of the SOI waveguide $n_{eff} = 2.8278$ (for $\lambda = 1.55 \mu\text{m}$) have been used for the PWE calculation. The best fit with the experimental dispersion of the coupled-cavity band has been obtained using the filling factor $f = 39\%$ for the guided-mode expansion method and $f = 47\%$ for the plane wave expansion method.

It is clearly seen from the Fig. 3.5 that the guided mode expansion method provides much better agreement with the experiment. The GME method can provide right shape and bandwidth of the CCW band and also have a good agreement with the experimental dispersion of the waveguide mode, while the PWE method significantly underestimate the bandwidth of the CCW band and overestimate the frequency of the waveguide mode.

Chapter 4

Analysis of small variations of photonic crystal parameters

Photonic crystals (PhC) are one of the key elements of the modern integrated optics. Utilization of PhC-based structures allows to tailor light propagation properties and create such devices as waveguides [5], microcavities [4, 51] etc. The design of these devices requires an extensive numerical modelling to determine, for example, the dispersion relation for propagating modes, frequency, field distribution, and the quality factor for the localized states. The computation speed becomes one of the critical parameters, because a large series of the calculation is usually required to find an optimal design. Since the computational time and the required resources growth very fast with the increasing of the device size and/or the spatial resolution it is important to have a method which can rapidly estimate the effect of the device parameters variation on the device performance.

The formalism of the perturbation theory, widely used in quantum mechanics, is very promising for the calculation of the response of the device properties to small variation of different parameters of the PhC structure. Unfortunately, the standard perturbation theory approach is inappropriate for most of photonic crystals because of the high index contrast and the sharp boundaries between the host material and PhC atoms (holes or pillars) [80, 81]. Another important problem is how to introduce the continuous perturbation parameter, which describes the variation of the PhC structure. The methods based on the decomposition of the electromagnetic field over the basis of the orthogonal functions (the plane wave expansion method and the guided mode expansion method) has proved to be powerful and efficient tools for determining the Bloch mode properties for any periodic structure. The representation of the permittivity and the electromagnetic field distributions using the orthogonal basis allows one to introduce the continuous variation of PhC structure parameters and overcome the issue due to the permittivity discontinuity [81, 82]. The developed method calculates the change of the state frequency and the field distribution as a result of the PhC parameters perturbation.

4.1 The Bloch mode calculation and the perturbation theory

As it has been discussed in the section 2.1, the monochromatic electromagnetic field is a solution of the Maxwell's equations:

$$\begin{aligned}\frac{1}{\varepsilon(\mathbf{r})} \nabla \times \nabla \times \mathbf{E}(\mathbf{r}) &= \left(\frac{\omega}{c}\right)^2 \mathbf{E}(\mathbf{r}) \\ \nabla \times \frac{1}{\varepsilon(\mathbf{r})} \nabla \times \mathbf{H}(\mathbf{r}) &= \left(\frac{\omega}{c}\right)^2 \mathbf{H}(\mathbf{r})\end{aligned}\quad (4.1)$$

for the electric (\mathbf{E}) and the magnetic (\mathbf{H}) fields, respectively. Here and later in this chapter it is assumed that the magnetic permeability $\mu(\mathbf{r}) \equiv 1$ and that the dielectric permittivity $\varepsilon(\mathbf{r})$ is a scalar real positive function of the coordinates.

The equations (4.1) can be written in a general form of an operator eigenvalue problem

$$\mathcal{L}\psi = \lambda\psi, \quad (4.2)$$

where ψ represents either the electric field \mathbf{E} or the magnetic field \mathbf{H} and λ is the eigenvalue. The operator \mathcal{L} is determined by the distribution of the dielectric permittivity and the type of the field.

The eigenvalues of the equation (4.2) determine the mode frequencies and the eigenfunctions determine the field distribution.

Variation of the permittivity distribution leads to change of the operator \mathcal{L} and new solutions of the equation (4.2). If the variation is small the new operator may be written as

$$\mathcal{L} = \mathcal{L}^{(0)} + \alpha\mathcal{L}^{(1)} + \alpha^2\mathcal{L}^{(2)} \quad (4.3)$$

where α is a perturbation parameter. Operator $\mathcal{L}^{(0)}$ corresponds to the original unperturbed permittivity distribution and operators $\mathcal{L}^{(1)}$ and $\mathcal{L}^{(2)}$ are the perturbation operators of the first and the second accuracy orders, respectively. The way how to describe the variations of the permittivity and how to introduce the perturbation parameter will be discussed in the section (4.2).

Then the equation (4.2) is converted into

$$(\mathcal{L}^{(0)} + \alpha\mathcal{L}^{(1)} + \alpha^2\mathcal{L}^{(2)})\psi = \lambda\psi \quad (4.4)$$

Mathematical formalism for the solution of this type of equations is well developed and is widely used, for example, in quantum mechanics. The permittivity in this case can be considered as a some equivalent of a potential energy of light in the Hamilton operator and the permittivity distribution determines the energy and the field distribution of the solution of the Maxwell's equations (4.1). Following this analogy, several useful methods, initially developed for quantum mechanics, can also be applied for the solution of the problem of the light propagation.

According to the perturbation theory, a small variation of the master operator produces new eigenvalues and eigenfunctions, which can be determined using the known solutions $\lambda_n^{(0)}$ and $\psi_n^{(0)}$ for the n -th state of the initial problem (4.2). For the perturbed equation (4.4) with a small perturbation the new solution for one particular

state (indicated by the index n) can be expressed as:

$$\begin{aligned}\psi_n &= \sum_m c_m \psi_m^{(0)}, \quad c_m = c_m^{(0)} + \alpha c_m^{(1)} + \alpha^2 c_m^{(2)} + \dots \\ \lambda_n &= \lambda_n^{(0)} + \alpha \lambda_n^{(1)} + \alpha^2 \lambda_n^{(2)} + \dots\end{aligned}\quad (4.5)$$

where functions $\psi_m^{(0)}$ are normalized solutions of the unperturbed eigenvalue problem

$$\mathcal{L}^{(0)} \psi_n^{(0)} = \lambda_n^{(0)} \psi_n^{(0)} \quad (4.6)$$

The summation over the index m in the expressions (4.5) is performed over all possible solutions of the initial problem (4.6) (the discrete spectrum is assumed) and the upper index of the terms in the series corresponds to the perturbation order. The derivation of the exact formulas for the coefficients of the series (4.5) can be found in many textbooks (see, for example [83]).

For the non-degenerated eigenstates of the equation (4.6) the corrections of the first order of the accuracy are:

$$\lambda_n^{(1)} = \mathcal{L}_{nn}^{(1)} \quad (4.7)$$

$$c_m^{(1)} = \begin{cases} 0, & m = n \\ \mathcal{L}_{mn}^{(1)} / (\lambda_n^{(0)} - \lambda_m^{(0)}), & m \neq n \end{cases} \quad (4.8)$$

Here $\mathcal{L}_{mn}^{(1)}$ is the perturbation matrix element

$$\mathcal{L}_{mn}^{(1)} = \langle \psi_m^{(0)} | \mathcal{L}^{(1)} | \psi_n^{(0)} \rangle = \int \psi_m^{*(0)} \mathcal{L}^{(1)} \psi_n^{(0)} d\mathbf{r} \quad (4.9)$$

Because the perturbation operator $\mathcal{L}^{(1)}$ is hermitian the matrix element $\mathcal{L}_{mn}^{(1)} = \mathcal{L}_{nm}^{*(1)}$. The second order corrections are:

$$\lambda_n^{(2)} = \mathcal{L}_{nn}^{(2)} + \sum_{m \neq n} |\mathcal{L}_{nn}^{(1)}|^2 / (\lambda_n^{(0)} - \lambda_m^{(0)}) \quad (4.10)$$

$$c_m^{(2)} = \begin{cases} -\frac{1}{2} \sum_{l \neq n} \frac{|\mathcal{L}_{ln}^{(1)}|^2}{(\lambda_n^{(0)} - \lambda_l^{(0)})^2}, & m = n \\ \frac{1}{\lambda_n^{(0)} - \lambda_m^{(0)}} \left[\mathcal{L}_{mn}^{(2)} - \frac{\mathcal{L}_{nn}^{(1)} \cdot \mathcal{L}_{mn}^{(1)}}{\lambda_n^{(0)} - \lambda_m^{(0)}} + \sum_{l \neq n} \frac{\mathcal{L}_{ml}^{(1)} \cdot \mathcal{L}_{ln}^{(1)}}{\lambda_n^{(0)} - \lambda_l^{(0)}} \right], & m \neq n \end{cases} \quad (4.11)$$

Here the matrix element $\mathcal{L}_{mn}^{(2)} = \langle \psi_m^{(0)} | \mathcal{L}^{(2)} | \psi_n^{(0)} \rangle$.

If the states of the operator $\mathcal{L}^{(0)}$ are degenerated the standard procedure of the diagonalization should be applied for using the perturbation theory.

Using the plane wave expansion method or the guided mode expansion method the solutions of the equation (4.6) are represented as a sum of orthonormal functions which form the basis in a functional space $\{\varphi_l\}$. Then the solutions can be written as:

$$\psi_n^{(0)} = \sum_l a_l \varphi_l, \quad \psi_m^{(0)} = \sum_k b_k \varphi_k \quad (4.12)$$

Then the matrix element

$$\langle \psi_m^{(0)} | \mathcal{L} | \psi_n^{(0)} \rangle = \sum_{l,k} a_l^* b_k \langle \varphi_l | \mathcal{L} | \varphi_k \rangle = \sum_{l,k} a_l^* b_k \mathbb{L}_{lk} \quad (4.13)$$

So, the matrix elements $\mathcal{L}_{mn}^{(1)}$ and $\mathcal{L}_{mn}^{(2)}$ for two solutions of the equation (4.6) can be calculated using the matrix elements of the basis functions $\mathbb{L}_{lk}^{(1)}$ and $\mathbb{L}_{lk}^{(2)}$.

The Maxwell's equation operator \mathcal{L} is determined by the permittivity distribution, hence, the perturbation operators $\mathcal{L}^{(1)}$ and $\mathcal{L}^{(2)}$ are determined by the perturbation of the permittivity.

4.2 Variations of the permittivity distribution

As it has been discussed before in the chapters 2 and 3 the coefficients of the Fourier decomposition of the permittivity distribution are used in order to calculate the operator matrix element for the basis functions. The following idea is applicable for the plane wave expansion and the guided mode expansion methods.

Consider a photonic crystal slab where the permittivity in the j -th layer is $\varepsilon_b^{(j)}$ (and the corresponding refractive index is $n_b^{(j)}$). The coefficient of the Fourier decomposition of the permittivity distribution for the photonic crystal which consists of cylindrical atoms can be written as:

$$\varepsilon^{(j)}(\mathbf{G}_m) = \varepsilon_m^{(j)} = \sum_{l \in \text{atoms}} \left[\left(n_l^{(j)} \right)^2 - \left(n_b^{(j)} \right)^2 \right] \frac{2\pi R_l}{S_c G_m} J_1(G_m R_l) e^{-i\mathbf{G}_m \mathbf{r}_l} + \varepsilon_b^{(j)} \delta_{\mathbf{G}_m, \mathbf{0}} \quad (4.14)$$

Here \mathbf{G}_m is the wave vector of the reciprocal lattice, l is the index of the atom in the computational cell, $n_l^{(j)}$ is the atom refractive index, R_l is the atom radius, S_c is the area of the cell, and \mathbf{r}_l is the position of the atom center. J_1 is the Bessel function of the first kind.

Later in this section it is assumed that all calculations required for the approximation of the permittivity matrix are performed for each layer in the case of using GME method and the index j of the layer is omitted for simplicity.

Using the plane wave expansion method there is only one effective layer and $n_b^{(j)}$ is the effective refractive index of the planar waveguide. The index j is not required in this case.

In general, the coefficients of the decomposition of the permittivity are functions of a set of parameters, which describe the positions and properties of all atoms in the cell. They can be defined as functions of variables in the multidimensional parametric space $\varepsilon(\mathbf{k}) = \varepsilon(\mathbf{k}, \mathbf{x})$, where the vector \mathbf{x} contains all coefficients which describe the photonic crystal structure (atom's radii, atoms's positions, etc.).

Because these functions are smooth enough we can write the change of the coefficients due to the variation of the parameters (up to the second order of accuracy) as:

$$\begin{aligned} \varepsilon(\mathbf{k}, \mathbf{x} + \Delta \mathbf{x}) &= \varepsilon(\mathbf{k}, \mathbf{x}) + (\Delta \mathbf{x} \cdot \nabla_{\mathbf{x}}) \varepsilon(\mathbf{k}, \mathbf{x}) + \frac{1}{2} (\Delta \mathbf{x} \cdot \nabla_{\mathbf{x}})^2 \varepsilon(\mathbf{k}, \mathbf{x}) \\ &= \varepsilon(\mathbf{k}, \mathbf{x}) + \Delta x_i \frac{\partial \varepsilon(\mathbf{k}, \mathbf{x})}{\partial x_i} + \frac{1}{2} \Delta x_i \Delta x_j \frac{\partial^2 \varepsilon(\mathbf{k}, \mathbf{x})}{\partial x_i \partial x_j} \end{aligned} \quad (4.15)$$

Here the summation over all components in the parametric space is assumed.

In order to facilitate calculation of the derivatives in the expression (4.15) we can note, that the expression (4.14) has the form

$$\varepsilon(\mathbf{k}) = \sum_{l \in \text{atoms}} g_1(n_l) g_2(R_l) g_3(\mathbf{r}_l) + \varepsilon_b \delta_{\mathbf{k},0} \quad (4.16)$$

where

$$g_1(n) = n^2 - n_b^2 \quad (4.17)$$

$$g_2(R) = \frac{2\pi R}{S_c k} J_1(kR) \quad (4.18)$$

$$g_3(\mathbf{r}) = e^{-i\mathbf{k}\mathbf{r}} \quad (4.19)$$

The constant term for the zero wave vector doesn't affect the derivatives.

So, the variations of the atoms refractive indices, atoms sizes, and atoms positions can be separated. It allows to calculate all partial derivatives in (4.15) using the expressions:

$$\frac{\partial g_1}{\partial n} = 2n \quad \frac{\partial^2 g_1}{\partial^2 n} = 2 \quad (4.20)$$

$$\frac{\partial g_2}{\partial R} = \frac{2\pi}{S_c} R J_0(kR) \quad \frac{\partial^2 g_2}{\partial^2 R} = \frac{2\pi}{S_c} [J_0(kR) - kR J_1(kR)] \quad (4.21)$$

$$\frac{\partial g_3}{\partial r_m} = -ik_m e^{-i\mathbf{k}\mathbf{r}} \quad \frac{\partial^2 g_3}{\partial r_m \partial r_n} = -k_m k_n e^{-i\mathbf{k}\mathbf{r}} \quad (4.22)$$

One particular case of the variation of the parameters of the photonic crystal will be considered here. In this case different components of the variation vector $\Delta \mathbf{x}$ are connected as

$$\Delta x_i = \alpha \Delta \tilde{x}_i, \quad (4.23)$$

where $\Delta \tilde{x}_i$ are arbitrary constants and α is a free variable. It corresponds to the variation of the parameter vector \mathbf{x} along a line in the parametric space. Hence, the variation can be described (with a given set of constants $\Delta \tilde{x}_i$) by only one perturbation parameter: α .

The coefficients of the decomposition of the permittivity and the corresponding permittivity matrix can be written as:

$$\varepsilon(\mathbf{G}_m) = \varepsilon(\mathbf{G}_m, \alpha) = \varepsilon_{0,m} + \alpha \varepsilon_{1,m} + \alpha^2 \varepsilon_{2,m} \quad (4.24)$$

$$\hat{\varepsilon}_{mn} = \hat{\varepsilon}_{mn}(\alpha) = \hat{\varepsilon}_{0,mn} + \alpha \hat{\varepsilon}_{1,mn} + \alpha^2 \hat{\varepsilon}_{2,mn} \quad (4.25)$$

Since the matrix elements of the operator \mathcal{W} depend on the inverse permittivity matrix $\Theta = \hat{\varepsilon}^{-1}$ the goal is to obtain the perturbation of the inverse permittivity matrix in the form:

$$\Theta = \Theta_0 + \alpha \Theta_1 + \alpha^2 \Theta_2 \quad (4.26)$$

where $\Theta_0 = (\hat{\varepsilon}_0)^{-1}$ and Θ_1, Θ_2 are correction matrices.

Assuming a small variation of the matrix $\hat{\varepsilon}$ ($\alpha \ll 1$) it can be approximated (up to the second order of accuracy) using the matrix Taylor series expansion:

$$\Theta = \Theta_0 - \alpha \Theta_0 \cdot \hat{\varepsilon}_1 \cdot \Theta_0 + \alpha^2 (\Theta_0 \cdot \hat{\varepsilon}_1 \cdot \Theta_0 \cdot \hat{\varepsilon}_1 \cdot \Theta_0 - \Theta_0 \cdot \hat{\varepsilon}_2 \cdot \Theta_0) \quad (4.27)$$

And hence

$$\Theta_1 = -\Theta_0 \cdot \hat{\varepsilon}_1 \cdot \Theta_0 \quad (4.28)$$

$$\Theta_2 = \Theta_0 \cdot \hat{\varepsilon}_1 \cdot \Theta_0 \cdot \hat{\varepsilon}_1 \cdot \Theta_0 - \Theta_0 \cdot \hat{\varepsilon}_2 \cdot \Theta_0 \quad (4.29)$$

The matrix elements $\mathbb{L}_{mn}^{(1)}$ and $\mathbb{L}_{mn}^{(2)}$ can be calculated using the formulas for the original operator \mathcal{L}_0 by substitution of the coefficients $\Theta_{1,mn}$ and $\Theta_{2,mn}$ instead of Θ_{mn} .

4.3 Application of the perturbation method

The perturbation method described above can be used to analyze the response of the optical properties of the photonic crystals on small variations of the photonic crystal parameters. Consider a triangular lattice photonic crystal consisting of circular holes etched in the thick waveguide with the effective refractive index $n_{eff} = 3.24$. The radius of the holes $R = 0.33a$, where a is the lattice constant. The dispersion relation of the TE polarized Bloch modes calculated using the PWE method is shown in the Fig. 4.1.

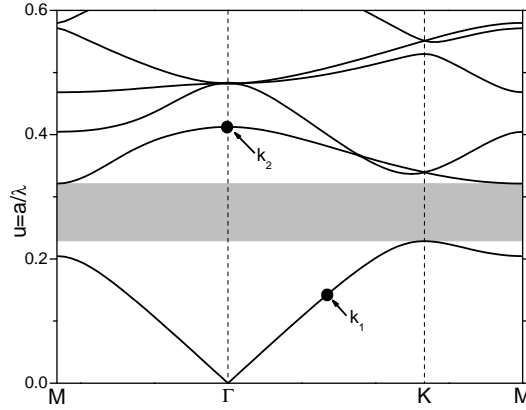


Figure 4.1: Dispersion of the TE polarized Bloch modes for the triangular lattice photonic crystal consisting of the circular air holes (the filling factor $f = 0.4$) in the dielectric slab with the effective refractive index $n_{eff} = 3.24$.

Two states are selected for the further analysis: the state of the first band with the Bloch vector \mathbf{k}_1 in the middle between the Γ and the K points and the state of the second band with the Bloch vector \mathbf{k}_2 at the Γ point.

The comparison of the results obtained by the standard PWE method and the perturbation method is discussed below. The maximum length of the reciprocal lattice vector $G_{max} = 7 \frac{2}{\sqrt{3}} \frac{2\pi}{a}$ and the number of used plane waves $N = 187$, which ensures a good accuracy of calculated Bloch modes frequencies.

Infiltration of the holes by a material changes the dispersion of the Bloch modes, because the photonic crystal “atoms” have new refractive index. Hence, the photonic crystals can be used as sensor to the refractive index of the environment. In order to design the photonic crystal structure with desired sensitivity and calibrate it a precise knowledge of the response of the dispersion on the variations of the atom refractive index is required. The perturbation method can analyze such variations with a high accuracy.

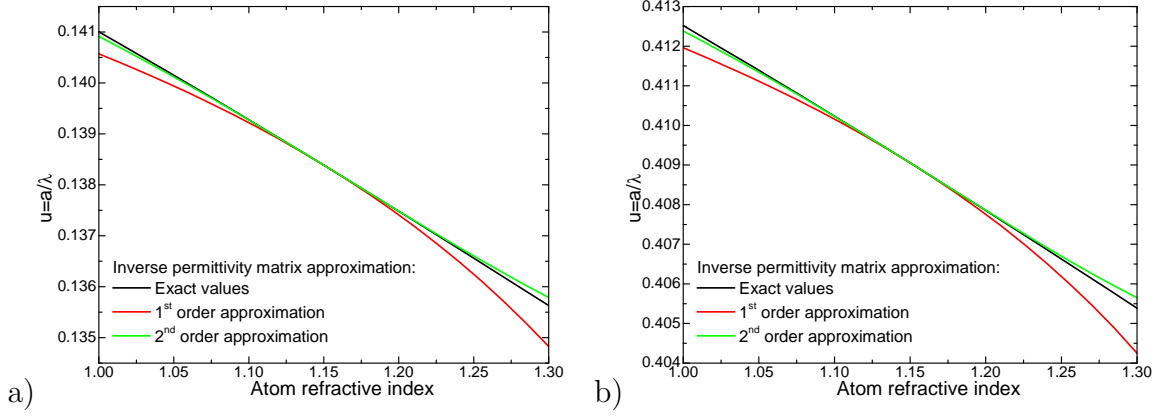


Figure 4.2: Dependence of the Bloch mode frequency on the variation of the hole refractive index for different accuracy of the inverse permittivity matrix approximation. a) The first state. b) The second state.

The dependence of the Bloch mode frequency on the variation of the hole refractive index is shown in the Fig. 4.2. Several different ways have been used to calculate the mode frequencies. The first uses exact inverse permittivity matrix for each values of the hole refractive index. The results obtained by this approach are plotted by black lines. The second way is to approximate variation of the inverse permittivity matrix with the first order of accuracy and then use the approximated matrices to construct the eigenvalue problem (red lines). The reference point for the hole refractive index have been taken in the middle of the variation range. The last way is to use the second order approximation for the inverse permittivity matrix (green lines). In all these cases the final mode frequencies have been obtained by exact solutions of the corresponding eigenvalue problems. Hence, the accuracy of the approximation of the inverse permittivity matrix variations are examined in this example.

The frequencies obtained using different approaches are quite close which proves the quality of the approximation of the inverse permittivity matrix using the Taylor series.

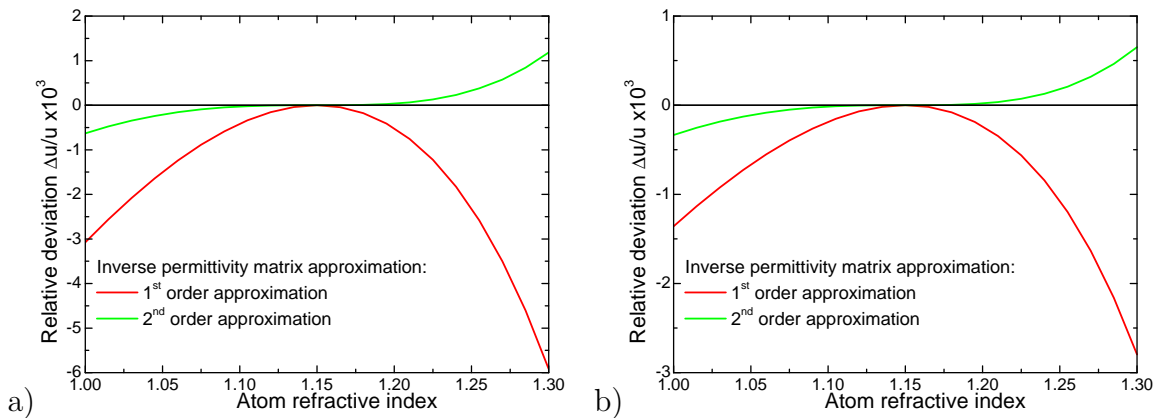


Figure 4.3: Relative error of the mode frequencies calculated with different accuracy of the inverse permittivity matrix approximation. a) The first state. b) The second state.

The frequencies calculated using the exact inverse permittivity matrix with conse-

quent solution of the corresponding eigenvalue problems are chosen as the reference frequencies u_{ref} and the relative frequency difference $(u - u_{ref})/u_{ref}$ is used to analyze the accuracy of the method.

The relative frequency difference as a function of the hole refractive index is plotted in the Fig. 4.3. The typical scale of the relative frequency difference is of the order of 10^{-3} , which prove high accuracy of the proposed approximation scheme. The results are similar for both states, which allows to expect similar approximation errors for all states with arbitrary Bloch vector within several first photonic bands.

It is clearly seen that utilization of the first approximation order leads to a systematic error roughly proportional to the square of the deviation of the hole refractive index from the reference value. Utilization of the second approximation order eliminate this error and greatly improves the accuracy.

The next step in the proposed perturbation method is to replace the solution of the eigenvalue problem for each value of the varied photonic crystal parameter by calculation of the corrections to the eigenvalues.

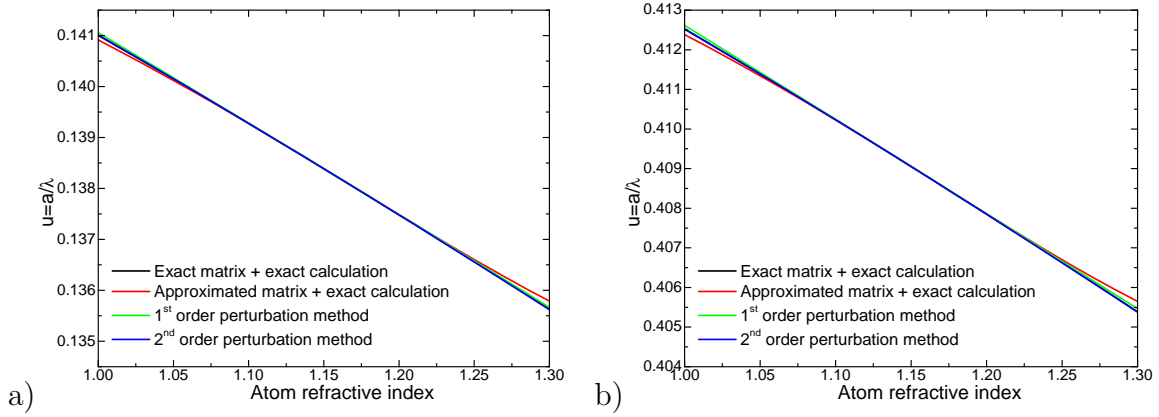


Figure 4.4: Dependence of the Bloch mode frequency on the variation of the hole refractive index for different orders of the perturbation method. a) The first state. b) The second state.

The comparison of the results obtained by utilization of the perturbation method and exact solution of the eigenvalue problem is presented in the Fig. 4.4. The results provided by the exact solutions of the exact eigenvalue problem for each values of the atom refractive index are shown as black lines. The results obtained as the exact solutions of the eigenvalue problems with the approximated inverse permittivity matrix (the second order approximation has been used) are plotted as red lines. Green and blue lines correspond to the results calculated using the perturbation method of the first and the second accuracy orders, respectively. All methods give very close results and detailed analysis of the relative frequency difference is required.

The relative frequency difference for different calculation methods is plotted in the Fig. 4.5. All methods exhibit very good accuracy with the typical relative error less than 10^{-3} . The first order approximation method also exhibit the systematic parabolic error which can be removed by using the second order perturbation method. The relative error in this case can be improved for up to 10^{-4} .

Another important example of variation of the parameters of the photonic crystal is change of the “atom” sizes. Because fabrication of the real-life samples always in-

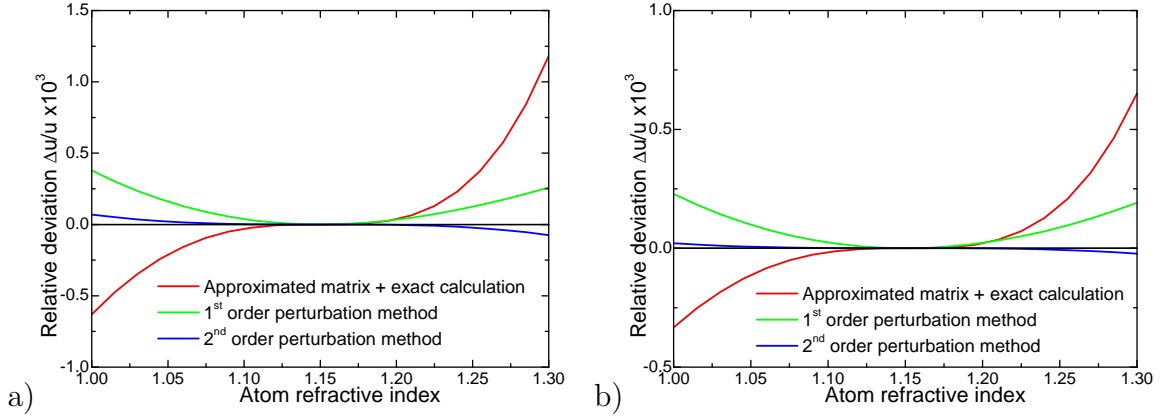


Figure 4.5: Relative error of the mode frequencies calculated with the perturbation method. a) The first state. b) The second state.

introduced some fabrication error and there is always some uncertainty in the sizes of the etched holes or pillars. The perturbation method can serve as an efficient tool to examine the tolerance of the photonic crystal structures to the fabrication errors.

Here the variation of the frequency of the same Bloch modes as have been used above is examined for the hole radius R changing from $0.31a$ until $0.35a$.

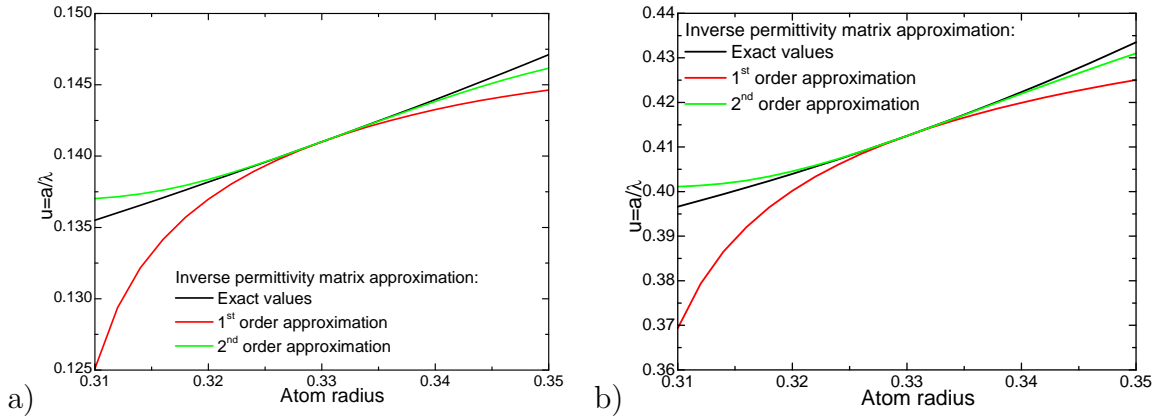


Figure 4.6: Dependence of the Bloch mode frequency on the variation of the hole size for different accuracy of the inverse permittivity matrix approximation. a) The first state. b) The second state.

The dependence of the Bloch mode frequency on the variation of the hole refractive index is shown in the Fig. 4.6. The notation of the results is the same as used in the Fig. 4.2. Approximation of the inverse permittivity matrix using the Taylor series in this case leads to larger errors in the mode frequencies, especially for the first order approximation.

The relative error of the calculated frequency is plotted in the Fig. 4.7. Typical relative error is the order 10^{-2} for both states. The first order approximation exhibits the systematic parabolic-like error which can be suppressed using the second order approximation of the inverse permittivity matrix.

Utilization of the perturbation method for calculation of the corrections to the eigenvalues allows to obtain the results quite close to the exact calculation, which is clearly

seen in the Fig. 4.8. The notation of the results is the same as in the Fig. 4.4.

The relative error in the mode frequency is shown in the Fig. 4.9. The typical error is of the order 10^{-3} for the first order perturbation method and is improved up to 10^{-4} for the second order. Surprisingly, the full perturbation method (approximation of the inverse permittivity matrix + approximation of the eigenvalue corrections) works better than partial perturbation method (approximation of the inverse permittivity matrix + exact solution of the corresponding eigenvalue problem). It seems that there is some intrinsic stability of the perturbation method which improves accuracy of the eigenvalue corrections approximation.

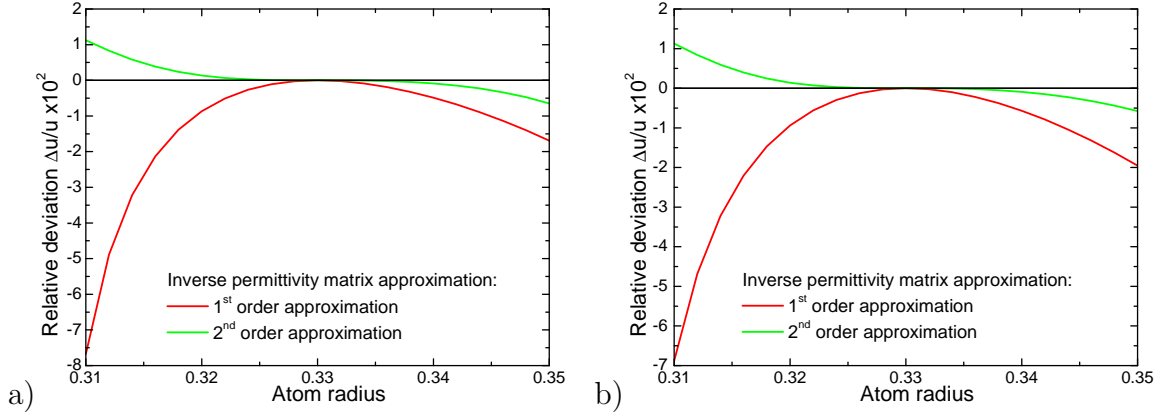


Figure 4.7: Relative error of the mode frequencies calculated with different accuracy of the inverse permittivity matrix approximation. a) The first state. b) The second state.

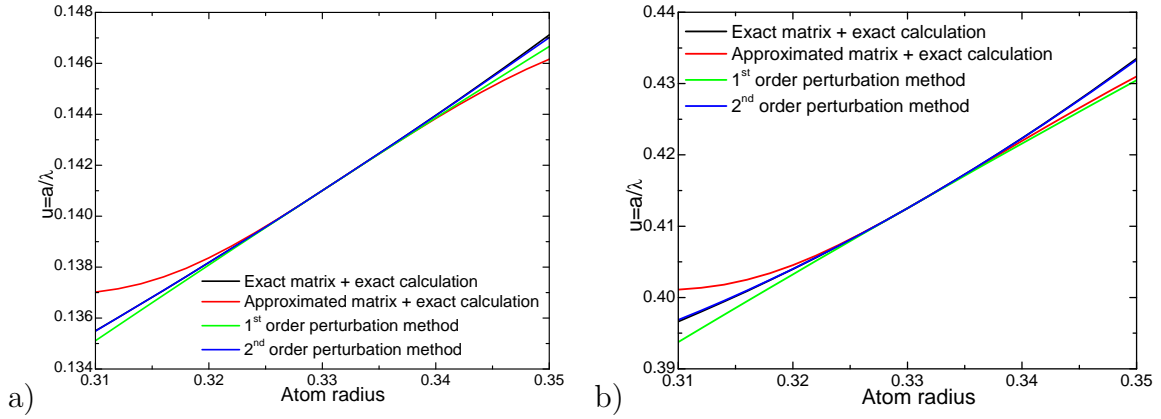


Figure 4.8: Dependence of the Bloch mode frequency on the variation of the hole size for different orders of the perturbation method. a) The first state. b) The second state.

Another example of the photonic crystal parameter variation is shifting positions of the “atoms”. Such disturbance of the photonic crystal lattice change dispersion of the structure and can be used to tune the photonic crystal optical properties for some specific applications.

Consider the L2 cavity in the triangular lattice photonic crystal consisting of the circular air holes etched in the thick planar waveguide with the effective refractive

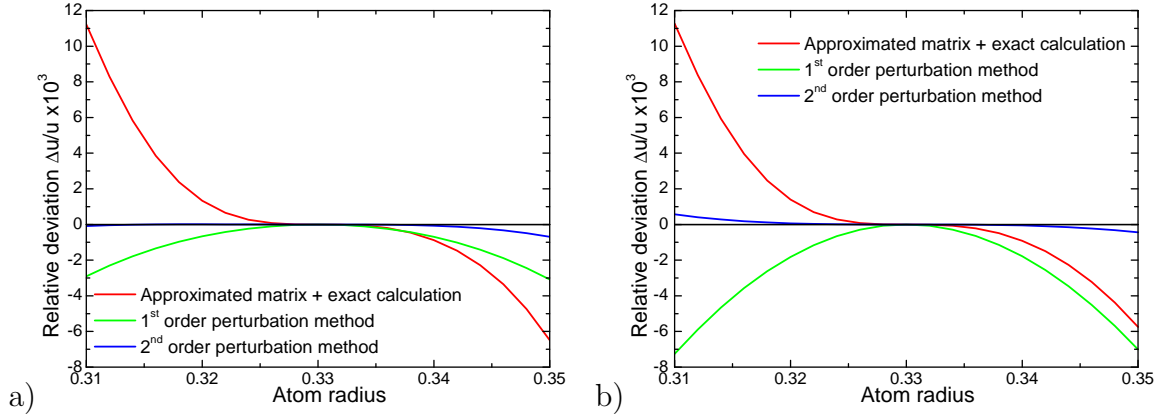


Figure 4.9: Relative error of the mode frequencies calculated with the perturbation method. a) The first state. b) The second state.

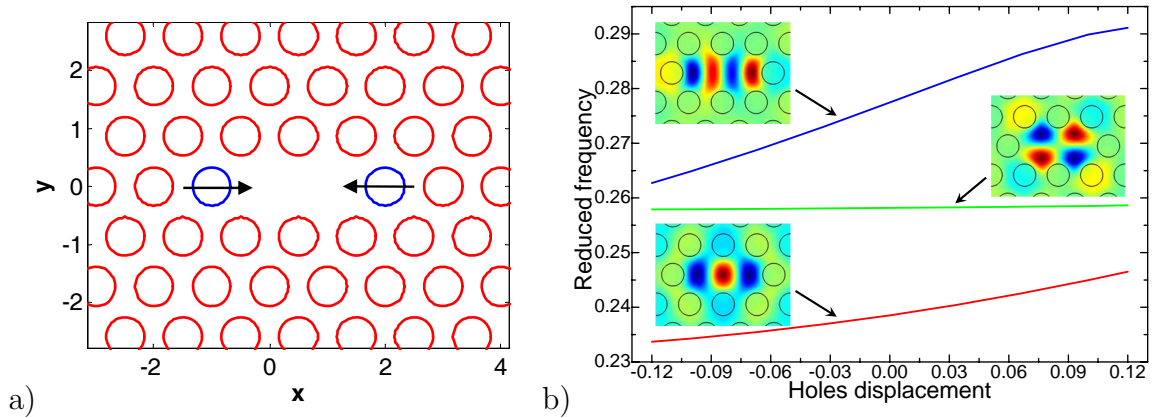


Figure 4.10: a) L3 cavity in the triangular lattice photonic crystal. b) Dependence of the cavity localized modes frequencies on the displacement of the side holes.

$n_{eff} = 3.36$. This cavity is schematically shown in the Fig. 4.10(a). Shifting the position of the side holes (indicated by blue color) along the x axis in the directions indicated by the black arrows modifies the cavity geometry and frequencies of the cavity localized states. Variation of the position of these holes (as well as variation of the hole size) also affect the quality factor of the localized states.

The dependence of the cavity localized modes frequencies on the displacement of the side holes is plotted in the Fig. 4.10(b). The magnetic field H_z profiles of the selected localized states (all are TE polarized) are shown in the insets.

Calculation of such dependencies is a challenging task for the plane wave expansion or the guided mode expansion methods. A large super-cell is required to represent the cavity surrounded by the photonic crystal area. Increasing the size of the super-cell leads to fast increasing of the number of used plane waves (or guided modes) and greatly increase the computer resources required to find the mode frequencies.

The perturbation method solve the matrix eigenvalue problem only once, which drastically reduces the time of the calculation.

Comparison of the selected localized mode frequencies obtained by the exact calcu-

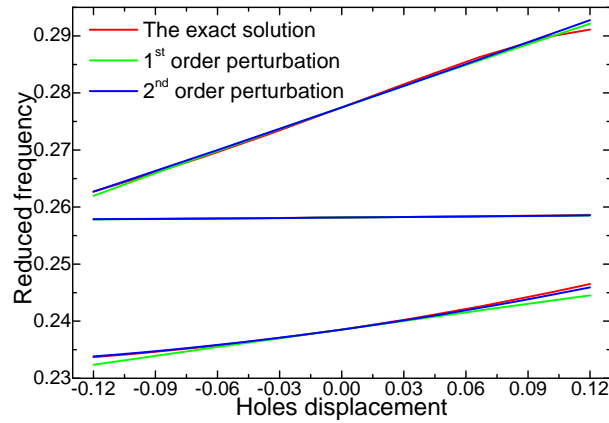


Figure 4.11: Comparison of the results obtained by the exact solution and using the perturbation method.

lation and using the perturbation method is presented in the Fig. 4.11.

The second order perturbation method exhibit a small relative error of the order 10^{-3} and can properly reproduce non-linear dependence of the mode frequency on the holes displacement (which is evident for the mode with the lowest frequency).

Chapter 5

Polarization Beam Splitter design

Photonic crystals are in the focus of extensive research for integrated optics applications. Through skilful engineering, PhC heterostructures offer a variety of appealing optical functionalities, that may be integrated in advanced photonic circuit chip as building block with a very small footprint. However, PhC structures are highly sensitive to the polarization of the light and there is a fundamental need for devices enabling polarization control. Polarization splitters belong to such class of devices, which can be of interest in a polarization diversity scheme where both orthogonal polarization states of the signal are treated independently.

Polarization beam splitter (PBS), that can split light into two orthogonal polarization states, is one of the important components in integrated photonics. A polarization splitter is a more demanding device compared to a polarizer, as it should perform equally well for both polarization. The key parameters to assess the quality of a polarization splitter device are transmission coefficients for both polarization outputs which should be as close to unity as possible and cross talk and back reflection which should be as low as possible.

Several types of PBSs have been reported based on ridge waveguides. However, the typically required guiding length is of the order of millimeters, making them less attractive for integration. Recently, a new type of PBSs, based on two-dimensional photonic crystals, has been proposed [84–93].

There are two major requirements to realize a compact high-efficiency PBS. First, both the TM and the TE polarized light must propagate with low loss in the device. Second, the difference between the propagating properties of the TM and the TE light must be large enough to ensure that the two polarizations can be separated after a short propagation distance. The first requirement might be satisfied by creating the device in a PC with a complete photonic band gap (PBG) for both polarizations, e.g., a triangular or square lattice of air holes in a high-index medium with a sufficiently large air-filling factor. Utilization of two parallel waveguides with low losses and different coupling efficiency for the TE and the TM polarized light and, consequently different coupling length, allows to transfer light with only desired polarization from one waveguide to another [84, 85]. Another approach is based on polarization-dependent dispersion properties of PhC, which may lead to different propagation direction for the TE and the TM polarized light. Utilization of positive refraction for one polarization and negative refraction effect for another allows one to separate light beams [86–89].

Two main types of 2D photonic crystals have been proposed for this type of the PBS: high permittivity pillars in air [86, 87] and air holes in a dielectric media [88, 89]. Weak vertical light localization in the case of the pillar-type photonic crystals leads to very high losses, unacceptable for any practical devices [87]. Long light path inside hole-type PhC and large air holes are detrimental to light guiding and lead to out-of-plane losses [24, 25]. Furthermore, the difference between the TM light and the TE light propagation properties will not be substantial if both polarization states are guided through a similar effect, which would violate the second requirement for a compact PBS.

The way to create a large difference of the propagation properties of two different polarization is working in the frequency range where there is the band gap only for one polarization. In this case the main idea of the PBS design is utilization of a PhC slab which can transmit light with one polarization and reflect light with another due to the band gap effect [90–93].

5.1 Simple design

The simple design of the polarization beam splitter contains PhC slab, operating as the splitter, input waveguide and output waveguides for transmitted and reflected light. It is presented in the Fig. 5.1.

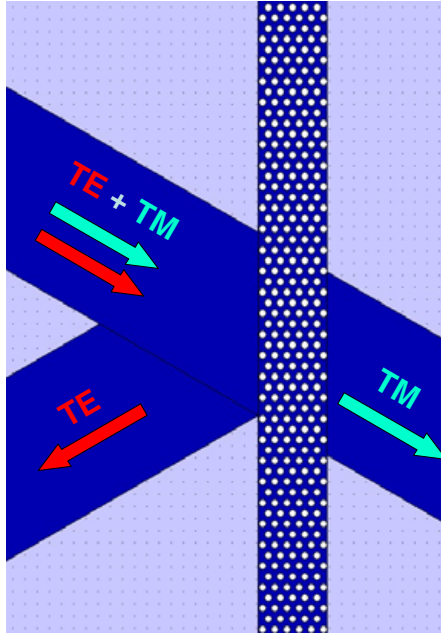


Figure 5.1: Schematic principal design of the polarization beam splitter.

The light beam comes from the input waveguide and TE polarized light is reflected into one output waveguide while TM polarized light is transmitted into the second output waveguide.

Straightforward implementation of such concept, where a PhC slab, exhibiting a band gap for only one polarization, is inserted into a regular or a PhC waveguide, proved to be inefficient. This is mainly due to the occurrence of strong in-plane light diffraction because the PhC slab interface acts as a grating as it is located at a PhC/non

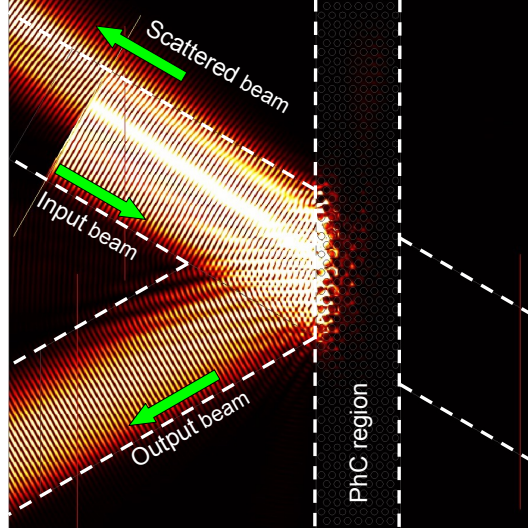


Figure 5.2: 2D FDTD simulation of the TE polarized field pattern for the simple design polarization beam splitter.

PhC crystal boundary. An example of the field distribution of the TE polarized light is shown in the Fig. 5.2. Strong backward scattering is observed which decreases the device performance. Because the direction of the scattered light depends on the light reduced frequency ($u = 0.3$ ($2\pi c/a$) in this example) usually there is small deviation between the direction of the backward scattered light and the direction of the input waveguide. In this example shallow etched waveguide with small refractive index contrast are used and the light localization is weak, so the light can propagate even outside of the input waveguide. Utilization of the waveguide with large index contrast also exhibit strong backward scattering but in this case the field pattern is more complex because of the interference with the input beam. So, only the case of the shallow etched waveguide is presented here for the sake of simplicity.

Strong scattering of the TE polarized light drastically decreases intensity of the light in the TE-output waveguide. This makes such a device an acceptable polarizer but not a good polarization beam splitter.

5.2 Self-collimation based design

It is therefore important to decrease the losses which arise due to the mismatch of the light modes inside the polarizer and the outer regions. It can be done by control of the possible mode propagation directions. As it has been discussed in the section 2.5.3, for specific frequencies and PhC lattice structure, light can propagate without diffraction. This effect, commonly referred to as self-collimation, relies on the special dispersion properties of Bloch waves in PhCs where the curvature of the equifrequency surface (EFS) moves away from the normally circular curvature in free space. As the direction of a propagating Bloch mode is always normal to the EFS, self-collimation is achieved when the EFSs are as flat as possible.

The self-collimation effect has been proposed to control the beam propagation in square lattice photonic crystal [32, 91] and suppress the light scattering at the heteroin-

interfaces. This effect is also used in several proposed designs of the PBS to decrease the in-plane losses for the propagating beams [92, 93].

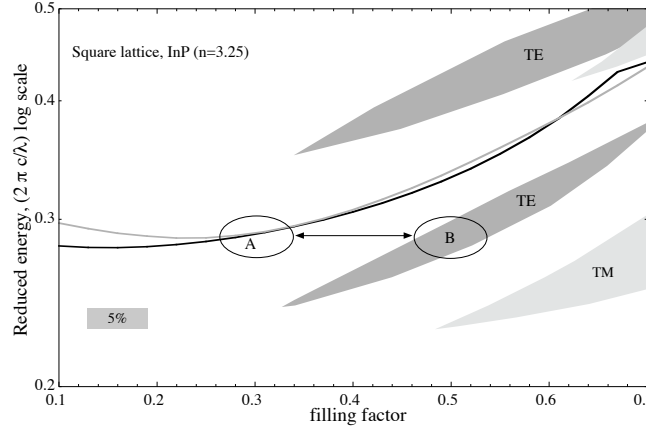


Figure 5.3: Gap map of a square lattice photonic crystal consisting of air holes in a dielectric with the effective index $n_{eff} = 3.25$. The shaded areas indicate the band gap energies. The black (grey) curve shows the self-collimating frequency for TM (TE) polarization. A pair of operating points are indicated (A and B). The shaded segment indicates a 5% operating range, corresponding to coarse CWDM operation.

Fig. 5.3 shows the gap map of a square lattice photonic crystal consisting of air holes in a dielectric with the effective index $n_{eff} = 3.25$. The shaded areas indicate the band gap energies as a function of the filling factor f . The grey (black) curve shows the self-collimating frequency for TE (TM) polarization as a function of f . The operating points should be chosen such that for a given frequency the first lattice has a band gap for one polarization but not for the other, whereas the second lattice exhibits self-collimation for both polarizations. Such a pair of operating points is indicated in the Fig. 5.3 (points A and B). The frequency range of operation depends on the frequency width of the band gap and is also related to the slope of the self-collimating curves; a steeper curve favours a wider operating range. A 5% frequency range, for coarse CWDM operation is indicated in Fig. 5.3 (shaded segment, note that the frequency axis is on a log-scale).

For low index contrast planar waveguide structure self-collimation has the desirable property that it occurs at nearly identical frequencies for both TE and TM polarizations and over a wide frequency range (several percents).

The proposed polarization splitter structure [94] is shown in the Fig. 5.4. It consists of a tile polarization splitter, comprised of a PhC working in the self-collimation mode (a square lattice working in the second band). Embedded in this is an intermediate PhC slab with identical lattice symmetry but different filling factor which exhibits a large reflection coefficient for TE and a high transmission coefficient for TM polarization. Note that the short path length of the TM light through the slab means that maintaining self-collimation in this region is not essential. Embedding the polarizing slab within a PhC structure of the same crystal lattice (only the filling factor changes) suppresses the in-plane diffraction losses at the PhC/non-PhC interface.

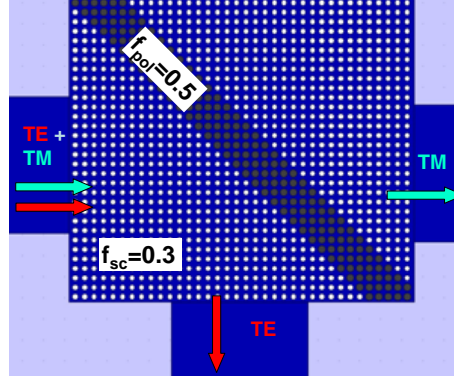


Figure 5.4: Schematic design of the polarization beam splitter based on the self-collimation effect.

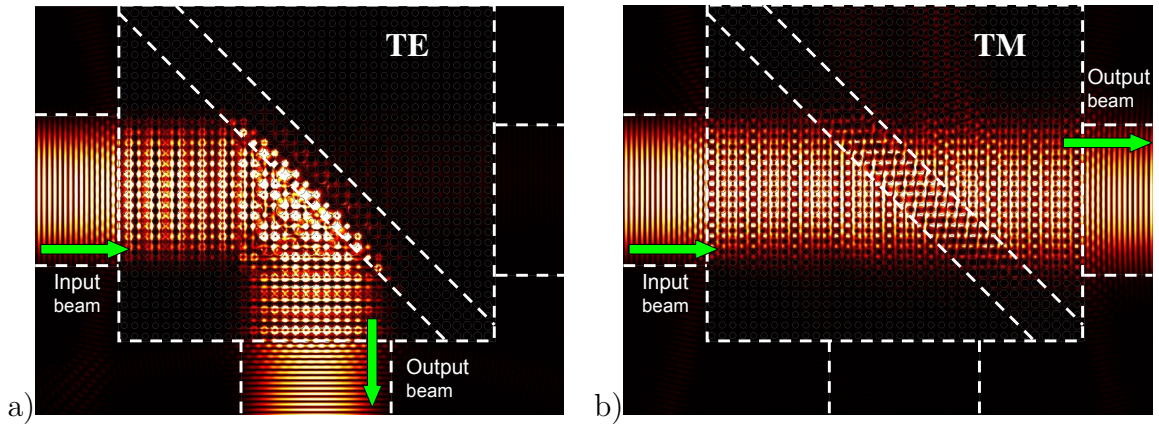


Figure 5.5: 2D FDTD modeling of (a) TE and (b) TM field patterns for the optimized self-collimating polarization splitter structure, showing transmission for TM light and high reflection for TE light.

The results of 2D finite-difference time-domain (FDTD) simulations of light propagation through the polarization beam splitter are shown in Fig. 5.5 for the TE (a) and TM (a) field patterns for the optimized self-collimating polarization splitter structure. Note the weak back reflection and the absence of in-plane diffraction at the boundary between the polarizer region and the cladding photonic crystal regions.

The light propagating in the photonic crystal regions exhibits out-of-plane scattering which give information about the field distribution and intensity. The top view of the polarization splitter obtained using a high-numerical-aperture microscope is presented in Fig. 5.6 for the TE (a) and the TM (b) input polarization states. It is clearly seen, that TE-polarized light is reflected while TM-polarized light is transmitted through the polarization splitter. The scattered light is observed only inside photonic crystal regions since the input and output waveguides have very weak radiation losses.

Performance of the polarization splitter has been estimated and optimized using 2D FDTD method. Calculated transmission for both light polarizations is shown in Fig. 5.7. The optimized filling factor for a square lattice structure of holes was found to be $f_{sc} = 30\%$ for the self-collimating tile and $f_{pol} = 50\%$ for the polarizer slab. Transmission for both polarizations of up to 83% is predicted including the insertion reflection, and

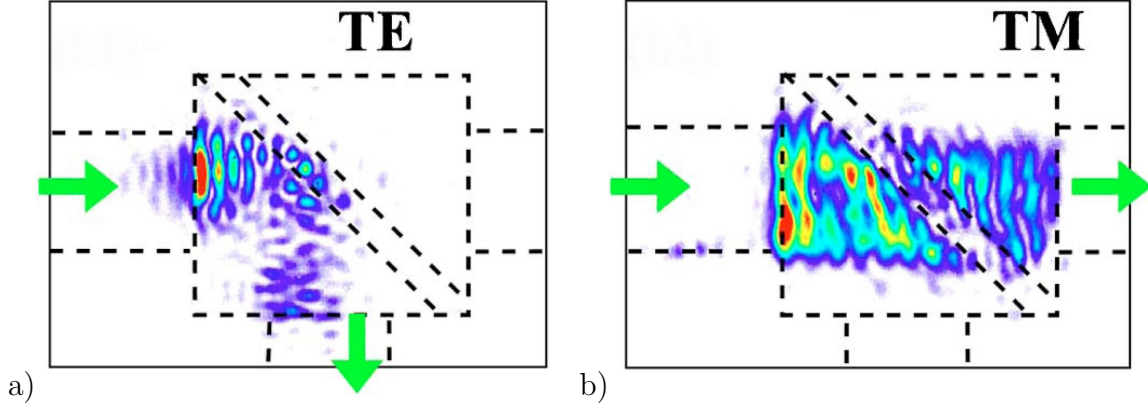


Figure 5.6: Top view from a high-numerical-aperture microscope image of the polarization splitter with TE and TM input polarization states. (a) TE-polarized beam is reflected; (b) TM-polarized beam propagates through the splitter. $\lambda = 1.55 \mu\text{m}$.

occurs over a bandwidth as large as $\Delta u/u = 7\%$ (shaded area in Fig. 5.7). As expected, the TE channel exhibits good transmission when the incident beam frequency lies within the photonic band gap, and the TM channel exhibits transmission over a broader range which is limited either by the band-edge of the TM band gap or when the frequency deviates too much from the self-collimation conditions.

The fabricated structure consists of six lines with nominal $f = 50\%$ embedded in a tile of 40 lines with $f = 30\%$. Refraction in the slab and Goos-Hänchen effect

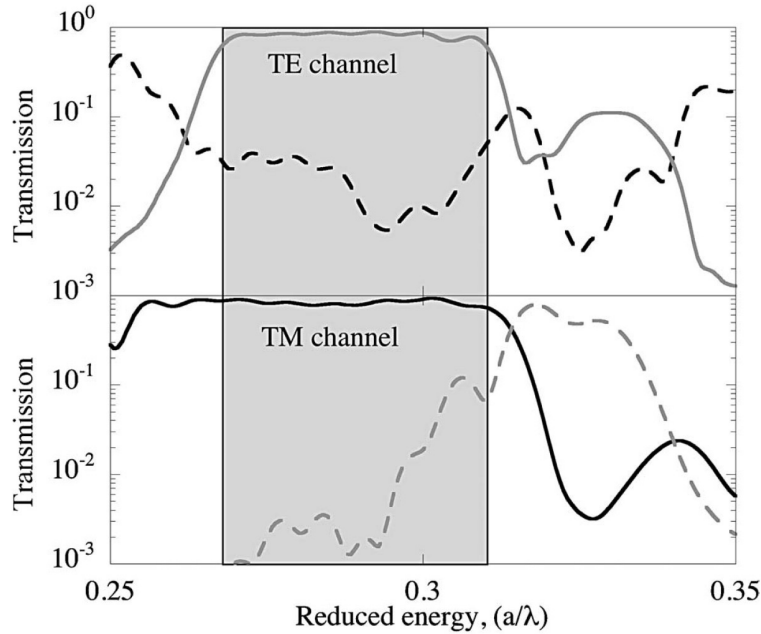


Figure 5.7: Solid curve, 2D FDTD modeling of the (top) TE and (bottom) TM output spectrum of the optimized structure ($f_{sc} = 30\%$ and $f_{pol} = 50\%$); dashed curve, cross-talk TE (TM) transmission in the TM (TE) channel.

[95] induce a small offset of the output axis waveguides compared with their nominal specular location which has to be taken into account in the final device design. The structure actually fabricated consist of a set of two splitters, the first splitter performs the polarization separation itself while the second splitter reflects the TE beam, thus allowing the two polarizations to be measured through parallel ridge waveguides. The structures were fabricated in a single- and a dual-block version (see Fig. 5.8). Note that TE measurements presented below are normalized to a single polarization splitter, *i.e.* the shown transmission spectra are the square root of the measured spectra.

The planar waveguide consists of an optimized GaInAsP/InP structure [48]. The lithography was performed on a LEO 1530/Raith Elphy electron-beam system, and structures were etched onto a custom-designed chemically assisted ion-beam etching (CAIBE) system by using Ar : Cl₂ and flowable oxide (FOx-12, Dow Corning) as the hard mask. While the PhC section was deeply etched, the access waveguides were defined in a second lithography step and were shallow etched to ensure single-mode operation.

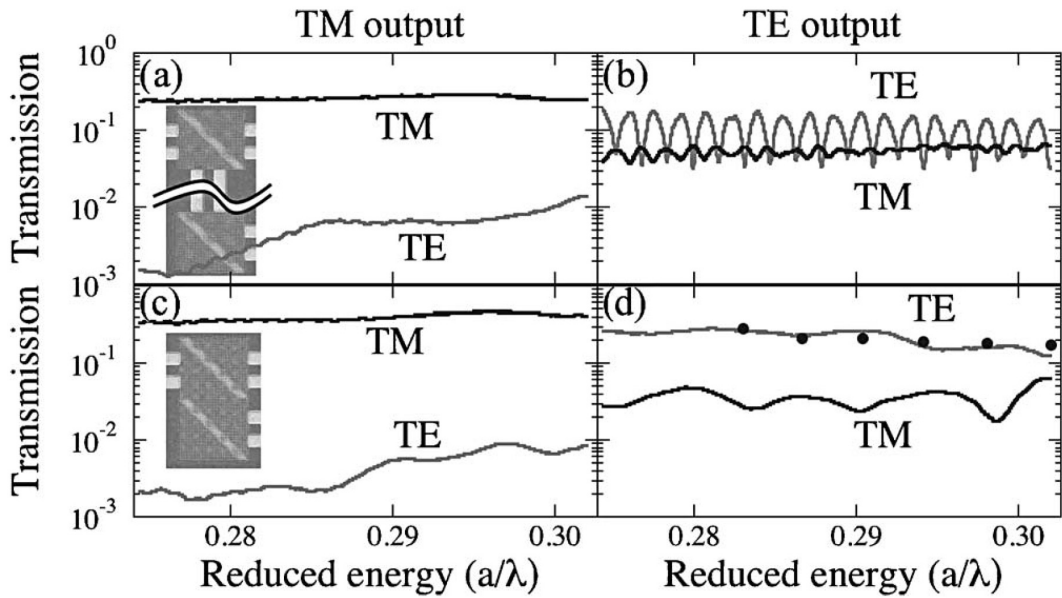


Figure 5.8: Output spectrum of the polarization splitter (lattice constant $a = 450 \text{ nm}$) in single (top) and dual (bottom) versions, TM (TE) channel left (right). TM, black; TE, gray. TE output is normalized to one device. Insets, microscope images of the single-block and dual-block version with or without an intermediate ridge waveguide.

Measurements were performed on a regular end-fire setup with a tunable laser (range $1.47 - 1.66 \mu\text{m}$) light source coupled into the sample via lensed optical fibers. Polarization control and analysis are inserted into the input and collection fibers. The samples as fabricated had filling factors close to the nominal values, as determined optically from calibration test structures. The transmission spectra for both output channels are shown in Fig. 5.8. The best results were obtained over a frequency bandwidth in excess of 5% and show an output transmission of 35% (25% - 30%) for the TM (TE) channel with 0.2% - 0.8% (3% - 4%) TE (TM) cross talk in the TM (TE) output, respectively. The frequency range is likely to be larger, as the low-energy cutoff could not be measured owing to the limited wavelength range of the tunable laser for the given lattice

constant of the sample. The free spectral range of the FabryPerot type fringes in the dual-block version [Fig. 5.8(b)] agrees with the optical length corresponding to back reflections at the tile interface or at the polarizing slab. The fringe contrast allows us to evaluate the reflection coefficient at 37% for TE and 10% for TM. The values obtained for the TE output were confirmed by an independent in situ measurement performed by N. Le Thomas and R. Houdré based on an analysis of the emission pattern of the light diffracted from the surface [black dots in Fig. 5.8(d)].

Two mechanisms reduce the transmission of the polarization splitter: (1) out-of-plane light scattering, which can be either intrinsic, because the sample always operates above the light cone, or extrinsic, due to sample imperfections (hole shape or disorder); and (2) back reflection of the light at the interfaces (the ridge waveguide with the PhC tile or the polarizing slab). Improving the processing could reduce light scattering; however, this can be a demanding task, given that the present processing is already of high quality. Back reflected light could be reduced by improved design of the interfaces, including antireflective coatings with, for example, rows of increasing hole sizes. Considering that back reflection was estimated at 37% (TE) and 10% (TM), this gives a potential for improvement of transmission in the range of 45% - 55% for the TM channel and 60% - 90% for the TE channel, which are acceptable values for a marketable device.

Chapter 6

Conclusions and perspectives

In this work the optical properties of two-dimensional photonic crystals have been theoretically investigated using the methods developed in the framework of the thesis. These methods are based on the general ideas of the mode expansion method and allow one to obtain detailed information about the Bloch modes in the photonic crystals.

The general formulation of the plane wave expansion method for arbitrary two-dimensional photonic crystal has been derived in the second chapter of the thesis. The Bloch vector based approach and the frequency based approach have been considered. These approaches are intended for investigation of the propagating Bloch modes and the evanescent Bloch modes, respectively. It has been shown that combination of these approaches allows one to analyze properties of complex photonic crystal based structures, like cavities and waveguides.

The effect of the discontinuity of the distribution of the dielectric permittivity and/or the magnetic permeability in the photonic crystal on the accuracy of the developed methods have been discussed. The discontinuity leads to the Gibbs phenomenon which deteriorate accuracy of the approximation of the dielectric permittivity and/or the magnetic permeability. New methods to filter out the oscillations related with the Gibbs phenomenon and improve the approximation accuracy have been proposed and tested. It has been shown that the proposed methods can significantly improve accuracy of the calculated distribution of the in-plane components of the electromagnetic field in 2D photonic crystals.

A detailed analysis of the optical properties (dispersion relation, group velocity, self-collimation effect, field distribution etc.) of the 2D photonic crystals has been performed using the developed methods.

An extension of the PWE method – the guided mode expansion method has been derived for the 2D photonic crystal slabs with the intrinsic planar waveguide. This method takes into account the electromagnetic field distribution in the planar waveguide, which improves accuracy of the method, especially for the case of thin waveguides with high refractive index contrast (*e. g.* SOI and membrane waveguides).

A new method of analysis of small variations of photonic crystal parameters has been developed. This approach has been proven to be fast and accurate method for calculation of the effect of the photonic crystal modification on the optical properties.

The developed methods have been used to design the polarization beam splitter based on the self-collimation of the Bloch modes and polarization-dependent dispersion

of light in 2D photonic crystals. Good agreement between the theoretical predictions and performances of the fabricated sample proves the validity of the methods.

The methods discussed in this thesis work well and provide many important information about the light modes in 2D photonic crystals. But several directions of the methods improvements may be proposed based on the gained experience.

First direction is based on the fact that all discussed methods work with photonic crystals with periodicity either at the micro scale (primitive photonic crystal cell) or the macro scale (artificial super-cell to represent lattice defects). All real life samples have imperfections due to fabrication, which are randomly distributed across the sample. A method to take into account the small disorder and estimate its effect on the sample optical properties is important for more detailed analysis of the real-life structures.

Another important point is further analysis of the effect of the permittivity and/or the permeability discontinuities on the accuracy of the methods. New ways to suppress the Gibbs phenomenon will improve the convergence rate and increase the calculation speed of the proposed methods.

One thing is certain. Since the numerical modelling is an essential tool for the integrated optics future advances in the modelling methods will have large and positive impact on development next-generation integrated optics devices.

Appendix A

Optical properties of the 2D photonic crystals

A.1 Dispersion properties of photonic crystals

A.1.1 Square lattice photonic crystals

The dispersion of the Bloch modes of the square lattice photonic crystal consisting of a semiconductor circular pillars with the effective refractive index $n_{eff} = 3.24$ in the air and with the filling factor $f = 0.4$ is presented in the Fig. A.1 and Fig. A.2. The maximum length of the reciprocal lattice vector $G_{max} = 8\frac{2\pi}{a}$ and the number of used plane waves $N = 197$. The dispersion of the first band near the Γ point is close to the dispersion of the light in a homogeneous media and only near the boundary of the first Brillouin zone the effect of the photonic crystal is visible. The noticeable difference is observed for the dispersion of the second band for the TE polarized light. The maximum mode frequency corresponds to the states with the Bloch vector at the corner of the first Brillouin zone (the M points) (in comparison with the Γ point for the photonic crystal made of the air holes in the dielectric background). The dispersion of the TM

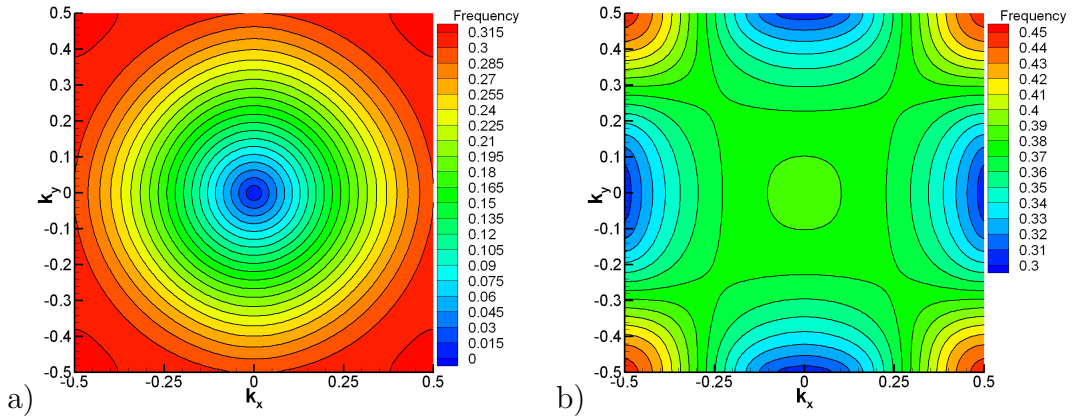


Figure A.1: Dispersion of the TE-polarized Bloch modes for the square lattice photonic crystal consisting of the circular dielectric pillars (the filling factor $f = 0.4$) with the effective refractive index $n_{eff} = 3.24$ in the air. a) The first band. b) The second band.

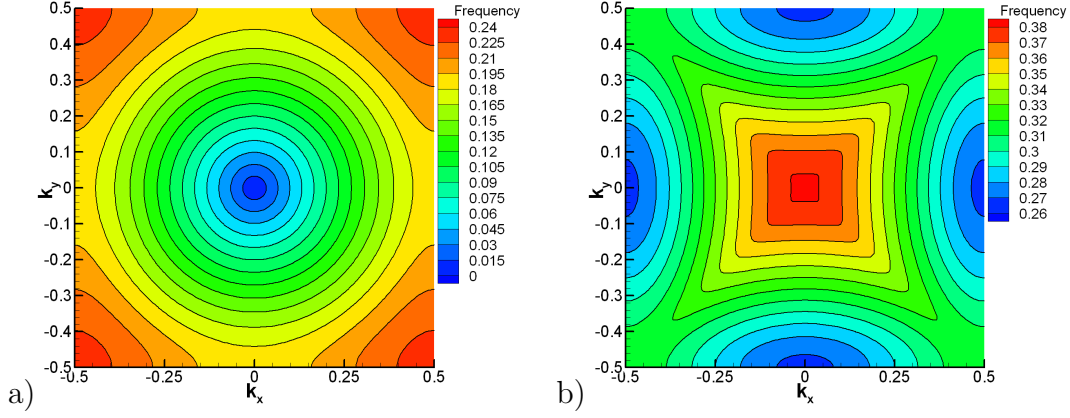


Figure A.2: Dispersion of the TM-polarized Bloch modes for the square lattice photonic crystal consisting of the circular dielectric pillars (the filling factor $f = 0.4$) with the effective refractive index $n_{eff} = 3.24$ in the air. a) The first band. b) The second band.

polarized Bloch modes is similar to the dispersion of the TM polarized modes of the hole-type photonic crystal.

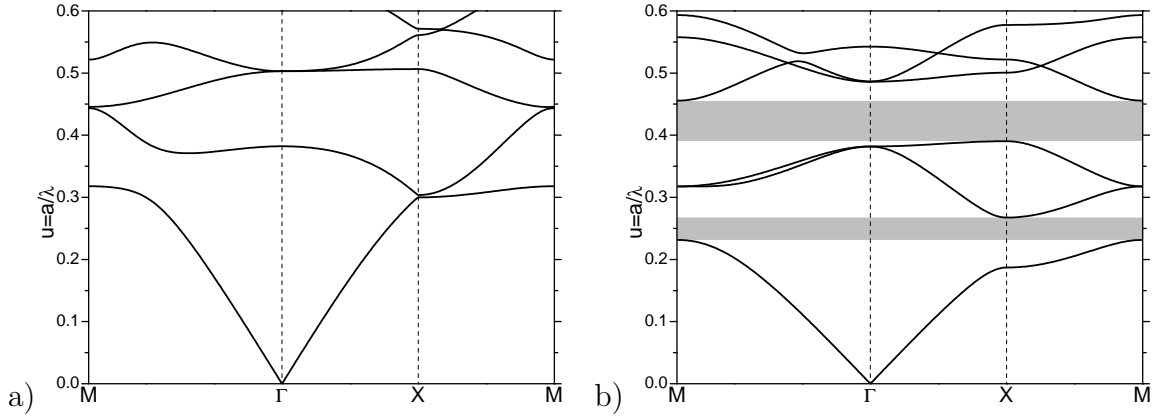


Figure A.3: Dispersion of the Bloch modes for the square lattice photonic crystal consisting of the circular dielectric pillars (the filling factor $f = 0.4$) with the effective refractive index $n_{eff} = 3.24$ in the air. a) TE polarization. b) TM polarization.

The cross-section of the light dispersion is shown in the Fig. A.3. In this case two full photonic band gaps (indicated by the gray regions) exist for the TM polarized light. Changing of the type of the permittivity contrast from “low index atoms, high index background” to “high index atoms, low index background” modifies the effect of the photonic crystal to different light polarization. The first type corresponds to a larger effect on the TE polarized light while the second one affects more the TM polarized states.

The dependence of the position and the width of the full photonic band gaps on the filling factor is shown in the Fig. A.4. The gaps exist for the TM polarized Bloch modes in a wide range of the filling factor and only a narrow full band gap for the TE polarized states opens for large filling factor $f \approx 0.65$.

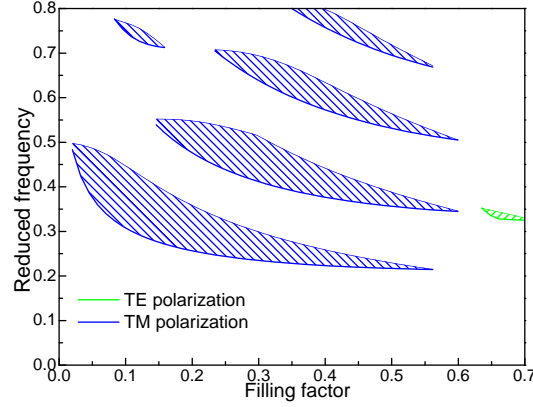


Figure A.4: The full photonic band gaps for the square lattice photonic crystals consisting of dielectric pillars ($n_{eff} = 3.24$) in the air.

A.1.2 Triangular lattice photonic crystals

The dispersion of the Bloch modes of the triangular lattice photonic crystal consisting of a semiconductor circular pillars in the air with the effective refractive index $n_{eff} = 3.24$ and with the filling factor $f = 0.4$ is presented in the Fig. A.5 and the Fig. A.6. The maximum length of the reciprocal lattice vector $G_{max} = 7\frac{2}{\sqrt{3}}\frac{2\pi}{a}$ and the number of used plane waves $N = 187$. Similar to the case of the square lattice photonic crystal the maximum frequency of the second band for the TE polarized light corresponds to the corners of the first Brillouin zone (the K points).

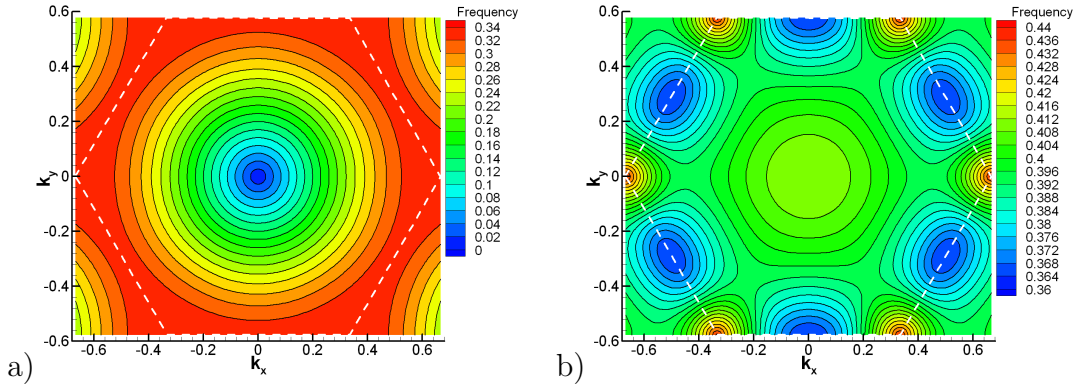


Figure A.5: Dispersion of the TE-polarized Bloch modes for the square lattice photonic crystal consisting of the circular dielectric pillars (the filling factor $f = 0.4$) with the effective refractive index $n_{eff} = 3.24$ in the air. a) The first band. b) The second band.

The cross-sections of the dispersion of the Bloch modes for the pillar type triangular lattice photonic crystal are presented in the Fig. A.7. The full photonic band gap exist for the TE polarized Bloch modes and two much larger full band gaps exist for the TM polarized states.

The dependence of the position and the width of the full photonic band gaps on the filling factor is shown in the Fig. A.8. The gaps exist for the TM polarized Bloch modes for almost all possible values of the filling factor and a narrow full band gap for the TE

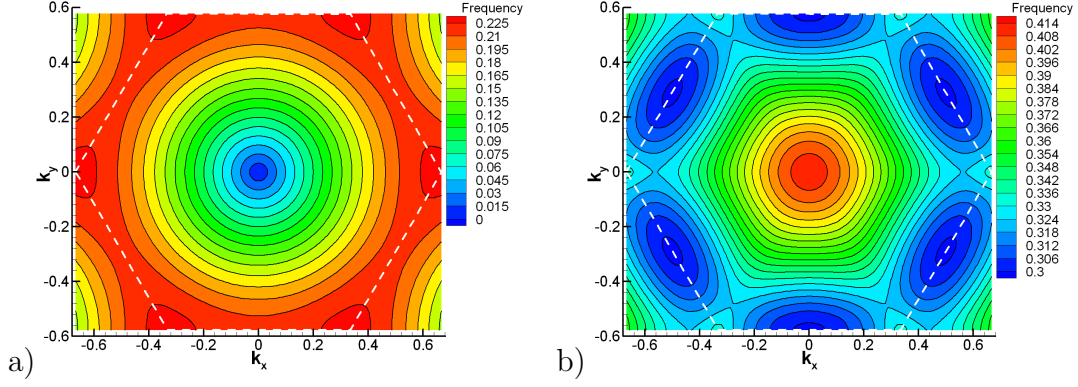


Figure A.6: Dispersion of the TE-polarized Bloch modes for the square lattice photonic crystal consisting of the circular dielectric pillars (the filling factor $f = 0.4$) with the effective refractive index $n_{eff} = 3.24$ in the air. a) The first band. b) The second band.

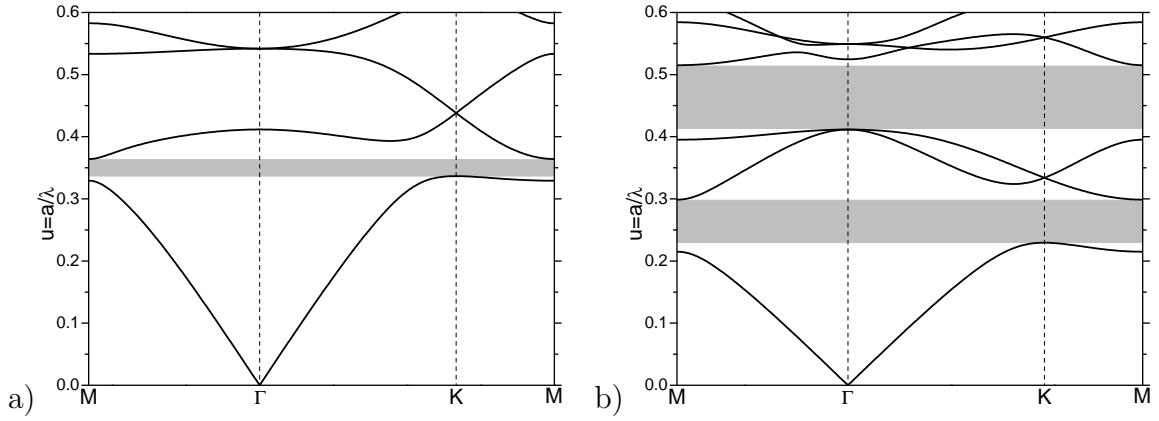


Figure A.7: Dispersion of the Bloch modes for the triangular lattice photonic crystal consisting of the circular dielectric pillars (the filling factor $f = 0.4$) with the effective refractive index $n_{eff} = 3.24$ in the air. a) TE polarization. b) TM polarization.

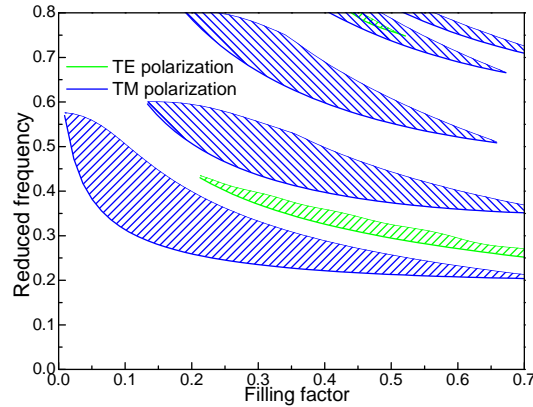


Figure A.8: The full photonic band gaps for the triangular lattice photonic crystals consisting of dielectric pillars ($n_{eff} = 3.24$) in the air.

polarized states opens for the filling factor f larger that about 0.2.

A.2 Group velocity of the propagating Bloch modes

A.2.1 Square lattice photonic crystals

The group velocity of the Bloch modes for the square lattice photonic crystal made of the dielectric pillars in the air is presented in the Fig. A.9 and the Fig. A.10. It exhibit the behavior similar to the case of the hole-based photonic crystal. The calculation parameters are the same as used for the results shown in the section A.1.1.

The difference can be observed for the direction of the group velocity for the TE polarized Bloch modes in the second band near the M points. Because the mode frequency is maximum at the M points the group velocity is directed towards the M points, which opposite to the case of the hole-based photonic crystal (see Fig. 2.29).

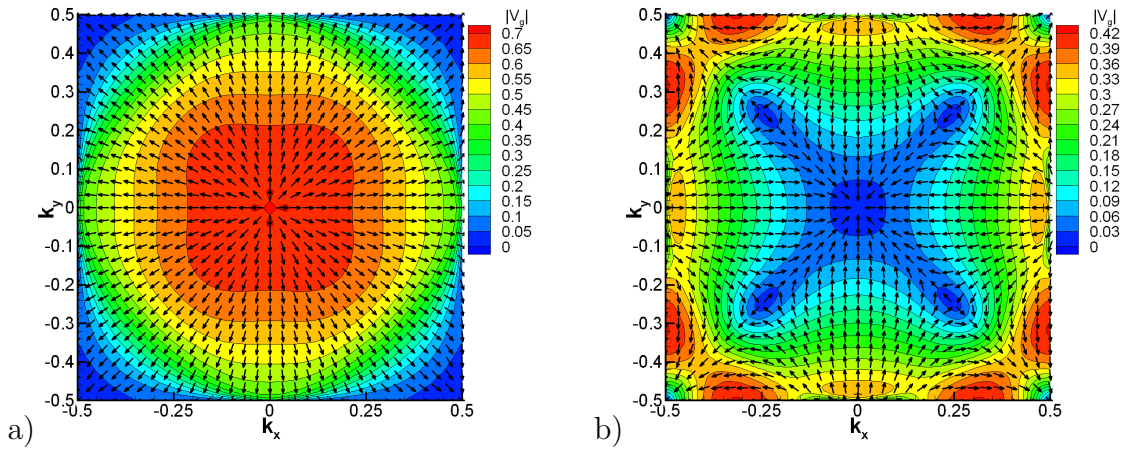


Figure A.9: Group velocity of the TE-polarized Bloch modes for the square lattice photonic crystal consisting of the circular dielectric pillars (the filling factor $f = 0.4$) with the effective refractive index $n_{eff} = 3.24$ in the air. a) The first band. b) The second band.

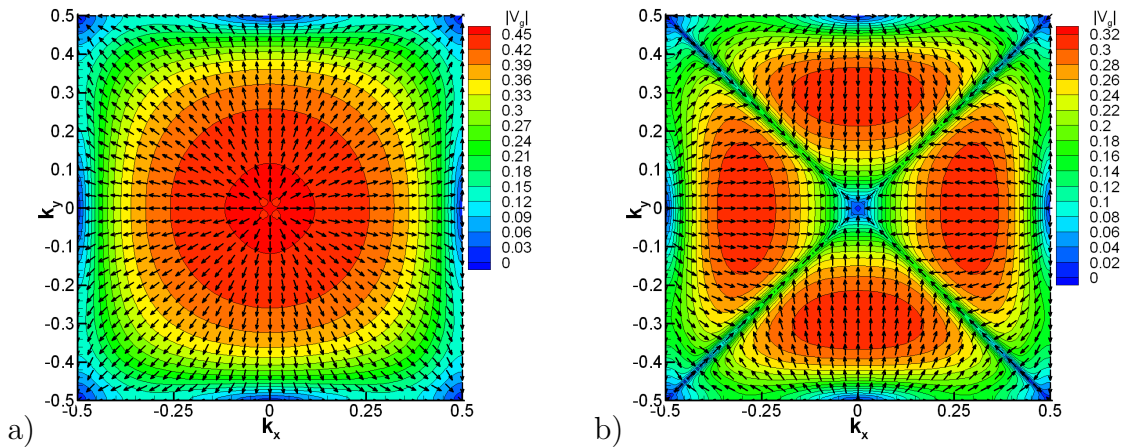


Figure A.10: Group velocity of the TM-polarized Bloch modes for the square lattice photonic crystal consisting of the circular dielectric pillars (the filling factor $f = 0.4$) with the effective refractive index $n_{eff} = 3.24$ in the air. a) The first band. b) The second band.

The group velocity of the Bloch modes for the Bloch vector along the high-symmetry directions is plotted for the first three bands in the Fig. A.11(a) for the TE light polarization and in the Fig. A.11(b) for the TM light polarization. The group velocity is maximum at the Γ point for the first band and decays when the Bloch vector approaches the boundary of the first Brillouin zone. The group velocity for higher bands has more complex dependence on the Bloch vector but in general it tends to be equal to zero at the Γ , M, and X points.

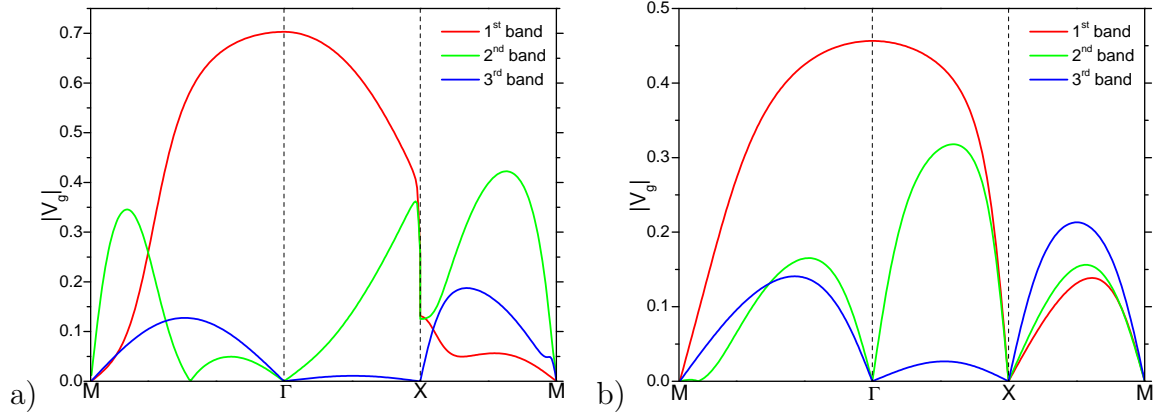


Figure A.11: Group velocity of the Bloch modes for the square lattice photonic crystal consisting of the circular dielectric pillars (the filling factor $f = 0.4$) with the effective refractive index $n_{eff} = 3.24$ in the air. a) TE polarization. b) TM polarization.

A.2.2 Triangular lattice photonic crystals

The group velocity of the Bloch modes for the triangular lattice photonic crystal made of the dielectric pillars in the air is presented in the Fig. A.12 and the Fig. A.13. The calculation parameters are the same as used for the results shown in the section A.1.2.

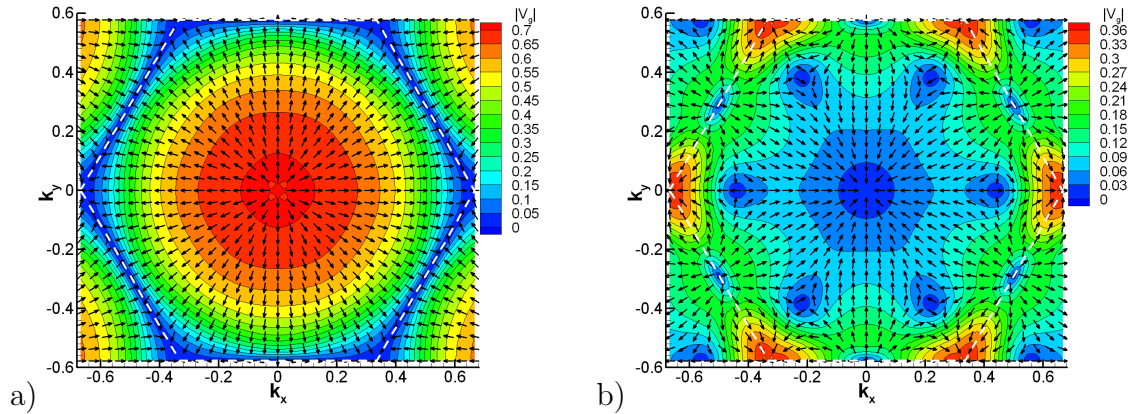


Figure A.12: Group velocity of the TE-polarized Bloch modes for the triangular lattice photonic crystal consisting of the circular dielectric pillars (the filling factor $f = 0.4$) with the effective refractive index $n_{eff} = 3.24$ in the air. a) The first band. b) The second band.

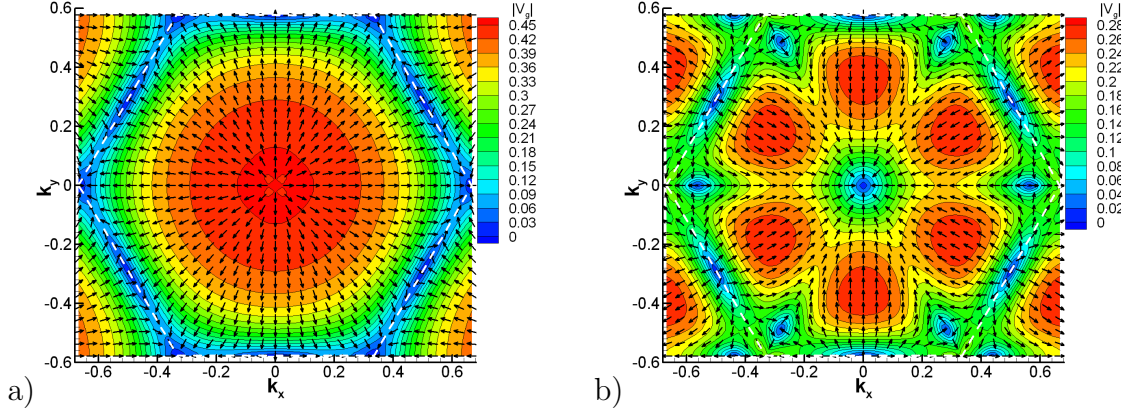


Figure A.13: Group velocity of the TM-polarized Bloch modes for the triangular lattice photonic crystal consisting of the circular dielectric pillars (the filling factor $f = 0.4$) with the effective refractive index $n_{eff} = 3.24$ in the air. a) The first band. b) The second band.

The group velocity of the Bloch modes for the Bloch vector along the high-symmetry directions is plotted for the first three bands in the Fig. A.14(a) for the TE light polarization and in the Fig. A.14(b) for the TM light polarization.

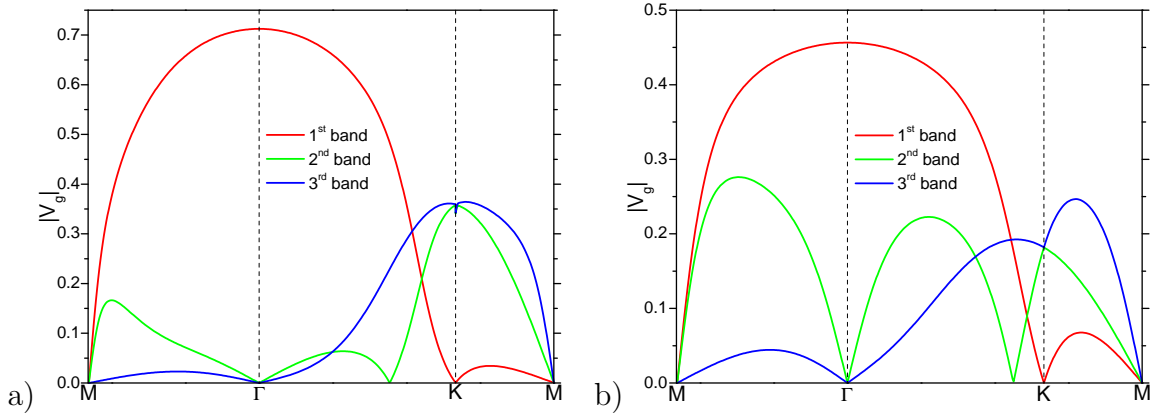


Figure A.14: Group velocity of the Bloch modes for the triangular lattice photonic crystal consisting of the circular dielectric pillars (the filling factor $f = 0.4$) with the effective refractive index $n_{eff} = 3.24$ in the air. a) TE polarization. b) TM polarization.

A.3 Shape of the frequency isolines

A.3.1 Square lattice photonic crystals

The maps of the EFS curvature as functions of the Bloch vector for the square lattice photonic crystal consisting of the dielectric pillars on the air are plotted in the Fig. A.15 for the TE polarized Bloch modes and in the Fig. A.16 for the TM polarized Bloch modes. The calculation parameters are the same as used for the results shown in the section A.1.1.

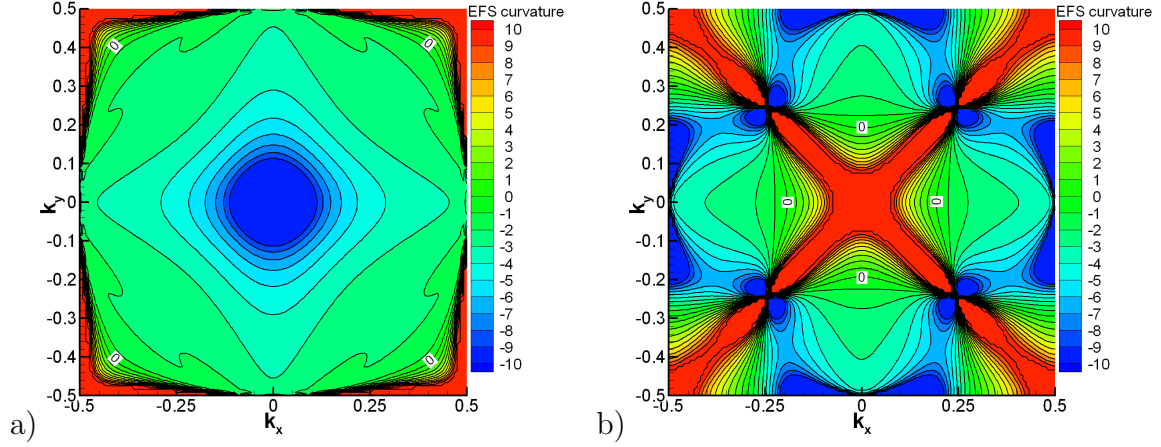


Figure A.15: EFS curvature of the TE-polarized Bloch modes for the square lattice photonic crystal consisting of the circular dielectric pillars (the filling factor $f = 0.4$) with the effective refractive index $n_{eff} = 3.24$ in the air. a) The first band. b) The second band.

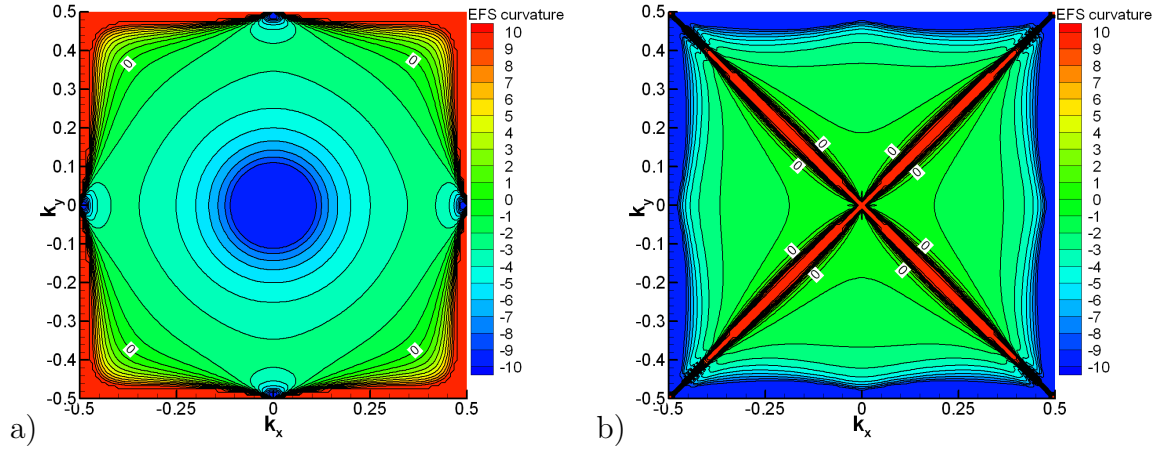


Figure A.16: EFS curvature of the TM-polarized Bloch modes for the square lattice photonic crystal consisting of the circular dielectric pillars (the filling factor $f = 0.4$) with the effective refractive index $n_{eff} = 3.24$ in the air. a) The first band. b) The second band.

The cross-sections of the EFS curvature are shown in the Fig. A.17 for the first three bands of the TE polarized Bloch modes (Fig. A.17(a)) and the TM polarized Bloch modes (Fig. A.17(b)).

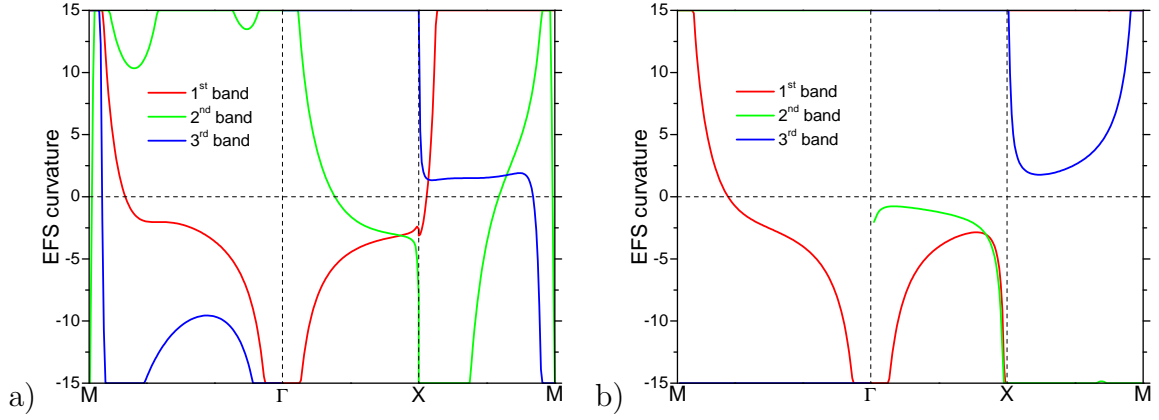


Figure A.17: EFS curvature of the Bloch modes for the square lattice photonic crystal consisting of the circular dielectric pillars (the filling factor $f = 0.4$) with the effective refractive index $n_{eff} = 3.24$ in the air. a) TE polarization. b) TM polarization.

A.3.2 Triangular lattice photonic crystals

The maps of the EFS curvature as functions of the Bloch vector for the triangular lattice photonic crystal consisting of the dielectric pillars on the air are plotted in the Fig. A.18 for the TE polarized Bloch modes and in the Fig. A.19 for the TM polarized Bloch modes. The calculation parameters are the same as used for the results shown in the section A.1.2.

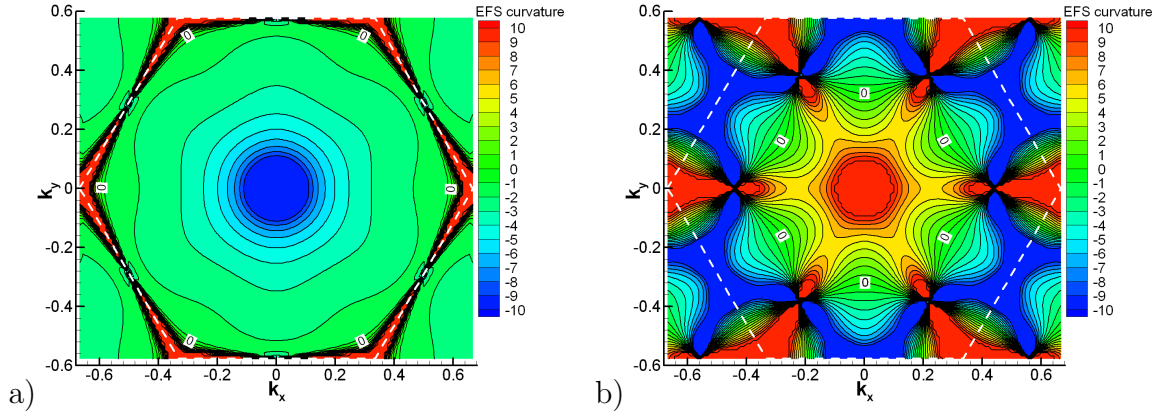


Figure A.18: EFS curvature of the TE-polarized Bloch modes for the triangular lattice photonic crystal consisting of the circular dielectric pillars (the filling factor $f = 0.4$) with the effective refractive index $n_{eff} = 3.24$ in the air. a) The first band. b) The second band.

The cross-sections of the EFS curvature are shown in the Fig. A.20 for the first three bands of the TE polarized Bloch modes (Fig. A.20(a)) and the TM polarized Bloch modes (Fig. A.20(b)).

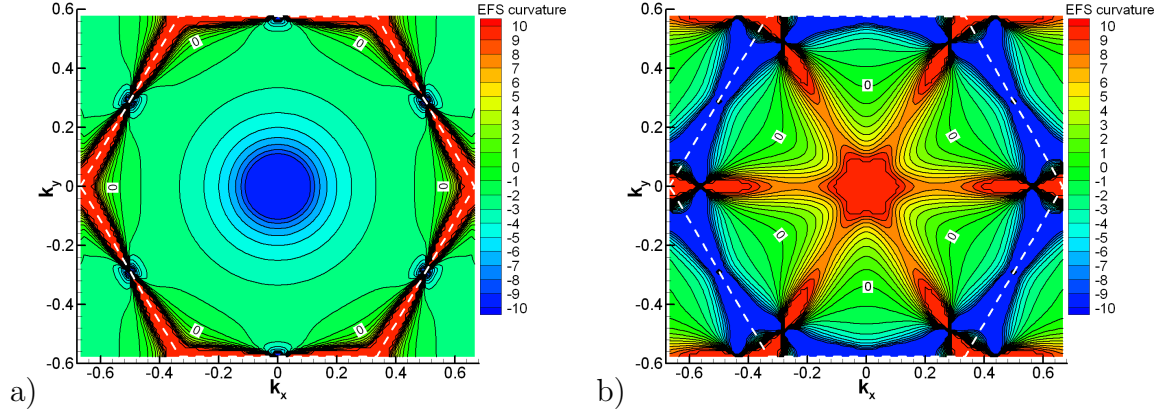


Figure A.19: EFS curvature of the TM-polarized Bloch modes for the triangular lattice photonic crystal consisting of the circular dielectric pillars (the filling factor $f = 0.4$) with the effective refractive index $n_{eff} = 3.24$ in the air. a) The first band. b) The second band.

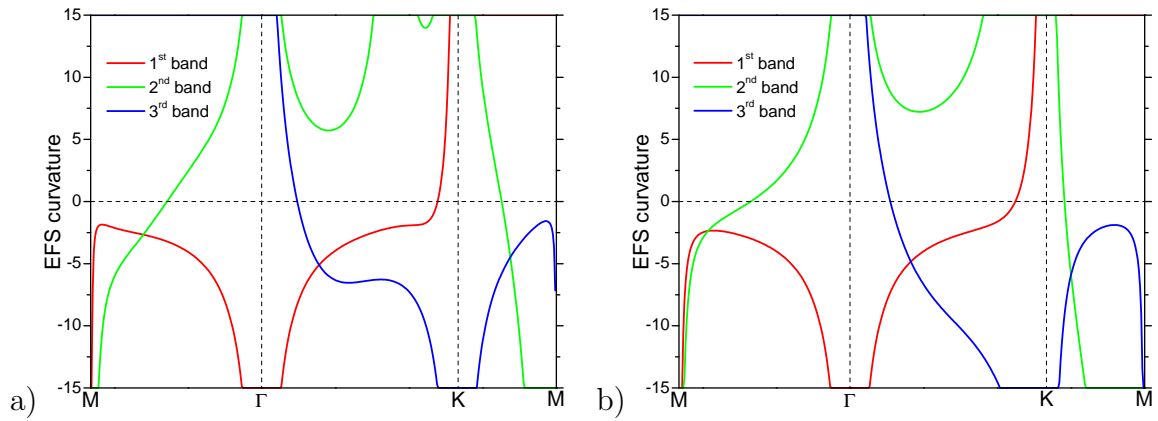


Figure A.20: EFS curvature of the Bloch modes for the triangular lattice photonic crystal consisting of the circular dielectric pillars (the filling factor $f = 0.4$) with the effective refractive index $n_{eff} = 3.24$ in the air. a) TE polarization. b) TM polarization.

Acknowledgments

I would like to take this opportunity to thank all the people who helped me to work on this thesis. First of all I would like to thank Dr. Romuald Houdré who accepted me for the position in his research group and was my supervisor during my stay in EPFL. He introduced me to the world of integrated optics and photonic crystals and always was an endless source of new ideas and advices which guided me in my work.

I also want to thank all members of our group for invaluable help and contribution they made for this work and for the stimulating and inspiring atmosphere which always supported me. Jan-Robert Van Look and Barbara Wild, who worked with me at the beginning of my stay in EPFL, helped me a lot in learning of the basis of photonic crystals and their optical properties. Andrea Dunbar helped me with her deep intuitive understanding of many physical phenomena, which greatly broaden my scientific experience. Very fruitful discussions with Hua Zhang allowed me really to understand many aspects of real-life sample fabrication and processing. Working together with Nicolas Le Thomas and Jana Jágerská was a real pleasure and their unique experience in optical characterization of photonic crystal structures allowed us to verify the theoretical results presented in this thesis.

I will always remember a friendly and stimulating atmosphere in EPFL campus and I want to thank all people who created it. I would like also especially thank all teachers of the courses I attended being a student of the doctoral program in physics. I had unique possibility to learn many fields of modern physics and I am very grateful them for that.

And of course I want to thank my family, which inspired my scientific career and have been supporting it for many years. Despite the long distance between Saint-Petersburg and Lausanne I always felt their love and care, which helped me in my work towards the PhD degree.

Bibliography

- [1] H. Benisty, C. Weisbuch, D. Labilloy, M. Rattier, C. J. M. Smith, T. F. Krauss, R. M. De La Rue, R. Houdré, U. Oesterle, C. Jouanin, and D. Cassagne, “Optical and confinement properties of two-dimensional photonic crystals,” *J. Of Lightwave Technology*, vol. 17, no. 11, pp. 2063–2077, 1999.
- [2] D. W. Prather, S. Shi, J. Murakowski, G. J. Schneider, A. Sharkawy, C. Chen, and B. Miao, “Photonic crystal structures and applications: Perspective, overview, and development,” *IEEE J. Of Selected Topics In Quantum Electronics*, vol. 12, no. 6, pp. 1416–1437, 2006.
- [3] P. R. Villeneuve, S. Fan, and J. D. Joannopoulos, “Microcavities in photonic crystals: Mode symmetry, tunability, and coupling efficiency,” *Phys. Rev. B*, vol. 54, no. 11, pp. 7837–7842, 1996.
- [4] S. Noda, M. Fujita, and T. Asano, “Spontaneous-emission control by photonic crystals and nanocavities,” *Nature Photonics*, vol. 1, pp. 449–458, 2007.
- [5] H. Benisty, “Modal analysis of optical guides with two-dimensional photonic band-gap boundaries,” *J. Appl. Phys.*, vol. 79, no. 10, pp. 7483–7492, 1996.
- [6] F. Glöckler, S. Peters, U. Lemmer, and M. Gerken, “Tunable superprism effect in photonic crystals,” *phys. stat. sol. (a)*, vol. 204, no. 11, p. 37903804, 2007.
- [7] L. C. Botten, N. A. Nicorovici, R. C. McPhedran, C. Martijn de Sterke, and A. A. Asatryan, “Photonic band structure calculations using scattering matrices,” *Phys. Rev. E*, vol. 64, p. 046603, 2001.
- [8] L. C. Botten, T. P. White, A. A. Asatryan, T. N. Langtry, C. Martijn de Sterke, and R. C. McPhedran, “Bloch mode scattering matrix methods for modeling extended photonic crystal structures. I. Theory,” *Phys. Rev. E*, vol. 70, p. 056606, 2004.
- [9] A. Taflove and S. C. Hagness, *Computational Electrodynamics: The Finite-Difference Time-Domain Method*. Norwood: Artech House INC, 2000.
- [10] Lord Rayleigh, “On the influence of obstacles arranged in rectangular order upon the properties of a medium,” *Philos. Mag.*, vol. 34, pp. 481–502, 1892.
- [11] F. Abelès, “Sur la propagation des ondes électromagnétiques dans les milieux stratifiés,” *Ann. de Phys.*, vol. 12, no. 3, pp. 504–520, 1948.

- [12] P. Yeh, A. Yariv, and C.-S. Hong, "Electromagnetic propagation in periodic stratified media. I. General theory," *J. Opt. Soc. Am.*, vol. 67, no. 4, pp. 423–438, 1977.
- [13] E. M. Purcell, "Spontaneous emission probabilities at radio frequencies," *Phys. Rev.*, vol. 69, no. 11-12, p. 681, 1946.
- [14] V. P. Bykov, "Spontaneous emission in a periodic structure," *Soviet Physics JETP*, vol. 35, no. 2, pp. 269–273, 1972.
- [15] K. M. Ho, C. T. Chan, and C. M. Soukoulis, "Existence of photonic gap in periodic dielectric structures," *Phys. Rev. Lett.*, vol. 65, no. 25, pp. 3152–3155, 1990.
- [16] E. Yablonovitch, T. J. Gmitter, and K. M. Leung, "Photonic band structure: The face-centered-cubic case employing nonspherical atoms," *Phys. Rev. Lett.*, vol. 67, no. 17, pp. 2295–2298, 1991.
- [17] C. C. Cheng, V. Arbet-Engels, A. Scherer, and E. Yablonovitch, "Nanofabricated three dimensional photonic crystals operating at optical wavelengths," *Physica Scripta.*, vol. T68, pp. 17–20, 1996.
- [18] S. Y. Lin, J. G. Fleming, D. L. Hetherington, B. K. Smith, R. Biswas, K. M. Ho, M. M. Sigalas, W. Zubrzycki, S. R. Kurtz, and J. Bur, "A three-dimensional photonic crystal operating at infrared wavelengths," *Nature*, vol. 394, pp. 251–253, 1998.
- [19] Y. A. Vlasov, X.-Z. Bo, J. C. Sturm, and D. J. Norris, "On-chip natural assembly of silicon photonic bandgap crystals," *Nature*, vol. 414, pp. 289–293, 2001.
- [20] K. M. Ho, C. T. Chan, C. M. Soukoulis, R. Biswas, and M. Sigalas, "Photonic band gaps in three dimensions: new layer-by-layer periodic structures," *Solid State Communications*, vol. 89, no. 5, pp. 415–416, 1994.
- [21] K. Aoki, H. T. Miyazaki, H. Hirayama, K. Inoshita, T. Baba, K. Sakoda, N. Shinya, and Y. Aoyagi, "Microassembly of semiconductor three-dimensional photonic crystals."
- [22] H. Míguez, C. López, F. Meseguer, A. Blanco, L. Vázquez, R. Mayoral, M. O. na V. Fornés, and A. Mifsud, "Photonic crystal properties of packed submicrometric SiO₂ spheres," *Appl. Phys. Lett.*, vol. 71, no. 9, pp. 1148–1150, 1997.
- [23] A. A. Zakhidov, R. H. Baughman, Z. Iqbal, C. Cui, I. Khayrullin, S. O. Dantas, J. Marti, and V. G. Ralchenko, "Carbon structures with three-dimensional periodicity at optical wavelengths," *Science*, vol. 282, pp. 897–901, 1998.
- [24] R. Ferrini, B. Lombardet, B. Wild, R. Houdré, and G.-H. Duan, "Hole depth- and shape-induced radiation losses in two-dimensional photonic crystals," *Appl. Phys. Lett.*, vol. 82, no. 7, pp. 1009–1011, 2003.
- [25] R. Ferrini, R. Houdré, H. Benisty, M. Qiu, and J. Moosburger, "Radiation losses in planar photonic crystals: two-dimensional representation of hole depth and shape by an imaginary dielectric constant," *J. Opt. Soc. Am. B*, vol. 20, no. 3, pp. 469–478, 2003.

- [26] P. T. Rakich, M. S. Dahlem, S. Tandon, M. Ibanescu, M. Soljačić, G. S. Petrich, J. D. Joannopoulos, L. A. Kolodziejski, and E. P. Ippen, "Achieving centimetre-scale supercollimation in a large-area two-dimensional photonic crystal," *Nature materials*, vol. 5, pp. 93–96, 2006.
- [27] S. J. McNab, N. Moll, and Y. A. Vlasov, "Ultra-low loss photonic integrated circuit with membrane-type photonic crystal waveguides," *Opt. Express*, vol. 11, no. 22, pp. 2927–2939, 2003.
- [28] H. Kosaka, T. Kawashima, A. Tomita, M. Notomi, T. Tamamura, T. Sato, and S. Kawakami, "Photonic crystals for micro lightwave circuits using wavelength-dependent angular beam steering," *Appl. Phys. Lett.*, vol. 74, no. 10, pp. 1370–1372, 1999.
- [29] ———, "Self-collimating phenomena in photonic crystals," *Appl. Phys. Lett.*, vol. 74, no. 9, pp. 1212–1214, 1999.
- [30] T. Baba, T. Matsumoto, and M. Echizen, "Finite difference time domain study of high efficiency photonic crystal superprisms," *Opt. Express*, vol. 12, no. 19, pp. 4608–4613, 2004.
- [31] L. Wu, M. Mazilu, J.-F. Gallet, and T. F. Krauss, "Dual lattice photonic-crystal beam splitters," *Appl. Phys. Lett.*, vol. 86, p. 211106, 2005.
- [32] S.-G. Lee, S. S. Oh, J.-E. Kim, H. Y. Park, and C.-S. Keeb, "Line-defect-induced bending and splitting of self-collimated beams in two-dimensional photonic crystals," *Appl. Phys. Lett.*, vol. 87, p. 181106, 2005.
- [33] M. Augustin, R. Iliew, C. Etrich, D. Schelle, H.-J. Fuchs, U. Peschel, S. Nolte, E.-B. Kley, F. Lederer, and A. Tünnermann, "Self-guiding of infrared and visible light in photonic crystal slabs," *Appl. Phys. B*, vol. 81, p. 313319, 2005.
- [34] D. N. Chigrin, S. Enoch, C. M. Sotomayor Torres, and G. Tayeb, "Self-guiding in two-dimensional photonic crystals," *Opt. Express*, vol. 11, no. 10, pp. 1203–1211, 2003.
- [35] J. L. Garcia-Pomar and M. Nieto-Vesperinas, "Waveguiding, collimation and sub-wavelength concentration in photonic crystals," *Opt. Express*, vol. 13, no. 20, pp. 7997–8007, 2005.
- [36] D. W. Prather, S. Shi, D. M. Pustai, C. Chen, S. Venkataraman, A. Sharkawy, G. J. Schneider, and J. Murakowski, "Dispersion-based optical routing in photonic crystals," *Opt. Letters*, vol. 29, no. 1, pp. 50–52, 2004.
- [37] J. Witzens, M. Lončar, and A. Scherer, "Self-collimation in planar photonic crystals," *IEEE J. Of Selected Topics In Quantum Electronics*, vol. 8, no. 6, pp. 1246–1257, 2002.
- [38] K. Staliunas and R. Herrero, "Nondiffractive propagation of light in photonic crystals," *Phys. Rev. E*, vol. 73, p. 016601, 2006.

- [39] T. Yamashita and C. J. Summers, "Evaluation of self-collimated beams in photonic crystals for optical interconnect," *IEEE J. On Selected Areas In Communications*, vol. 23, no. 7, pp. 1341–1347, 2005.
- [40] P.-T. Lee, T.-W. Lu, F.-M. Tsai, and T.-C. Lu, "Investigation of whispering gallery mode dependence on cavity geometry of quasiperiodic photonic crystal microcavity lasers," *Appl. Phys. Lett.*, vol. 89, p. 231111, 2006.
- [41] A. Lavrinenko, A. Têtu, L. F. J. Fage-Pedersen, and P. Borel, "Optimization of photonic crystal 60° waveguide bends for broadband and slow-light transmission," *Appl. Phys. B*, vol. 87, pp. 53–56, 2007.
- [42] K. Nozaki, H. Watanabe, and T. Babab, "Photonic crystal nanolaser monolithically integrated with passive waveguide for effective light extraction," *Appl. Phys. Lett.*, vol. 92, p. 021108, 2008.
- [43] Y. Tanaka, T. Asano, and S. Noda, "Design of photonic crystal nanocavity with Q-Factor of 10^9 ," *J. Of Lightwave Technology*, vol. 26, no. 11, pp. 1532–1539, 2008.
- [44] L. C. Andreani and D. Gerace, "Lightmatter interaction in photonic crystal slabs," *phys. stat. sol. (b)*, vol. 244, no. 10, p. 35283539, 2007.
- [45] S. Fan and J. D. Joannopoulos, "Analysis of guided resonances in photonic crystal slabs," *Phys. Rev. B*, vol. 65, p. 235112, 2002.
- [46] S. G. Johnson, S. Fan, P. R. Villeneuve, J. D. Joannopoulos, and L. A. Kolodziejski, "Guided modes in photonic crystal slabs," *Phys. Rev. B*, vol. 60, no. 8, pp. 5751–5758, 1999.
- [47] T. Ochiai and K. Sakoda, "Dispersion relation and optical transmittance of a hexagonal photonic crystal slab," *Phys. Rev. B*, vol. 63, p. 125107, 2001.
- [48] R. Ferrini, A. Berrier, L. A. Dunbar, R. Houdré, M. Mulot, S. Anand, S. de Rossi, and A. Talneau, "Minimization of out-of-plane losses in planar photonic crystals by optimizing the vertical waveguide," *Appl. Phys. Lett.*, vol. 85, no. 18, pp. 3998–4000, 2004.
- [49] W. Śmigaj and B. Gralak, "Validity of the effective-medium approximation of photonic crystals," *Phys. Rev. B*, vol. 77, p. 235445, 2008.
- [50] Y. Akahane, T. Asano, B.-S. Son, and S. Noda, "High-Q photonic nanocavity in a two-dimensional photonic crystal," *Nature*, vol. 425, pp. 944–947, 2003.
- [51] A. R. A. Chalcraft, S. Lam, D. OBrien, T. F. Krauss, M. Sahin, D. Szymanski, D. Sanvitto, R. Oulton, M. S. Skolnick, A. M. Fox, D. M. Whittaker, H.-Y. Liu, and M. Hopkinson, "Mode structure of the L3 photonic crystal cavity," *Appl. Phys. Lett.*, vol. 90, p. 241117, 2007.
- [52] M. Plihal and A. A. Maradudin, "Photonic band structure of two-dimensional systems: The triangular lattice," *Phys. Rev. B*, vol. 44, no. 16, pp. 8565–8571, 1991.

- [53] R. Meade, A. M. Rappe, K. D. Brommer, J. D. Joannopoulos, and O. L. Alerhand, "Accurate theoretical analysis of photonic band-gap materials," *Phys. Rev. B*, vol. 48, no. 11, pp. 8434–8437, 1993.
- [54] K. Sakoda, "Transmittance and bragg reflectivity of two-dimensional photonic lattices," *Phys. Rev. B*, vol. 52, no. 12, pp. 8992–9002, 1995.
- [55] L. Li, "Use of fourier series in the analysis of discontinuous periodic structures," *J. Opt. Soc. Am. A*, vol. 13, no. 9, pp. 1870–1876, 1996.
- [56] A. David, H. Benisty, and C. Weisbuch, "Fast factorization rule and plane-wave expansion method for two-dimensional photonic crystals with arbitrary hole-shape," *Phys. Rev. B*, vol. 73, p. 075107, 2006.
- [57] A. J. Jerry, *The Gibbs Phenomenon in Fourier Analysis, Splines and Wavelet Approximations*. Kluwer Academic Publishers, 1998.
- [58] M. Dems, R. Kotynski, and K. Panajotov, "Plane wave admittance method a novel approach for determining the electromagnetic modes in photonic structures," *Opt. Express*, vol. 13, no. 9, pp. 3196–3207, 2005.
- [59] S. Shi, C. Chen, and D. W. Prather, "Revised plane wave method for dispersive material and its application to band structure calculations of photonic crystal slabs," *Appl. Phys. Lett.*, vol. 86, p. 043104, 2005.
- [60] L.-M. Zhao and B.-Y. Gua, "Applications of the expanded basis method to study the behavior of light in a two-dimensional photonic crystal slab," *Eur. Phys. J. B*, vol. 52, p. 275280, 2006.
- [61] Y.-C. Hsue and T.-J. Yang, "Applying a modified plane-wave expansion method to the calculations of transmittivity and reflectivity of a semi-infinite photonic crystal," *Phys. Rev. E*, vol. 70, p. 016706, 2004.
- [62] A. Kirchner, K. Busch, and C. M. Soukoulis, "Transport properties of random arrays of dielectric cylinders," *Phys. Rev. B*, vol. 57, no. 1, pp. 277–288, 1998.
- [63] T. Baba, "Slow light in photonic crystals," *Nature Photonics*, vol. 2, pp. 465–473, 2008.
- [64] J. Li, T. P. White, L. O'Faolain, A. Gomez-Iglesias, and T. F. Krauss, "Systematic design of flat band slow light in photonic crystal waveguides," *Opt. Express*, vol. 16, no. 9, pp. 6227–6232, 2008.
- [65] A. Figotin and I. Vitebskiy, "Slow light in photonic crystals," *Waves in Random and Complex Media*, vol. 16, no. 3, p. 293382, 2006.
- [66] M. Burrelli, R. J. P. Engelen, A. Opheij, D. van Oosten, D. Mori, T. Baba, and L. Kuipers, "Observation of polarization singularities at the nanoscale," *Phys. Rev. Lett.*, vol. 102, p. 033902, 2009.

- [67] R. Ferrini, J. Martz, L. Zuppiroli, B. Wild, V. Zabelin, L. A. Dunbar, R. Houdré, M. Mulot, and S. Anand, “Planar photonic crystals infiltrated with liquid crystals: optical characterization of molecule orientation,” *Opt. Letters*, vol. 31, no. 9, pp. 1238–1240, 2006.
- [68] G. Alagappan, X. W. Sun, P. Shum, and M. B. Yu, “Tunable superprism and polarization splitting in a liquid crystal infiltrated two-dimensional photonic crystal made of silicon oxynitride,” *Opt. Letters*, vol. 31, no. 8, pp. 1109–1111, 2006.
- [69] E. P. Kosmidou, E. E. Kriezis, and T. D. Tsiboukis, “Analysis of tunable photonic crystal devices comprising liquid crystal materials as defects,” *IEEE J. Of Quantum Electronics*, vol. 41, no. 5, pp. 657–665, 2005.
- [70] D. Englund, I. Fushman, and J. Vučković, “General recipe for designing photonic crystal cavities,” *Opt. Express*, vol. 13, no. 16, pp. 5961–5975, 2005.
- [71] L. C. Andreani and D. Gerace, “Photonic-crystal slabs with a triangular lattice of triangular holes investigated using a guided-mode expansion method,” *Phys. Rev. B*, vol. 73, p. 235114, 2006.
- [72] J. Vučković, M. Lončar, H. Mabuchi, and A. Scherer, “Optimization of the Q factor in photonic crystal microcavities,” *IEEE J. Of Quantum Electronics*, vol. 38, no. 7, pp. 850–856, 2002.
- [73] K. Srinivasan and O. Painter, “Momentum space design of high-q photonic crystal optical cavities,” *Opt. Express*, vol. 10, no. 15, pp. 670–684, 2002.
- [74] N. Le Thomas, V. Zabelin, R. Houdré, M. V. Kotlyar, and T. F. Krauss, “Influence of residual disorder on the anticrossing of bloch modes probed in k space,” *Phys. Rev. B*, vol. 71, p. 125301, 2008.
- [75] N. Le Thomas, R. Houdré, M. V. Kotlyar, D. O’Brien, and T. F. Krauss, “Exploring light propagating in photonic crystals with fourier optics,” *J. Opt. Soc. Am. B*, vol. 24, no. 12, pp. 2964–2971, 2007.
- [76] M. Ibanescu, E. J. Reed, and J. D. Joannopoulos, “Enhanced photonic band-gap confinement via van hove saddle point singularities,” *Phys. Rev. Lett.*, vol. 96, p. 033904, 2006.
- [77] L. C. Andreani and M. Agio, “Photonic bands and gap maps in a photonic crystal slab,” *IEEE J. Of Quantum Electronics*, vol. 38, no. 7, pp. 891–898, 2002.
- [78] D. O’Brien, M. D. Settle, T. Karle, A. Michaeli, M. Salib, and T. F. Krauss, “Coupled photonic crystal heterostructure nanocavities,” *Opt. Express*, vol. 15, no. 3, pp. 1228–1233, 2007.
- [79] J. Jágorská, N. Le Thomas, V. Zabelin, R. Houdré, W. Bogaerts, P. Dumon, and R. Baets, “Experimental observation of slow mode dispersion in photonic crystal coupled-cavity waveguides,” *Opt. Letters*, vol. 34, no. 3, pp. 359–361, 2009.

- [80] S. G. Johnson, M. Ibanescu, M. A. Skorobogatiy, O. Weisberg, J. D. Joannopoulos, and Y. Fink, "Perturbation theory for maxwells equations with shifting material boundaries," *Phys. Rev. E*, vol. 65, p. 066611, 2002.
- [81] L. Rindorf and N. A. Mortensen, "Non-perturbative approach to high-index-contrast variations in electromagnetic systems," *Optics Communications*, vol. 261, p. 181186, 2006.
- [82] M. Skorobogatiy, S. G. Johnson, S. A. Jacobs, and Y. Fink, "Dielectric profile variations in high-index-contrast waveguides, coupled mode theory, and perturbation expansions," *Phys. Rev. E*, vol. 67, p. 046613, 2003.
- [83] K. T. Hecht, *Quantum mechanics*. New York: Springer-Verlag, 2000.
- [84] T. Liu, A. R. Zakharian, M. Fallahi, J. V. Moloney, and M. Mansuripur, "Design of a compact photonic-crystal-based polarizing beam splitter," *IEEE Photonics Technology Lett.*, vol. 17, no. 7, pp. 1435–1437, 2005.
- [85] Y. Kalra and R. K. Sinha, "Design of ultra compact polarization splitter based on the complete photonic band gap," *Optical and Quantum Electronics*, vol. 37, pp. 889–895, 2005.
- [86] X. Ao and S. He, "Polarization beam splitters based on a two-dimensional photonic crystal of negative refraction," *Opt. Letters*, vol. 30, no. 16, pp. 2152–2154, 2005.
- [87] X. Ao, L. Liu, L. Wosinski, and S. He, "Polarization beam splitter based on a two-dimensional photonic crystal of pillar type," *Appl. Phys. Lett.*, vol. 89, p. 171115, 2006.
- [88] Z. Lu, Y. Tang, Y. Shen, X. Liu, and J. Zi, "Polarization beam splitting in two-dimensional photonic crystals based on negative refraction," *Phys. Lett. A*, vol. 346, pp. 243–247, 2005.
- [89] V. Mocella, P. Dardano, L. Moretti, and I. Rendina, "A polarizing beam splitter using negative refraction of photonic crystals," *Opt. Express*, vol. 13, no. 19, pp. 7699–7707, 2005.
- [90] S. Kim, G. P. N. amd Jingbo Cai, and J. Jiang, "Ultracompact high-efficiency polarizing beam splitter with a hybrid photonic crystal and conventional waveguide structure," *Opt. Letters*, vol. 28, no. 23, pp. 2384–2486, 2003.
- [91] D. M. Pustai, S. Shi, C. Chen, A. Sharkawy, and D. W. Prather, "Analysis of splitters for self-collimated beams in planar photonic crystals," *Opt. Express*, vol. 12, no. 9, pp. 1823–1831, 2004.
- [92] X. Shen, K. Han, Y. Shen, H. Li, Y. Wu, and G. Tang, "Dispersion-based all photonic crystals polarization beam splitter," *Phys. Lett. A*, vol. 369, p. 524527, 2007.

- [93] E. Schonbrun, Q. Wu, W. Park, T. Yamashita, and C. J. Summers, “Polarization beam splitter based on a photonic crystal heterostructure,” *Opt. Letters*, vol. 31, no. 21, pp. 3104–3106, 2006.
- [94] V. Zabelin, L. A. Dunbar, N. Le Thomas, R. Houdré, M. V. Kotlyar, L. O’Faolain, and T. F. Krauss, “Self-collimating photonic crystal polarization beam splitter,” *Opt. Letters*, vol. 32, no. 5, pp. 530–532, 2007.
- [95] D. Felbacq and R. Smaâli, “Bloch modes dressed by evanescent waves and the generalized Goos-Hänchen effect in photonic crystals,” *Phys. Rev. Lett.*, vol. 92, no. 19, p. 193902, 2004.

Conference presentations and publications

Conference presentations:

- *The analysis of light propagation in AlGaInN/GaN LED chips and selection of an optimal chip design*, **V. Zabelin**, D.A. Zakheim, and S.A. Gurevich
Postgraduate Research Conference PREP2005, Lancaster, UK, March 2005 (poster presentation)
- *Modeling of light propagation properties and electromagnetic field distribution in 2D photonic crystals*, **V. Zabelin** and R. Houdré
International School of Quantum Electronics, Erice, Italy, August 2005 (poster presentation)
- *Comparison of polarization splitter devices based on planar photonic crystals*, **V. Zabelin**, J.-R. van Look, N. Le Thomas, and R. Houdré
SPIE Photonics Europe Symposium, Strassbourg, France, April 2006 (oral presentation)
- *Numerical modelling of the optical properties of infiltrated photonic crystals*, **V. Zabelin** and R. Houdré
XV International Workshop on Optical Waveguide Theory and Numerical Modelling OWTNM 2006, Varese, Italy, April 2006 (oral presentation)
- *The perturbation method for photonic crystals using the plane wave expansion*, **V. Zabelin** and R. Houdré
XVI International Workshop on Optical Waveguide Theory and Numerical Modelling OWTNM 2007, Copenhagen, Denmark, April 2007 (oral presentation)

Regular papers:

- R. Ferrini, J. Martz, L. Zuppiroli, B. Wild, **V. Zabelin**, L.A. Dunbar, R. Houdré, M. Mulet, and S. Anand, “Planar photonic crystals infiltrated with liquid crystals: optical characterization of molecule orientation”, *Opt. Letters*, vol. 31, no. 9, pp. 1238-1240, 2006.
- **V. Zabelin**, L.A. Dunbar, N. Le Thomas, R. Houdré, M.V. Kotlyar, L. O’Faolain, and T.F. Krauss, “Self-collimating photonic crystal polarization beam splitter”, *Opt. Letters*, vol. 32, no. 5, pp. 530-532, 2007.
- N. Le Thomas, **V. Zabelin**, R. Houdré, M.V. Kotlyar, and T.F. Krauss, “Influence of residual disorder on the anticrossing of Bloch modes probed in k space”, *Phys. Rev. B*, vol. 71, p. 125301, 2008.
- J. Jágorská, N. Le Thomas, **V. Zabelin**, R. Houdré, W. Bogaerts, P. Dumon, and R. Baets, “Experimental observation of slow mode dispersion in photonic crystal coupled-cavity waveguides”, *Opt. Letters*, vol. 34, no. 3, pp. 359-361, 2009.

Not related to the PhD thesis:

- V.V. Kalaev, **V.A. Zabelin**, and Yu.N. Makarov, “Modeling of impurity transport and point defect formation during Cz Si crystal growth”, *Solid State Phenomena*, vols. 82-84, pp. 41-46, 2002.
- V.V. Kalaev, D.P. Lukanin, **V.A. Zabelin**, Yu.N. Makarov, J. Virbulis, E. Dornberger, W. von Ammon, “Prediction of bulk defects in CZ Si crystals using 3D unsteady calculations of melt convection”, *Materials Science in Semiconductor Processing*, vol. 5, pp. 369-373, 2003.
- V.V. Kalaev, D.P. Lukanin, **V.A. Zabelin**, Yu.N. Makarov, J. Virbulis, E. Dornberger, W. von Ammon, “Calculation of bulk defects in CZ Si growth: impact of melt turbulent fluctuations”, *J. Crystal Growth*, vol. 250, pp. 203-208, 2003.
- **V.A. Zabelin**, V.V. Kalaev, “Modeling of point defect formation in silicon monocrystals”, *Microelectronic Engineering*, vol. 69, pp. 641-645, 2003.
- **V. Zabelin**, D.A. Zakheim, S.A. Gurevich, “AlGaInN LED efficiency improvement advanced by ray-tracing analysis”, *IEEE J. Quantum Electronics*, vol. 40, pp. 1675-1686, 2004.

Curriculum Vitae

Vasily Zabelin

Tel (office): (+41) 21 693 5315

Mobile: (+41) 76 215 8775; (+7) 911 912 8775

E-mail: *vasily.zabelin@gmail.com*

Birthday: 15 June 1980

Nationality: Russian



Professional experience

Institute of Quantum Electronics and Photonics, EPFL, Lausanne, Switzerland

2005–2009

PhD student, research assistant

Numerical modeling of optical properties of photonic crystals. New methods for the calculation of the light modes properties and for the optimization of photonic crystal structures have been developed and used to design photonic crystal based devices.

Laboratory of Semiconductor Quantum Electronics, A.F. Ioffe Institute, Saint-Petersburg, Russia

2003–2004

PhD student, junior research assistant

Theoretical investigation of AlGaInN-based light-emitting diodes. The numerical model of light generation and propagation inside an LED chip has been developed. New methods of light extraction efficiency improvement have been proposed and examined theoretically.

Soft-Impact Ltd, Saint-Petersburg, Russia

2000–2003

Research engineer

Theoretical investigation of point defect formation in silicon single crystal and dislocation formation during crystal growth. The model of point defects evolution and the model of thermo-elastic stress calculation for anisotropic crystals have been developed. The models have been applied in the developed software package for numerical simulation of the crystal growth process and crystal quality prediction.

Education

PhD student, doctoral program in Physics

2005–2009

Institute of Quantum Electronics and Photonics, EPFL, Lausanne, Switzerland

PhD student

2003–2004

Laboratory of Semiconductor Quantum Electronics, A.F. Ioffe Institute RAS, Saint-Petersburg, Russia

M.S. diploma with honours in Physics

1997–2003

Saint-Petersburg State Polytechnic University, Saint-Petersburg, Russia

Professional experience fields

Solid state physics. Semiconductor physics and semiconductor-based devices. Semiconductor light-emitting devices. Optoelectronics, integrated optics, and photonic crystals. Phase transition and point defect formation in amorphous and crystalline materials. Numerical simulation and programming. Programming languages: C/C++, Fortran, Matlab.

Languages

Russian: native language

English: fluent

French: intermediate

Selected awards and honours

- *The best student research project* medal at the National Competition of Student Research Projects, Russia, 2003
- *The 1st Photonics Poster Presentation* award at the Postgraduate Research Conference "PREP2005", Lancaster, UK, 2005
- *The Best Poster Presentation* award at the "Nano and Giga Challenges in Microelectronics" workshop, Moscow, Russia, 2002
- The scholarship for PhD students in theoretical physics from the Dynasty Foundation, 2004
- Six student scholarships for academic achievements from the International Soros Science Educational Program, 1998–2003
- Two student scholarships from the Vladimir Potanin Federal Scholarship Program, 2000–2001